



UNIVERSIDADE TÉCNICA DE LISBOA
INSTITUTO SUPERIOR TÉCNICO

INSTITUTO
SUPERIOR
TÉCNICO

Seismic Vulnerability of *Pombalino* Buildings

Helena Alves Meireles

Supervisor: Doctor Rita Maria do Pranto Nogueira Leite Pereira Bento
Co-Supervisor: Doctor Andreas Kappos

**Thesis approved in public session to obtain the PhD
Degree in Civil Engineering**

Jury final classification

Pass with Merit

Jury

Chairperson: Chairman of the IST Scientific Board

Members of the Committee:

Doctor Sergio Lagomarsino, Professor Catedrático da Universidade de Génova, Itália

Doctor Andreas Kappos, Professor Catedrático da Universidade Aristotle Thessaloniki, Grécia

Doctor Humberto Salazar Amorim Varum, Professor Associado (com Agregação) da Universidade de Aveiro

Doctor Rita Maria do Pranto Nogueira Leite Pereira Bento, Professora Associada (com Agregação) do Instituto Superior Técnico da Universidade Técnica de Lisboa

Doctor Augusto Martins Gomes, Professor Associado do Instituto Superior Técnico da Universidade Técnica de Lisboa

Doctor Mário Manuel Paisana dos Santos Lopes, Professor Auxiliar do Instituto Superior Técnico da Universidade Técnica de Lisboa

Funding Institutions

Fundaçao para a Ciênci a e Tecnologia

2012

Abstract

The heritage value of the mixed wood-masonry 18th century *Pombalino* buildings of downtown Lisbon is recognized both nationally and internationally. The present thesis focuses, first, on the definition of soil characteristics of downtown Lisbon and on the definition of seismic action for assessment. The site selected (downtown Lisbon) is set on an alluvium-filled valley of soft, unconsolidated sediments where considerable seismic site amplification of ground motion is expected. Despite the importance and susceptibility of the site, not much information is available in the literature on seismic ground characterization. Therefore, data has been gathered from various sources, mostly geological and geotechnical surveys. Additional measurements of ambient vibrations have been performed based on the H/V spectral ratio technique (HVSRT). Based on the combination of geological and geotechnical data with HVSRT, it was possible to characterize the alluvium site in terms of average shear wave velocity of the soil ($V_{s,av}$) and depth to bedrock estimates, as well as mapping the site neighbourhoods where seismic ground amplifications are expected. The site $V_{s,av}$ of the soil is estimated at approximately 194 m/s.

Secondly, focus was put on the interior walls of the *Pombalino* buildings, known as “frontal” walls. An experimental campaign to obtain the hysteretic behaviour of these “frontal” walls was carried out using static cyclic shear testing with imposed displacements. A total of three tests were conducted on three identical real size walls. The hysteretic behaviour of such walls subjected to cyclic loading exhibits highly nonlinear force-displacement responses and high ductility.

Thirdly, based on the experimental results obtained, a macro-element was developed for “frontal” walls. This was obtained based on the development of a hysteretic model to describe the cyclic behaviour of the *Pombalino* “frontal” walls. The hysteretic model, based on a phenomenological approach, aims to reproduce the response of a wall under general monotonic, cyclic or earthquake loading and is related to a minimum number of path-following rules. The model was set-up using a series of exponential and linear functions. There are a total of nine identifiable parameters in this model to capture the nonlinear hysteretic response of the wall. These were all calibrated against experimental data.

Finally, the last part of this study focuses on the modelling of a typical *Pombalino* building with a structural software called 3Muri (www.stadata.com) wherein the previously described macro-element for “frontal” walls has been incorporated. The modelling includes macro-elements for the masonry panels and, as a new accomplishment for the state of the art, macro-elements also for the internal “frontal” walls. Pushover analyses were carried out and a seismic assessment of the building was carried out. Beyond this, fragility curves and damage probability plots were obtained. The most important application of such curves is in loss estimation studies and this is suggested work for the future. Last, some retrofitting strategies were also modelled in the 3Muri program and the seismic assessment and fragility analysis were also carried out for these situations.

Keywords: *Pombalino* buildings, H/V spectral ratio technique, cyclic static shear testing, hysteresis curve, macro-element modelling, fragility analysis.

Resumo

O valor patrimonial dos edifícios Pombalinos mistos de alvenaria-madeira do século XVIII da Baixa de Lisboa é reconhecido tanto nacionalmente como internacionalmente. A tese apresentada baseia-se, primeiro, na definição das características do solo da baixa Pombalina e na definição da acção sísmica para avaliação das estruturas. A baixa Pombalina está assente num vale de aluvião com sedimentos brandos e pouco consolidados onde considerável amplificação da acção sísmica é esperada. Apesar da importância e susceptibilidade do local, pouca informação está disponível na literatura para a caracterização sísmica do solo. Consequentemente, foi recolhido de várias fontes informação principalmente geológica e geotecnica. Medições adicionais foram efectuadas baseadas na técnica do H/V rácio espectral. Baseadas na combinação de informação geológica e geotecnica com a técnica do H/V rácio espectral, foi possível caracterizar a Baixa Pombalina em termos de velocidade média das ondas S ($V_{s,av}$) e estimativas de profundidade ao maciço rochoso, assim como demarcar os quarteirões que serão susceptiveis à amplificação da acção sísmica. A $V_{s,av}$ no solo foi estimada igual a aproximadamente 194 m/s.

De seguida, atenção foi dada às paredes frontais dos edifícios Pombalinos. Uma campanha experimental foi levada a cabo tendo-se realizado testes cílicos com imposição de deslocamentos. Um total de três testes foram efectuados em três paredes idênticas à escala real. O comportamento histerético destas paredes exibe uma grande não linearidade e uma grande ductilidade. Como ensaios anteriores em paredes frontais Pombalinhas são bastante escassos, estes resultados são bastante importantes para o estado da arte.

Em terceiro lugar, baseados nos ensaios experimentais, um macro-elemento foi proposto para as paredes frontais. Este é obtido baseado no desenvolvimento de um modelo histerético que descreve o comportamento cílico das paredes frontais. O modelo histerético, baseado numa abordagem fenomenológica, tem como objectivo reproduzir a resposta das paredes sob cargas monotónicas, cílicas ou sísmicas. O modelo é construído com uma série de funções lineares e exponenciais. Há um total de nove parâmetros para definir a resposta não-linear histerética da parede. Estes parâmetros são calibrados com os resultados experimentais.

Finalmente, a última parte, é dedicada à modelação de um edifício tipo Pombalino com um programa estrutural chamado 3Muri (www.stadata.com) onde o macro-elemento descrito previamente foi incorporado. A modelação inclui macro-elementos para as paredes de alvenaria, e também, como uma contribuição nova para o estado da arte, macro-elementos para as paredes frontais. Análises *pushover* foram desenvolvidas e a avaliação sísmica dos edifícios foi efectuada. De seguida, curvas de fragilidade e gráficos de probabilidade de danos foram obtidos. A aplicação mais importante destas curvas é em estudos de perdas e isto é proposto como trabalho futuro. Por último, técnicas de reforço foram também propostas e modeladas no 3Muri e a avaliação sísmica das estruturas efectuada assim como as análises de fragilidade.

Palavras-chave: Edifícios Pombalinos, H/V técnica do rácio espectral, ensaios cílicos com imposição de deslocamentos, curvas histeréticas, modelação com macro-elementos, análise de fragilidade.

Acknowledgements

This space is dedicated to those who have contributed towards the completion of this dissertation. To all of them I would like to pass on my sincere gratitude.

The author would like to acknowledge the financial support of the Portuguese Foundation for Science and Technology (Ministry of Science and Technology of Portugal) through the research project PTDC/ECM/100872/2008 and through the PhD scholarship SFRH/BD/41710/2007.

In Chapter 3, the author also strongly acknowledges the indispensable contribution to this work of the following: SOPECATE (Teresa Simões), Tecnasol FGE (Pedro Lopes and Paulo Rodrigues), COMPOREST, Geocontrole (Carlos Sacadura), Rodio (Ricardo Nicolas), CML-Câmara Municipal de Lisboa (geology dept. and Baixa-Chiado dept.), João Fonseca, Carlos Sousa Oliveira and Joana Pinho.

In Chapter 4, the helpful advice of Doctor António Sousa Gago, Engineer Pedro Palma and Doctor Jorge Proença for the work carried out at the structural laboratory of IST is also acknowledged.

In Chapter 6 my gratitude goes to Doctor Sergio Lagomarsino and Doctor Serena Cattari for kindly hosting me for 3 months at the University of Genoa, Italy.

Acknowledgement is also due to Doctor Rita Bento and Doctor Andreas Kappos for their valuable guidance regarding the orientation of the work, and to Doctor Rui Pinho for his comments and orientation in the initial part of the work.

A very special acknowledgement to the indispensable support of the friends made in my four years at IST and beyond, for making the most difficult moments less heavy. Last but not least, to my family, for their patience, tolerance and infinite support in my decision to endeavour in my PhD.

Index

ABSTRACT	3
RESUMO	5
ACKNOWLEDGEMENTS	7
INDEX.....	8
LIST OF FIGURES.....	11
LIST OF TABLES.....	16
LIST OF SYMBOLS.....	18
LIST OF ABBREVIATIONS.....	20
1. INTRODUCTION	23
1.1. INITIAL CONSIDERATIONS	23
1.2. OBJECTIVES.....	23
1.3. THESIS OUTLINE.....	24
2. THE POMBALINO BUILDINGS.....	27
2.1. HISTORICAL BACKGROUND	27
2.2. CONSTRUCTING ELEMENTS OF POMBALINO BUILDINGS	38
2.2.1. <i>The foundation system</i>	39
2.2.2. <i>The ground floor</i>	40
2.2.3. <i>The gaiola: “frontal” walls and floors</i>	41
2.2.4. <i>The façade</i>	47
2.2.5. <i>The roof</i>	48
2.2.6. <i>The stairs</i>	48
2.2.7. <i>The floor plan</i>	49
2.3. SIMILAR CONSTRUCTIONS	50
2.4. BIBLIOGRAPHY.....	55
3. DEFINITION OF THE SOIL CHARACTERISTICS AND SEISMIC ACTION FOR ASSESSMENT	59
3.1. SUMMARY	59
3.2. INTRODUCTION.....	59
3.3. PRIOR INVESTIGATION OF THE SITE.....	61
3.4. H/V MEASUREMENT TECHNIQUE FOR SITE CHARACTERIZATION.....	63
3.4.1. <i>Method and assumptions</i>	63
3.4.2. <i>Measurements</i>	66
3.4.3. <i>Processing</i>	68
3.4.4. <i>Interpretation</i>	69
3.4.4.1. Measurement point PF	71
3.4.4.2. Measurement point DN	72
3.4.4.3. Measurement point P12	73
3.4.4.4. Measurement point P11	74
3.4.4.5. Measurement point P89	75
3.4.4.6. Measurement point SC	75
3.4.4.7. Measurement point S2a	76
3.4.4.8. Measurement point P10	78
3.4.4.9. Measurement point P6	78
3.4.4.10. Measurement point S3	79
3.5. DISCUSSION.....	79
3.6. CONCLUSIONS	83

3.7. BIBLIOGRAPHY.....	84
4. CYCLIC LOAD TESTING OF POMBALINO “FRONTAL” WALLS.....	87
4.1. SUMMARY	87
4.2. INTRODUCTION.....	87
4.3. DESCRIPTION OF THE SUBASSEMBLY	94
4.4. DESCRIPTION OF THE EXPERIMENTAL SET-UP	97
4.5. DEFINITION OF THE LOADING PROTOCOL.....	100
4.6. VERTICAL LOADING CALCULATION	101
4.7. RESULTS.....	102
4.8. CONCLUSIONS	112
4.9. BIBLIOGRAPHY.....	112
5. DEVELOPMENT AND VALIDATION OF A MACRO-ELEMENT FOR “FRONTAL” WALLS.....	115
5.1. SUMMARY	115
5.2. INTRODUCTION.....	115
5.3. LATERAL DISPLACEMENT MECHANISMS	116
5.4. MASONRY FILLING.....	119
5.5. PINCHING EFFECT	121
5.6. PROPOSED MACRO-ELEMENT MODEL	122
5.6.1. <i>Hysteresis model - Presentation of the model</i>	123
5.6.2. <i>Path-following rules</i>	124
5.6.3. <i>Definition of the envelope curves</i>	124
5.6.4. <i>Definition of the unloading curves</i>	125
5.6.5. <i>Definition of the reloading curves</i>	126
5.6.6. <i>Small cycle hysteresis</i>	128
5.7. CALIBRATION OF THE PARAMETERS	129
5.7.1. <i>Force intercept parameter - Z</i>	129
5.7.2. <i>Envelope curve parameters - F_0, K_0, r_l, r_u, F_u, δ_{ult}</i>	130
5.7.3. <i>Unloading curve parameters - α, λ_u</i>	131
5.7.4. <i>Reloading curve parameter - a</i>	132
5.8. EXPERIMENTAL VERSUS ANALYTICAL HYSTERESIS	133
5.9. EXAMPLES OF HYSTERETIC MODEL RESPONSES FOR DIFFERENT INPUT LOADING ..	134
5.10. OTHER CONFIGURATIONS OF WALLS.....	138
5.10.1. <i>Experimental initial stiffness estimation</i>	138
5.10.2. <i>Analytical modelling of the wall</i>	139
5.10.3. <i>Initial stiffness for other configurations of walls and for other Young's modulus</i>	143
5.10.4. <i>Strength associated with collapse of most loaded diagonal</i>	144
5.10.5. <i>Estimation of strength for other configurations of walls</i>	146
5.10.6. <i>Envelope curves for other configurations of walls</i>	149
5.10.7. <i>Estimation of hysteresis curve for experimental test G2 of LNEC</i>	150
5.11. CONCLUSIONS	151
5.12. BIBLIOGRAPHY	151
6. MACRO-ELEMENT APPROACH FOR THE SEISMIC ANALYSIS OF A POMBALINO BUILDING	153
6.1. SUMMARY	153
6.2. OVERVIEW OF METHODS USED	153
6.2.1. <i>Software TREMURI</i>	156
6.2.2. <i>Nonlinear static procedures</i>	157
6.2.3. <i>Fragility analysis</i>	162
6.2.4. <i>Soil-structure interaction</i>	164

6.3. CASE STUDY	165
6.4. ORIGINAL BUILDING – ANALYSIS AND RESULTS.....	172
6.5. STRENGTHENING SOLUTIONS	177
6.5.1. <i>Increase the in-plane stiffness of floors.....</i>	178
6.5.2. <i>Increase the in-plane stiffness of floors plus reinforcement of five ground floor pillars</i>	186
6.5.3. <i>Increase the in-plane stiffness of floors plus inclusion of four shear walls on the ground floor</i>	190
6.5.4. <i>Increase the in-plane stiffness of floors plus inclusion of eight steel frames on the ground floor.....</i>	194
6.5.5. <i>Increase the in-plane stiffness of floors plus inclusion of tie-rods at front and back façades.....</i>	198
6.6. COMPARISON OF THE SEVERAL RETROFITTING STRATEGIES	202
6.7. FRAGILITY ANALYSIS.....	204
6.7.1. <i>Definition of damage limit states</i>	204
6.7.2. <i>Fragility curves and damage probabilities</i>	204
6.7.2.1. Original building.....	205
6.7.2.2. Increase the in-plane stiffness of floors.....	207
6.7.2.3. Increase the in-plane stiffness of floors plus reinforcement of five ground floor pillars	209
6.7.2.4. Increase the in-plane stiffness of floors plus inclusion of four shear walls on the ground floor	211
6.7.2.5. Increase the in-plane stiffness of floors plus inclusion of steel frames on the ground floor	213
6.7.2.6. Increase the in-plane stiffness of floors plus inclusion of tie-rods at front and back façades.....	215
6.7.2.7. Comparison between original building and retrofitted cases.....	217
6.8. CONCLUSIONS	219
6.9. BIBLIOGRAPHY.....	220
7. FINAL CONCLUSIONS AND FURTHER WORK.....	223
ANNEX A	227
ANNEX B	229

List of figures

FIGURE 2-1: THE <i>BAIXA POMBALINA</i> SEEN FROM AN AERIAL VIEW [HTTP://MJFS.WORDPRESS.COM/CATEGORY/MADRE-DEUS/]	27
FIGURE 2-2: PLAN OF LISBON BEFORE THE 12 TH CENTURY [JULIO DE CASTILHO, 1893]	29
FIGURE 2-3: BIPARTITE GERMAN ENGRAVING. ABOVE THE REPRESENTATION OF THE CITY BEFORE THE EARTHQUAKE OF 1755. BELOW THE REPRESENTATION OF THE FIRE AND TSUNAMI THAT STRUCK THE CITY IN 1755. [AUGSBURG, MATTHAUS SEUTTER, S. COES MAG. GEORG. AUG. VINDEL, AROUND 1756.].....	31
FIGURE 2-4: ABOVE, LISBON BEFORE THE 1755 EARTHQUAKE. BELOW, SEVERAL FIRES CAUSED BY THE CATACLYSM. [ZURICH, DAVID KERLIBERG, 1756].....	32
FIGURE 2-5: PICTURE OF JOSÉ I, KING OF PORTUGAL, WHILE ORDERING THE RE-BUILDING OF LISBON DESTROYED BY THE EARTHQUAKE. [VENICE, P. NOVELLI, ANTONIO ZATTA AND FIGLI, 1757 – 1797]	33
FIGURE 2-6: LIMITS OF THE FIRE THAT STRUCK THE CAPITAL AFTER THE EARTHQUAKE IN DASHED LINE AND THE MOST Affected AREAS OF THE EARTHQUAKE OF 1755 IN ORANGE	34
FIGURE 2-7: MARQUIS OF <i>POMBAL</i> IN PAINTING.....	35
FIGURE 2-8: ENGINEER MANUEL DA MAIA (1672-1768)	36
FIGURE 2-9: ARCHITECT EUGÉNIO DOS SANTOS DE CARVALHO (1711-1760) [AUTHOR NOT IDENTIFIED, 18 TH CENTURY, ASSOCIATION OF THE PORTUGUESE ARCHAEOLOGISTS]	37
FIGURE 2-10: THE WINNING PLAN OF THE RECONSTRUCTION	38
FIGURE 2-11: EXAMPLE OF A <i>POMBALINO</i> BUILDING [MASCARENHAS, 1996].....	39
FIGURE 2-12: THE FOUNDATION SYSTEM [MASCARENHAS, 1996].....	40
FIGURE 2-13: TWO FOUNDATION PILES UNDER WATER	40
FIGURE 2-14: LEFT: GROINED VAULTS OVER THE ARCHES; RIGHT: WOODEN FLOORS, ARCHES AND PIERS [MASCARENHAS, 1996]	41
FIGURE 2-15: PHOTO OF BRICK GROINED VAULT ON THE GROUND FLOOR.....	41
FIGURE 2-16: THE <i>GAIOLA</i> : FLOORS AND “FRONTAL” WALL [PINTO COSTA, 1993].....	42
FIGURE 2-17: “FRONTAL” WALL OF 3X2 MODULES	42
FIGURE 2-18: “FRONTAL” WALL OF 3X3 MODULES	43
FIGURE 2-19: “FRONTAL” WALL OF 3X4 MODULES	43
FIGURE 2-20: “FRONTAL” WALL OF 2 MODULES HIGH.....	44
FIGURE 2-21: DETAILS OF THE MIDDLE CENTRAL CONNECTION.....	44
FIGURE 2-22: DIAGONAL ELEMENTS CONNECTING DETAILS	44
FIGURE 2-23: “FRONTAL” WALL CONNECTION DETAILS (A) LEFT MIDDLE CONNECTION (B) UPPER MIDDLE CONNECTION (C) MIDDLE CENTRAL CONNECTION	45
FIGURE 2-24: DETAIL OF THE CONNECTION OF THE FLOORS WITH (A) THE FAÇADES; (B) THE “FRONTAL” WALLS (LEGEND IN PORTUGUESE) [RAMOS, 2002].....	45
FIGURE 2-25: CONNECTION DETAIL OF “FRONTAL” WALL AT FLOOR 1 WITH UPPER FLOOR 2	46
FIGURE 2-26: OTHER POSSIBLE TRUSS LAYOUTS FOR “FRONTAL” WALLS. [1755 O GRANDE TERRAMOTO DE LISBOA, 2005]	46
FIGURE 2-27: DETAILS OF THE “FRONTAL” WALLS COVERED WITH LATH IN A BUILDING IN GUIMARÃES.....	46
FIGURE 2-28: A TYPICAL FAÇADE OF THE BUILDINGS [DRAWING BY SEBASTIÃO JOSEPH DE CARVALHO E MELLO AND EUGÉNIO DOS SANTOS E CARVALHO, TAKEN FROM 1755 O GRANDE TERRAMOTO DE LISBOA, 2005].....	47
FIGURE 2-29: CUT OF THE MAIN AND BACK MASONRY FAÇADES [1755 O GRANDE TERRAMOTO DE LISBOA, 2005].....	48
FIGURE 2-30: ABOVE: MANSARD ROOF; BELOW: HIPPED ROOF [MASCARENHAS, 1996].....	48
FIGURE 2-31: THE STRUCTURE OF THE STAIRS [MASCARENHAS, 1996]	49
FIGURE 2-32: THE FIRST FLOOR PLAN OF A GIVEN BLOCK [MASCARENHAS, 1996]	49
FIGURE 2-33: THE PLAN VIEW WITH THREE DIVISION FRONTS [MASCARENHAS, 1996].....	50
FIGURE 2-34: CASA BARACCATA.....	51
FIGURE 2-35: HİMİŞ HOUSE IN GöLCÜK, TURKEY [LANGENBACH, 2008].....	51
FIGURE 2-36: DHAJJI-DEWARI CONSTRUCTION IN SRINAGAR, KASHMIR IN 1989 [LANGENBACH, 2003]	52

FIGURE 2-37: TYPICAL MORPHOLOGY OF TIMBER-FRAMED MASONRY INFILL WALLS OF LEFKAS ISLAND, GREECE [VINTZILEOU, 2007].....	52
FIGURE 2-38: DETAILS OF THE FOUNDATION OF TRADITIONAL BUILDINGS OF TOWN OF LEFKAS, GREECE [MAKARIOS, 2006].....	53
FIGURE 2-39: THE DUAL BEARING SYSTEM OF TRADITIONAL BUILDINGS IN LEFKAS [MAKARIOS, 2006].....	53
FIGURE 2-40: GINGER-BREAD HOUSE IN HAITI - BUILDING.....	54
FIGURE 2-41: GINGER-BREAD HOUSE IN HAITI - FAÇADE.....	54
FIGURE 2-42: A TRADITIONAL HOUSE IN LUND (SWEDEN) [COPANI, 2007].....	55
FIGURE 3-1: LOCATION OF THE SITE WITHIN THE URBAN AREA OF LISBON. THE EXTENSION OF THE AREA (WITHIN THE STREETS MARKED IN GREEN) IS ABOUT 250 M WIDE BY 490 M LONG, COMPRISING 36 BLOCKS. MAP IS COPYRIGHT OF GOOGLE EARTH.....	61
FIGURE 3-2: GEOLOGICAL MAP OF THE MUNICIPALITY OF LISBON, SCALE 1/10 000, SHEET 4 (LEGEND IN PORTUGUESE)	62
FIGURE 3-3: COMPARISON BETWEEN H/V RATIO OF AMBIENT VIBRATIONS AND STANDARD SPECTRAL RATIO OF EARTHQUAKES. (A) COMPARISON OF PEAK FREQUENCIES F_0 , (B) COMPARISON OF PEAK AMPLITUDES A_0 [DELIVERABLE D13.08].....	65
FIGURE 3-4: LOCATION OF THE GEOTECHNICAL SURVEYS AVAILABLE (RED DOTS) AND OF THE SELECTED MEASUREMENT POINTS FOR RECORDING OF AMBIENT VIBRATIONS (BLACK DOTS)	67
FIGURE 3-5: H/V CURVE OBTAINED FOR MEASUREMENT POINT PF	71
FIGURE 3-6: H/V CURVE OBTAINED FOR MEASUREMENT POINT DN.....	72
FIGURE 3-7: H/V CURVE OBTAINED FOR MEASUREMENT POINT P12	73
FIGURE 3-8: H/V CURVE OBTAINED FOR MEASUREMENT POINT P11	74
FIGURE 3-9: H/V CURVE OBTAINED FOR MEASUREMENT POINT P89	75
FIGURE 3-10: H/V CURVE OBTAINED FOR MEASUREMENT POINT SC	75
FIGURE 3-11: H/V CURVE OBTAINED FOR MEASUREMENT POINT S2A	76
FIGURE 3-12: H/V CURVE OBTAINED FOR MEASUREMENT POINT P10.....	78
FIGURE 3-13: H/V CURVE OBTAINED FOR MEASUREMENT POINT P6	78
FIGURE 3-14: H/V CURVE OBTAINED FOR MEASUREMENT POINT S3	79
FIGURE 3-15: COMPARISON OF THE OBTAINED H/V CURVES IN ALL MEASURED POINTS	80
FIGURE 3-16: ELASTIC RESPONSE SPECTRUM FOR LISBON DOWNTOWN	81
FIGURE 3-17: INTERPRETATIVE CUTS OF GROUND PROFILE (NO HORIZONTAL SCALE).....	82
FIGURE 4-1: PHOTOGRAPH OF “FRONTAL” G2 WOOD TRUSS, TAKEN AT LNEC.....	88
FIGURE 4-2: AT WALL G2: (A) CONNECTION TYPE B AT THE LEFT CORNER AND FIRST ROW OF NODES, (B) CONNECTION TYPE A AT THE LEFT CORNER AND SECOND ROW OF NODES AND (C) CONNECTION TYPE A AT THE MIDDLE AND SECOND ROW OF NODES.....	88
FIGURE 4-3: NAILS FOUND IN “FRONTAL” WALLS IN LNEC SPECIMEN.....	88
FIGURE 4-4: SCHEMATIC DRAWING OF THE LAYOUT OF EXPERIMENT AT LNEC, POMPEU SANTOS [1997]	89
FIGURE 4-5: PHOTOGRAPH OF THE “FRONTAL” WALL MOUNTED, POMPEU SANTOS [1997].....	89
FIGURE 4-6: PHOTOGRAPH OF THE WALL WHILE BEING TESTED, POMPEU SANTOS [1997]	90
FIGURE 4-7: SCHEMATIC OF CONCRETE SHOE FOR SUPPORT CONDITIONS IN EXPERIMENTAL SET-UP OF POMPEU SANTOS [1997].....	90
FIGURE 4-8: DIAGRAM LATERAL FORCES VERSUS TOP DISPLACEMENTS IN “FRONTAL” WALL G1, POMPEU SANTOS [1997].....	91
FIGURE 4-9: DIAGRAM LATERAL FORCES VERSUS TOP DISPLACEMENTS IN “FRONTAL” WALL G2, POMPEU SANTOS [1997].....	91
FIGURE 4-10: DIAGRAM LATERAL FORCES VERSUS TOP DISPLACEMENTS IN “FRONTAL” WALL G3, POMPEU SANTOS [1997].....	92
FIGURE 4-11: DIAGONAL COMPRESSION APPARATUS OF THE WALL PANEL, CRUZ ET AL. [2001]	93
FIGURE 4-12: FORCE-DISPLACEMENT DIAGRAMS OBTAINED IN DIAGONAL COMPRESSION OF THE WALL PANELS, PRIOR TO AND AFTER STRENGTHENING, 1REF TO 6REF: STRENGTHENED PANELS; 2 TO 6: INITIAL STATE PANELS; CRUZ ET AL. [2001].....	93
FIGURE 4-13: SCHEMATIC OF THE “FRONTAL” WALL SPECIMEN (UNITS IN METERS OTHERWISE SPECIFIED)	94
FIGURE 4-14: NAILS USED IN THE PRESENT STUDY	95
FIGURE 4-15: ELEMENTS OF THE WALL SET HORIZONTALLY ON THE FLOOR.....	96
FIGURE 4-16: PLACING THE WALLS IN THE VERTICAL POSITION: (A) FRONT VIEW, (B) SIDE VIEW	96
FIGURE 4-17: STEEL SHAPED OMEGAS TO TIGHTEN THE LOWER WOOD BEAM (BROWN) TO THE HORIZONTAL REACTION BEAM (YELLOW)	96

FIGURE 4-18: CLOSE-UP VIEW OF THE MASONRY FILLING.....	97
FIGURE 4-19: WALL ON TOP OF THE HORIZONTAL REACTION BEAM (A) WITH HEAVY CORDS, (B) WITH LATERAL BRACES AND (C) WITH LATERAL ROLLER BEARINGS	98
FIGURE 4-20: (A) LEFT HORIZONTAL BEARING; (B) RIGHT HORIZONTAL BEARING; (C) PRE-STRESSING SCHEME	98
FIGURE 4-21: FINAL LAYOUT OF THE EXPERIMENT WITH LOAD CELL, LVDT AND JACKS	99
FIGURE 4-22: SCHEMATIC DRAWING OF SPECIMEN SC MOUNTED	99
FIGURE 4-23: SYSTEM OF ANCHORAGE ONTO THE HORIZONTAL REACTION BEAM.....	100
FIGURE 4-24: THE LOADING PROTOCOL FOR THE TESTS PERFORMED	101
FIGURE 4-25: HYSTERESIS CURVE OF WALL SC1	102
FIGURE 4-26: DETACHMENT OF THE MASONRY FROM THE WOOD TRUSS	103
FIGURE 4-27: FAILURE BY CRACKING OF THE WOOD AT THE CONNECTIONS: (A) N1A, (B) N1B, (C) N1C. PHOTO AT A DISPLACEMENT OF PLUS 90 MM	103
FIGURE 4-28: FAILURE BY PULL OUT OF NAILS AT CONNECTION N1D AT A DISPLACEMENT OF PLUS 90 MM	103
FIGURE 4-29: DETAILED OF THE CONNECTIONS AT A LOADING OF PLUS 60 MM (FROM THE RIGHT TO THE LEFT).....	104
FIGURE 4-30: DETAILED OF THE CONNECTIONS AT A LOADING OF MINUS 60 MM (FROM THE LEFT TO THE RIGHT)	104
FIGURE 4-31: REINFORCEMENT LAYOUT AT THE UPPER AND LOWER ROWS OF CONNECTIONS IN SPECIMEN: (A) SC2 AND (B) SC3	105
FIGURE 4-32: HYSTERESIS CURVE OF WALL SC2	105
FIGURE 4-33: BEHAVIOUR OF THE UPPER CONNECTIONS AT DISPLACEMENT OF 90 MM. (A) NODE N2A, (B) NODE N2C.....	106
FIGURE 4-34: BEHAVIOUR OF THE CONNECTION N2D WITH ALMOST PULL OUT OF NAILS	106
FIGURE 4-35: BUCKLING OF DIAGONAL IN THE UPPER MODULE: (A) FRONT; (B) BACK.....	107
FIGURE 4-36: HYSTERESIS CURVE OF WALL SC3	107
FIGURE 4-37: DETACHMENT OF THE MASONRY PANEL FROM THE WOOD TRUSS.....	107
FIGURE 4-38: INITIAL OUT OF PLANE INSTABILITY OF THE UPPER LEFT MODULE, DISPLACEMENT OF 60 MM IN THE POSITIVE DIRECTION OF LOADING	108
FIGURE 4-39: FAILURE BY BUCKLING OF THE UPPER LEFT MODULE DIAGONAL, DISPLACEMENT OF 90 MM IN THE POSITIVE DIRECTION OF LOADING: (A) SIDE, (B) BACK	108
FIGURE 4-40: FAILURE OF DIAGONAL OF LOWER LEFT MODULE: (A) FRONT, (B) BACK; AT DISPLACEMENT OF 90 MM IN THE NEGATIVE DIRECTION OF LOADING	109
FIGURE 4-41: GENERAL STATE OF THE WALL CORRESPONDING TO A DISPLACEMENT OF 120 MM IN THE POSITIVE DIRECTION OF LOADING: (A) COMPLETE WALL, (B) LOWER LEFT MODULE.....	109
FIGURE 4-42: EXPERIMENTAL ENVELOPE CURVES.....	110
FIGURE 4-43: CUMULATIVE ENERGY FOR THE THREE TESTS, WALLS SC1, SC2 AND SC3	111
FIGURE 4-44: STIFFNESS DEGRADATION FOR THE THREE TESTS, WALLS SC1, SC2 AND SC3	111
FIGURE 5-1: EQUIVALENT ROCKING LATERAL DISPLACEMENT MECHANISM.....	117
FIGURE 5-2: (A) BEHAVIOUR OF THE CONNECTION Ng, UPWARDS MOVEMENT (B) BEHAVIOUR OF THE CONNECTION Ni, DOWNWARDS MOVEMENT.....	117
FIGURE 5-3: EQUIVALENT SHEAR LATERAL DISPLACEMENT MECHANISM.....	118
FIGURE 5-4: LATERAL DISPLACEMENTS DUE TO EQUIVALENT ROCKING AT COLLAPSE (UNITS IN M).....	118
FIGURE 5-5: LATERAL DISPLACEMENTS DUE TO EQUIVALENT SHEAR AT COLLAPSE [UNITS IN M].....	119
FIGURE 5-6: (A) ORIGINAL MODULE (B) DISTORTED MODULE AT COLLAPSE.....	120
FIGURE 5-7: GAP BETWEEN LOOSE DIAGONAL AND TIMBER FRAME AND DETACHMENT OF MASONRY FILLING FROM TIMBER FRAME	120
FIGURE 5-8: SKETCH OF PINCHING EFFECT.....	121
FIGURE 5-9: HYSTERESIS BEHAVIOUR WITH PINCHING EFFECT	121
FIGURE 5-10: PULL-OUT OF NAILS LEADING TO GAPS AND RESIDUAL DISPLACEMENTS; MASONRY CRACK	122
FIGURE 5-11: HYSTERESIS MODEL.....	123
FIGURE 5-12: HYSTERESIS MODEL: UNLOADING	125
FIGURE 5-13: HYSTERESIS MODEL: RELOADING.....	127
FIGURE 5-14: TYPICAL CYCLIC RESPONSE WITH SMALL CYCLE HYSTERESIS FOR CONCRETE [CRISAFULLI, 1997]	128
FIGURE 5-15: MODEL ASSUMPTIONS FOR THE SMALL CYCLE HYSTERESIS.....	129
FIGURE 5-16: AVERAGE FORCE INTERCEPT POINT Z	130

FIGURE 5-17: ANALYTICAL EXPONENTIAL ENVELOPE CURVE AND EXPERIMENTAL POINTS.....	131
FIGURE 5-18: ANALYTICAL LINEAR ENVELOPE CURVE AND EXPERIMENTAL POINTS.....	131
FIGURE 5-19: UNLOADING CURVE PARAMETER A.....	132
FIGURE 5-20: UNLOADING CURVE PARAMETER A_u	132
FIGURE 5-21: PARAMETER A AS A FUNCTION OF THE DAMAGE.....	133
FIGURE 5-22: RELOADING CURVE COEFFICIENT RL AS A FUNCTION OF DAMAGE.....	133
FIGURE 5-23: EXPERIMENTAL VERSUS ANALYTICAL HYSTERESIS.....	134
FIGURE 5-24: INPUT LOADING FOR TEST 1.....	135
FIGURE 5-25: MODEL RESPONSE FOR TEST 1.....	135
FIGURE 5-26: INPUT LOADING FOR TEST 2.....	135
FIGURE 5-27: MODEL RESPONSE FOR TEST 2.....	136
FIGURE 5-28: INPUT LOADING FOR TEST 3.....	136
FIGURE 5-29: MODEL RESPONSE FOR TEST 3	136
FIGURE 5-30: INPUT LOADING FOR TEST 4.....	137
FIGURE 5-31: MODEL RESPONSE FOR TEST 4.....	137
FIGURE 5-32: INPUT LOADING FOR TEST 5.....	138
FIGURE 5-33: MODEL RESPONSE FOR TEST 5	138
FIGURE 5-34: ANALYTICAL MODEL ADOPTED FOR ESTIMATING INITIAL STIFFNESS (UNITS IN METERS).....	139
FIGURE 5-35: CONFIGURATIONS OF WALLS STUDIED.....	143
FIGURE 5-36: ANALYTICAL/STRUCTURAL MODEL ADOPTED FOR ESTIMATING COLLAPSE LOAD	145
FIGURE 5-37: AXIAL FORCES IN MEMBERS FOR WALL BEING LOADED WITH UNIT LOADS ($E_{WOOD}=12\,000$ MPA, CONFIGURATION 2x2)	145
FIGURE 5-38: AXIAL FORCES IN MEMBERS FOR WALL BEING LOADED WITH UNIT LOADS WITH $E_{WOOD}=6000$ MPA	146
FIGURE 5-39: AXIAL FORCES IN MEMBERS FOR WALL BEING LOADED WITH UNIT LOADS, CONF 2x3.....	147
FIGURE 5-40: AXIAL FORCES IN MEMBERS FOR WALL BEING LOADED WITH UNIT LOADS, CONF 2x4.....	147
FIGURE 5-41: AXIAL FORCES IN MEMBERS FOR WALL BEING LOADED WITH UNIT LOADS, CONF 3x2.....	147
FIGURE 5-42: AXIAL FORCES IN MEMBERS FOR WALL BEING LOADED WITH UNIT LOADS, CONF 3x3.....	148
FIGURE 5-43: AXIAL FORCES IN MEMBERS FOR WALL BEING LOADED WITH UNIT LOADS, CONF 3x4.....	148
FIGURE 5-44: VARIOUS ENVELOPE CURVES FOR DIFFERENT WALL CONFIGURATIONS	150
FIGURE 5-45:LNEC EXPERIMENTAL VERSUS ANALYTICAL HYSTERESIS.....	150
FIGURE 6-1: IN-PLANE FAILURE MECHANISMS (SECOND-MODE): A) SHEAR FAILURE (DIAGONAL CRACKING); B) ROCKING/FLEXURE FAILURE; C) SLIDING-SHEAR FAILURE [MACCHI AND MAGENES 2002]	154
FIGURE 6-2: MASONRY PANELS FAILURE MECHANISM OBSERVATION [COSTA, 2007].....	155
FIGURE 6-3: INFLUENCE OF AXIAL LOAD ON PANELS FAILURE MODES [COSTA, 2007]	155
FIGURE 6-4: MASONRY PANELS FOR A WALL. [CATTARI ET AL., 2005]	156
FIGURE 6-5: EQUIVALENT FRAME MODEL FOR A MASONRY WALL [KAPPoS ET AL., 2002]	156
FIGURE 6-6: SKETCH OF FAÇADE OF BUILDING (FRONT) – UNITS IN METRES.....	165
FIGURE 6-7: SKETCH OF FAÇADE OF BUILDING (BACKWARDS) – UNITS IN METRES.....	166
FIGURE 6-8: SKETCH OF THE PLAN VIEW OF BUILDING: GROUND FLOOR – UNITS IN METRES.....	166
FIGURE 6-9: SKETCH OF THE PLAN VIEW OF BUILDING: UPPER FLOORS – UNITS IN METRES	167
FIGURE 6-10: SECTIONS OF FLOOR JOISTS AND PAVEMENT (MATERIAL WOOD) – UNITS IN CM	168
FIGURE 6-11: SKETCH OF PLAN VIEW OF BUILDING: FLOOR ACTIONS – UNITS IN METRES.....	168
FIGURE 6-12: GROUND FLOOR MODELLING ELEMENTS	169
FIGURE 6-13: FINAL MODEL OF THE BUILDING	170
FIGURE 6-14: NUMBERING THE ALIGNMENTS OF THE ELEMENTS OF THE MODEL	171
FIGURE 6-15: MACRO-ELEMENT MESH OF FRONT FAÇADE	171
FIGURE 6-16: MACRO-ELEMENT MESH OF BACK FAÇADE	172
FIGURE 6-17: PUSHOVER CURVES FOR ORIGINAL BUILDING IN THE TWO DIRECTIONS FOR BOTH UNIFORM AND TRIANGULAR LOAD PATTERNS	172
FIGURE 6-18: BI-LINEARIZATION OF THE FORCE-DISPLACEMENT RELATIONSHIPS.....	173
FIGURE 6-19: BI-LINEARIZED CURVE IN THE XX DIRECTION FOR ORIGINAL BUILDING.....	174
FIGURE 6-20: BI-LINEARIZED CURVE IN THE YY DIRECTION FOR ORIGINAL BUILDING.....	174
FIGURE 6-21: CAPACITY DIAGRAM IN AD FORMAT IN THE XX DIRECTION	175
FIGURE 6-22: CAPACITY DIAGRAM IN AD FORMAT IN THE YY DIRECTION	176
FIGURE 6-23: (A) EXAMPLE OF THE REINFORCEMENT OF A WOODEN FLOOR WITH A COOPERATING REINFORCED-CONCRETE SLAB, (WWW.TECNARIA.COM) (B) BASIC CONNECTORS TECNARIA (WWW.TECNARIA.COM)	179

FIGURE 6-24: IN-PLANE STIFFENING WITH METALLIC DIAGONALS AND REINFORCEMENT OF CONNECTION FLOOR-WALL [PICTURE FROM EDIFER]	179
FIGURE 6-25: PUSHOVER CURVES, CONTRIBUTION OF EACH WALL TO THE BASE SHEAR, XX DIRECTION	180
FIGURE 6-26: PUSHOVER CURVES, CONTRIBUTION OF EACH WALL TO THE BASE SHEAR, YY DIRECTION	180
FIGURE 6-27: COMPARISON BETWEEN A MASONRY WALL AND A “FRONTAL” WALL OF THE SAME DIMENSIONS.....	181
FIGURE 6-28: PUSHOVER CURVES FOR RETROFITTED BUILDING 1 IN THE TWO DIRECTIONS	182
FIGURE 6-29: PILLAR DRIFTS AS A FUNCTION OF THE TOP DISPLACEMENT IN THE XX DIRECTION.....	182
FIGURE 6-30: BI-LINEARIZED CURVE IN THE XX DIRECTION FOR RETROFITTED BUILDING 1.....	183
FIGURE 6-31: PILLAR DRIFTS AS A FUNCTION OF THE TOP DISPLACEMENT IN THE YY DIRECTION.....	183
FIGURE 6-32: BI-LINEARIZED CURVE IN THE YY DIRECTION FOR RETROFITTED BUILDING 1.....	183
FIGURE 6-33: CAPACITY DIAGRAM IN AD FORMAT IN THE XX DIRECTION FOR RETROFITTED BUILDING 1	185
FIGURE 6-34: CAPACITY DIAGRAM IN AD FORMAT IN THE YY DIRECTION FOR RETROFITTED BUILDING 1	185
FIGURE 6-35: PUSHOVER CURVES FOR RETROFITTED BUILDING 2 IN THE TWO DIRECTIONS	186
FIGURE 6-36: PILLAR DRIFTS AS A FUNCTION OF THE TOP DISPLACEMENT IN THE XX DIRECTION.....	187
FIGURE 6-37: BI-LINEARIZED CURVE IN THE XX DIRECTION FOR RETROFITTED BUILDING 2.....	187
FIGURE 6-38: PILLAR DRIFTS AS A FUNCTION OF THE TOP DISPLACEMENT IN THE YY DIRECTION.....	188
FIGURE 6-39: BI-LINEARIZED CURVE IN THE YY DIRECTION FOR RETROFITTED BUILDING 2.....	188
FIGURE 6-40: CAPACITY DIAGRAM IN AD FORMAT IN THE XX DIRECTION FOR RETROFITTED BUILDING 2	189
FIGURE 6-41: CAPACITY DIAGRAM IN AD FORMAT IN THE YY DIRECTION FOR RETROFITTED BUILDING 2	190
FIGURE 6-42: POSITIONING OF THE FOUR SHEAR WALLS AT GROUND FLOOR – UNITS IN METERS	191
FIGURE 6-43: PUSHOVER CURVES FOR RETROFITTED BUILDING 3 IN THE TWO DIRECTIONS	191
FIGURE 6-44: PILLAR DRIFTS AS A FUNCTION OF THE TOP DISPLACEMENT IN THE XX DIRECTION.....	192
FIGURE 6-45: BI-LINEARIZED CURVE IN THE XX DIRECTION FOR RETROFITTED BUILDING 3	192
FIGURE 6-46: CAPACITY DIAGRAM IN AD FORMAT IN THE XX DIRECTION FOR RETROFITTED BUILDING 3	193
FIGURE 6-47: POSITIONING OF THE EIGHT STEEL FRAMES AT GROUND FLOOR – UNITS IN METERS.....	195
FIGURE 6-48: PUSHOVER CURVES FOR RETROFITTED BUILDING 4 IN THE TWO DIRECTIONS	195
FIGURE 6-49: PILLAR DRIFTS AS A FUNCTION OF THE TOP DISPLACEMENT IN THE XX DIRECTION.....	196
FIGURE 6-50: BI-LINEARIZED CURVE IN THE XX DIRECTION FOR RETROFITTED BUILDING 4.....	196
FIGURE 6-51: CAPACITY DIAGRAM IN AD FORMAT IN THE XX DIRECTION FOR RETROFITTED BUILDING 4	197
FIGURE 6-52: PUSHOVER CURVES FOR RETROFITTED BUILDING 5 IN THE TWO DIRECTIONS	199
FIGURE 6-53: PILLAR DRIFTS AS A FUNCTION OF THE TOP DISPLACEMENT IN THE XX DIRECTION.....	199
FIGURE 6-54: BI-LINEARIZED CURVE IN THE XX DIRECTION FOR RETROFITTED BUILDING 5.....	200
FIGURE 6-55: CAPACITY DIAGRAM IN AD FORMAT IN THE XX DIRECTION FOR RETROFITTED BUILDING 5	201
FIGURE 6-56: CAPACITY CURVES COMPARISON IN THE XX DIRECTION	202
FIGURE 6-57: CAPACITY CURVES COMPARISON IN THE YY DIRECTION (NOTE: “RIGID FLOOR+REINF PILLAR”, “RIGID FLOOR+SW” AND “RIGID FLOOR+TR” COINCIDES WITH “RIGID FLOOR”).....	202
FIGURE 6-58: MAXIMUM ADMISSIBLE GROUND ACCELERATION, AG^{MAX} , FOR THE ORIGINAL AND RETROFITTED BUILDINGS.....	203
FIGURE 6-59: DAMAGE LIMIT STATES ON THE CAPACITY DIAGRAM	204
FIGURE 6-60: FRAGILITY CURVES FOR EARTHQUAKE TYPE 1 (A) XX DIRECTION (B) YY DIRECTION.....	206
FIGURE 6-61: FRAGILITY CURVES FOR EARTHQUAKE TYPE 2 (A) XX DIRECTION (B) YY DIRECTION.....	206
FIGURE 6-62: DAMAGE PROBABILITIES FOR EARTHQUAKE TYPE 1 IN THE (A) XX DIRECTION (B) YY DIRECTION	206
FIGURE 6-63: DAMAGE PROBABILITIES FOR EARTHQUAKE TYPE 2 IN THE (A) XX DIRECTION (B) YY DIRECTION.....	207
FIGURE 6-64: FRAGILITY CURVES FOR EARTHQUAKE TYPE 1 (A) XX DIRECTION (B) YY DIRECTION.....	208
FIGURE 6-65: FRAGILITY CURVES FOR EARTHQUAKE TYPE 2 (A) XX DIRECTION (B) YY DIRECTION.....	208
FIGURE 6-66: DAMAGE PROBABILITIES FOR EARTHQUAKE TYPE 1 IN THE (A) XX DIRECTION (B) YY DIRECTION	208

FIGURE 6-67: DAMAGE PROBABILITIES FOR EARTHQUAKE TYPE 2 IN THE (A) XX DIRECTION (B) YY DIRECTION	209
FIGURE 6-68: FRAGILITY CURVES FOR EARTHQUAKE TYPE 1 (A) XX DIRECTION (B) YY DIRECTION.....	210
FIGURE 6-69: FRAGILITY CURVES FOR EARTHQUAKE TYPE 2 (A) XX DIRECTION (B) YY DIRECTION.....	210
FIGURE 6-70: DAMAGE PROBABILITIES FOR EARTHQUAKE TYPE 1 IN THE (A) XX DIRECTION (B) YY DIRECTION.....	210
FIGURE 6-71: DAMAGE PROBABILITIES FOR EARTHQUAKE TYPE 2 IN THE (A) XX DIRECTION (B) YY DIRECTION	211
FIGURE 6-72: FRAGILITY CURVES FOR EARTHQUAKE TYPE 1 (A) XX DIRECTION (B) YY DIRECTION.....	212
FIGURE 6-73: FRAGILITY CURVES FOR EARTHQUAKE TYPE 2 (A) XX DIRECTION (B) YY DIRECTION.....	212
FIGURE 6-74: DAMAGE PROBABILITIES FOR EARTHQUAKE TYPE 1 IN THE (A) XX DIRECTION (B) YY DIRECTION.....	212
FIGURE 6-75: DAMAGE PROBABILITIES FOR EARTHQUAKE TYPE 2 IN THE (A) XX DIRECTION (B) YY DIRECTION.....	213
FIGURE 6-76: FRAGILITY CURVES FOR EARTHQUAKE TYPE 1 (A) XX DIRECTION (B) YY DIRECTION.....	214
FIGURE 6-77: FRAGILITY CURVES FOR EARTHQUAKE TYPE 2 (A) XX DIRECTION (B) YY DIRECTION.....	214
FIGURE 6-78: DAMAGE PROBABILITIES FOR EARTHQUAKE TYPE 1 IN THE (A) XX DIRECTION (B) YY DIRECTION.....	214
FIGURE 6-79: DAMAGE PROBABILITIES FOR EARTHQUAKE TYPE 2 IN THE (A) XX DIRECTION (B) YY DIRECTION	215
FIGURE 6-80: FRAGILITY CURVES FOR EARTHQUAKE TYPE 1 (A) XX DIRECTION (B) YY DIRECTION.....	216
FIGURE 6-81: FRAGILITY CURVES FOR EARTHQUAKE TYPE 2 (A) XX DIRECTION (B) YY DIRECTION.....	216
FIGURE 6-82: DAMAGE PROBABILITIES FOR EARTHQUAKE TYPE 1 IN THE (A) XX DIRECTION (B) YY DIRECTION.....	216
FIGURE 6-83: DAMAGE PROBABILITIES FOR EARTHQUAKE TYPE 2 IN THE (A) XX DIRECTION (B) YY DIRECTION	217
FIGURE 6-84: PROBABILITY OF DAMAGE FOR EARTHQUAKE TYPE 1 IN THE XX DIRECTION.....	217
FIGURE 6-85: PROBABILITY OF DAMAGE FOR EARTHQUAKE TYPE 1 IN THE YY DIRECTION.....	218
FIGURE 6-86: PROBABILITY OF DAMAGE FOR EARTHQUAKE TYPE 2 IN THE XX DIRECTION.....	218
FIGURE 6-87: PROBABILITY OF DAMAGE FOR EARTHQUAKE TYPE 2 IN THE YY DIRECTION.....	219

List of tables

TABLE 3-1: RESULTS OBTAINED FOR MEASUREMENT POINT PF	72
TABLE 3-2: RESULTS OBTAINED FOR MEASUREMENT POINT DN	73
TABLE 3-3: RESULTS OBTAINED FOR MEASUREMENT POINT P11	74
TABLE 3-4: RESULTS OBTAINED FOR MEASUREMENT POINT SC	76
TABLE 3-5: SUMMARY OF THE RESULTS WITH OBTAINED PEAK FREQUENCIES AND ESTIMATED GROUND PARAMETERS	80
TABLE 3-6: PARAMETERS OF THE ELASTIC RESPONSE SPECTRUM FOR SEISMIC ACTION TYPE 1, SEISMIC ZONE 3 AND GROUND TYPE C	81
TABLE 3-7: PARAMETERS OF THE ELASTIC RESPONSE SPECTRUM FOR SEISMIC ACTION TYPE 2, SEISMIC ZONE 1 AND GROUND TYPE C	81
TABLE 4-1: VERTICAL LOADS IMPOSED IN SPECIMEN SC1 TO SC3	101
TABLE 4-2: SUMMARY OF VALUES OBTAINED FOR TESTS.....	110
TABLE 5-1: ENVELOPE CURVE PARAMETERS.....	130
TABLE 5-2: COUPLE VALUES OF (F_u, A_u) AND (F_{ULT}, A_{ULT})	130
TABLE 5-3: POSITIVE AND NEGATIVE LOADING FORCE AT 3MM DISPLACEMENT FOR ALL THE TESTS....	138
TABLE 5-4:MECHANICAL PROPERTIES OF WOOD ACCORDING TO LNEC.....	140
TABLE 5-5:MECHANICAL PROPERTIES OF WOOD ACCORDING TO EUROPEAN NORM	141
TABLE 5-6: MECHANICAL PROPERTIES ADOPTED FOR WOOD.....	141
TABLE 5-7: MECHANICAL PROPERTIES ADOPTED FOR MASONRY	142
TABLE 5-8: RESULTS FOR SPRING STIFFNESS OF 6 000 KN/M. (RESULTS IN MM)	142
TABLE 5-9: RESULTS FOR SPRING STIFFNESS OF 10 000 KN/M. (RESULTS IN MM).....	142
TABLE 5-10: RESULTS FOR SPRING STIFFNESS OF 15 000 KN/M (RESULTS IN MM)	142

TABLE 5-11: RATIO OF ANALYTICAL OVER EXPERIMENTAL STIFFNESS FOR DIFFERENT SPRING STIFFNESS	142
.....
TABLE 5-12: INITIAL STIFFNESS FOR DIFFERENT CONFIGURATIONS OF WALLS AND DIFFERENT MODULUS	142
OF ELASTICITY OF WOOD	144
TABLE 5-13: AXIAL FORCE ACTING ON THE MOST LOADED DIAGONAL	145
TABLE 5-14: CALCULATION OF FU FOR THE OTHER CONFIGURATIONS OF WALLS.....	148
TABLE 5-15: CONSTANT VALUES OF Z, R1xK ₀ AND R2xK ₀	149
TABLE 5-16: VALUES OF K ₀ , FU AND FULT FOR DIFFERENT CONFIGURATIONS OF WALLS ($E_{WOOD}=12\ 000$ MPA).....	149
TABLE 6-1: THICKNESS/AREA AND MATERIAL OF BUILDING COMPONENTS.....	167
TABLE 6-2: MECHANICAL CHARACTERISTICS OF MASONRY TYPES.....	169
TABLE 6-4: VERTICAL LOADS CONSIDERED.....	170
TABLE 6-5: BI-LINEAR VALUES FOR THE TWO DIRECTIONS.....	175
TABLE 6-6: MODAL PARTICIPATION FACTORS, EQUIVALENT MASS AND PERIOD OF VIBRATION IN THE TWO DIRECTIONS.....	175
TABLE 6-7: N2 METHOD PARAMETERS FOR EACH EARTHQUAKE TYPE AND EACH DIRECTION.....	176
TABLE 6-8: BI-LINEAR VALUES FOR THE TWO DIRECTIONS.....	184
TABLE 6-9: MODAL PARTICIPATION FACTORS, EQUIVALENT MASS AND PERIOD OF VIBRATION IN THE TWO DIRECTIONS.....	184
TABLE 6-10: N2 METHOD PARAMETERS FOR EACH EARTHQUAKE TYPE AND EACH DIRECTION	185
TABLE 6-11: BI-LINEAR VALUES FOR THE TWO DIRECTIONS	189
TABLE 6-12: MODAL PARTICIPATION FACTORS, EQUIVALENT MASS AND PERIOD OF VIBRATION IN THE TWO DIRECTIONS.....	189
TABLE 6-13: N2 METHOD PARAMETERS FOR EACH EARTHQUAKE TYPE AND EACH DIRECTION	190
TABLE 6-14: BI-LINEAR VALUES FOR THE XX DIRECTION	193
TABLE 6-15: MODAL PARTICIPATION FACTORS, EQUIVALENT MASS AND PERIOD OF VIBRATION IN THE XX DIRECTION.....	193
TABLE 6-16: N2 METHOD PARAMETERS FOR EACH EARTHQUAKE TYPE IN THE XX DIRECTION.....	194
TABLE 6-17: BI-LINEAR VALUES FOR THE XX DIRECTION	197
TABLE 6-18: MODAL PARTICIPATION FACTORS, EQUIVALENT MASS AND PERIOD OF VIBRATION IN THE XX DIRECTION.....	197
TABLE 6-19: N2 METHOD PARAMETERS FOR EACH EARTHQUAKE TYPE IN THE XX DIRECTION.....	198
TABLE 6-20: BI-LINEAR VALUES FOR THE XX DIRECTION	200
TABLE 6-21: MODAL PARTICIPATION FACTORS, EQUIVALENT MASS AND PERIOD OF VIBRATION IN THE XX DIRECTION.....	200
TABLE 6-22: N2 METHOD PARAMETERS FOR EACH EARTHQUAKE TYPE IN THE XX DIRECTION.....	201
TABLE 6-23: VALUES OF THE VARIOUS UNCERTAINTIES FOR EACH DAMAGE LIMIT STATE	205
TABLE 6-24: PARAMETERS OF THE LOGNORMAL DISTRIBUTION FUNCTION FOR THE EARTHQUAKE TYPE 1 FOR BOTH XX AND YY DIRECTIONS.....	205
TABLE 6-25: PARAMETERS OF THE LOGNORMAL DISTRIBUTION FUNCTION FOR THE EARTHQUAKE TYPE 2 FOR BOTH XX AND YY DIRECTIONS.....	205
TABLE 6-26: PARAMETERS OF THE LOGNORMAL DISTRIBUTION FUNCTION FOR THE EARTHQUAKE TYPE 1 FOR BOTH XX AND YY DIRECTIONS.....	207
TABLE 6-27: PARAMETERS OF THE LOGNORMAL DISTRIBUTION FUNCTION FOR THE EARTHQUAKE TYPE 2 FOR BOTH XX AND YY DIRECTIONS.....	207
TABLE 6-28: PARAMETERS OF THE LOGNORMAL DISTRIBUTION FUNCTION FOR THE EARTHQUAKE TYPE 1 FOR BOTH XX AND YY DIRECTIONS.....	209
TABLE 6-29: PARAMETERS OF THE LOGNORMAL DISTRIBUTION FUNCTION FOR THE EARTHQUAKE TYPE 2 FOR BOTH XX AND YY DIRECTIONS.....	209
TABLE 6-30: PARAMETERS OF THE LOGNORMAL DISTRIBUTION FUNCTION FOR THE EARTHQUAKE TYPE 1 FOR BOTH XX AND YY DIRECTIONS.....	211
TABLE 6-31: PARAMETERS OF THE LOGNORMAL DISTRIBUTION FUNCTION FOR THE EARTHQUAKE TYPE 2 FOR BOTH XX AND YY DIRECTIONS.....	211
TABLE 6-32: PARAMETERS OF THE LOGNORMAL DISTRIBUTION FUNCTION FOR THE EARTHQUAKE TYPE 1 FOR BOTH XX AND YY DIRECTIONS.....	213
TABLE 6-33: PARAMETERS OF THE LOGNORMAL DISTRIBUTION FUNCTION FOR THE EARTHQUAKE TYPE 2 FOR BOTH XX AND YY DIRECTIONS.....	213
TABLE 6-34: PARAMETERS OF THE LOGNORMAL DISTRIBUTION FUNCTION FOR THE EARTHQUAKE TYPE 1 FOR BOTH XX AND YY DIRECTIONS.....	215

List of symbols

Chapter 3

- f_0 : frequency at the peak of the H/V curve
- A_0 : peak amplitude of the H/V curve
- w : width of the valley
- H : depth of the valley (depth to bedrock)
- H_{\min} : minimum depth to bedrock
- l_w : window length
- n_w : number of windows
- n_c : total number of cycles
- $\sigma_A(f)$: standard deviation of the H/V curve amplitude at frequency f .
- f^- : frequency on the left of f_0
- $A_{H/V}(f^-)$: amplitude of the H/V curve at point f^-
- f^+ : frequency on the right of f_0
- $A_{H/V}(f^+)$: amplitude of the H/V curve at point f^+
- σ_{f0} : standard deviation of the H/V peak frequency
- $\sigma_A(f_0)$: standard deviation of the H/V amplitude at peak
- N_{spt} : penetration resistance (non corrected) or number of blows
- ρ_{soil} : density of the soil
- ρ_{rock} : density of the bedrock
- $V_{s,av}$: average shear wave velocity of the soil layer
- V_r : shear wave velocity of the bedrock
- SH : incident horizontal S wave

Chapter 5

- d : structure's top displacement
- l : in equivalent rocking behaviour – displacement of nodes Ng and Ni
- l : in equivalent shear behaviour – shortening of the compressed diagonal braces
- γ : in equivalent shear behaviour – distortion of the panel
- δ : general displacement
- F : general force
- $\Delta\delta$: gradient of the displacement
- Z : pinching parameter; force at zero displacement
- K_0 : initial stiffness
- r_1 : parameter of the exponential envelope
- r_2 : parameter of the linear envelope
- F_0 : parameter of the exponential envelope
- K_u : unloading stiffness
- α : parameter of the unloading exponential curve
- λu : parameter of the unloading exponential curve defining the shape of the curve
- $(\delta_{ou}; f_{ou})$: random point where the unloading starts
- Δx : drift
- K_l : reloading stiffness

r_l : reloading stiffness coefficient
 δ_{max} : maximum displacement reached by the wall taking into account all the cycles
 α : force reduction parameter
 P_i : point at which the damage of the wall starts
 $(\delta u; F_u)$: point of maximum force attained by the panel
 $(\delta_{ult}; F_{ult})$: point of maximum displacement attained by the panel
 F_u : ultimate load (strength)
 δ_{ult} : maximum displacement of wall before failure
 $f_{m,k}$: bending strength of wood
 $f_{t,0,k}$: tensile strength parallel to grain of wood
 $f_{t,90,k}$: tensile strength perpendicular to grain of wood
 $f_{c,0,k}$: compression strength parallel to grain of wood
 $f_{c,90,k}$: compression strength perpendicular to grain of wood
 $f_{v,k}$: shear strength of wood
 E_{mean} : modulus of elasticity parallel to grain, mean, of wood
 $E_{0,05}$: modulus of elasticity parallel to grain, characteristic value, of wood
 $E_{90, mean}$: Modulus of elasticity perpendicular to grain, mean, of wood
 G_{mean} : shear modulus, mean, of wood
 ρ_{mean} : density, mean, of wood
 ρ_k : density, characteristic value, of wood
 E_{wood} : mean modulus of elasticity of wood parallel to grain
 ρ_{wood} : mean density of wood
 $E_{masonry}$: modulus of elasticity of masonry
 $\rho_{masonry}$: mean density of masonry
 K_{anal} : analytical initial stiffness
 K_{exp} : experimental initial stiffness
 K_{spring} : spring stiffness
 $F_{vertical}$: vertical force applied at the experimental tests
Factor F_v : axial load on most loaded diagonal per unit vertical load applied
Factor F_u : axial load on most loaded diagonal per unit horizontal load applied
 $F_{diagonal}$: axial force acting in the most loaded diagonal

Chapter 6

S_{ae} : elastic acceleration response spectrum
 T : natural period of the structure
 S_{de} : elastic displacement response spectrum
 μ : ductility factor defined as the ratio between the maximum displacement and the yield displacement
 R_μ : reduction factor due to ductility
 T_c : characteristic period of the ground motion
 m^* : equivalent mass of the SDOF system
 Φ : assumed displacement shape
 D^* : displacement of the equivalent SDOF system
 F^* : force of the equivalent SDOF system
 D_t : top displacement of the MDOF system
 V : base shear of the MDOF system
 Γ : modal participation factor
 T^* : elastic period of the idealized bilinear system

F_y^* : yield strength of the approximate elasto-plastic diagram
 D_y^* : yield displacement of the approximate elasto-plastic diagram
 S_{ay} : yield acceleration on the capacity diagram in AD format
 S_d : inelastic displacement demand
 a_g : design ground acceleration on type A ground
 D_k : damage state
 ϕ : normal cumulative distribution function
 β_k : coefficient of dispersion
 $a_{g,k}$: design ground acceleration that produces damage state D_k
 D_u : ultimate displacement of the MDOF system (structure)
 F_{max} : maximum force on the pushover curve
 $0.7F_{max}$: force at 70% of maximum force (F_{max})
 $Disp\ 0.7$: displacement at 70% of maximum force (F_{max})
 K : stiffness of bilinear system
 $Area$: area under the pushover curve
 F_y : maximum force of bilinear system
 $Area\ bilinear$: area under the bilinear system
 $Sde(T^*)$: elastic displacement demand at period T^*
 Sd^{MDOF} : inelastic displacement demand of the MDOF structure
 a_g^{max} : maximum admissible ground acceleration for the structure's ultimate displacement D_u
 S : soil factor or soil related parameter
 S_{dy} : yielding displacement on the capacity diagram in AD format
 S_{du} : ultimate displacement on the capacity diagram in AD format

List of abbreviations

Chapter 3

HVSRT : H over V spectral ratio technique
 H/V: H over V
 SPT : standard penetration test
 1D : One dimensional
 2D/3D : Two dimensional or three dimensional
 FFT : Fast Fourier transform
 V : Vertical
 NS : North – South
 EW : East – West
 EQ : Earthquake

Chapter 4

LNEC : National Laboratory of Civil Engineering
 LERM : Laboratory of structures in IST
 LVDT : Linear variable displacement transducer
 M24 : bolts with $353\ mm^2$ in section area

Chapter 6

URM : Unreinforced masonry
 MDOF : Multi – degree of freedom

SDOF : Single degree of freedom

PGA : Peak ground acceleration

CAV : Cumulative absolute velocity

AI : Arias intensity

AD format : Acceleration – Displacement format

1. Introduction

1.1. Initial considerations

The downtown area of Lisbon is an important historical site in the capital of Portugal. Set here are buildings constructed after the 1755 earthquake, called *Pombalino* buildings. The heritage value of these buildings is recognized both nationally and internationally. They are mixed wood-masonry buildings. These buildings have not yet been carefully investigated in terms of seismic resistance and this is the main purpose of this thesis. It is important to evaluate the seismic capacity of these buildings that is to assess their nonlinear seismic response. It is also important to identify their critical parts and based on that adopt retrofit measures.

In order to do that the following has been developed. The soil of the downtown area of Lisbon is known for its susceptibility to significantly altering the incident ground motion and cause catastrophic damage in the building stock. For this reason, it was decided to focus first on the soil characterization of the site for seismic assessment.

The *Pombalino* buildings have the so-called “frontal” walls as their main internal walls. These internal walls have a structural function in the behaviour of the *Pombalino* buildings and are also deemed to resist seismic loads, so it is important to understand their behaviour under seismic loading. This has been another focus of this thesis.

Beyond this, the work led to the development of a macro-element for “frontal” walls. This is an important part of this research, as no macro-element exists in the literature for such walls.

In the last part of the work, fragility curves and damage probability plots were obtained for the *Pombalino* buildings. These are also an addition to the literature and are crucial for carrying out loss estimation studies. The work concludes with the development of fragility analyses for retrofitted buildings.

1.2. Objectives

The main objective of this work is to assess the seismic vulnerability of the *Pombalino* buildings. Here, the first objective is to focus on the soil where the *Pombalino* buildings are situated. Despite the susceptibility of the soil to earthquake damage, not much information is available for seismic ground characterization. A technique based on ambient vibrations was found suitable for application at the site. This technique has been applied before here in Lisbon but not in a systematic way. The objective of this work is to apply this technique in a systematic way and this enables the soil to be characterized in terms of the average shear wave velocity of the soil and depth to bedrock estimates.

In the second part the objective is to focus on the internal “frontal” walls. Despite the importance of these walls as structural parts of the building, not much information exists in the literature on the behaviour of such walls under seismic loading. There has only been one experimental study performed on a real specimen brought from a building under demolition, where cyclic static shear testing was performed in the national laboratory for civil engineering (LNEC). This was carried out as far back as 1997. Since then, no more experimental studies on such walls have been carried out. The objective is then to carry out experimental tests on such walls. The tests performed are static cyclic shear tests with imposed displacements. The main objective of this part of the work is to obtain the hysteretic behaviour of such walls in terms of a force-displacement relationship.

In the next part, the objective is to develop a macro-element for “frontal” walls. This is obtained based on the development of a hysteretic model to describe the cyclic behaviour of the *Pombalino* “frontal” walls. Additionally, the objective is to obtain the hysteretic behaviour (in terms of envelope curves) of walls with different sizes (height and length), different from the size tested, since in reality these can exist in a single building.

Finally, the last part of the work has the development of fragility analyses on *Pombalino* buildings as its main objective. For this purpose, modelling of a *Pombalino* building has been performed incorporating the previously developed macro-element for the modelling of the “frontal” walls. In this way, in a single model one has the masonry walls and the “frontal” walls modelled with macro-elements. Fragility curves and damage probability plots are obtained. Beyond this, the objective is to propose some retrofitting strategies. These are modelled and new fragility curves and damage probability plots are obtained for this case.

1.3. Thesis outline

The thesis is divided into seven chapters. The first chapter, this one, is an introductory chapter. Some initial considerations are made here and the objectives of the thesis are presented as well as the thesis outline.

The second chapter refers to the *Pombalino* buildings presentation. It includes a historical background of the development of the *Baixa Pombalina* until now, followed by a description of the structural elements of the *Pombalino* buildings and, finally, a remark about the structures that existed in the past and also that exist nowadays that resemble the *Pombalino* construction system.

The third chapter focuses on soil characterization in the area where the *Pombalino* buildings are constructed. It refers to the definition of soil characteristics and ends with the definition of seismic action for further assessment of the structures. Data has been gathered here from various sources, mainly geological and geotechnical surveys. Additional measurements of ambient vibrations have been performed based on the H/V spectral ratio technique. Based on the combination of geological and geotechnical data with this technique, it has been possible to characterize the site in terms of average shear wave velocity of the soil and depth to bedrock estimates.

The fourth chapter described the experimental part of this study. It refers to the cyclic load testing of *Pombalino* internal (“frontal”) walls. A total of three tests were conducted on three identical real size walls. The hysteretic behaviour of such walls was described in terms of a force-displacement relationship. These walls, when subjected to cyclic loading, exhibit highly nonlinear force-displacement responses and a high ductility. As previous experimental studies on such walls are very limited, these results are very useful for further research.

The next chapter, number five, is related to the development of a macro-element for the “frontal” walls based on the experimental results obtained. Here, a hysteretic model is presented based on the obtained experimental hysteresis. The hysteretic model, developed using a phenomenological approach, aims to reproduce the response of the wall under general monotonic, cyclic or earthquake loading. The model incorporates a set of exponential and linear functions. There are a total of nine identifiable parameters in this model. The model developed also accounts for characteristics such as the pinching effect, strength and stiffness degradation that have been observed in the experimental data. The chapter concludes with the definition of the envelope curves for different heights and lengths of the walls since, in reality, one can find other heights and lengths of the walls in a single building.

The sixth chapter focuses on the modelling of a typical Pombalino building with structural software wherein the previously developed macro-element has been incorporated. This enables the modelling with macro-elements of the masonry panels together with the “frontal” walls, in a single model. This is an original research. Pushover analyses have been carried out and a seismic assessment of the building has been carried out. In addition, fragility curves and damage probability plots have been obtained. The most important application of such curves is in loss estimation studies and this is suggested future work. Lastly, some retrofitting strategies have been modelled and seismic assessment and fragility analysis have been carried out for these new states of the building.

The last chapter presents all the conclusions obtained and further work is proposed.

2. The *Pombalino* buildings

2.1. Historical background

The area of Lisbon known as *Baixa Pombalina* (**Figure 2-1**), runs into the city's central area, which lies at the foot of the hill crowned by the Castle and has the Cathedral halfway up. It is further surrounded on the left by S. Roque hill, at the top by another hill and at the bottom by the river Tagus. This area developed gradually from Medieval times onwards, going on to become Portugal's main political, administrative, economic and business centre.

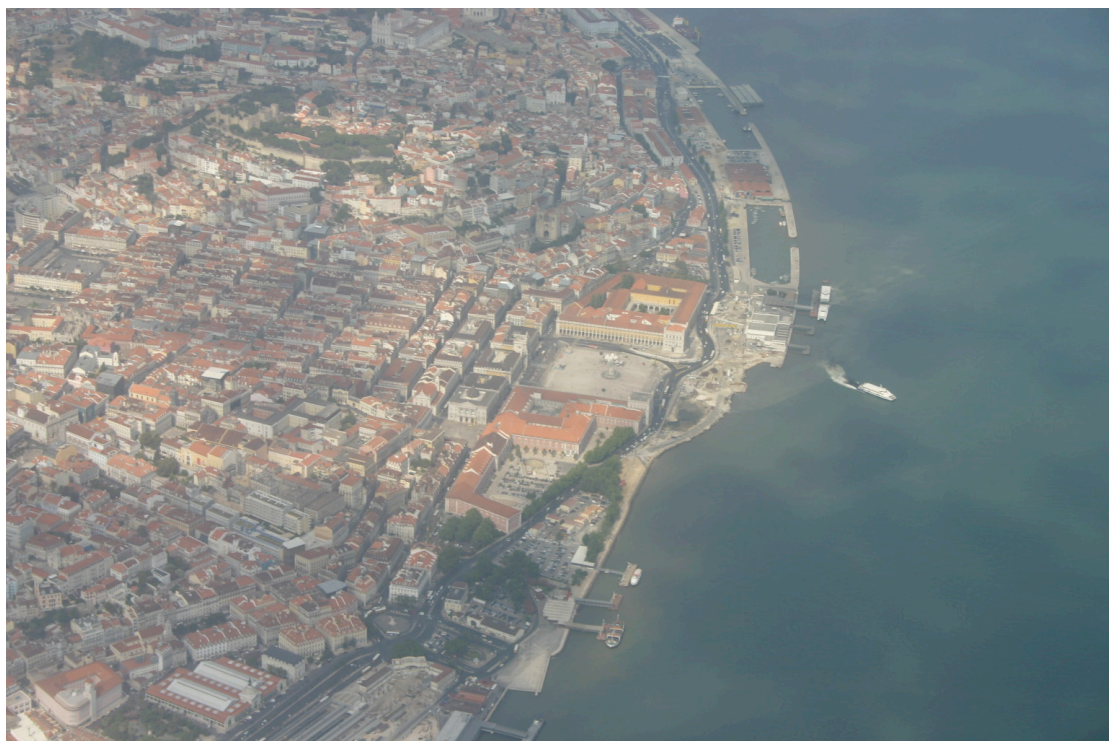


Figure 2-1: The *Baixa Pombalina* seen from an aerial view
[<http://mjfs.wordpress.com/category/madre-deus/>]

The settlement and historical development of the heart of the city of Lisbon is further described here.

Prehistory, Roman period, Barbarians and Muslims

This heart of the city of Lisbon was set in a small creek which was the outcome of the action of two water courses: the streams of S. Sebastião da Pereira and of Arroios. During prehistoric times, the two streams converged into a valley that separated two hills, those of S. Roque and Castle Hill. To form the valley, an immense Miocene bedrock formation had been eroded. Before the bedrock formation eroded, this place, situated on the vast Tagus estuary, offered excellent conditions for settlement. The abundance of fish, fresh water, arable soil and good defence conditions against attackers made it possible to set up a hamlet. The river was also navigable far above the river's mouth and downstream it opened widely into the sea.

Before the Christian Era, it is thought that this bedrock formation was slowly but successfully eroded by sands lodged in the river current or by the constant collapse of the slopes due to the action of the rain.

The Phoenicians seem to have been the first to settle due to the exceptionally good exposition of the Castle Hill. They named the city “Olisipo”, which was later to become “Lixbuna” [França, 1983; Vieira da Silva, 1960].

“Olisipo” was characterized by a nucleus of a fixed population defended by a small armed force. In the surroundings, a number of families aggregated continuously, who would farm the land in exchange of food, shelter and defence [<http://www.lisboacidade.com/lx/index99pt.asp?pa=ptihist.htm>].

The Romans took the city after conquering the Lusitanians between the years 100 B.C. and 45 B.C. [Mascarenhas, 1996]. The Emperor Julius Cesar named the city after Felicitas Julia and promoted the city to a Roman Municipality, which implied it had urban infrastructures such as monuments, theatres, thermal treatments, etc. By the kind of remains found it seems that it was an important city full of life and splendour and remained so for nearly 400 years [Mascarenhas, 1996].

The crises that struck the Roman Empire in the 3rd century had their own consequences throughout the Iberian Peninsula. The successive invasions of new people, whether Germanic (Visigoths and Swabians) in the 5th century or Arabs in the 7th century, transformed the physiognomy of the population. Due to the climate of successive wars and insecurity, the city acquired a fortress where the inhabitants would seek protection and defence against the attacks [<http://www.lisboacidade.com/lx/index99pt.asp?pa=ptihist.htm>].

According to Pradalié [1975], the Muslims occupied the city in 714 A.D. They built walled compartments on the Castle Hill transforming it into a prime war fortress. Further ahead, in the beginning of the 9th century, it was taken by Alfonso, “The Chaste”, king of Galicia and Asturias. Then, the city was re-taken by the Arabs in 831 A.D. In 851 A.D. it was instead taken by Alfonso IV, king of León, although later it was again reoccupied by the Arabs. In 1093 A.D. it was taken by Alfonso VI, king of León and Castile but a few years later it was once again retaken by the Muslims.

Lisbon was at this time an important trade centre for all Africa and for a big part of Europe. It had silver and gold and there was no shortage of blacksmiths. Its fields were arable and good for all crops. Furthermore, there were hot bathes in the city. On top of the hill there was a circular wall and the walls of the city descended on the south side of the hill until the river Tagus [<http://www.lisboacidade.com/lx/index99pt.asp?pa=ptihist.htm>].

The following figure (**Figure 2-2**) shows, in a schematic way, what the aspect of Lisbon would have been before the 12th century with its main hills, Roman monuments, fortress and river streams.

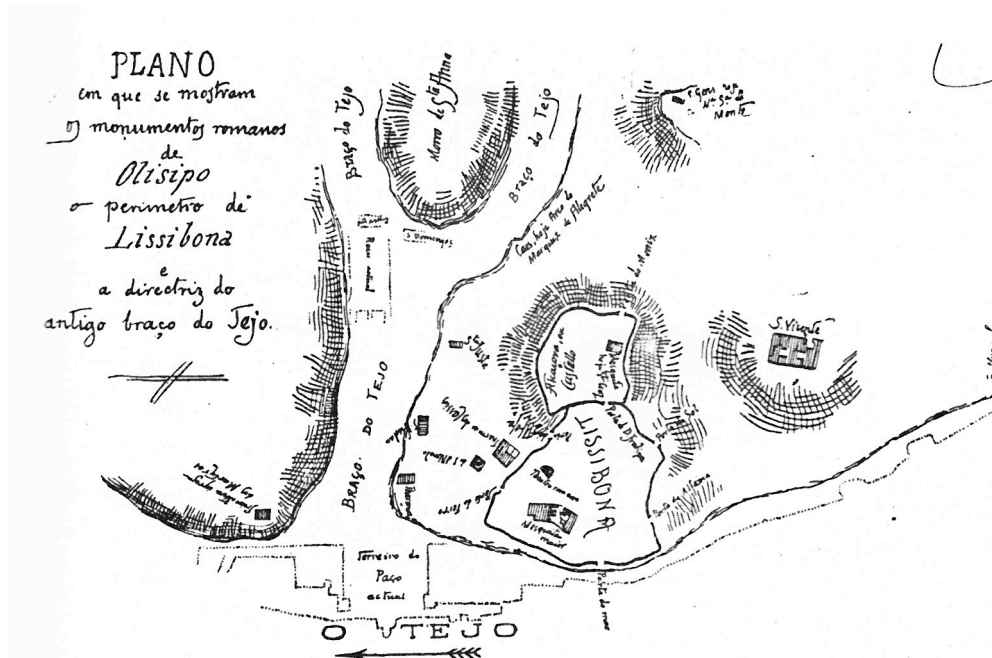


Figure 2-2: Plan of Lisbon before the 12th century [Julio de Castilho, 1893]

First dynasty

In the year 1147 A.D., Dom Afonso Henriques, first king of Portugal, conquered the city and Lisbon was finally taken into the Christian faith. This was accomplished after a 3-month siege. Dom Afonso Henriques was helped by the Crusades of English, German and French origins. With the Christian conquest, the city expanded outside its walls and joined the surrounding neighbourhoods of Baixa and Alfama. The two streams disappeared for good in the 8th century. [http://www.lisboa-cidade.com/lx/index99pt.asp?pa=ptihist.htm; Mascarenhas, 1996].

In 1225 A.D., Lisbon became the new capital with Dom Afonso III being the first king to establish residence in Lisbon. This fact helped increase the trading with Mediterranean ports. According to Pradalié [1975], the nature of building form and construction was determined by the abundance of local calcareous materials and clay and the lack of forests in the Lisbon area. This fact plus the surviving Arab building tradition of single storey dwellings may have restricted the development of multi-storey buildings.

In 1356, a big earthquake struck the city and caused considerable damage. The earthquake was grade IX on the Mercalli scale [Mascarenhas, 2005]. In 1373 and due to the war between Castile and Portugal, Lisbon was placed under siege by an enormous Castilian army. The city was the stage of many horrors as the suburbs were set on fire. Due to the war, Dom Fernando, the king of Portugal, built a new wall of defence called “Cerca Nova” [Mascarenhas, 1996; <http://www.lisboa-cidade.com/lx/index99pt.asp?pa=ptihist.htm>].

In 1384, Dom Juan I of Castile attacked the city by land and sea. This lasted five severe months, after which the enemy withdrew leaving behind many warships and buildings ruined. In 1385, Dom Fernando died and many rebellions took place both in

Lisbon and throughout the country because of the lack of succession and because people wanted Dom Joao I for king. During this period, the health conditions were not very good. The drainage systems were very poor and most of the houses were small in area and their façades out of line. Furthermore, the streets were badly paved and irregular in layout [Sequeira, 1947; “História de Portugal”, 1929; “Grande Enciclopédia Portuguesa e Brasileira”, 1945].

Second and third dynasty and the Portuguese discoveries

In the second dynasty, during the reign of Dom Joao I came the beginning of the Portuguese sea voyages. Also, Dom Joao I was the king struggling to conquer Ceuta [Mascarenhas, 1996]. Dom Joao I also created the first neighbourhood on the Carmo hill (1400), he hoped with this to accommodate a larger population, one which was always on the increase by then [<http://www.lisboa-cidade.com/lx/index99pt.asp?pa=ptihist.htm>].

The golden era of discoveries really began during the reign of King Dom Manuel I and after the arrival of Vasco da Gama in India (in 1498) [Mascarenhas, 1996]. At this time the court of Dom Manuel abandoned the Castle and installed itself in *Terreiro do Paço*. This was the site of all the commercial life in Lisbon. The city port was modernized in order to accommodate the Royal Palace and several port services.

Around this time the first neighbourhood was created in *Bairro Alto* which transformed the crops into streets and buildings, suddenly turning into a popular neighbourhood, although later on it would become an area where the aristocracy would build their own palaces. *Bairro Alto* set the transition between the 16th and the 17th centuries in the urban life of Lisbon and created a new concept of urbanism and architecture [<http://www.lisboa-cidade.com/lx/index99pt.asp?pa=ptihist.htm>]. The orthogonal layout of the neighbourhood of *Bairro Alto* may have given some insight on the design of the *Pombalino* area after the earthquake of 1755 [Mascarenhas, 1996].

The second quarter of the 16th century was not at all positive: the spice trade from India declined, the tribunal of the Inquisition was established and the great plague brought suffering and death to the population [Mascarenhas, 1996]. Furthermore, there was a big earthquake on January 1531 which must have caused significant loss of life and suffering. The earthquake was grade X on the Mercalli scale [Mascarenhas, 2005]. The earth struck again with another devastating earthquake in January 1551. This earthquake was again grade X on the Mercalli scale [Mascarenhas, 2005]. Finally, in July 1576 there was yet another big earthquake this one of grade IX on the Mercalli scale [Mascarenhas, 2005]. All these earthquakes plus the plague that struck again in 1569 must have been devastating to the city.

In 1578 a crisis erupted due to the death of the Portuguese king Dom Sebastião in the war with Morocco. The crisis enabled Dom Filipe II, King of Spain, to invade the country and transform it into a Spanish Province in 1580. This period was one of pain and ruin for Lisbon [Mascarenhas, 1996]. It lasted 60 years and the Portuguese independence was only restored in 1640. At this point the situation changed rapidly. Dom Joao IV achieved the reorganization of the economy in a nation eager to overcome the crisis. Many new buildings were constructed in Lisbon. According to

Gastão de Melo Matos [1947], with Brazilian settlement in the latter part of the 17th century, there was an expansion of religious buildings, typical of that period in Lisbon, but the streets of the capital were unhygienic and in many parts obstructed by buildings. By the beginning of the 18th century, the downtown area of Lisbon was a labyrinth of streets between the two main squares: *Rossio* and *Terreiro do Paço* and the city was then a Medieval city densely populated. Still according to Gastão de Melo Matos [1947], the country was going into economic decline.

Pombalino times and beyond

Another terrible catastrophe then struck the city of Lisbon. In 1755 an earthquake followed by a no less destructive fire and tsunami reached the city of Lisbon.

In the **Figure 2-3** one can see a picture of a bipartite German engraving with, above, the representation of the city of Lisbon before the earthquake of 1755 and below, the representation of the city under the subsequent fire and tsunami.



Figure 2-3: Bipartite German engraving. Above the representation of the city before the earthquake of 1755. Below the representation of the fire and tsunami that struck the city in 1755. [Augsburg, Matthaus Seutter, S. Coes Mag. Geogr. Aug. Vindel, around 1756.]

Dom Joao V died in 1750 and its successor was Dom José I (1750-1777) [Saraiva, 2007]. The destruction brought about by the earthquake of 1 November 1755 made it

necessary to rebuild the heart of the city of Lisbon. The work was led by the Marquis of *Pombal*, under the orders of the king Dom José I, and carried out by the competent architects and engineers (Manuel da Maia, Eugénio dos Santos, Carlos Mardel) at his service. As a result, *Baixa Pombalina* became an excellent example of enlightenment urban planning and architecture [Baixa Pombalina 250 anos em imagens, 2004]. The conditions were created for this area to play an even more important role and to occupy a centre stage in the country's major events. It is this memory of grandeur and of the country's emblematic centre that those who rebuilt *Baixa* would try and recreate with a new language based on order, modernity and monumentality [Baixa Pombalina 250 anos em imagens, 2004].

Later on, the *Pombalino* epoch that was initiated in 1759-1761 in its second stage, was one of economic crises. Crises for the state savings, crises for the production and for commerce or transactions [Macedo, 1989].

The rebuilding of the downtown area of the city was initiated in 1756 and was carried out over many decades. The French invasions occurred within this period (1806-1812) and also Brazil became independent in 1822 creating a certain amount of economic instability. Later on came the Liberal Struggles (1826-1830) and after this, around 1830, the population of Lisbon stabilised at around 200 000 inhabitants [Mascarenhas, 1996].

The 1755 earthquake

In **Figure 2-4** a bipartite German engraving is depicted. Above, Lisbon before the 1755 earthquake. Below, several fires caused by the cataclysm.

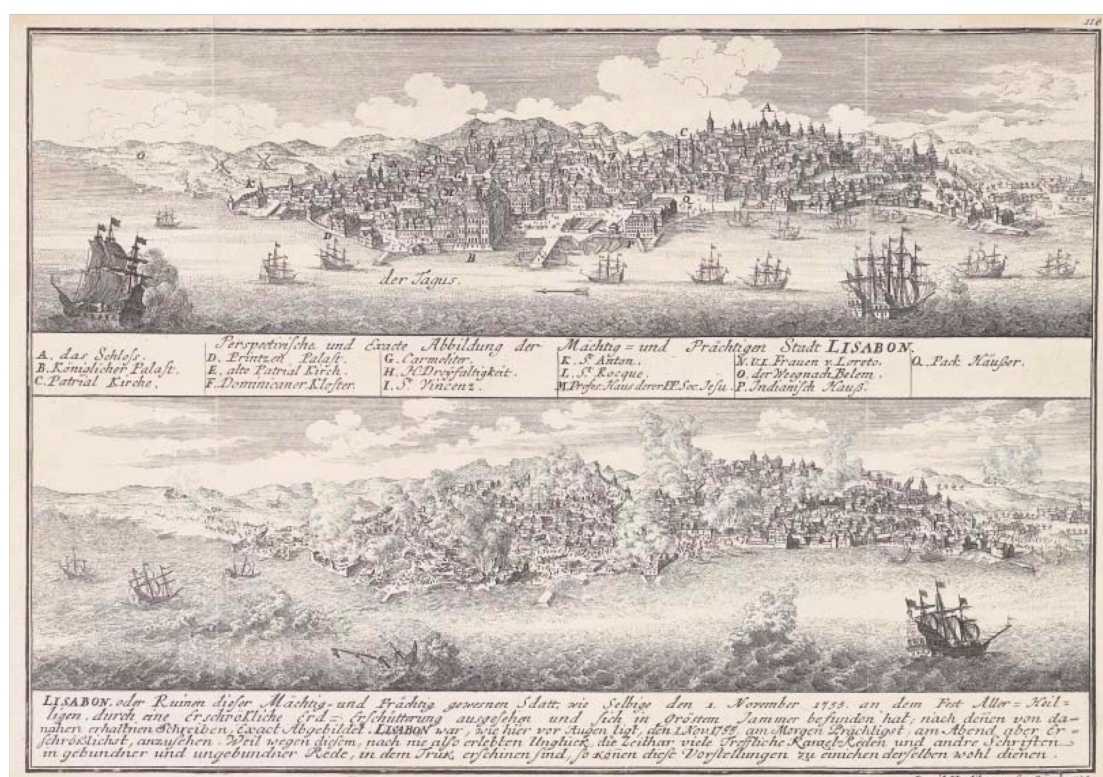


Figure 2-4: Above, Lisbon before the 1755 earthquake. Below, several fires caused by the cataclysm. [Zurich, David Kerliberg, 1756]

In **Figure 2-5** a picture of José I, King of Portugal, while ordering the re-building of Lisbon destroyed by the earthquake is shown.



Figure 2-5: Picture of José I, King of Portugal, while ordering the re-building of Lisbon destroyed by the earthquake. [Venice, P.Novelli, Antonio Zatta and Figli, 1757 – 1797]

On 1 November 1755 the earth shook and the city became a dramatic ruin. This was the morning of All Saints day and the churches were full of people attending services. About 10 000 buildings were destroyed including a lot of churches [Saraiva, 2007]. The amount of people dying was between 10 000 to 15 000 [Mascarenhas, 1996]. According to Saraiva [2007] the destructions of the earthquake and the fire that followed it led to a major collapse of the constructions in Lisbon city centre or downtown. The old neighbourhoods (Alfama, Mouraria, Madre de Deus, Xabregas) were slightly damaged. The younger neighbourhoods (Jesus, Rato, S. José, S. Sebastião da Pedreira, Arroios) were also saved from hard damage. According to <http://www.lisboa-cidade.com/lx/index99pt.asp?pa=ptihist.htm>, the neighbourhoods of the Castle Hill and the Carmo area were significantly affected. In **Figure 2-6** one can see the limits of the fire that struck the capital after the earthquake in dashed lines and the most affected areas struck by the earthquake in orange.

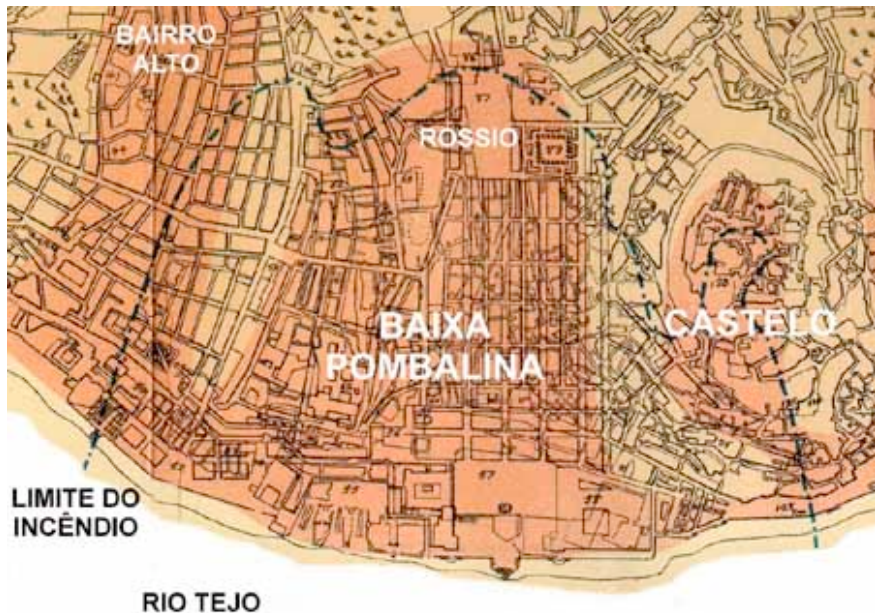


Figure 2-6: Limits of the fire that struck the capital after the earthquake in dashed line and the most affected areas of the earthquake of 1755 in orange

The earthquake was also strongly felt in the Algarve, Southern Spain and Morocco. Though not causing significant damage it was also felt throughout Europe, in the Azores and Madeira [1755 O grande terramoto de Lisboa, 2005].

At 9:40 a.m. on Saturday 1st November 1755 there was the big shake. This was the first of four big tremors felt that day in Lisbon. In Lisbon (the duration of the tremors depends on the locations felt), the first tremor lasted about 1 minute and a half. This was not very destructive. There was an interval of about 1 minute and then there was another shake which lasted about 2 minutes and a half. Here, considerable damage was probably seen. Another interval came of about another minute and the third tremor came for even more time, about 3 minutes. This was even more violent than the preceding tremors. During the next 24 hours that followed the main shake, the earth did not stop moving in almost a continuous way. The first aftershock with less intensive means but still lasting some seconds was felt at 11 a.m. that day. On the first 8 days it were felt more than 28 aftershocks, about 250 aftershocks were felt on the first 6 months and more than 500 aftershocks were felt until September 1756 [1755 O grande terramoto de Lisboa, 2005].

Regarding the epicentre of the earthquake, it is difficult to identify one. Research is still undergoing but it is rather clear that the epicentre was located southwest of the Algarve, in the ocean. However, this issue is still under discussion as some authors [Vilanova *et al*, 2003], for instance, believe this was not the only epicentre and that the catastrophe was constituted by two episodes: one, the rupture at the fault at the southwest of the *Algarve* in the ocean and the other, a rupture somewhere in the region of *Vale Inferior do Tejo* in the mainland.

The magnitude is also difficult to estimate as there were no seismometers or accelerometers in that epoch (the magnitude is usually associated with the amplitude of the movements of the soil measured in these instruments). So, when it comes to historical earthquakes this is accomplished by studying the distribution of damage

over a large area (at different countries) or by studying a specific structure which, by being simple enough, can be treated as a seismometer. For the earthquake of 1755, it has been given a magnitude of $Mw=8.5-8.75$ (associated with the rupture mechanism at the southwest of the *Algarve*).

Almost immediately after the tremors, several fires, probably with many sources, exploded and spread all over the city. It seems to have lasted about six days causing considerable additional damage to the constructions [1755 O grande terramoto de Lisboa, 2005]. It might be due to the fact that it was All Saints day and there were a lot of candles being lightened up in the churches that many fires started in the churches.

At about 11 a.m. on 1 November 1755, the water front of a tsunami born at the time of the first shake (9:40) reached the city. Initially, the Tagus river waters descended to start rising afterwards. The waters overpassed the harbour and moved onto the downtown about 300 to 400 metres inwards. The waters reached *Terreiro do Paço* and the streets next to it. Only at 7 a.m. the next day, Sunday, did the tide reached its normal state again. The tsunami was felt not only on the Portuguese coast but also in the southwest of Spain, in the north of Africa, in the British Isles and in the Netherlands [1755 O grande terramoto de Lisboa, 2005].

The reconstruction of Lisbon

After the disaster struck the capital of Portugal causing severe damage, it became necessary at all costs to start working for the benefit of the city and to find an urgent solution for the reconstruction. The prime minister of the time, the Marquis of *Pombal*, under the orders of King José I, was made responsible for the reconstruction of the city and to bring it back to normality as fast as possible. In **Figure 2-7** below one can see a painting of the Marquis of *Pombal*.

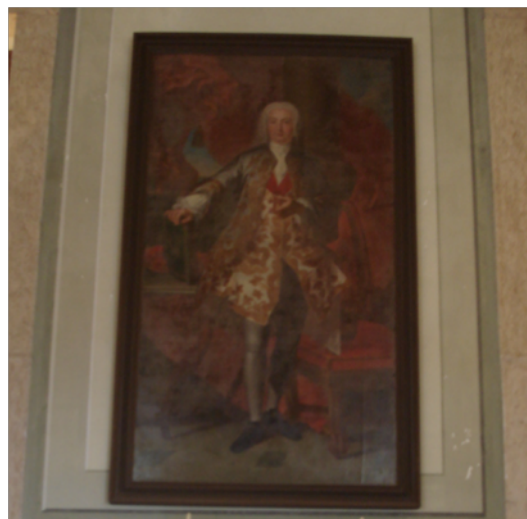


Figure 2-7: Marquis of *Pombal* in painting

He immediately mobilised all the available resources to clear paths through the debris and to search for survivors. So, aiming to avoid the danger of plague, the dead were promptly buried [França, 1989]. Provisional hospitals were created to care for the sick and camp sites were set up to give shelter to the injured and homeless. As early as the day following the earthquake, he took measures to study the reconstruction of new buildings [Mascarenhas, 1996]. A few days later a survey was carried out to gather information about what had been destroyed. All types of construction outside the city limits was forbidden. Plus, no construction was to take place until there was a plan for the reconstruction. Meanwhile, food prices were fixed to prevent speculation.

With no time lost, he delegated the development of proposals for the reconstruction of the destroyed city to a group of architects and engineers. Pombal relied on technicians such as Manuel da Maia, the kingdom's official engineer. **Figure 2-8** shows a sculpture of the engineer Manuel da Maia.



Figure 2-8: Engineer Manuel da Maia (1672-1768)

It was this man, at the time aged about 80, who was made technically responsible for the coordination of the reconstruction of the destroyed part of the city. He is one of those responsible for the *Baixa Pombalina* as we have it nowadays. The proposals by Manuel da Maia for the reconstruction of the city comprised three major phases. The first phase, dated 4 December 1755, consisted of five possible approaches. The first approach consisted of rebuilding exactly what had previously existed. The second approach was to rebuild to the former height but to convert the narrow streets into wide ones. The third approach was to restrict the buildings to two floors and widen the narrow streets. The fourth approach was to demolish any remnants of the previous buildings and to draw a completely new plan. Finally, the fifth approach consisted of rebuilding the city in a completely different location (either between *Alcântara* and *Pedrouços* or in *Belém*). After considering the proposals the king decided to build the new royal palace at *Belém* but, as far as the city was concerned, he decided for the fourth approach, i.e., setting a completely new plan for the city centre[Mascarenhas, 1996].

For the second phase of the proposals, dated 16 February 1756, Manuel da Maia suggested three different possibilities for downtown Lisbon reconstruction. The first was to completely demolish Lisbon to the ground and rebuild it following a rational plan. The second possibility was to demolish Lisbon but keeping the wide streets and widening the narrow ones. Finally, the third was not to demolish Lisbon but just

change the alleys and lanes into wide streets. Manuel da Maia recommended the first approach and this was the one selected [Mascarenhas, 1996].

Lastly, the third phase of the proposals was dated 31 March 1756. For this last phase, three teams were constituted preparing six drafts of plans for the reconstruction of the city. All the plans presented tried to preserve *Rossio* and *Terreiro do Paço*. The winning plan was the fifth plan prepared by architect Eugénio dos Santos de Carvalho, known as plan number 5. It consisted of an orthogonal grid with eight streets perfectly parallel and rectilinear, oriented in the north-south direction. Nine streets cross orthogonally in an east-west direction. A painting of the architect Eugénio dos Santos de Carvalho can be seen in **Figure 2-9**.



Figure 2-9: Architect Eugénio dos Santos de Carvalho (1711-1760) [Author not identified, 18th century, Association of the Portuguese archaeologists]

Eugénio dos Santos was an inspector of the royal construction works and an architect of the Senate. Manuel da Maia may have been influenced by his standing background when selecting the winning plan. The plan was particularly successful in integrating two separate areas with different functions: *Rossio*, with its daily social functions and *Praça do Comércio* (Commerce Square) with its commerce and administrative functions [Mascarenhas, 1996]. The winning plan of the reconstruction can be seen in **Figure 2-10**. For a more detailed explanation of all the phases of the proposals please see Mascarenhas [1996].

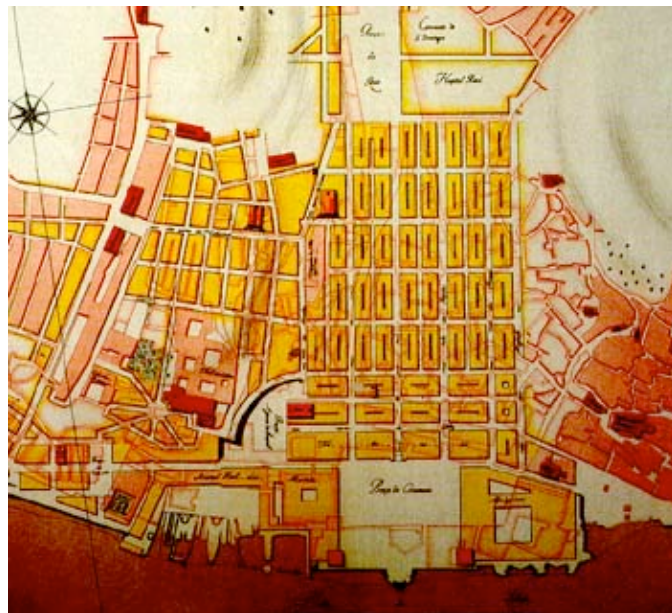


Figure 2-10: The winning plan of the reconstruction

The buildings were to be constructed in accordance with the plans produced by the Senate architect, Captain Eugénio dos Santos.

The rebuilding of the downtown area of the city initiated in 1756 and was carried out over many decades (about 70 years). However, on the 24 of February 1777, King José I died and this ended *Pombal*'s ruling as prime minister. The Marquis of *Pombal* was then ordered into exile at his palace in Pombal. All public building works which had already been progressing very slowly were temporarily suspended [França, 1983]. After 1830, due to a series of crises and an appalling economic situation, all building construction was practically paralyzed. Gradually the reconstruction plans came to be ignored [Macedo, 1938].

2.2. Constructing elements of *Pombalino* buildings

The Marquis of *Pombal* delegated the development of a structural solution that would guarantee the required seismic resistance of the buildings to a group of engineers and architects. Based on the know-how of that time and on the empirical knowledge gathered from the buildings that survived the earthquake, a new construction type was created, this being generally referred to as *Pombalino* buildings. This is characterized generically by its economy of style, its solidity, its regularity and its simplicity. In **Figure 2-11** an example of one of these buildings is depicted.

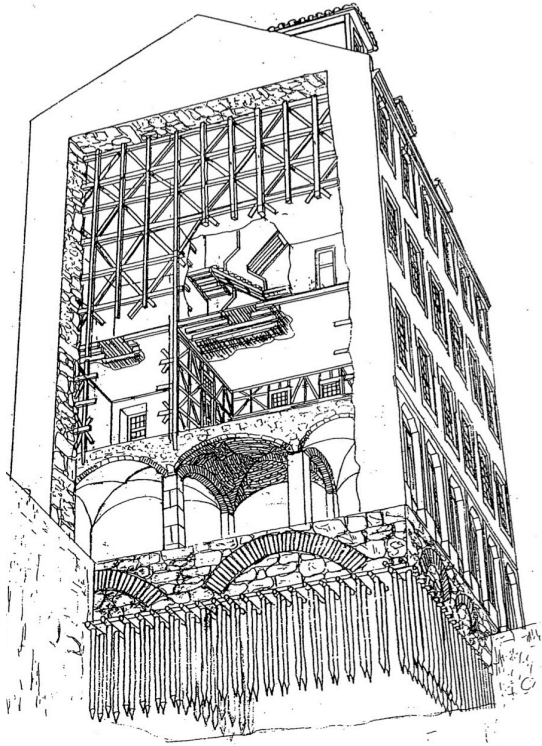


Figure 2-11: Example of a *Pombalino* building [Mascarenhas, 1996]

2.2.1. The foundation system

The architect Mascarenhas [1996] had the chance to observe directly the constituent elements of the *Pombalino* buildings from many buildings that were being completely or partially demolished some decades ago. He observed the foundation system had been developed using wooden piles that allowed the buildings to “float” on the underlying alluvium. He observed the piles were similar and repetitive, on average 15 cm in diameter and under 1.5 m in length, forming two parallel rows in the directions of the main walls, which were linked at the top by horizontal cross members attached by thick iron nails. Three rows of poles, three to five metres in length, were longitudinally nailed on top of the cross members. The system of using piles consisting of green pine logs below the water table, without light or air, made it impossible for any kind of infestation to develop; thus the wood was preserved for a long time [Mascarenhas, 1996].

Below the internal walls, the use of piles was limited to the points of intersection. At these points, a stone foundation pier was built. The continuity of the construction was established by connecting the foundation walls and piers with brick arches, surmounted by stone walls which were the base for the walls or piers of the building [Mascarenhas, 1996]. **Figure 2-12** shows the foundation system in drawing.

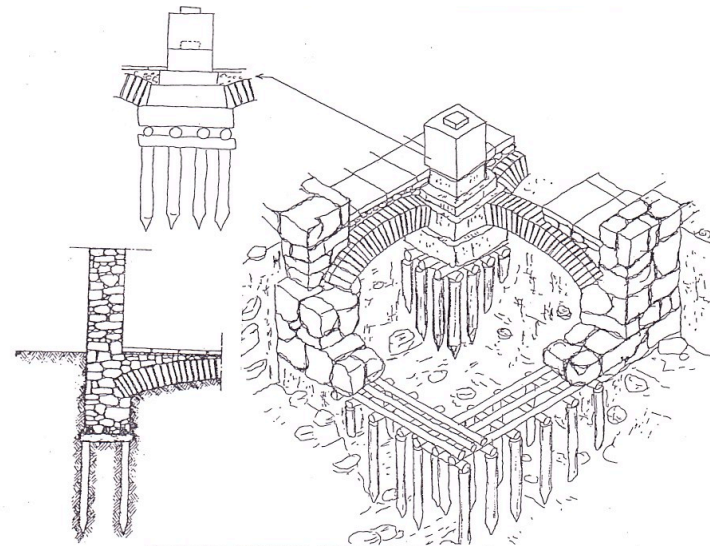


Figure 2-12: The foundation system [Mascarenhas, 1996]

The following photo (**Figure 2-13**) shows two foundation piles under water. The photo was taken at Foundation Millennium BCP, Archaeological Nucleus of street Rua dos Correeiros.



Figure 2-13: Two foundation piles under water

2.2.2. The ground floor

At ground floor level the building consisted in solid walls and piers linked by a system of arches. Especially on secondary streets, where stores and stables were located, thick-groined vaults spanned between the arches. At ground floor level the structure of the cage was rarely incorporated into the walls [Mascarenhas, 1996]. It is believed that this was to prevent the spread of any fire that might start at ground floor level. At the points where internal walls crossed on the upper floors, thick piers of stones were built at ground floor level. On the drawing of **Figure 2-14** one can see on the left groined vaults spanning between the arches; on the right one can see wooden floors, arches and piers.

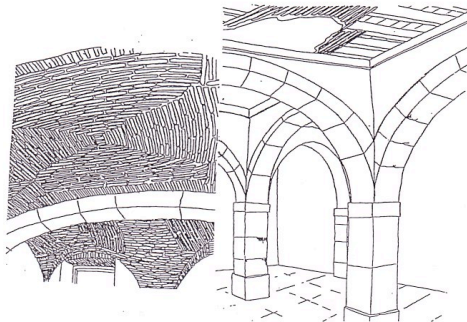


Figure 2-14: Left: groined vaults over the arches; right: wooden floors, arches and piers
[Mascarenhas, 1996]

On the following photo, **Figure 2-15**, a brick groined vault, on the ground floor, from a certain building in downtown is shown.



Figure 2-15: Photo of brick groined vault on the ground floor

2.2.3. The *gaiola*: “frontal” walls and floors

The *gaiola* or wooden cage structure may have been based on traditional wooden structures such as those of some houses on the Castle Hill in Lisbon. The cage in the *Pombalino* buildings was quite ingenious in its simplicity of construction and was a structural element of the buildings being able to support the floors and also resist horizontal seismic forces. The structure of the *gaiola* is basically made up of a matrix of modules with horizontal, vertical and diagonal members, which form a series of Saint Andrew’s crosses. In **Figure 2-16** one can see a sketch of the *gaiola* with floors and “frontal” walls (vertical elements). As the structure is made up of a series of repetitive struts, with reduced lengths, it was possible to overcome the problem of scarcity of wood in the Lisbon area, and at the same time allow for better modulation in plan and elevation, with the options of being able to leave open spaces whenever they were required.

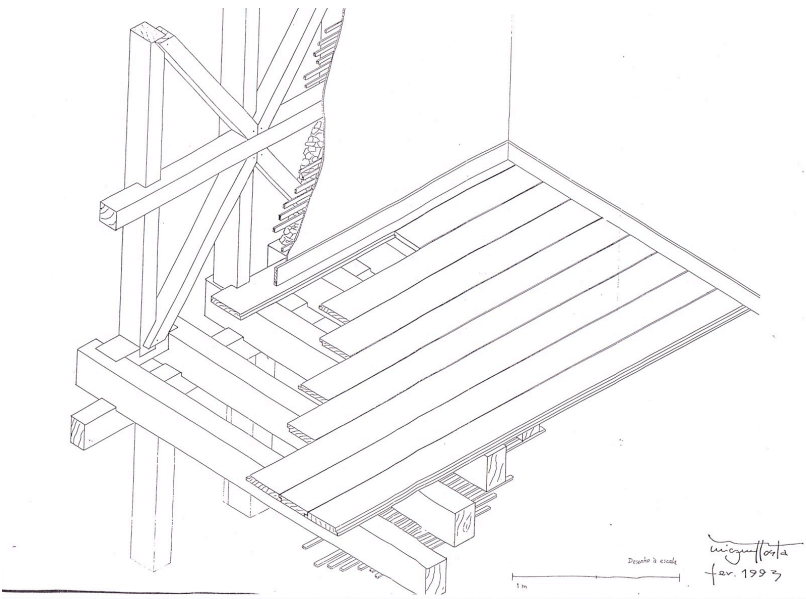


Figure 2-16: The *gaiola*: floors and “frontal” wall [Pinto Costa, 1993]

In the following **Figure 2-17**, **Figure 2-18**, **Figure 2-19** and **Figure 2-20** one is able to see how different sizes of walls (heights and lengths) can exist. **Figure 2-17** shows a “frontal” wall of 3x2 modules (3 modules high and 2 modules in length).



Figure 2-17: “Frontal” wall of 3x2 modules

In **Figure 2-18** one can see a wall of 3x3 modules and in **Figure 2-19** a wall of 3x4 modules is depicted.



Figure 2-18: “Frontal” wall of 3x3 modules



Figure 2-19: “Frontal” wall of 3x4 modules

The module size allowed for the lower floors, which had higher ceilings, to be three modules high while the attic would only be two modules high. The section dimensions of the *gaiola* members varied with specie of timber used and the location, with larger sections generally being used for lower floors. On the attic floor, the sizing of the timber sections was extremely inconsistent. The sections were always smaller and irregular and often consisted of small, circular logs which even had bark left on them [Mascarenhas, 1996]. In **Figure 2-20** one can see a “frontal” wall of two modules high generally used in the attic as mentioned.

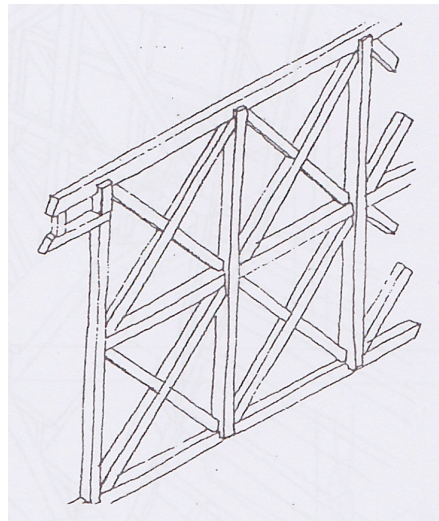


Figure 2-20: “Frontal” wall of 2 modules high

In **Figure 2-21** a sketch of the details of the middle central connection is presented. It can be seen that the vertical and horizontal struts are cut at their mid-sections to attach them together.

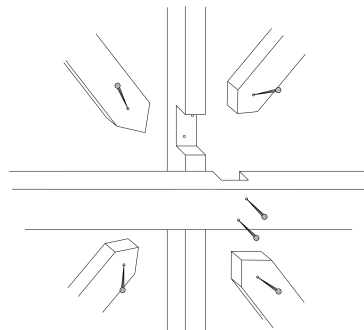


Figure 2-21: Details of the middle central connection

In **Figure 2-22** one can see a sketch of how two diagonal elements are attached together. These are also cut at half their thicknesses to attach them together.

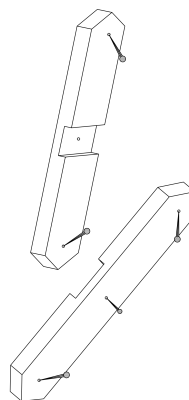


Figure 2-22: Diagonal elements connecting details

In **Figure 2-23** (a) to (c) a sketch of the “frontal” wall connection details at left and middle (a), at the upper middle (b) and at the middle central connection (c) is shown. It is possible to notice that in (b) the horizontal element is not cut to half its thickness.

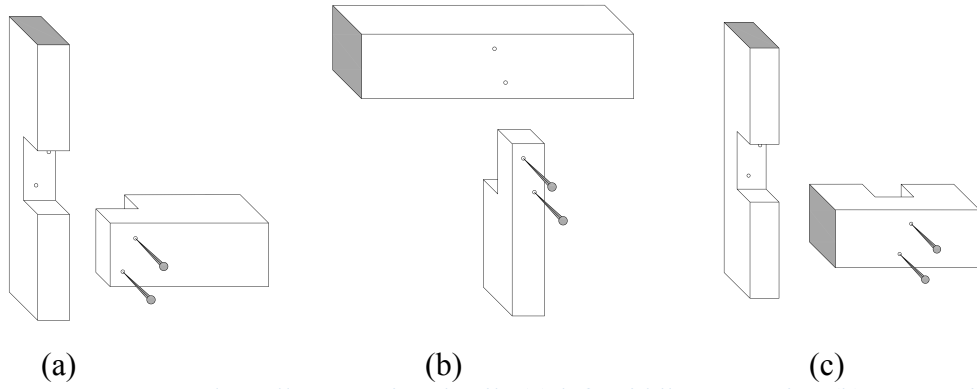


Figure 2-23: “Frontal” wall connection details (a) left middle connection (b) upper middle connection (c) middle central connection

In **Figure 2-24** a sketch of the detail of the connection of the floors with (a) the façades and (b) the “frontal” walls is presented.

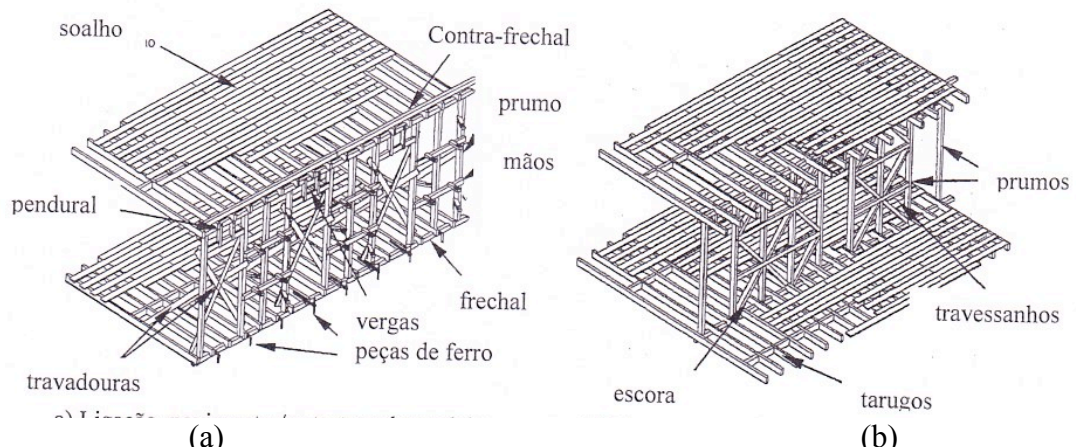


Figure 2-24: Detail of the connection of the floors with (a) the façades; (b) the “frontal” walls (legend in Portuguese) [Ramos, 2002]

Figure 2-25 shows that the “frontal” walls of the upper and lower floors share the same beam. In **Figure 2-26** one is able to see that other possible truss layouts of “frontal” walls exist in other buildings and also, in the same building, for instance in the walls of the staircases. Finally, **Figure 2-27** depicts details of the “frontal” walls covered with lath in a building in Guimarães.

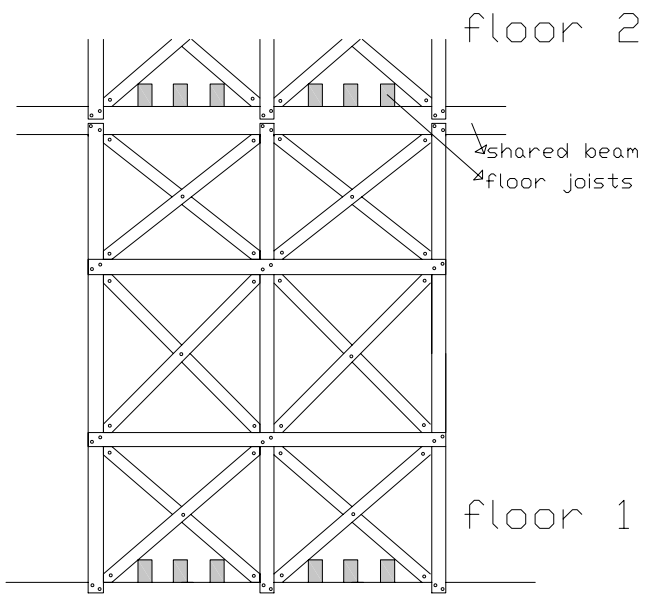


Figure 2-25: Connection detail of “frontal” wall at floor 1 with upper floor 2

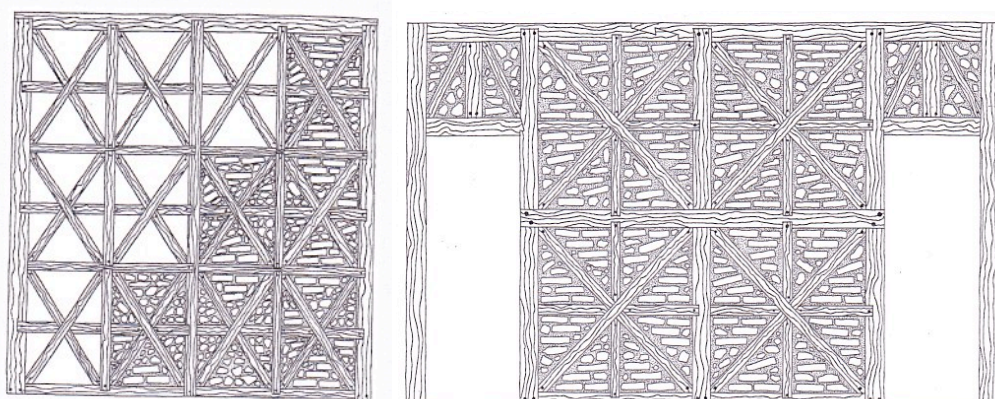


Figure 2-26: Other possible truss layouts for “frontal” walls. [1755 O grande terramoto de Lisboa, 2005]



Figure 2-27: Details of the “frontal” walls covered with lath in a building in Guimarães

The wooden partition walls (*tabiques*) do not belong to the *gaiola* as they do not continue on the floor above and below. They were made only in order to subdivide a space in a storey. They are formed with planks nailed onto the struts then covered with laths and plastered.

2.2.4. The façade

In the Pombalino buildings the design of the façades follows a rigid scheme. Visual enrichment or conversely impoverishment of the façades is limited to variation in small details. According to Mascarenhas [1996], the variations in small details do not occur in individual buildings or blocks but according to the “hierarchy” or relative importance of the streets. The design of the façades in the main streets is more elaborate than that seen in the secondary and side streets. The rectangular blocks generally run north-south and define both main and secondary streets running in that direction. The ends of the blocks which normally comprise two buildings (occasionally one) define the side street.

In **Figure 2-28** a typical façade of the buildings is presented. Here one can see the ground floor, usually commercial, the three residential floors plus the attic giving a total of five storeys. Occasionally one can find even six storey high buildings in *Baixa* but this is not common.

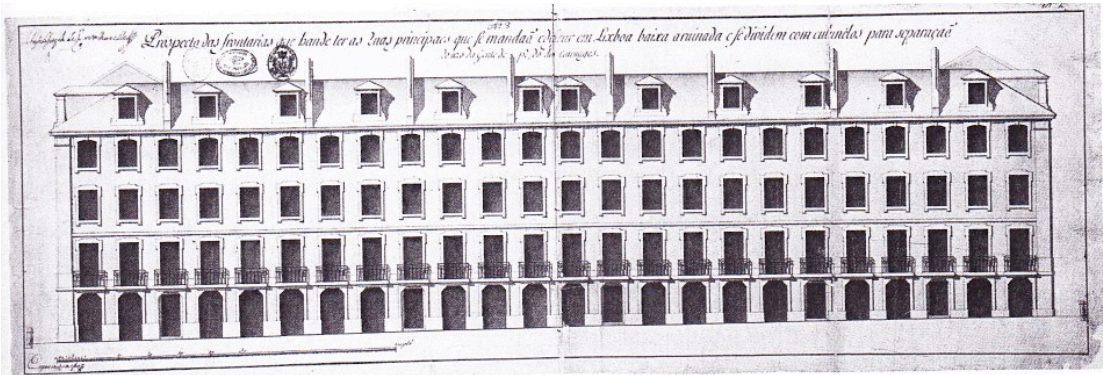


Figure 2-28: A typical façade of the buildings [drawing by Sebastião Joseph de Carvalho e Mello and Eugénio dos Santos e Carvalho, taken from 1755 O grande terramoto de Lisboa, 2005]

The thickness of the wall of the main and back façades decreases with height as shown in **Figure 2-29**.

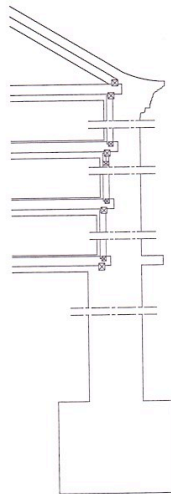


Figure 2-29: Cut of the main and back masonry façades [1755 O grande terramoto de Lisboa, 2005]

2.2.5. The roof

There is an attic storey, set back from the others above the cornices, which, in the main streets and squares takes the form of a mansard roof, while elsewhere it takes the form of a hipped roof. The hipped and mansard roofs (Figure 2-30) have dormer windows set back from the face of the wall with small hipped roofs over them. There were also gable walls rising 0.80 m above the roof to prevent fire from spreading between the adjacent buildings.

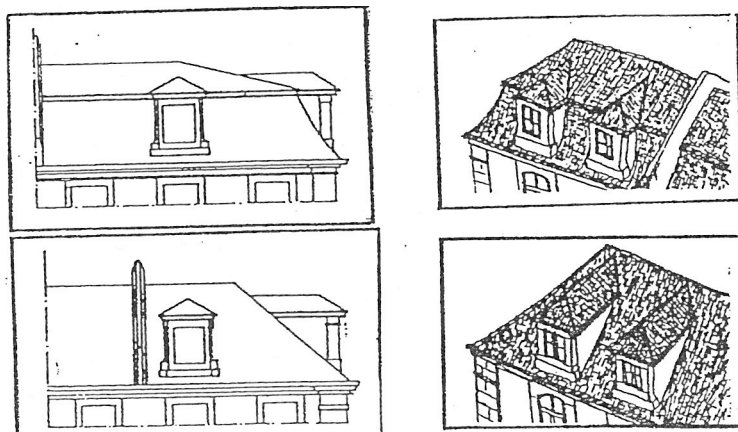


Figure 2-30: Above: Mansard roof; below: Hipped roof [Mascarenhas, 1996]

2.2.6. The stairs

For safety reasons related to the spread of fire, in most buildings, the steps of the first flight of stairs that give access to the residential floors were made of stone and in the following flights the stair was made of wood. This can be seen in Figure 2-31. The stairs are resting on the “frontal” walls that are on the side of the stairs.

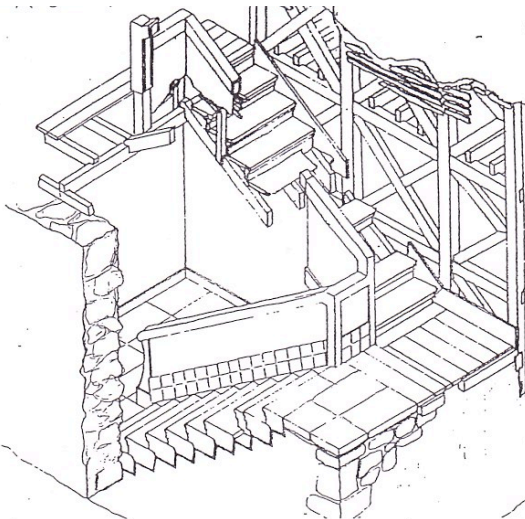
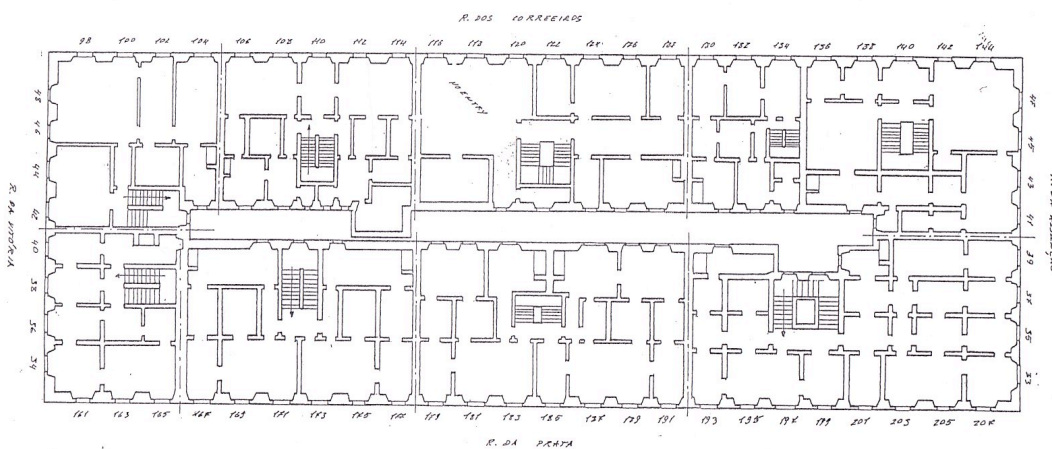


Figure 2-31: The structure of the stairs [Mascarenhas, 1996]

2.2.7. The floor plan

Each block comprised approximately ten buildings. As can be seen from **Figure 2-32** in the inside of the block there was an open space – internal courtyard (*saguão*) not covered by the roof tiles. There was access to the courtyard. The internal walls surrounding the courtyard had smaller openings than the main outside façade. **Figure 2-32** also shows how each building is separated by gable walls. The block is not necessarily symmetrical and the buildings may not all have been constructed at the same time.



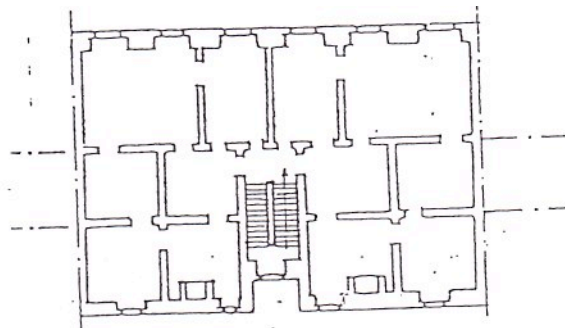


Figure 2-33: The plan view with three division fronts [Mascarenhas, 1996]

2.3. Similar Constructions

Certainly no one knows where the idea of using internal “frontal” walls came about. Nevertheless, it is believed by many authors that this constructing element was based on older buildings that survived past earthquakes.

Langenbach [2003], in answer to the question: *How did the engineers at the time of Pombal believe the Pombalino building system would work?*, thinks that there must have been buildings in Lisbon constructed with a timber frame and infill masonry that were seen to have survived the earthquake. The area of *Alfama* next to *Baixa*, which dates back to Medieval Lisbon, was reportedly not destroyed during the 1755 earthquake. There were probably in-filled timber frame buildings there since this form of construction was common throughout Medieval Europe, including the Iberian Peninsula. For example, in Madrid, which has not historically been subjected to earthquakes, most of the historical buildings within the walled city area around the Plaza Major, which from the front look like standard masonry buildings, are in fact almost completely timber framed structures. Only the street façades are bearing wall masonry and the internal structure of the buildings rests completely on timber columns with a rubble masonry infill. Some of these buildings are six or seven stories in height. Thus, the adoption of the *Pombalino* system serves to systematize specifically for earthquake resistance a building tradition that extends back over 1500 to 3000 years to Roman and pre-Roman precedents. According to Copani [2007] one of the oldest examples of timber frame buildings is one of the surviving houses at the archaeological site of Herculaneum: it hands down to us the well known technique called *opus craticium* by Vitruvius and is a formidable evidence of the diffusion of the timber-frame during the Roman period. The *opus craticium* was widespread in the Roman Provinces, and later developed in different ways in a large number of Mediterranean and European areas.

On the other hand, as documented by Barucci [Barucci, 1990], the development of the Italian “*Casa Baraccata*” (Figure 2-34) system in Calabria and Sicily, where devastating earthquakes had occurred with astonishing frequency, was contemporary with the *gaiola* in Portugal, and each one may have been influenced by the other. In Italy, the “*Casa Baraccata*” became the underlying basis for a series of manuals of practice and even of patent applications for seismic resistive construction techniques, throughout the 19th century and the first two decades of the 20th century [Barucci, 1990].

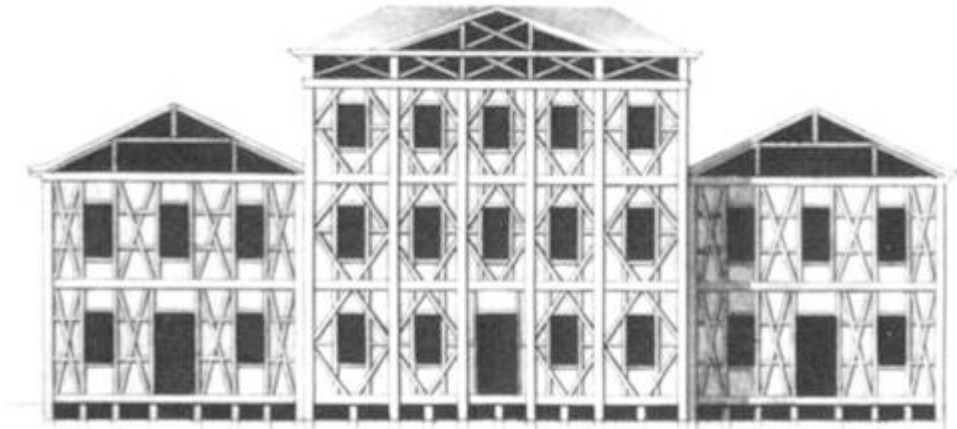


Figure 2-34: Casa Baraccata

Still standing nowadays, one can find timber-framed masonry in-filled buildings, for instance, in Turkey (**Figure 2-35**).



Figure 2-35: Hımitş house in Gölcük, Turkey [Langenbach, 2008]

Hımitş construction is simply described as a timber frame with masonry infill. The masonry is usually a single “wythe” or layer, often with bricks laid at angles to fit between the studs, or instead, if stones are used, random rubble set into thick layers of mortar. Depending on the place, the mortar is usually a lime mortar but in some cases, in rural areas for example, a mud mortar may be used. Hımitş was a characteristic form of construction in many parts of Turkey during the Ottoman period, and has continued to be commonly used up until it was rapidly displaced by reinforced concrete frames with hollow clay brick infill construction in the middle of the 20th century.

Hümüş construction is a variation on a shared construction tradition that has existed through history in many parts of the world, from Elizabethan England to 19th century Central and South America. In Britain, for example, it would be referred to as “*half-timbered*”; in Germany as “*fachwerk*”; in France as “*colombage*” and in Kashmir as “*Dhajji-Dewari*” (**Figure 2-36**) [Langenbach, 2003].

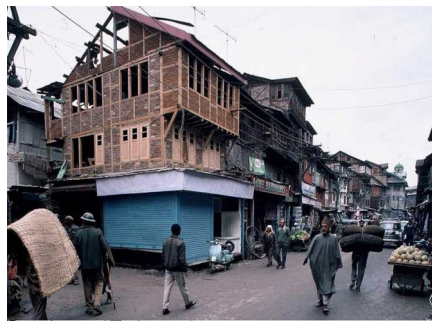


Figure 2-36: *Dhajji-Dewari* construction in Srinagar, Kashmir in 1989 [Langenbach, 2003]

According to Langenbach [2003], the significance of the *Pombalino* building system lies in the fact that it was deliberately developed and selected as earthquake resistant construction for a major multi-storey urban area.

Although similar, these two building systems are not the same. The *Pombalino* buildings, usually 5 storeys, are taller than most of the Turkish Hümüş houses and have external masonry walls encompassing the timber frames.

Close to Turkey, in Greece, one can currently also find timber-frame masonry infill structures for instance in Lefkadas Island (**Figure 2-37**).



Figure 2-37: Typical morphology of timber-framed masonry infill walls of Lefkas island, Greece [Vintzileou, 2007]

According to Vintzileou [2007], the island of Lefkada, one of the Ionian Islands, is situated in the most earthquake prone region of Greece. A local structural system was developed before the 19th century in Lefkada. The strong earthquake which occurred in 1821 proved the adequacy of the system to sustain seismic actions. Typical buildings (one to maximum three storey buildings) consist of a stone masonry ground floor plus one or two timber framed brick masonry storeys. Intermediate floors and

roof are made of timber. The roof is covered with tiles. Like downtown Lisbon, the city of Lefkada is founded on low strength alluvia. Therefore, special care was given to the foundations of the buildings. The buildings were founded on a grid of trunks (**Figure 2-38**) at a depth of 0.6-1.0 m. The space between the timber elements is filled with sand, rubble stones and hydraulic mortar.

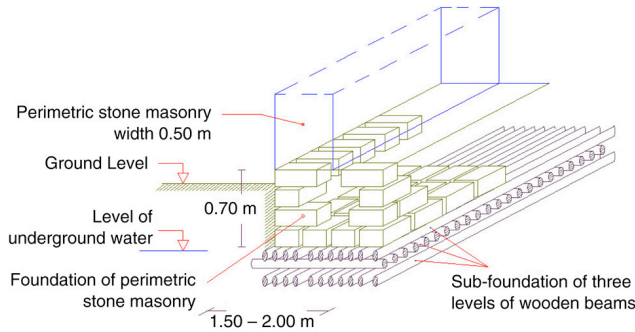


Figure 2-38: Details of the foundation of traditional buildings of town of Lefkas, Greece
[Makarios, 2006]

Sill according to Vintzileou [2007], bearing walls in the ground floor are no more than 3.0 m high and they are made of stone masonry (0.6-1.0 m thick). The external leaf of walls is made with roughly cut stones, whereas cut stones are used in the corners of the buildings as well as along the perimeter of openings. Rubble stones are used in the internal leaf of ground floor walls. The space between the two leaves is filled with small-sized stones mixed with pieces of bricks and mortar. In addition to the masonry walls a secondary (timber) bearing system is present in the ground floor which consists of timber columns (**Figure 2-39**) arranged close to the masonry walls. The upper storey arrangement of timber elements in the timber-framed walls can also be seen in **Figure 2-39**. On the upper storeys, the wooden 3D frame possesses diagonal wooden trusses. Single bricks with lime mortar fill the wooden trusses.

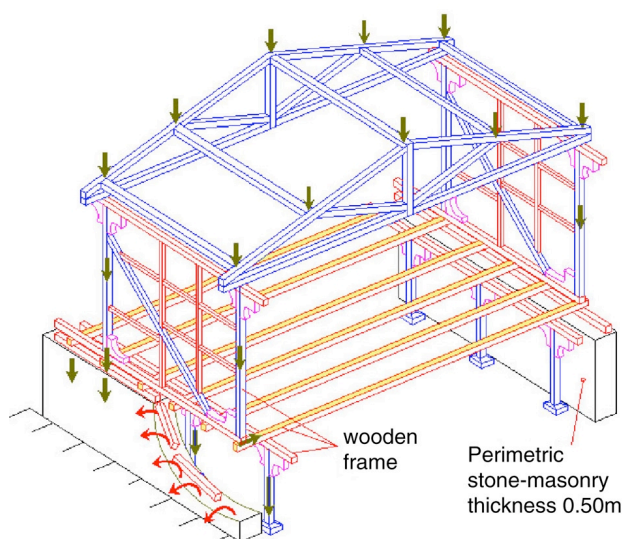


Figure 2-39: The dual bearing system of traditional buildings in Lefkas [Makarios, 2006]

The diligence of the foundation construction and the dual bearing system at the ground floor combined with the relatively low mass of the upper storeys, exhibit a remarkably reduced vulnerability of these type of structures to earthquake actions [Makarios, 2006].

Also in Haiti there are two floor traditional houses with timber frame with in-filled masonry as can be seen in **Figure 2-40** and **Figure 2-41**.



Figure 2-40: Ginger-bread house in Haiti - building

One can see how the façade of the building in Haiti very much resembles the “frontal” walls of the *Pombalino* construction (**Figure 2-41**). There are, in this case, no external masonry walls and the building is entirely in-filled timber frame.

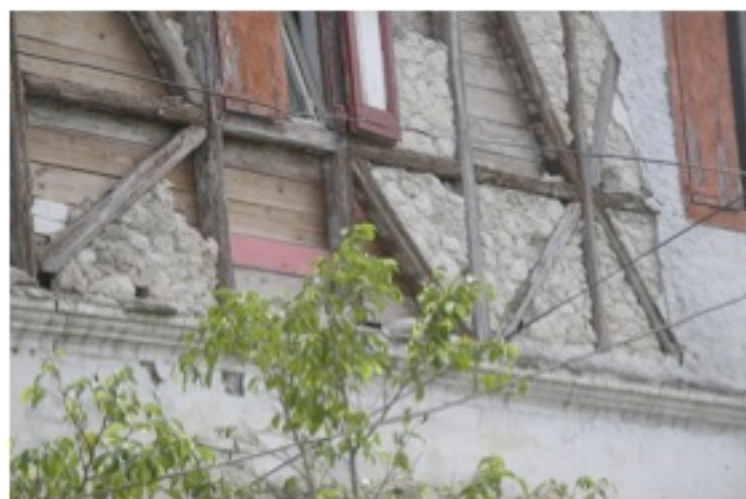


Figure 2-41: Ginger-bread house in Haiti - façade

In another point of view, Copani [2007] believes, by studying in-filled timber frame buildings in Scandinavia, that one cannot explain the large spread of the timber frame with in-filled masonry just considering its seismic resistant nature; off course, its

because it is also possible to find infill frame construction in areas where there is no earthquake risk. Moreover, their features in terms of economy and strength can support this assertion. In some areas of Scandinavia the timber-frame with in-filled masonry was the most common way of constructing buildings, both private and public, especially in areas where bricks could be easily supplied. This happened, for example, in Denmark and Sweden, more than in Norway or Finland, inside towns or villages more than in the countryside. In Scandinavia the traditional in-filled timber frame construction is not so different from the others in the rest of Europe: a timber cage based on the repetition of a little module in plan lied over a masonry foundation and the vertical walls rise up for two or three floors. Nevertheless, by observing carefully the constructions in seismic and non-seismic areas (based on the images provided by Copani [2007]) it seems that the Scandinavian houses have a configuration of the wooden frame lacking the presence of crossed braces (see **Figure 2-42**), indicating this configuration (crossed braces) is typical of seismic countries.



Figure 2-42: A traditional house in Lund (Sweden) [Copani, 2007]

Based on all the presented timber frame in-filled masonry buildings one can observe that the Pombalino buildings may be similar to these constructions but are not the same. This proves their uniqueness in the worldwide building stock. The monumental five storeys of the buildings (higher than most in-filled timber frame constructions), the presence of thick masonry walls encompassing the timber frames, the ingenious foundation system, the presence of the ground floor entirely made of stone, the spread of the system throughout a major multi-storey urban area and other small features and thoughts that were deliberately planned as earthquake resistant make this construction system unique in the world. It is thus our duty to study it in order to be able to preserve it and, if possible, to improve it.

2.4. Bibliography

1755 O Grande Terramoto de Lisboa, 2005, Volume 1, Publishing Público

Barrucci C., 1990, La casa antisismica, prototipi e brevetti, Gangemi Editore, Reggio Calabria

Baixa Pombalina 250 anos em imagens, 2004, Printing Jorge Fernandes Lda

Castilho, Julio, 1893, *A Ribeira de Lisboa, descrição histórica da margem do Tejo desde a Madre de Deus até Santos-o-Velho*, Lisboa.

Copani P., 2007, Timber-Frame Buildings in Scandinavia: High Deformation Prevent the System from Collapse, From Material to Structure – Mechanical behaviour and Failures of the Timber Structures, ICOMOS IWC – XVI International Symposium, Florence, Venice and Vicenza

França, Jose Augusto, 1983, *Lisboa Pombalina e o Iluminismo*, Bertrand Editora, Lisboa

França, José Augusto, 1989, *A reconstrução de Lisboa e a arquitectura Pombalina*, Biblioteca Breve, vol 12, 3^a edição, Instituto de Cultura e Lingua Portuguesa, Ministério da Educação, Lisboa

Gastão de Melo Matos, 1947, Lisboa oito séculos de História, vol 1, Lisboa na Restauração, Câmara Municipal de Lisboa, Publicações comemorativas do oitavo Centenário da Tomada de Lisboa aos Mouros, Lisboa

“Grande Enciclopédia Portuguesa e Brasileira”, 1945, vol 15, Editora Enciclopédia Limitada, Lisboa e Rio de Janeiro

História de Portugal, 1929, Edição Monumental da Portucalense Editora, vol 2, Barcelos

<http://www.lisboa-cidade.com/lx/index99pt.asp?pa=ptihist.htm>

Langenbach R., 2008, Learning from the past to protect the future: Armature Crosswalls, Engineering Structures

Langenbach R., 2003, “Crosswalls” instead of Shearwalls – A Proposed Research Project for the retrofit of Vulnerable Reinforced Concrete Buildings in Earthquake areas based on traditional Hümş Construction, Fifth National Conference on Earthquake Engineering, 26-30 May, Istanbul, Turkey

Mascarenhas J., 1996, A study of the Design and Construction of Buildings in the Pombaline quarter of Lisbon, PhD thesis of the University of Glamorgan, UK

Mascarenhas J., 2005, Sistemas de Construção V – O Edifício de rendimento da Baixa Pombalina de Lisboa, Livros Horizonte, 2nd edition (in Portuguese)

Macedo LP, 1938, *A Baixa Pombalina*, ed. Grupo amigos de Lisboa, Lisboa

Macedo, Jorge Borges, 1989, A situação económica no tempo de Pombal, Edições Gradiva

Makarios T. and Demosthenous M., 2006, Seismic response of traditional buildings of Lefkas Island, Greece, Engineering structures 28, pp. 264-278

Oliveira Martins, J.P., 1985, *História de Portugal*, Imprensa Nacional - Casa da Moeda, Lisboa

Pinto Costa, MLF, 1993, *Técnicas de Construção, Sistema Construtivo Pombalino*, Évora

Pradalié, Gerard, 1975, *Lisboa da Reconquista ao fim do século XII*, 1st edition, Lisboa

Ramos JLSF, 2002, Analise Experimental e Numerica de Estruturas Historicas de Alvenaria, Msc Thesis, University of Minho, Guimaraes. (in portuguese)

Sequeira, Gustavo Matos, 1947, *Lisboa oito séculos de História, vol 1, D. Dinis – A cidade Medieval*, Câmara Municipal de Lisboa, Publicações comemorativas do oitavo Centenário da Tomada de Lisboa aos Mouros, Lisboa

Saraiva, José Hermano, 2007, *História Concisa de Portugal*, Publicações Europa-América, 24^a edição

Segurado, Jorge, 1971, *Lisboa no Passado e no Presente*, Edições Excelsior, Lisboa

Vieira da Silva, Augusto, 1960, *Dispersos*, Biblioteca de estudos Oliponenses, Lisboa.

Vilanova SP; Nunes ACF, Fonseca JFBD, 2003, *Lisbon 1755: a case of triggered intraplate rupture?*, Bulletin of the Seismological Society of America, vol 93(5), pp 2056-2068

Vintzileou E., Zagkotsis A., Repapis C. and Zeris Ch., 2007, Seismic behaviour of the historical structural system of the island of Lefkada, Greece, *Construction and Building materials* 21, pp. 225-236

3. Definition of the soil characteristics and seismic action for assessment

3.1. Summary

This section addresses the seismic ground characterization of the downtown area of Lisbon. The site selected is set on an alluvium-filled valley of soft unconsolidated sediments where considerable site amplification of ground motion is expected. Despite the importance and susceptibility of the site, only a little information is available in the literature for seismic ground characterization. Given that situation, data has been gathered from various sources, mostly from geological and geotechnical surveys. Additional measurements of ambient vibrations have been performed based on the H/V spectral ratio technique (HVSRT). Based on the combination of geological and geotechnical data with HVSRT, it was possible to characterize the alluvium site in terms of average shear wave velocity of the soil ($V_{s,av}$) and depth to bedrock (H) estimates, as well as mapping the site neighbourhoods where seismic ground amplifications are expected. The site $V_{s,av}$ of the soil is estimated at approximately 194 m/s. Additional information can be obtained with the HVSRT. The horizontally layered (1D) structure assumption may predict the average response of the soil near the centre of the valley but will probably not at the edges and this is explained by the mapping of changes in the H/V curves. Nevertheless, not too strong lateral variations of the underground structure (which lead to 2D/3D effects) are expected for this relatively shallow basin (depth/width=0.15). Finally the seismic action for the assessment of the structures studied in Chapter 6 is obtained.

3.2. Introduction

For the adequate seismic vulnerability assessment of structures it is important to take into account the influence of local site effects on strong ground motion. Soils can greatly amplify the shaking of an earthquake. The susceptibility of certain sites, such as, for instance, Mexico City lake zone, San Francisco bay area or downtown Lisbon is well known and documented. They significantly alter the incident ground motion causing catastrophic damage in some cases. In this way, adequate attention should be given to the characterization of the site in terms of ground parameters relevant for seismic action estimation. Very important ground parameters for seismic site characterization are the shear wave velocity of the unconsolidated sediments, the shear wave contrast between bedrock and sediments and the geometry and depth of the bedrock-sediment interface. Techniques for estimating ground parameters are usually grouped in geophysical and geotechnical (mechanical) methods. Generally, geophysical methods can differ on the possibilities and information these tests provide with the trade-off of cost. For instance, when estimating shear wave velocities, in-situ tests realized on the ground surface (e.g. seismic refraction) give global information on the medium but do not allow for an accurate definition of the shear wave velocity profile with depth; while in-situ tests realized with a borehole and especially the cross-hole test, are more powerful but have a high associated cost as a consequence. Additionally, more powerful tests tend to require enormous apparatus for the

equipment, which can make them unpractical for use in densely urbanized areas, at least not in a systematic way. Geotechnical in situ tests can be a very important source of information for ground site characterization. The Standard Penetration Test (SPT) is certainly the most commonly employed method of this type in Portugal. These tests directly aim to obtain soil resistance parameters but will also provide important information on stratigraphy and lithology, depth to bedrock or geometry of the bedrock-sediment interface if a reasonable amount of surveys have been done in an area so that a pattern is defined. Above all, geotechnical (mechanical) surveys are an abundant source of information in urbanized areas due to construction purposes, as opposed to geophysical surveys which are not so frequently found, especially in low to medium seismicity areas.

An average estimation of the shear wave velocity of the soil for the shallowest layers of soft material can be obtained with good quality by means of measurement of ambient vibrations. A good compromise is achieved with the in-situ technique based on the measurement of ambient vibrations named H/V spectral ratio technique (HVSRT). With simple means but under specific circumstances, the technique estimates the fundamental frequency of the site from which one is able to retrieve the average S-wave velocity of the associated soil layers provided some prior knowledge is gained on the site. Techniques based on the measurement of ambient vibrations have long been applied in Japan with an important application in seismic microzonation of sites [e.g. Horike, 1985]. Either single station or array station methods are used. Among the single station methods the HVSRT is the most popular. Nogoshi *et al.* [1972] first proposed the technique but this is recognized to have been widespread afterwards by Nakamura [1989, 2000] so that in the last two decades the number of related publications has increased tremendously (see D13.08 [2004] for an extensive list). The technique succinctly consists of deriving the ratio between the Fourier spectra of the horizontal and vertical components of the ambient vibrations obtained through measurements at the surface of a specific site. The frequency at the peak of such a curve (f_0) would be indicative of the S-wave resonance frequency of the soil layer (which is given by the transfer function of S-waves) and to some authors, although this is not consensus between researchers, the corresponding peak amplitude (A_0) would provide a satisfactory estimate of the site amplification of ground motion (as given by the S-wave transfer function). It is interesting to note that Nakamura himself [2000] claims that the theoretical background of the technique is not clear, but the many successful experimental studies performed are evidence of its reliability. In contrast, the major advantage of the technique is its attractiveness in terms of ease of data collection due to the short durations of measurements and the minor equipment required and, as a consequence, the associated insignificant cost of the technique.

The scope of this chapter is to gather all available information useful for the seismic ground characterization of the downtown area of Lisbon, aiming at identifying the areas (that is, neighbourhoods) susceptible to local site effects amplification of ground motion. Furthermore, the scope of this chapter is to define the respective soil classes according to Eurocode 8 [2004] and with this to obtain the seismic action for the downtown area of Lisbon to be used in the analysis to be carried out in Chapter 6. For this purpose research and gathering of data was carried out comprising information on geology, stratigraphy and also available geotechnical surveys. For a detailed ground site characterization additional measurements of ambient vibrations have also been

conducted based on the H/V spectral ratio technique, and these have been compared and validated with the gathered data [Meireles and Bento, 2008].

3.3. Prior investigation of the site

The site under study (**Figure 3-1**) located at GPS coordinates of the center $38^{\circ}42'37.28''N$ - $9^{\circ}08'12.95''W$ is the area of downtown in the city of Lisbon, Portugal. The site is set on an alluvium-filled valley which is surrounded by three hills, on the north, west and east sides and by the mouth of the river Tagus on the south side. A satellite view of the site can be seen in **Figure 3-1**. This is the heart of the city of Lisbon with significant historical importance mainly due to the heritage value of its structures, the so-called *Pombalino* buildings. As it has been detailed and explained in the previous chapter, in 1755 a catastrophic earthquake followed by a considerable tsunami struck the capital of Portugal, causing severe damage to the city and completely destroying its downtown.

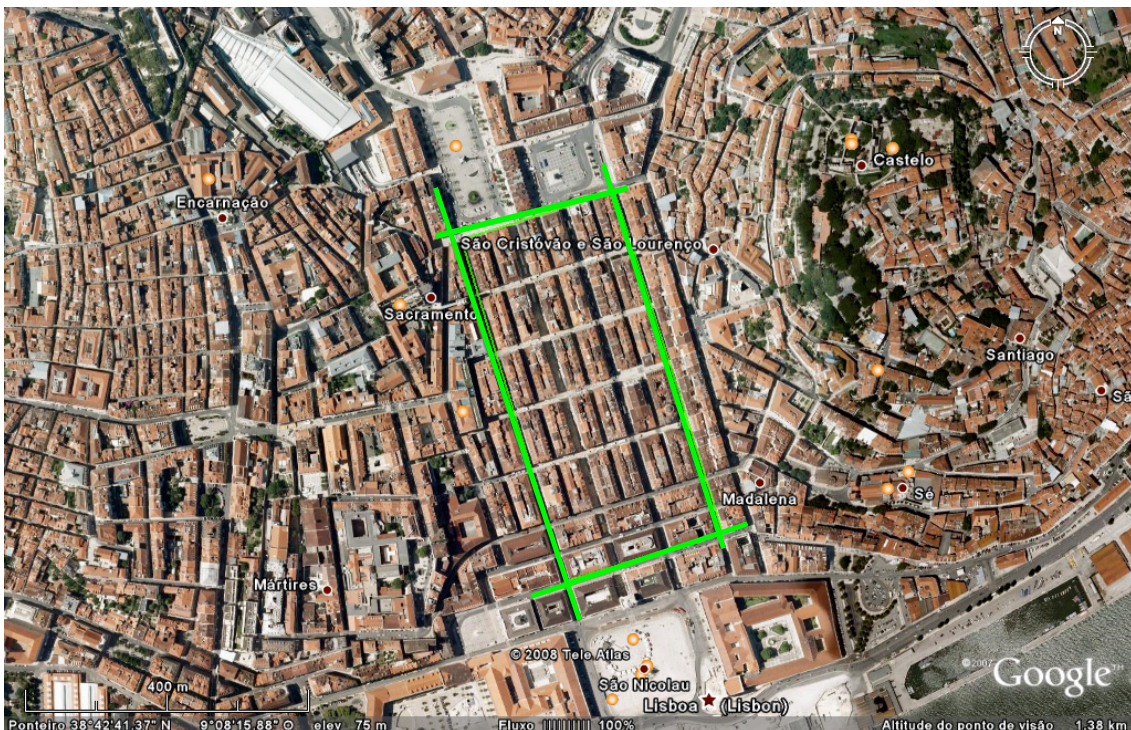


Figure 3-1: Location of the site within the urban area of Lisbon. The extension of the area (within the streets marked in green) is about 250 m wide by 490 m long, comprising 36 blocks. Map is copyright of Google Earth

According to the Geological map of the municipality of Lisbon (scale 1:10 000, sheet 4), depicted in **Figure 3-2**, the basement of the valley is composed of the Miocene formations named *Argilas e Calcários dos Prazeres* (these are green and grey clay material, frequently intercalated with levels of calcareous material); *Argilas do Forno do Tijolo* (these are dark grey consolidated clays); *Calcários de Entre-Campos* (these are yellowish calcareous materials) and *Areolas da Estefânia* (these are greyish fine sand materials).

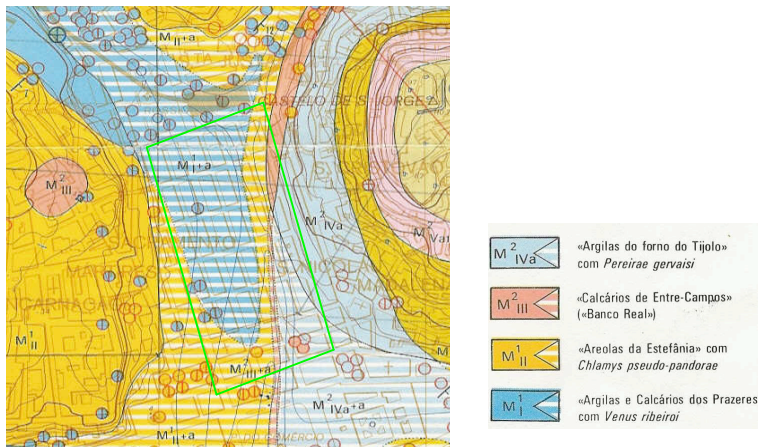


Figure 3-2: Geological map of the municipality of Lisbon, scale 1/10 000, sheet 4 (legend in Portuguese)

Geotechnical surveys kindly provided by some design offices and prospecting companies, have provided the following information: the valley basin is filled with layers of alluvium deposits from the Holocene. These are mainly composed of fine sand with greater or lesser quantities of organic soils (although clayey sand materials can also be found), defining in this way variations of alluvium layers, sometimes intercalated among each other and presenting different resistances. These have a total thickness that varies from 22.0 to 33.5 m at the centre of the basin. The topmost layer sets over the alluvium layers or directly above the bedrock formation. This layer is a normal consequence of urban activity but also results from the debris accumulated on the site after the 1755 earthquake. At the time, the decision to rebuild the city at the same site where it previously stood made the new buildings to be erected over the remains of the destroyed city making also the ground surface level to raise some metres over sea level. Thus, this topmost material is found to be very heterogeneous, with sporadic elements of stone or debris of wood or ceramic fragments, all set in a matrix of a sandy clay material. This layer thickness varies from 1.5 to 9.0 m over the entire site.

Depth to bedrock values obtained with the several surveys consulted show that the thickness of the soil layer slightly increases towards the south. At the centre of the valley, the depth to bedrock will be 31.5 m at the northern side and increasing up to 42.4 m at the south side of the site, at a length of approximately 490 m. The width of the valley (w) is approximately 250 m. This may be considered to be a relatively shallow valley with a depth (H) to width ratio of H/w approximately $(31.5+42.4)/2/250=0.15$. The geotechnical surveys available consisted essentially of SPT. The results present very broad values of the soil resistance, given by the number of blows in the tests, varying from 4 to 60 in the topmost layer of deposits or ranging between 2 and 60 in the alluvium layers. Even if this aspect reveals the heterogeneity of the materials it is also certain that the higher values of the number of blows are associated with the sporadic debris encountered for the topmost layer and that generally this layer is softer than the alluvium one. The geotechnical surveys consulted have also indicated the Miocene formation *Argilas do Forno do Tijolo* to present characteristics of a stiff soil, soft to hard rock behaviour for the formation of *Calcários de Entre-Campos* and stiff soil to soft rock behaviour for *Areolas da Estefânia*. Ground water level is generally found at 6.5 m (north side) to 2.5 m (south side) above sea level.

Even though seismic site effects are known to be a concern at this site, not too many studies have focused on the seismic response of the basin. A relevant but wide-ranging study was done by Teves-Costa *et al.* [1995]. In order to evaluate the predominant frequencies of the soil formations, the HVSRT was applied to the city of Lisbon with 114 points measured in a range of frequencies from 0.5 to 12 Hz. A detailed analysis was found to be complicated, however, since not much was known about the underlying formations but a general comparison was made between the HVSRT results and the geological map. In the area of downtown a predominant frequency of about 2 Hz was found.

3.4. H/V measurement technique for site characterization

3.4.1. Method and assumptions

The reason for a lack of a consistent theoretical background of the technique is because there is no established theory concerning what kind of wave motions ambient vibrations are composed of. Until the present there is no consensus among researchers with respect to the nature of these ambient vibrations, whether these would be surface or body waves or if both types of wave appear and at what relative ratio to each other.

Nakamura [1989] believes that the H/V curve at peak frequency range can be explained with a vertical incident SH wave. Here the author gives a theoretical definition of HVSRT with the multiple refraction of SH waves. On the other hand he states there is a group of researchers who try to explain the peak of the H/V curve with the evidence of Rayleigh waves, assuming that noise predominantly consists of surface waves. Nevertheless, this approach simply comes from the similarity of the figures of the HVSRT curve and H/V fundamental mode of Rayleigh waves but (the author claims) just looking to this similarity this conclusion cannot be reached.

Understanding that the correct interpretation of the H/V spectral ratio technique depends substantially on the understanding of the composition of the seismic wave field responsible for the ambient vibrations, which is related to the sources that generate the ambient vibrations and to the specific underground structure being investigated, the research programme SESAME (<http://sesame-fp5.obs.ujf-grenoble.fr>) devoted attention to the nature and origin of ambient vibrations wavefield.

Origin of ambient vibration wavefield means: which are the sources generating the ambient vibrations? Sources of ambient vibrations are usually separated into natural and human sources and these usually correspond to different frequency bands. Depending on this origin, one would expect a different frequency content such that there is usually a limit established between natural and human sources around 1 Hz. For low frequencies, the origin is essentially natural with emphasis on ocean waves and coastal waves, frequencies of 1 Hz are usually associated with wind effects and local meteorological conditions and higher frequencies are mainly associated with human and industrial activity and thus often exhibit a strong day/night and week/weekend dependence.

Bonefoy [2004] carried out research work in order to determine the nature of seismic ambient vibrations so as to better understand the principles that validate the HVSRT. This study was developed in the scope of the research programme SESAME. The extensive work has conducted several numerical simulations to reproduce the composition of the seismic wave field under controlled conditions (different types of sources, several types of underground structure, etc.). Controlled array numerical simulations were also conducted. The work is based on the initial assumption that the peak originated by the HVSRT curves is due to the ellipticity of the Rayleigh waves. However, the numerical simulations performed have proved that the H/V ratio cannot always be governed by the ellipticity of the Rayleigh waves. These results have shown that in case of local (close) and superficial sources, the wavefield generated is mainly consisting of surface waves and that, in this situation, only one peak is observed in the H/V curves. On the other hand, far away and deep sources will mainly generate volume waves and in this case more peaks can be observed at other natural frequencies either than the fundamental S-wave frequency, corresponding to higher modes of vibration for S-waves. Even though it is believed there is not a unique solution to the question of which type of waves originate the peak, it is concluded that local and superficial sources will most probably dominate the ambient vibrations wavefield for an urban environment.

No matter what the justification is for the appearance of the peak, the work claims that the corresponding frequency of the peak gives a good estimation of the resonance frequency of the soil layer, which is given by the transfer function of S-waves. The deviation will not be higher than 20%. On the other hand, it is stated that the amplitude of the peak does not give a good estimation of the site amplification (given by the S-wave transfer function), which is justified by the fact that surface waves are always present in the seismic noise (ambient vibrations) wavefield.

The results obtained although relevant are valid for 1D theoretical structures but what is their applicability to non-simple 3D structures such as sedimentary valleys? Research under the scope of the SESAME project shows that when the 3D structure can be approximated locally by a 1D structure, such as in valley basins, then the peak frequency is able to give a good estimation of the resonance frequency of the idealized 1D local structure [Cornou et al, 2004]. Additional research is needed, however, on such a topic focusing on more complex (3D) structures.

Under the scope of the SESAME project, some guidelines for the implementation of the HVSRT on ambient vibrations have been delivered. Recommendations on measurements, processing and interpretation are given on which the present work is based. For more detailed information consult the deliverable D23.12 [2004] of the project, here only selected interpretations applicable to the present case study are mentioned.

The project mentions the following. The main information looked for within the H/V ratio is the fundamental natural frequency of the deposits, corresponding to the peak of the H/V curve. While the reliability of its value will increase with the sharpness of the H/V peak, no straightforward information can be directly linked to the H/V peak amplitude, A_0 , as mentioned before. However, this latter value may be considered as indicative of the impedance contrasts at the site under investigation. The project also states that: it is not scientifically justified to use A_0 as the actual site amplification.

However, there is a general trend for the H/V peak amplitude to underestimate the actual site amplification. In other words, the H/V peak amplitude could generally be considered as a lower boundary of the actual site amplification. **Figure 3-3** shows a comparison between the H/V ratio of ambient vibrations and the standard spectral ratio of earthquakes. The first plot shows the comparison of peak frequencies and the plot on the right the comparison of peak amplitudes, testifying what has been said. The comparison is performed using all the sites investigated in the framework of the SESAME project.

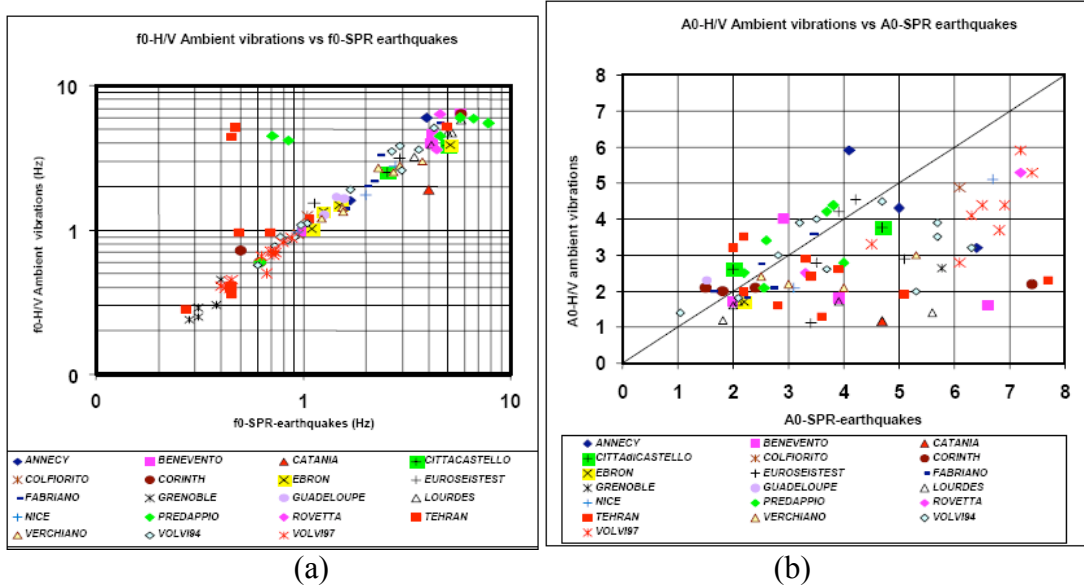


Figure 3-3: Comparison between H/V ratio of ambient vibrations and standard spectral ratio of earthquakes. (a) comparison of peak frequencies f_0 , (b) comparison of peak amplitudes A_0 [Deliverable D13.08]

For the interpretation of H/V curves and peaks the following has been observed (mentioned in the project SESAME):

- “The results are clearer in the case of horizontally layered structures with large impedance contrasts, but become more and more fuzzy for decreasing contrasts and/or for increasing underground interface slopes.”
- “In fact, in the case of large impedance contrast, the H/V curve exhibits a clear peak for horizontal underground interfaces and a broader peak and generally associated lower maxima at sites with rapidly varying thickness such as valley edges. The bandwidth of the broad peaks is generally an indicative of the fundamental frequency variations between the shallowest and deepest sections, although the amplitude of this peak is often too small to allow clear identification. For laterally varying structures the wavefield associated with local noise sources is more complex, since it also includes additional waves diffracted from the lateral heterogeneities.”
- “As a consequence, one should always gather geological and geotechnical information, looking in particular for a priori rough estimations of impedance contrasts, depths to bedrock and indications of lateral variability of underground structures.”
- “For 1D media and if the site is located at an urban environment, the noise sources are essentially local and superficial; the wavefield predominantly consists of surface waves with a slight proportion of body waves. The H/V

- curve should exhibit one single peak, at frequency that is within +- 20% of the S-wave resonance frequency of the site. The amplitude of that peak should not be interpreted in terms of amplification values.”
- “For 2D/3D structures such as, for instance, “transition zones” between more or less horizontal layering, numerical simulations have consistently shown how, for high frequencies (human sources) and local surface sources, the H/V curve at such transition sites exhibit broader and lower maxima, which may be hard to identify: surface waves cannot develop with one single pure mode nor can resonance of body waves occur.”
- “Theoretical and numerical results are by far more numerous and easier to interpret for local, human sources, i.e., essentially above 1 Hz.”
- “Ambient vibration recordings may also include unwanted sources such as wind or industrial harmonic machinery, which may affect the estimation of the H/V curve and complicate the interpretations of the peaks. These should be avoided.”

The main recommended application of the HVSRT in microzonation studies is to map the fundamental period of the site and help constrain the geological and geotechnical models used for numerical computations. The project also mentions: “interpretation of the H/V results will be greatly enhanced when combined with geological, geophysical and geotechnical information.”

With the fundamental frequency (f_0) one is able to retrieve the average shear wave velocity ($V_{s,av}$) if the depth to bedrock (H) is known, according to **Equation 3-1**.

$$f_0 = \frac{V_{s,av}}{4H} \quad (\text{Equation 3-1})$$

If instead we know the fundamental frequency of the soil and the average shear wave velocity we can retrieve the depth to bedrock.

3.4.2. Measurements

The HVSRT has been applied to the site in a total of 10 measurement points intentionally placed at the locations where geotechnical surveys had been conducted. In this way a direct comparison was made between the results of the recordings and the geotechnical and geological data. The location of each measurement point (DN, PF, P12, P11, P10, P89, SC, P6, S2a, S3) and the location of the geotechnical surveys conducted in the area (DN, P13, PF, P10, P11, P12, P6, P7, P89, SC, S2a, S2b, M, B) can be seen in **Figure 3-4**. To be noted that DN means “Diário de Notícias” and this measurement point was placed next to this office; PF stands for “Praça da Figueira” and this measurement point was placed at “Praça da Figueira”. Several geotechnical surveys were found here but only the one found next to the measurement point PF were compared with this.

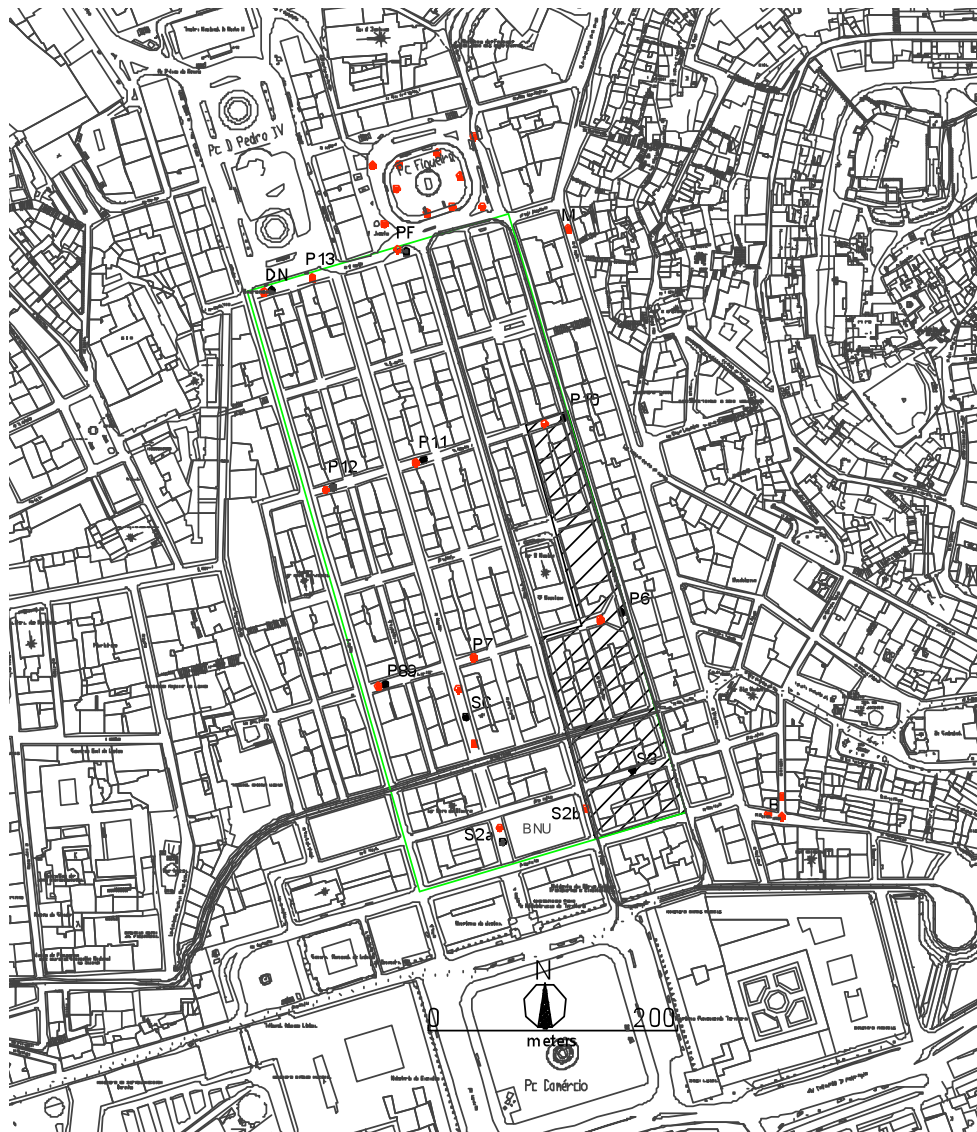


Figure 3-4: Location of the geotechnical surveys available (red dots) and of the selected measurement points for recording of ambient vibrations (black dots)

The measurement campaign lasted 3 nights; measurements were conducted at night, aiming to avoid perturbations due to human activity; 30 minutes recording time was considered for each point; low to moderate noise from pedestrians, cars, trucks or buses was observed; none to little wind (up to 5 m/s) and no rain was observed. The presence of underground structures such as pipes for waste water and telecommunications is known. Their position is estimated by the connection boxes at the surface. Furthermore, it is known that a sewer system was originally thought for the *Pombalino* buildings in the downtown area. A major duct in the middle of the streets would collect the sewers from the blocks. There is also a car park in *Pc. da Figueira*. Care was taken so as to avoid placing the sensor close to these underground structures. Data was obtained at the sidewalks and paved streets. Furthermore, no car engine was turned on during recordings.

The sensor used was the broadband seismometer CMG-40TD by Guralp Systems Limited, designed for medium noise sites, with 1-50Hz response options and 3-component model and associated digitiser CMG-DM24. This was not expected to

require a long stabilization time. Since the estimated frequencies of interest are above 1 Hz this seismometer seems suitable and practical. Nevertheless, in order to make sure that the digitiser was stable, the measurements were extended by a further 10 minutes. The sampling rate of recordings was 50 Hz.

3.4.3. Processing

The computations of H/V ratios were facilitated by the available free software downloadable at <http://www.geopsy.org>, current release version sesarray-2.0.0-beta, developed under the framework of the SESAME European Research Programme (2001-2004). Geopsy is a graphical user interface for organising, viewing, and processing geophysical signals. It performs H/V spectral ratio computations, calculating the average H/V spectral ratio for each individual window and the associated standard deviation estimates. Other associated processing such as DC-offset removal, filtering, smoothing, etc., is also performed.

The software performs the computation from the three files of a recording (North-South, East-West, Vertical) through the following steps:

1. Offset removal: the mean of the entire signal recorded is deducted from each sample value. No sensor nor station correction is applied to the rough signal.
2. Single window processing: the second step of the process consists of selecting portions of the signal that do not contain transients. There is an automatic window selection available, only designed to eliminate transients that appeared on signal in a given frequency range without taking into account neither the nature of these transients nor their effect on the resulting curves. Windows can also be selected manually, which is a more reliable solution and feasible in the case of a small amount of data. The processing of individual windows is done as follows:
 - a. A cosine tapering with a length of 5% is applied on both sides of the window signal of the Vertical (V), North-South (NS) and East-West (EW) components.
 - b. A FFT is applied to the signal of the three components to obtain the three spectral amplitudes.
 - c. A Konno and Ohmachi smoothing, with a bandwidth of 40 and arithmetical average, is applied to the three spectral amplitudes.
 - d. H in H/V is computed by merging the horizontal (NS and EW) components with a quadratic mean (**Equation 3-2**):

$$H = \sqrt{(NS^2 + EW^2)/2} \quad (\text{Equation 3-2})$$

Thus, in each of the windows the distribution of $\log_{10}(H/V)$ is obtained as a function of the frequency.

3. Average of result by measurement point: the geometric mean of H/V is calculated as follows:

a. H/V is averaged over all window results (**Equation 3-3**):

$$H/V_{average} = \frac{\sum \log_{10}(H/V)}{n_{windows}} \quad (\text{Equation 3-3})$$

b. H/V standard deviation is calculated (**Equation 3-4**):

$$\sigma_{H/V} = \sqrt{\frac{\sum \log_{10}^2(H/V) - n_{windows} \times \log_{10}^2(H/V_{average})}{n_{windows} - 1}} \quad (\text{Equation 3-4})$$

4. $H/V_{average}$ and $\sigma_{H/V}$ are set back to a linear scale by means of **Equation 3-5** and **Equation 3-6**:

$$\overline{H/V} = 10^{H/V_{average}} \quad (\text{Equation 3-5})$$

$$\sigma_{\overline{H/V}} = 10^{\sigma_{H/V}} \quad (\text{Equation 3-6})$$

The data only has significance, due to sampling frequency, window length and equipment functionalities between the interval of 1-20 Hz, which is also the interval of frequencies of interest for the specific soil profile under analysis. The time windows were selected manually for better accuracy. It is important to remove the transient loading to obtain a clearer peak. Transient loading was not considered in the time windows and this was done by visual inspection of the data. No overlap was considered for two subsequent windows. All digitizers show a better stability in the recordings after some minutes of warming up. In this way, the first 10 minutes of data have been rejected for the first measurement point being recorded. For the subsequent measurement points being recorded, only the first 2 minutes of data have been rejected.

3.4.4. Interpretation

Identification of f_0

In principle, the fundamental frequency of the soil layer corresponds to the peak frequency at the H/V curves. The following criteria are recommended to identify the peak frequency [D23.12, 2005].

Criteria for reliability of results

Reliability implies stability, i.e., the fact that the actual H/V curve obtained with the selected recordings is representative of H/V curves that could be obtained with other ambient vibration recordings and/or with other physically reasonable window selection. The following 3 criteria are proposed (**Equation 3-7**, **Equation 3-8** and **Equation 3-9**):

1.

$$f_0 > 10/l_w \quad (\text{Equation 3-7})$$

Where f_0 is the H/V curve peak frequency and l_w is the window length. This condition is proposed so that, at the frequency of interest, there be at least 10

significant cycles in each window. In our case of study if f_0 is 1.5 Hz then l_w should be higher than 7 s.

2.

$$n_c = l_w n_w f_0 > 200 \quad (\text{Equation 3-8})$$

Where n_w is the number of windows selected for the average H/V curve. A large number of windows and of cycles is needed, it is recommended to have a significant total number of cycles (n_c). In our case of study if f_0 is 1.5 Hz and l_w is set to 20 s then n_w should be higher than 7.

3.

$$\sigma_A(f) < 2 \quad \text{for } 0.5f_0 < f < 2f_0 \text{ if } f_0 > 0.5\text{Hz} \quad (\text{Equation 3-9})$$

Where $\sigma_A(f)$ is the standard deviation of the H/V curve amplitude at frequency f . This condition is proposed so that an acceptably low level of scattering between all windows is accomplished.

In the geopsy toolbox a window length of 20 s has been set for most measurement points. Measurement points P10, P6 and S3 are expected to behave differently due to the non-existing layer of alluvium deposits at these points. For these points a window length of 1 s would be enough; nevertheless, a window length of 10 s has been set as the data permitted. All measurement points have at least 40 windows; exceptionally, measurement point P6 has 30 windows and measurement point P10 has 25 windows. The minimum number of windows has been easily attained. Condition number 3 has also been fulfilled. In this way, the criteria for the reliability of the results are easily fulfilled for all measurement points.

Criteria for clear peak

It is recommended that at least 5 out of 6 of the following criteria be fulfilled. Three amplitude conditions are set (**Equation 3-10**, **Equation 3-11** and **Equation 3-12**):

1.

$$\exists f^- \in [f_0/4, f_0] \mid A_{H/V}(f^-) < A_0/2 \quad (\text{Equation 3-10})$$

2.

$$\exists f^+ \in [f_0/4, f_0] \mid A_{H/V}(f^+) < A_0/2 \quad (\text{Equation 3-11})$$

3.

$$A_0 > 2 \quad (\text{Equation 3-12})$$

Additionally, three stability conditions are set (**Equation 3-13**, **Equation 3-14** and **Equation 3-15**):

1.

$$f_{peak}[A_{H/V}(f) \pm \sigma_A(f)] = f_0 \pm 5\% \quad (\text{Equation 3-13})$$

i.e., the peak should appear at the same frequency within a percentage of $\pm 5\%$ on the H/V curves corresponding to mean + and - one standard deviation.

2.

$$\sigma_{f_0} < 0.10f_0 \quad \text{for } 1.0\text{Hz} < f_0 < 2.0\text{Hz} \quad (\text{Equation 3-14})$$

Where σ_{f_0} is the standard deviation of the H/V peak frequency.

3.

$$\sigma_A(f_0) < 1.78 \text{ for } 1.0 \text{ Hz} < f_0 < 2.0 \text{ Hz}$$

(Equation 3-15)

The H/V curves obtained for each measurement point can be seen from Figure 3-5 to **Figure 3-14**. In these figures the continuous line represents the mean of the results and the dashed lines represent plus and minus one standard deviation of the results. In addition, the interpretation of the results obtained and the necessary comments for each case are presented. The interpretation of the results was made based on all information gathered for each measurement point.

3.4.4.1. Measurement point PF

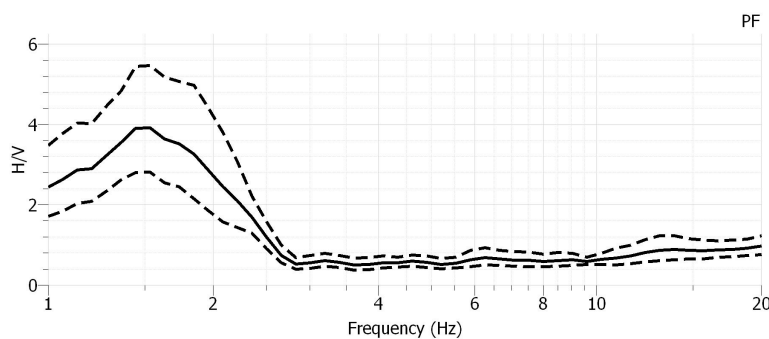


Figure 3-5: H/V curve obtained for measurement point PF

In Figure 3-5 one can see the H/V curve for measurement point PF. Measurement point PF is situated in *Pc. da Figueira*. In this case, the criteria for *clear peak* is fulfilled. The fundamental frequency of the soil layer for measurement point PF is reliably estimated at 1.53 Hz.

A series of SPT surveys were carried out at *Pc. da Figueira* where an underground car park was built. Additionally there were several piezometers installed to measure the level of ground water. Two of the drilled boreholes were set close to the measurement point PF (see **Figure 3-4**). The geotechnical in-situ testing at these two boreholes presented the generic results: the site consists of a top layer of recent deposits of 6.5 to 7 m thick under which there are several layers of alluvium deposits that will either consist of organic soils, fine sand or a clayey sand material. The measured penetration resistance (not corrected), N_{spt} , for the top layer of deposits stands between $4 \leq N_{spt} \leq 19$, for the alluvium layers stands between $4 \leq N_{spt} \leq 35$ and for the Miocene formation it is found that $N_{spt} > 60$, with a lower value of N_{spt} occurring at the start of the Miocene formation (indicating some weathering of the rock). The ground water levels were found at 4 to 5 m depth from the surface. The apparent density of the uppermost layers of deposits (ρ_{soil}) were found to be 17.6 kN/m³, between 19.7 and 20 kN/m³ for the alluvium layers and 20.3 kN/m³ for the Miocene formation (ρ_{rock}). Even though the depth of the Miocene was found to be at 28.0 m and at 30.5 m deep for the two boreholes penetrated, the depth at which the number of blows would be larger than 60 ($N_{spt} > 60$) for three consecutive sets was found to be at 31.5 m at both boreholes, which was the depth to bedrock considered (H). These results are coherent with the results obtained from another geotechnical

survey at point PF. For this in situ test, the thickness of the top layer of deposits is 7.3 m with $7 \leq N_{spt} \leq 23$; for the layer of alluvium deposits the boreholes only reached a depth of 13.5 m, still a broad range of values could also be found for the number of blows $6 \leq N_{spt} \leq 30$. The ground water table was found at 3.7 m.

From the above data it is possible to estimate the average shear wave velocity of the soil layer ($V_{s,av}$) and roughly estimate the shear wave velocity of bedrock (V_r), assuming that the impedance contrast will be higher than approximately 4 or 5. According to the guidelines D23.12 [2005] when f_0 is clear and does not have an industrial origin, then there is a quasi-certitude that the site under study presents a large impedance contrast ($>\sim 4$) at some depth, and is very likely to amplify the ground motion. The geological formation at this point is *Argilas e Calcários dos Prazeres* and typical values would be for near surface fractured limestones of 700 to 1500 m/s, agreeing well with the summary of the results obtained in **Table 3-1**.

Table 3-1: Results obtained for measurement point PF

Measurement point	f_0 (Hz)	$\rho_{\text{soil}}/\rho_{\text{rock}}$	H (m)	$V_{s,av}$ (m/s)	V_r (m/s)
PF	1.53	18.7/20.3	31.5	~193	>741-926

3.4.4.2. Measurement point DN

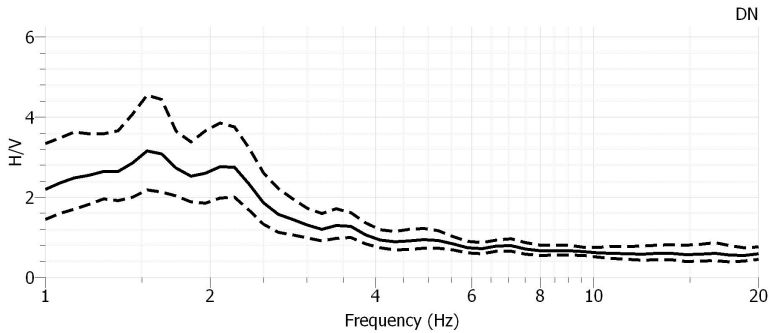


Figure 3-6: H/V curve obtained for measurement point DN

In **Figure 3-6** one can see the H/V curve for measurement point DN. In this situation a *multiple peak* case with two peaks fulfilling the *clarity* criteria, stable for different values of the smoothing bandwidth, is found. The criteria for *clarity* are fulfilled for peak $f_0 = 1.55$ Hz and peak $f_1 = 2.21$ Hz. It is important to validate and interpret these results with the geological/geotechnical information available in order to be able to draw any conclusions. If the geology of the site were to show the possibility of having two large impedance contrasts ($>\sim 4$) at two different scales, one for a thick structure and the other for a shallow structures, then f_0 ($f_0 < f_1$) would be the fundamental frequency and f_1 another natural frequency referring to the shallow structure. However, from the several cases analysed in the SESAME project it is seen that the two frequencies should be sufficiently apart for this to be the case. For measurement point DN the two frequencies fulfilling the clarity criteria are close frequencies and it is also thought not to be the case of two large impedance contrasts at two distant depths from the geological/geotechnical data available. On the other hand, it could be possible that one of the peaks had industrial origin; this is, however, not thought to be

the case as the site is a residential area with no known industries. In this way, the presence of the two peaks, with rather low amplitudes, is thought to be explained by the location of the point relatively close to a valley edge by contrast to the *clear peak* found at measurement point PF, with larger amplitude, located at the central part of the valley.

The geotechnical in-situ testing at this measurement point presented the following results: the top layer of recent deposits is 3 m thick; the underlying layers of alluvium deposits consisting of the same materials as the ones found at point PF, have values of the penetration resistance between $3 \leq N_{spt} \leq 22$ and are about 8 m thick in total. The Miocene formation is found to start at about 11 m in depth with values of N_{spt} of 22 and 27 at the first two blows, indicating significant weathering of the rock. Even though N_{spt} reached 60 in the next blow, it decreases again to 40 in the following indicating that the weathering of the rock continues at least for 4.5 into the rock. The test finished at this depth. As a consequence, the in situ test indicates that the layer of soil deposits is higher than 15.5 m thick, so depth to bedrock formation is unknown. From the results of the H/V measurements it has been found that the fundamental frequency would be given by either 1.55 Hz or by 2.21 Hz. If it is assumed that the shear wave velocity of the soil layer is similar to the one found at measurement point PF, one is able to find two estimates of possible depths of the soil for this point; it is however inconclusive which one of the two represents the true depth. The ground water level is found at 4.2 m. The summary of the results is presented in **Table 3-2**.

Table 3-2: Results obtained for measurement point DN

Measurement point	f_0 (Hz)	$V_{s,av}$ (m/s)	H (m)
DN	2.21	193	~21.8
	1.55	193	~31.1

3.4.4.3. Measurement point P12

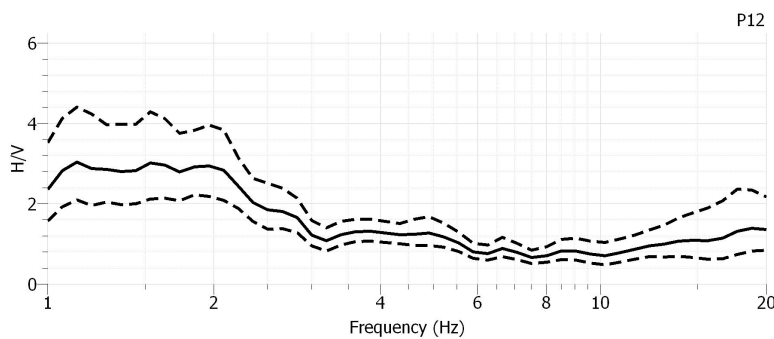


Figure 3-7: H/V curve obtained for measurement point P12

In **Figure 3-7** one can see the H/V curve for measurement point P12. For this point, a *broad peak* case with no peaks fulfilling the clarity criteria was found. As well as for measurement point DN, the same explanation may be given for the appearance of a non *clear peak*. This may happen because the measurement point is close to an edge of the valley and to possible underground slopes in the soil profile. It is not recommended to extract any information from the obtained frequencies but it is

noticed that the range of frequencies for which there is amplification is at the same interval as the previous measurements.

The geotechnical in-situ testing at this point presents the following results: the top layer of recent deposits is 3 m thick; the underlying layers of alluvium deposits consisting of the same materials as the ones found at point PF, have values of the penetration resistance between $2 \leq N_{spt} \leq 34$ and are about 10 m thick in total. The Miocene formation is found to start at about 13 m in depth with values of N_{spt} of 24 and 30 at the first 2 blows, indicating significant weathering of the rock. The test finished at this depth so depth to bedrock formation is unknown. The ground water level is found at 4.0 m.

3.4.4.4. Measurement point P11

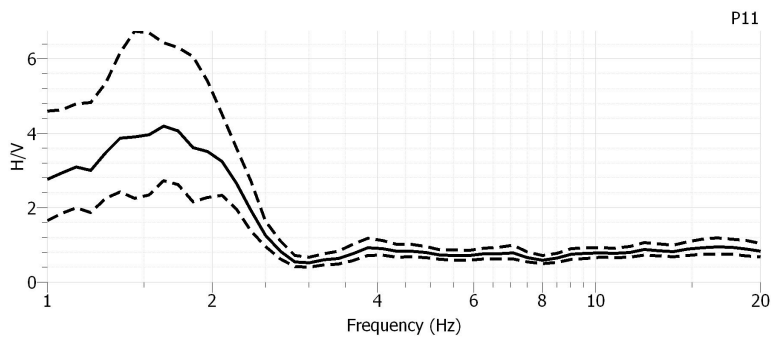


Figure 3-8: H/V curve obtained for measurement point P11

In **Figure 3-8** one can see the H/V curve for measurement point P11. In this case, the peak fulfils 4 out of 6 criteria for *clarity*. Criteria 4 is not fulfilled, at the upper curve for the standard deviation estimates of amplitude. It can be assumed that the site fundamental frequency for this point is between 1.44 Hz and 1.61 Hz if it is possible to validate these results with the available geological/geotechnical data.

The results obtained from the geotechnical SPT performed at point P11 presented a thickness of the top layer of deposits of 1.5 m with no measured N_{spt} ; it follows a 6 m thick soft layer of alluvium organic soils with $4 \leq N_{spt} \leq 6$ followed by another layer of alluvium of fine sand material with values ranging from $5 \leq N_{spt} \leq 42$ for which the measurements only reached 15 m. The ground water table was found at 3.8 m from the surface. The estimated site characteristics are given on the following table. Since there is no information available on the depth to the bedrock, a lower bound of this value, H_{min} , has been estimated by using the average shear wave velocity found at measurement point PF. The summary of the results is presented in **Table 3-3**.

Table 3-3: Results obtained for measurement point P11

Measurement point	f_0 (Hz)	$V_{s,av}$ (m/s)	H_{min} (m)
P11	1.44-1.66	193	$\sim 30.0 - 33.5$

3.4.4.5. Measurement point P89

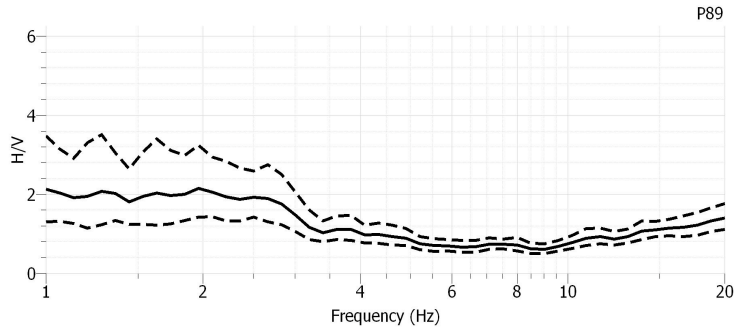


Figure 3-9: H/V curve obtained for measurement point P89

In **Figure 3-9** one can see the H/V curve for measurement point P89. This is a case of *broad peak* with no peaks fulfilling the clarity criteria. Even though there is a noticeable amplification in the same frequency range as for the previous measurements, no conclusions can be drawn from these results. Probably the presence of underground structures or the proximity to valley edges has influenced the results.

The geotechnical in situ testing at this measurement point has shown the following results: the top layer of recent deposits is 4.0 m thick; the underlying layers of alluvium deposits consisting of organic soils and fine sand materials, have values of the penetration resistance between $14 \leq N_{spt} \leq 34$ and are about 12.5 m thick in total. The Miocene formation is found to start at about 16.5 m in depth with values of $N_{spt} = 60$ at the first blow although the next 2 blows (3 m) have lower penetration resistances, indicating weathering of the rock formation; after these the two consequent blows with $N_{spt} = 60$ are found to start at 22 m depth. The ground water level is found at 3.7 m.

3.4.4.6. Measurement point SC

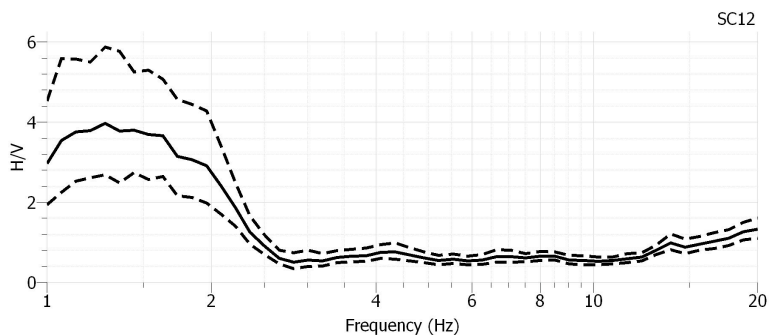


Figure 3-10: H/V curve obtained for measurement point SC

In **Figure 3-10** one can see the H/V curve for measurement point SC. In this measurement point a *clear peak* was identified. The fundamental frequency of the site for measurement point SC may be reliably estimated at 1.28 Hz.

The measurement point SC of the ambient vibrations has been set between SPT boreholes SC1 (north side) and SC2 (south side), as can be seen in **Figure 3-4**. The geotechnical in-situ testing at these two boreholes presented the generic results: the top layer of recent deposits is 3 m thick; the underlying layers of alluvium deposits consisting of fine to average sized sand or a clayey sand material with intercalations of organic soils and where pebbles and sea shells are also found, have values of the penetration resistance, N_{spt} , very disperse. These can range from 5 until 60. The Miocene formation is found for SC1 to be at 36.5 m deep and non weathered. Nevertheless, for point SC2 it was found the Miocene formation at the same depth but only at the depth of 39 m could the value of $N_{spt} = 59$ be found, indicating significant weathering of the rock material in the beginning of the Miocene formation. The test finished at this depth. The average S-wave velocity of the soil layer is obtained with the mean depth to bedrock between points SC1 and SC2.

These results are coherent with the results obtained from another geotechnical survey at the north side of the quarter (P7). For this in situ test, the thickness of the top layer of deposits is 2.7 m with no measured N_{spt} ; for the layer of alluvium deposits the boreholes only reached a depth of 15 m, still a broad range of values could be found also for the number of blows ($3 \leq N_{spt} \leq 31$). The ground water table was found at 3.8 m. The resume of the results is presented in **Table 3-4** where the values of $V_{s,av}$ have been estimated. These are coherent with the values found for measurement point PF.

Table 3-4: Results obtained for measurement point SC

Measurement point	f_0 (Hz)	H (m)	$V_{s,av}$ (m/s)
SC	1.28	38	~195

3.4.4.7. Measurement point S2a

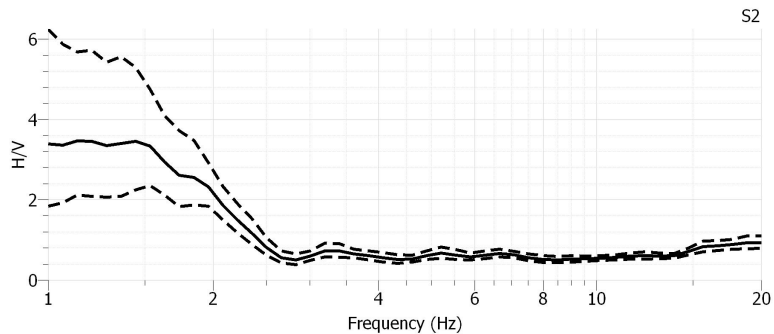


Figure 3-11: H/V curve obtained for measurement point S2a

In **Figure 3-11** one can see the H/V curve for measurement point S2a. Here we can find another *broad peak* case with no peaks fulfilling the clarity criteria. Since there is not a clear peak it is not recommended to extract any information from these results. Probably the presence of underground structures or the proximity to valley edges has influenced the results.

A geotechnical in-situ testing performed at this measurement point (S2a, *Rua Augusta*) was associated with another borehole which was done on the other side of

the block at *Rua da Prata* (S2b). The surveys revealed the following information: the soil layer, constituted by recent deposits and alluviums, has the thickness of 42.4 m (S2a) and 10.0 m (S2b). It is interesting to notice that the difference of the soil layer thickness is so pronounced between these two points, indicating maybe the presence of a small fault between them. For point S2b the recent layer of deposits was only found at a depth of 4.0 m since above this level a wall of masonry was intercepted by the probe. The recent layer of deposits is essentially composed of sand and clay material with inclusions of fragments of masonry, wood, etc., that go until the depth of 9.0 m (S2a). For point S2b this lithology occurs below the mentioned masonry wall from 4.0 m to 9.0 m deep. These deposits have very varying colorations from brown to black. The SPT results for this soil layer vary between 2 and 60 blows without total penetration, being that the results sometimes increased considerably (for this type of formation) due to the presence of stones and pebble or fragments. On the other hand, the high variability of the results obtained reveals the heterogenic nature of this soil layer. In this way it was stated that these deposits vary from very dense to very loose.

Alluvium soil layers occur underlying the deposits layer in both boreholes S2a and S2b being constituted by either fine sands with more or less quantities of organic soils or medium to large sized sand with incursions of small basaltic pebble. It is found within the layers some occurrences of stone and pebble as well as fragments of sea shells, disperse or at specific levels/spots. This formation is coloured brownish yellow or grey to black depending on the amount of organic soils (more organic soils, more dark). The thickness of this formation is found to be 33.4 m (S2a) and 5.0 m (S2b). The number of blows for this layer (N_{spt}) varies between 15 and 60 without total penetration, depending essentially on the percentage of organic soils material (the higher the percentage the lower the number of blows).

The Miocene formation corresponds to the units *Argilas do Forno do Tijolo*, *Calcários de Entre-campos e Areolas da Estefânia*. From the observations above it can be seen that the difference in level between the Miocene formations from S2a to S2b is much accentuated. This difference in level originated that different units were intercepted in the two boreholes, that is, *Areolas da Estefânia* were intercepted in S2a and *Argilas do Forno do Tijolo* and *Calcários de Entre-Campos* at S2b, being that the first is the oldest unit. The *Argilas do Forno do Tijolo* unit constituted of dark grey to dark clays was intercepted in S2b at 14.0 m depth with the approximate thickness of 1.0 m. The only set of blows done revealed $N_{spt} = 56$, presenting characteristics of stiff soil. Underlying this unit at 15.0 m depth it is found the *Calcários de Entre-Campos*, which is mainly constituted of limestone with coloration yellow, yellowish orange and yellowish white. It is stated that this rock unit is presented as medially to very weathered/ altered, corresponding to a weak to hard rock behaviour. The *Areolas da Estefânia* unit was intercepted at 42.4 m at S2a. It is constituted of fine sand, grey to brown or grey to white, presenting characteristics of stiff soil to weak rock. The only set of blows performed revealed $N_{spt} = 60$. The ground water level occurs at approximately 3.0 m (S2a) and 4.0 m (S2b) deep from the surface.

The location of the measurement point S2a at the centre of the east and west hills and on the same line as points SC and P11, would suggest that S2 would be placed at the centre of the valley. In this situation one would expect a *clear peak* to show in the H/V results such as the one obtained for measurement point SC. Nevertheless, by observing both the geological map and the geotechnical in-situ testing results

performed at this location it can be revealed that measurement point S2a is in fact close to an extremity of the valley found at its southwest side (to the point). It is thought, similarly as for previous measurements, this is the reason for the appearance of a *broad peak* in the H/V results.

3.4.4.8. Measurement point P10

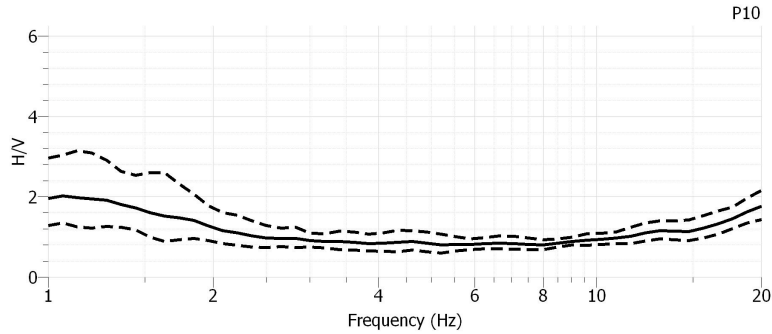


Figure 3-12: H/V curve obtained for measurement point P10

Figure 3-12 shows the H/V curve for measurement point P10. At this point no peak was found at the H/V curve. For all frequency range examined the curve lies below the value of two. If the available geological/geotechnical information indicates this is a hard rock site, then, no amplification is expected at this point.

The geological/geotechnical information confirms this is a rock site ($N_{spt} = 60$ for three consecutive blows), found at no more than 1.5 m deep. In this way, no relevant seismic ground amplification is expected at this point.

3.4.4.9. Measurement point P6

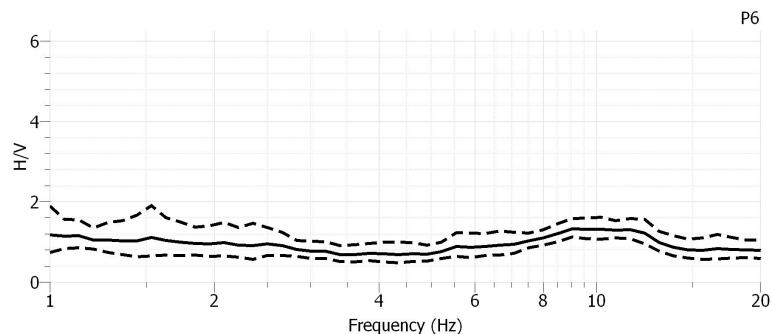


Figure 3-13: H/V curve obtained for measurement point P6

In **Figure 3-13** one can see the H/V curve for measurement point P6. In the same way, at this point no peak was found at the H/V curve. The curve is flat over the all frequency range examined. If the available geological/geotechnical information indicates this is a hard rock site then no amplification is expected at this point.

The geological/geotechnical information confirms this is a rock site ($N_{spt} = 60$ for three consecutive blows) found at no more than 6 m deep. In this way, the flat H/V curve obtained can be indicative of a good, non-weathered rock free from any relevant amplification.

3.4.4.10. Measurement point S3

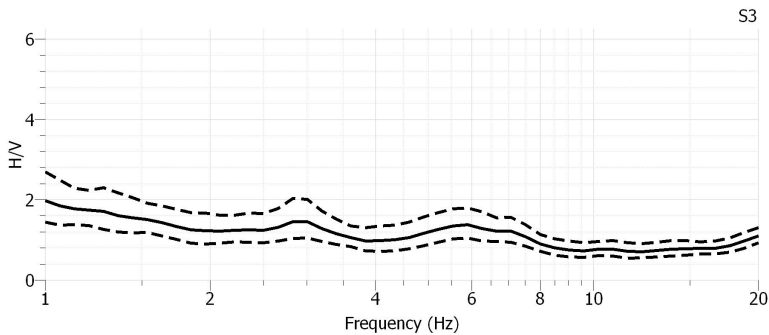


Figure 3-14: H/V curve obtained for measurement point S3

Figure 3-14 depicts the H/V curve for measurement point S3. Again, at this point, no peak was found at the H/V curve. For all frequency ranges examined the curve lies below the value of two. If the available geological/geotechnical information indicates this is a hard rock site then no amplification is expected at this point.

No geotechnical information is available for this point. Nonetheless, the point is set at the same geological formation as points P6 and P10; also based on the geotechnical survey found closest to the point (S2b) where depth to bedrock was 15 m, and given the position of the point towards the east side hill, it is possible to predict that the bedrock formation will be found at less than 15 m deep and possibly at $(15+6)/2=10$ m for measurement point S3 (depth to bedrock at P6 is 6 m). No relevant seismic ground amplification is expected at this point.

3.5. Discussion

Figure 3-15 shows a comparison between all the obtained H/V curves where only the mean of all windows is plotted (the associated H/V standard deviation curves are not plotted for better comparison between the curves).

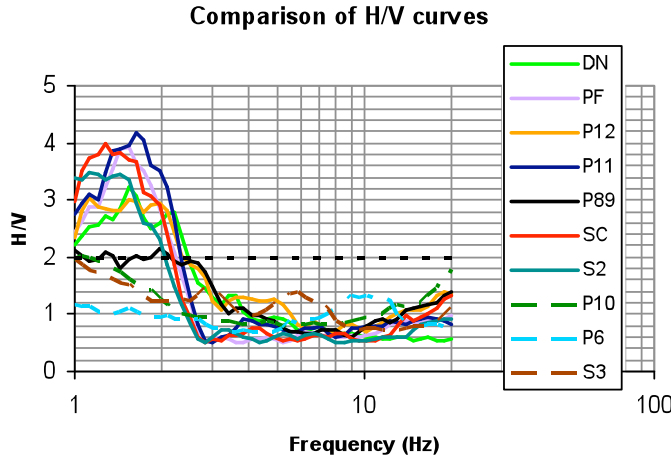


Figure 3-15: Comparison of the obtained H/V curves in all measured points

By direct comparison of all the obtained H/V curves in **Figure 3-15** it is possible to observe two distinct seismic behaviours clearly, which are presented in full and dashed lines. All points except measurement points P10, P6 and S3 are set on a location where significant amplification of the ground motion is expected (considered to be significant above the value of 2 at the H/V curves). At these points, it is noticeable that the amplification is restricted to the same frequency band \sim 1-2.5 Hz. **Table 3-5** depicts the summary of the results including obtained peak frequencies and estimated ground parameters.

Table 3-5: Summary of the results with obtained peak frequencies and estimated ground parameters

Meas. Point	H/V curves results	H (m)	$V_{s,av}$ (m/s)
DN	Reliable/Multiple peak $f_0=1,55$ and $f_1=2,21$ Hz	~ 31.3 or 21.9	-
PF	Reliable/Clear peak $f_0=1,53$ Hz	31.5	~ 193
P11	Reliable/Clear peak $f_0=1,44$ to $1,66$ Hz	~ 33.7 to 29.2	-
SC	Reliable/Clear peak $f_0=1,28$ Hz	38.0	~ 195
P12, P89, S2a	Reliable/Broad peak	-	-
P10, P6, S3	Reliable/No peak	-	-

As can be seen in **Table 3-5**, the obtained shear wave velocity of the soil profile is estimated at approximately 194 m/s. This can be said to be the average shear wave velocity of the soil profile valid for the whole valley, given that geotechnical surveys identified similar compositions of the soil layers within the valley. Based on the value of $V_{s,av}$ obtained, it was possible to select a soil class based on Eurocode 8 [2004] for each of the site quarters. Soil class C (deep deposits, dense medium dense sand, stiff clay; several tens to few hundred metres site; $180 < V_{s,30} < 360$ m/s) could be appointed to all the quarters that are set on a site location susceptible to ground motion amplification, represented by the measurement points PF, DN, P11, SC, P12, P89 and S2a. Nevertheless, the value obtained for the $V_{s,av}$ is close to the lower limit. In this way, if one wants to be conservative, it could be appointed to this soil the soil class D. Soil class A (rock or rock-like site with less than 5 m of weak material; $V_{s,30} > 800$ m/s) can be attributed to all the quarters that are set at a location where no significant seismic amplification is expected and these are represented by the

measurement points P10, P6 and S3. In **Figure 3-4** one can observe the mapping of the quarters according to these two groups: the former group are identified with the quarters with no diagonal stripes and the later group are the quarters marked in **Figure 3-4** with diagonal stripes.

Now the seismic action for the downtown area of Lisbon can be obtained. In Portugal, for the design and assessment of structures one must consider two types of seismic actions:

- Seismic action **type 1** corresponding to a scenario of faraway earthquake;
- Seismic action **type 2** corresponding to a scenario of nearby earthquake.

For each seismic action, a seismic zone should be selected depending on where our structure is located. For Lisbon city, and for normal residential buildings, the seismic zone 3 is defined for seismic action type 1 with design ground acceleration on soil type A (a_g) of 1.5 m/s^2 and for seismic action type 2 seismic zone 1 is chosen with $a_g=1.7 \text{ m/s}^2$. The parameters for defining the configurations of the response spectra for the two types of seismic action, the mentioned seismic zones and for ground type C, are presented on **Table 3-6** and **Table 3-7** [National Annex (version 16 September 2007) of Eurocode 8, 2004]. The ground type C was chosen since it is the most demanding situation corresponding to the downtown Lisbon soil type.

Table 3-6: Parameters of the elastic response spectrum for seismic action type 1, seismic zone 3 and ground type C

EQ type 1 and seismic zone 3 -> $a_g=1.5 \text{ m/s}^2$				
Ground type	S	T _B (s)	T _C (s)	T _D (s)
C	1.5	0.1	0.6	2

Table 3-7: Parameters of the elastic response spectrum for seismic action type 2, seismic zone 1 and ground type C

EQ type 2 and seismic zone 1 -> $a_g=1.7 \text{ m/s}^2$				
Ground type	S	T _B (s)	T _C (s)	T _D (s)
C	1.5	0.1	0.25	2

The corresponding elastic response spectrum for downtown Lisbon can be seen in **Figure 3-16** for the two types of seismic action.

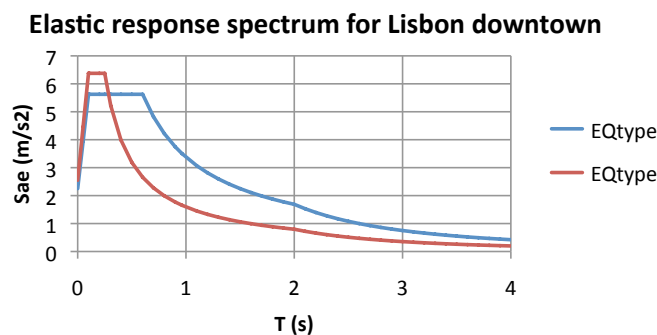


Figure 3-16: Elastic response spectrum for Lisbon downtown

It can be seen that, for most of the range of periods of the structure, the seismic action type 1 is the most demanding but, for the range of low values of the period (high frequencies), the seismic action type 2 is seen to be more demanding. The two seismic actions must be considered in the subsequent analyses performed in Chapter 6.

Apart from the direct estimation of the average shear wave velocity of a soil profile, other relevant information can be deduced based on the H/V curves. For instance, obtaining a *clear peak* can be an indicative of impedance contrast $>\sim 4$, being that the larger the peak the larger the impedance contrast and expected amplification. Additionally, as seen from the aforementioned results, when the H/V curve exhibits a *broad peak* it is not easy to extract any information about the peak frequency of this *broad peak*. In this situation, and as mentioned previously, there are large chances that the underground structure of the site at these positions exhibits significant lateral variations, which lead to significant 2D or 3D effects. Such *broad peaks* or *plateau-like* H/V curves are indeed observed on many valley edges [D23.12, 2005]. In this way, broad peak may be an indicative of valley edge even if no information can be extrapolated regarding shear wave velocity or soil layer depth to bedrock.

In **Figure 3-17 (a) to (e)** some interpretative cuts of the ground profile are sketched for the area under study. These include the thickness of the different soil layers, their average N_{spt} , the ground water table and the depth to bedrock. Based on all the information gathered and obtained it was possible to sketch North-South and East-West cuts of the ground profile that include all measured points and their location relative to the streets in a condensed way.

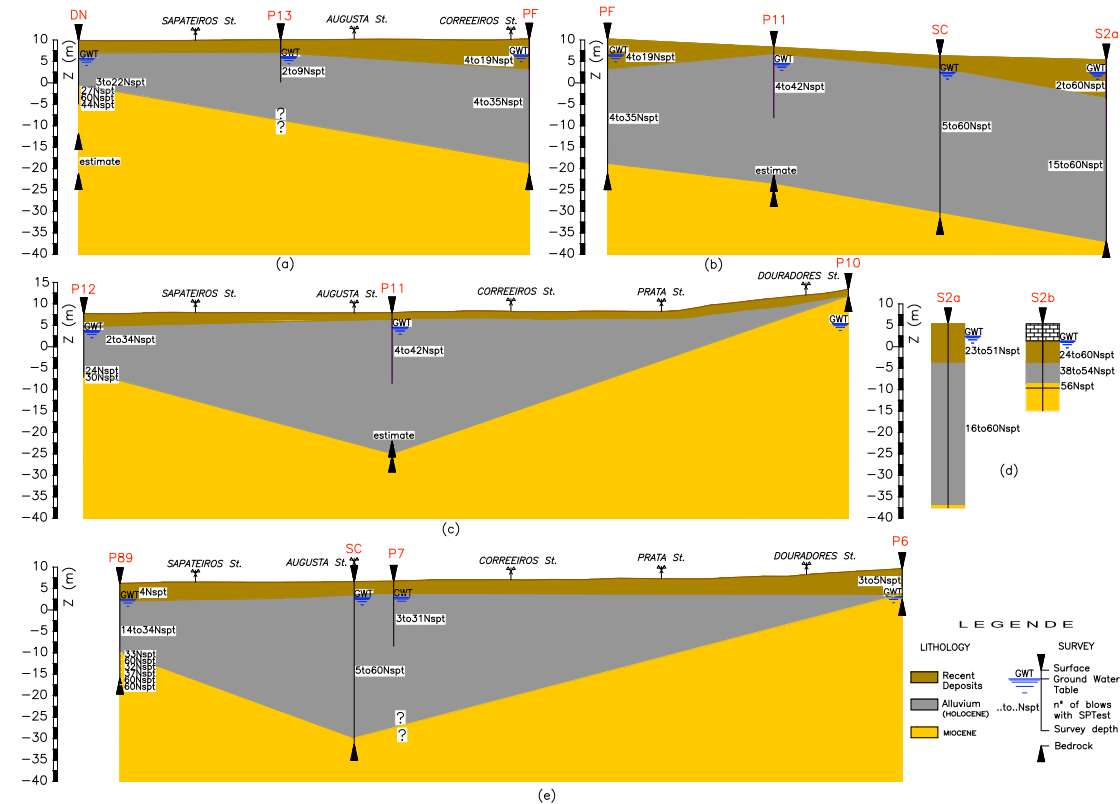


Figure 3-17: Interpretative cuts of ground profile (no horizontal scale)

3.6. Conclusions

From the procedure carried out in the present study, based on the combination of geological and geotechnical data with HVSRT, it was possible to characterize the alluvium site of downtown area of Lisbon in terms of shear wave velocity of the unconsolidated sediments and general geometry and depth of the bedrock-sediment interface, as well as mapping the site quarters where seismic ground amplifications are expected and defining respective soil classes according to Eurocode 8 [2004]. The seismic action for downtown Lisbon was then obtained. The site $V_{s,av}$ of the soil, unknown in the literature, is estimated at approximately 194 m/s. It is assumed reasonably that the same sedimentary process formation has taken place in the basin so that similar soil properties are found throughout the site (as indicated by the geotechnical data) and the obtained $V_{s,av}$ of the soil is the representative value for the whole site.

Solely based on the information gathered from the geotechnical surveys on the resistance of the soil layer, namely the standard penetration resistance, N_{spt} , it would not be possible to classify the site in terms of the soil classes of Eurocode 8 [2004]. The heterogeneity of the soil profile layers is too pronounced in terms of this parameter, with values ranging from 2 up to 60. By conjugating the geotechnical and geological data for the site with the H/V spectral ratio technique on ambient vibrations, it is possible to obtain a fine site characterization.

Apart from the direct estimation of $V_{s,av}$ of the soil profile, HVSRT may give us other important information. For instance, testing of the hypothesis of a horizontally layered (1D) structure (important for numerical modelling purposes) could also be performed by mapping the change in f_0 and shape of the H/V curve in the area, as pointed out by Fäh *et al.* [2003]. As expected, the 1D structure assumption may predict the average response of the soil near the centre of the valley but will probably not at the edges and this could be mapped by the appearance of *broad peaks* in the H/V results. On the other hand, Guéguen *et al.* [2007], based on results obtained in the Grenoble basin ($H/w=0.25$) with strong 2D/3D effects, states that care must be taken when using the technique as an exploration tool since basin geometry can disturb f_0 measurements using the HVSRT. Interpretation of f_0 values in terms of bedrock depth gave rise to estimation errors of about 10% found at the central parts of the valley. Since the site of downtown Lisbon has much less pronounced 2D/3D effects ($H/w=0.15$), one can reasonably assume an even lower error has been accomplished on the estimation of ground parameters at the analysed site.

One of the most important conclusions to point out is the ease of obtaining important site characteristics with very few resources and contrary to more common geophysical prospecting techniques, which would not be suitable for the academic work being conducted. The HVSRT was found to be a practical mean of site characterization in the analysed case study. Its main advantages are its attractiveness in terms of ease of data collection, its consistency and the minor equipment required, having, as a consequence, the technique an associated insignificant cost.

3.7. Bibliography

- Bonnefoy-Claudet S, 2004, Nature du bruit de fond sismique: implications pour les études des effets de site. PhD Dissertation, Joseph Fourier University, Grenoble, France.
- Cornou C, Kristek J, Bonnefoy-Claudet S, Fäh D, Bard PY, Moczo P, Ohrnberger M, Wathenlet M, 2004, Simulation of seismic ambient vibrations: II. H/V and array techniques for real sites. Proc. 13th World Conference in Earthquake Engineering, Vancouver, paper 1130.
- Deliverable D13.08 of the SESAME European Project., 2004, Nature of noise wavefield. Web. <http://SESAME-FP5.obs.ujf-grenoble.fr>, accessed 31 March 2008.
- Deliverable D23.12 of the SESAME European Project, 2005, Guidelines for the Implementation of the H/V Spectral Ratio Technique on Ambient Vibrations Measurements, Processing and Interpretation. Web. <http://SESAME-FP5.obs.ujf-grenoble.fr>, accessed 31 March 2008.
- EN 1998-1, Eurocode 8: Design of structures for earthquake resistance - Part 1: General rules, seismic actions and rules for buildings, 2004, CEN, Brussels (including National Annex, version 16 September 2007).
- Fäh D, Kind F and Giardini D, 2003, Inversion of local S-wave velocity structures from average H/V ratios, and their use for the estimation of site effects. Journal of Seismology, 7, 449-467.
- Guéguen P, Cornou C, Garambois S, Banton J, 2007, On the limitation of the H/V Spectral Ratio Using Seismic Noise as an Exploration Tool: Application to the Grenoble Valley (France), a Small Apex Ratio Basin. Pure appl. Geophysics, 164, 115-134.
- Horike, M, 1985, Inversion of phase velocity of long-period microtremors to the s-wave-velocity structure down to the basement in urbanized areas. J. Phys. Earth, 33, 59-96.
- Meireles H, Bento R, 2008, Estimation of site specific ground motion for the downtown area of Lisbon, Proc. of the 14th World Conference on Earthquake Engineering, Beijing, China.
- Nakamura, Y, 1989, A method for dynamic characteristics estimation of subsurface using microtremor on the ground surface. R.T.R. 30:1, 25-33.
- Nakamura, Y, 2000, Clear identification of fundamental idea of Nakamura's technique and its applications. Proc. 12th World Conference on Earthquake Engineering.
- Nogoshi M, Ogoshi M and Igarashi T, 1972, On the amplitude characteristics of microtremor (Part 2). Journal Seismol. Soc. Japan, 24, 26-40. (in Japanese with English abstract).

Software Sesarray package, Web. <http://www.geopsy.org>.

Teves-Costa P, Costa Nunes JA, Senos L, Oliveira CS and Ramalhete D, 1995, Predominant Frequencies of Soil Formations in the Town of Lisbon Using Microtremor Measurements. Proc. 5th Int. Conf. on Seismic Zonation, vol II: 1683-1690, Nice (France).

4. Cyclic load testing of *Pombalino* “frontal” walls

4.1. Summary

The mixed wood-masonry 18th century *Pombalino* buildings of downtown Lisbon have a recognized heritage value, both nationally and internationally. These buildings have a three-dimensional timber structure enclosed in surrounding masonry walls aimed at providing increased seismic resistance. This section describes an experimental campaign to obtain the hysteretic behaviour of these interior walls, named “frontal” walls, by static cyclic shear testing with imposed displacements. The vertical load applied assumed that the wall was placed at the first floor. The loading protocol used was the CUREE [Krawinkler *et al.*, 2000] for ordinary ground motions, tailored specifically for wood structural components. A total series of three tests were conducted in three identical real size walls. The hysteretic behaviour of such walls subjected to cyclic loading exhibit high nonlinear force-displacement responses and high ductility. As previous experimental studies on “frontal” walls are very limited, these results are very useful and essential for further analytical work in modelling the non-linear behaviour of such walls.

4.2. Introduction

Very little data, analytical or experimental, exists on the monotonic, cyclic and seismic behaviour of the “frontal” walls. Such data can be obtained from experiments consisting of physical tests of representative specimens. This is a reason to carry out experimental work that can further back up analytical computer models. The experimental activity carried out on these walls so far is limited to Pompeu Santos [1997, 1999] and Cruz *et al.* [2001]. In the first paper quoted, three (although not exactly with the same configuration or dimensions) real site specimen were transported to the national laboratory for civil engineering (LNEC) and further tested under static cyclic loading with imposed displacements. The study was the first to test such walls under static cyclic shear testing. However, in this study, it is important to notice that no loading protocol was used for the imposed displacements. Furthermore no vertical loading was applied to the specimen to reproduce the vertical loads that the wall is being subjected to in reality. These are found to be downsides of this study.

In a visit to the laboratory LNEC, in 2009, it was possible to take a look at some of the tested specimen in 1997, which were still kept in the laboratory until this year. This visit was fortunate as the specimens were going to be destroyed to further carry out tests on each of the individual timber elements to determine their mechanical properties and identify the wood species used. In **Figure 4-1** it is possible to see a photograph of the specimen, called G2, which had already been cleaned from all the in-filling masonry.



Figure 4-1: Photograph of “frontal” G2 wood truss, taken at LNEC

In the visited specimen it was possible to identify two types of connections in the wood truss. The connections found at the upper and lower rows of nodes (type B) are different from the connections found at the interior rows of nodes (type A). In type A connections, the two elements crossing each other (vertical and horizontal) are cut at half thickness and they penetrate each other. In opposition, in type B connection, only the vertical element is cut at half thickness while the horizontal beam is kept at its original shape. This can be seen in **Figure 4-2**, where the details of the type B connection are shown in **Figure 4-2 (a)** and the cuts on the type A connections can be seen in **Figure 4-2 (b)** and **(c)**, for a left corner interior node and for a middle interior node, respectively.

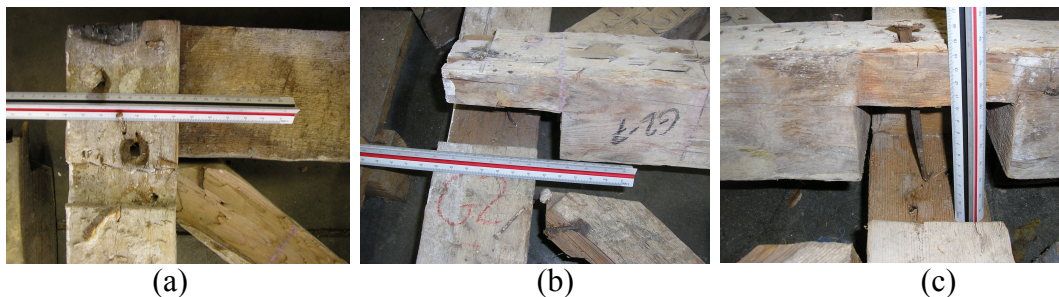


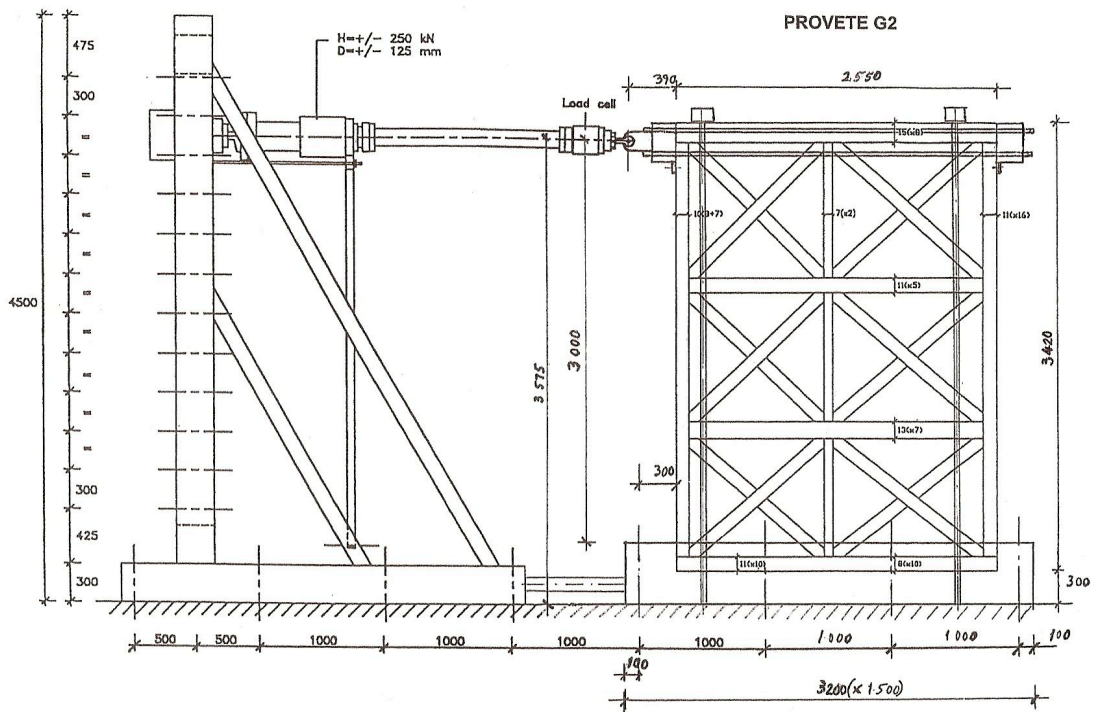
Figure 4-2: At wall G2: (a) connection type B at the left corner and first row of nodes, (b) connection type A at the left corner and second row of nodes and (c) connection type A at the middle and second row of nodes

The system of nailing used is shown in **Figure 4-3**. Here two dimensions of nails are represented: the longer square section nails were used to connect the main elements to each other and the smaller nails were adopted to connect the diagonals to each other.



Figure 4-3: Nails found in “frontal” walls in LNEC specimen

A schematic drawing of the layout of the experiment carried out at LNEC can be seen in **Figure 4-4** with specimen G2 installed. The figure is shown in a bigger size in Annex A.



A photograph of the “frontal” wall mounted at the LNEC laboratory can be seen in **Figure 4-5**. The apparatus shows vertically inclined rods that are not meant to input any vertical loading but simply avoid the lateral collapse of the wall.



Figure 4-5: Photograph of the “frontal” wall mounted, Pompeu Santos [1997]

A picture of the wall while being tested is depicted in **Figure 4-6**. The masonry filling is shown in this figure.

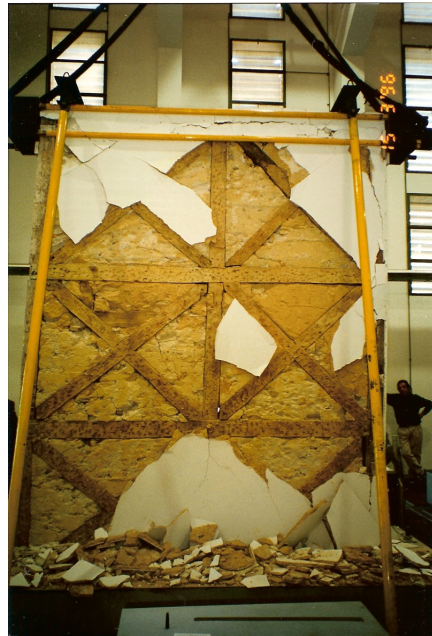


Figure 4-6: Photograph of the wall while being tested, Pompeu Santos [1997]

The experimental work discussed has the advantage of using real site specimen, however. This fact also has disadvantages with regards to the difficulty of transportation of the specimen to the laboratory and of imitation of the real support (boundary conditions) expected in the building. For the transportation a steel cage was built minimizing the deformations and shocks on the specimen; for the support conditions a concrete shoe plate was built to assure that the lower horizontal beam would remain still with relation to the ground floor. The concrete shoe can be seen in **Figure 4-7** in a schematic way.

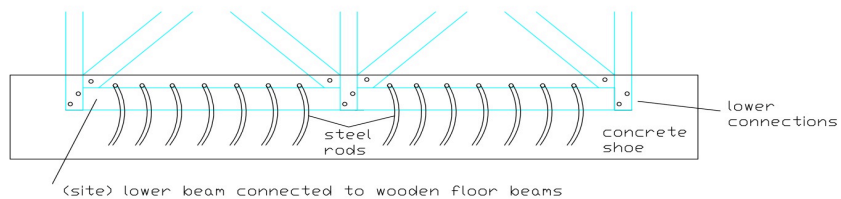


Figure 4-7: Schematic of concrete shoe for support conditions in experimental set-up of Pompeu Santos [1997]

While building this concrete shoe, however, the lower connections were covered by the concrete. It is believed that this solution for the support conditions is not the best one since it certainly increases the stiffness and strength of the tested walls when compared to the reality of the site. At the site only the lower horizontal beam is connected to the wooden floor joists, leaving the lower connections free to rotate.

The results, plotted in a diagram of lateral forces versus top displacements, obtained for the three specimen tested (G1, G2 and G3) can be seen in **Figure 4-8**, **Figure 4-9** and **Figure 4-10**.

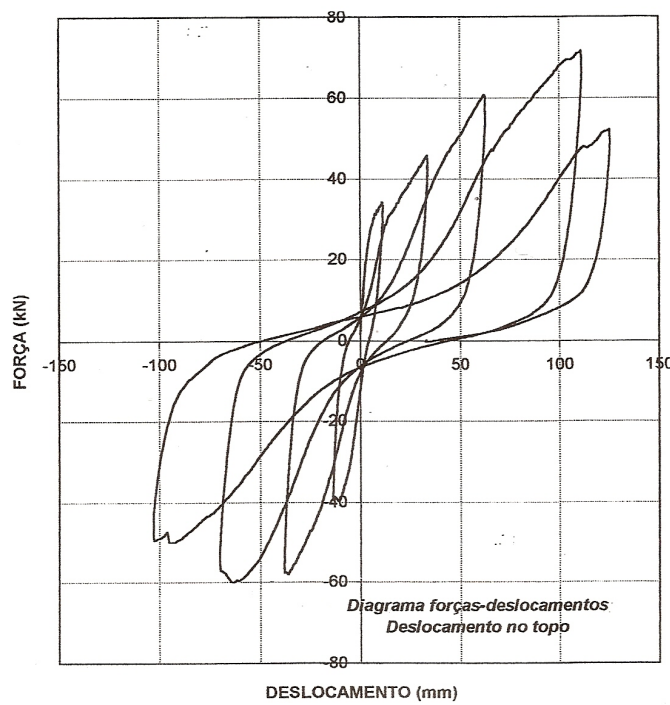


Figure 4-8: Diagram lateral forces versus top displacements in “frontal” wall G1, Pompeu Santos [1997]

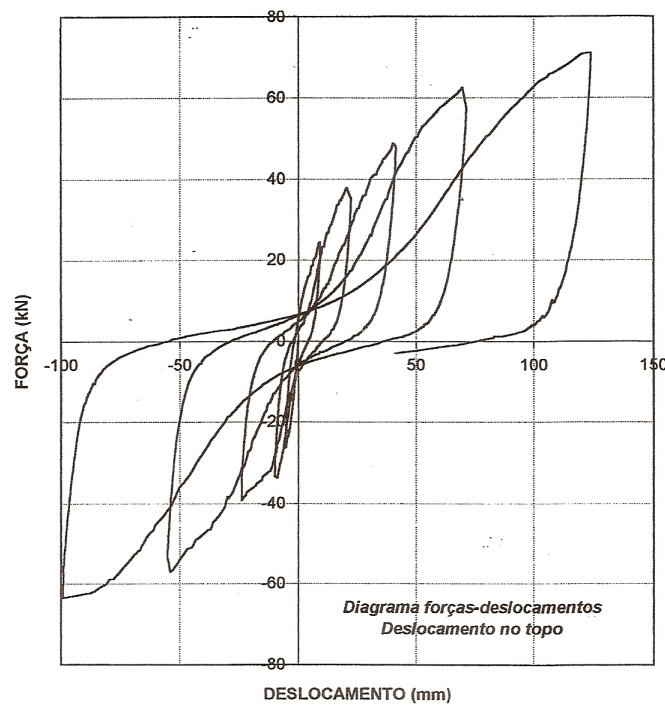


Figure 4-9: Diagram lateral forces versus top displacements in “frontal” wall G2, Pompeu Santos [1997]

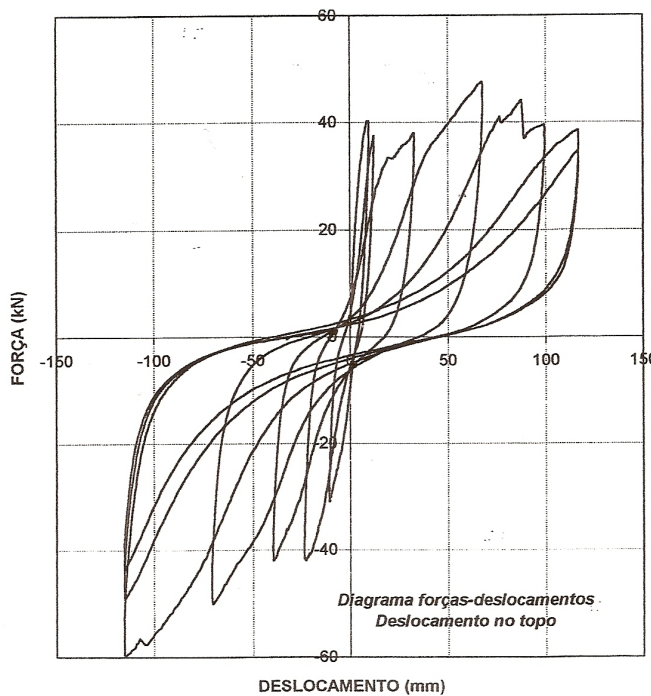


Figure 4-10: Diagram lateral forces versus top displacements in “frontal” wall G3, Pompeu Santos [1997]

It can be observed that the results obtained for the three walls are similar in terms of the general hysteresis shape observed and nonlinear behaviour characterizing the monotonic envelope. Pinching behaviour in the reloading cycles is also observed and generally fat loops dissipating reasonable amounts of energy can be identified. It is to be noticed that specimen G3 had a slight different truss layout not symmetrical in the plane of the wall resulting in unsymmetrical diagram of lateral forces versus top displacements. The strength of the walls varies between 50 and 70 kN. The ultimate displacement obtained without collapse of the structure is around 120 mm (or higher in wall G2 but it is not possible to deduce this from the diagram), resulting in an ultimate drift of around 3.5%.

In Cruz *et al.* [2001] it was intended to assess the possibility and efficiency of using fibre reinforced polymers (FRP) rods and glass fibre fabric, together with epoxy adhesives, in the strengthening of damaged “frontal” walls. Six scaled models of a typical timber frame wall panel were built and tested in diagonal compression close to complete failure. After testing, the distorted panels were brought back to their initial configuration, strengthened and subjected to diagonal compression again. What is relevant to point out from this experimental work is that **scaled** models (1:3) of the wall panels were built and not real size specimen. The models had 2 by 2 modules (diagonal crosses) of dimensions 20.8x31.6 cm², giving a total dimension of each model of 53x75 cm². Furthermore the panels were tested in **diagonal compression** (under monotonic loading), according to the apparatus that can be seen in **Figure 4-11** aiming to evaluate the shear strength of the panel. Although these tests are much less time consuming and easy to perform than panel cyclic shear tests on real size walls, the data obtained with monotonic testing is preliminary and limited to the most to backbone curves on force-displacement relationships of scaled models. This is seen to be a downside of this study even though interesting results were obtained.

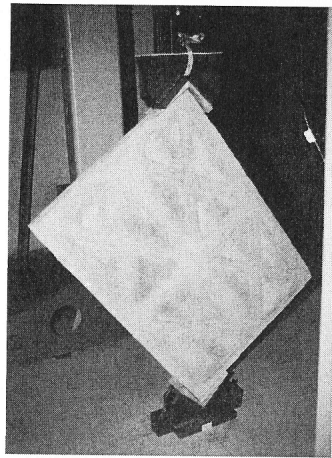


Figure 4-11: Diagonal compression apparatus of the wall panel, Cruz *et al.* [2001]

A low strength cement-based mortar was used for the in-filling of the panels. For every one of the six tested panels, from an early stage of the deformation, the cement-based mortar fissured on the contact line between the timber frame elements and the in-filling mortar and eventually detached from the panel. Soon after this, the tensioned joints started to open. The tests were finished when the outer timber member of the frame (on the shortest sides of the panel) failed in bending. Load displacement diagrams are presented in **Figure 4-12**, including both the diagrams obtained for each wall panel prior to and after strengthening. It can be seen in the figure that the original panels are less ductile. The strengthened wall panels present a very reasonable recovery of strength (between 73% and 127% of the strength of the initial panel) and a very good improvement of their ductility (between 158% and 316% of the maximum diagonal deformation withstood in the first test).

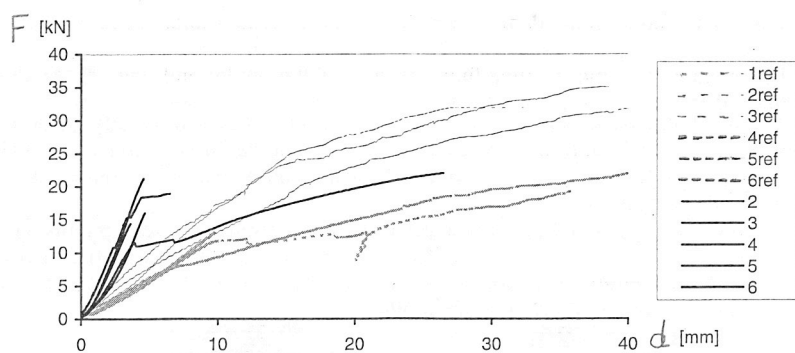


Figure 4-12: Force-displacement diagrams obtained in diagonal compression of the wall panels, prior to and after strengthening, 1ref to 6ref: strengthened panels; 2 to 6: initial state panels; Cruz *et al.* [2001]

The objective of the experimental work developed and presented in this chapter is to estimate the cyclic behaviour of the “frontal” walls. These results will enable the author to develop a macro-element of the “frontal” walls as will be presented and explained in the subsequent chapters. The test specimen and experimental set-up tries to replicate the construction details, support conditions and loading conditions that can be found in a *Pombalino* building. A total of three walls were constructed and

tested at the structural laboratory of IST (LERM). Succinctly, the main objective of this study is to obtain, by means of static cyclic shear testing with controlled displacements, the hysteretic behaviour of the “frontal” walls [Meireles and Bento, 2010].

4.3. Description of the subassembly

A schematic of the wall construction details is shown in **Figure 4-13**. The aim is to build three specimens to test at the laboratory LERM that very much resemble the real site specimen brought to test at LNEC by Pompeu Santos [1997]. The main difference is, however, the height of the specimens that in the LNEC study are three modules high with a total height of 3.5 m and are in the work presented in this thesis two modules high with a total height of 2.6 m.

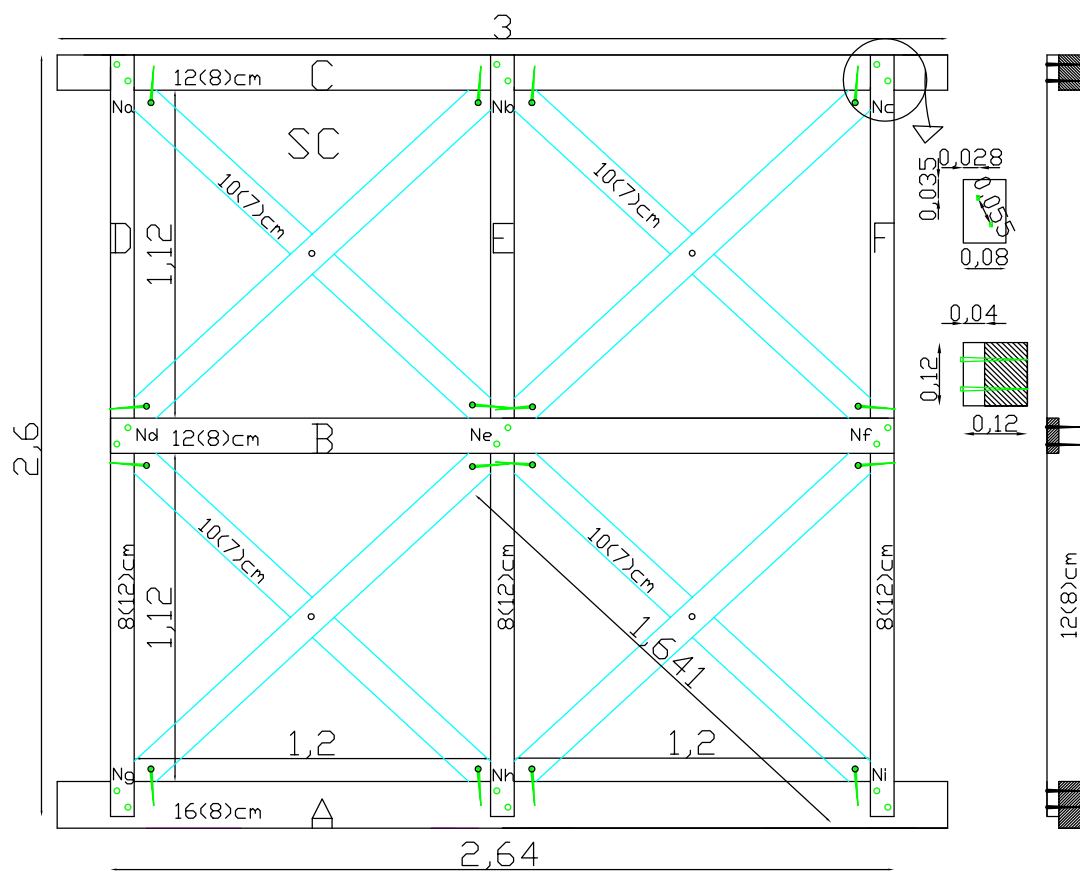


Figure 4-13: Schematic of the “frontal” wall specimen (units in meters otherwise specified)

However, the timber species used are probably not the same and the section dimensions in the real site specimen are slightly higher than the ones used herein. The timber used in the walls tested in this study consists of pine ordered from the timber mill. A typical softwood Portuguese species: *Pinus Pinaster Ait.*, *Pinho Bravo*, was ordered. One of the reasons for selecting this species was that this is one of the most common species found commercially and therefore easy to find in quantity. The typical timber species found on the *Pombalino* buildings vary from hardwood species such as Oaks and Chestnuts to softwood species such as Pines; unfortunately,

hardwood species are harder to find in abundance in the timber mills, which inhibit their use.

The wood was ordered dried from green wood to 12% moisture content (the moisture content found in woods at an ambient temperature of 20° and ambient relative moisture of 65%), given that in the old Pombalino buildings the woods have had sufficient time to dry to the ambient moisture content. The wood sections were limited to the common sections found in the timber sawmill: 16x8 cm²; 12x8 cm² and 10x7cm² section area. Then, the wood beams were cut in the carpentry and transported to the university laboratory, LERM.

As far as the connections are concerned (number of nails, positioning of nails) these were reproduced in more detail according to what was possible with nails commercially available nowadays. The nails used (**Figure 4-14**) were all pyramidal of 12.5 cm in length by a section of 10x6 mm² in the base section. Exceptionally, the nails used to connect the crossed braces to each other are smaller, of 7.5 cm in length by a base section of 5x5 mm². In the main elements a pre-drilling was made of 7.5 mm in diameter only on the upper wood element. It should be noted that the nails were bought from a store and were the only ones found, which are still handmade, and of forged steel, thus a good imitation of what existed in the past. For this reason the nails can also vary slightly in their dimensions (for instance up to 0.5 cm in length and/or up to 0.5 mm in side base section).



Figure 4-14: Nails used in the present study

Afterwards the walls were mounted as described in the following steps. First, the elements were set horizontally on the floor (**Figure 4-15**) and the main elements (all except the crossed braces) were attached together. Later on, the diagonal crossed braces were fit to the available space and nailed to the main elements with the longer nails. Special care was taken to assure that no empty spaces were found on the connection of the diagonals with the main elements. The nails were nailed manually with a hammer.



Figure 4-15: Elements of the wall set horizontally on the floor

Later on, the walls were set in the vertical position to proceed with the filling of the masonry. The walls were lifted with a heavy rope and placed in the vertical position with the help of a steel frame. This is shown in **Figure 4-16 (a) and (b)**.



Figure 4-16: Placing the walls in the vertical position: (a) front view, (b) side view

To tighten the walls to the horizontal reaction beam, six steel shaped omega flanges were built to connect the walls to the horizontal reaction beam (**Figure 4-17.**) with M24 screws. These were set in the proper location according to the positioning of the holes in the reaction beam. This was done before filling the wall with the masonry.



Figure 4-17: Steel shaped omegas to tighten the lower wood beam (brown) to the horizontal reaction beam (yellow)

Later on, the walls were filled with the masonry. The masonry dried for more than 90 days. A close-up view of the in-filled masonry can be seen in **Figure 4-18**.



Figure 4-18: Close-up view of the masonry filling

The issue of the masonry filling is important. It was foreseen that the experimental results obtained with different masonry fillings would vary significantly. Therefore it was important to try and reproduce the usual filling that was used for these buildings. However, the problem was not easy to solve since, firstly, a great variety of fillings could be found for these walls and, secondly, the workmanship in the laboratory greatly surpasses, in terms of quality, the workmanship actually found in the buildings. From the observations made by companies carrying out rehabilitation or demolition works, for instance, different types of masonry such as fillings of mortar with bricks or mortar with tiles or even mortar mixed with small stones (which is thought to be the debris or leftovers from the earthquake) were found. As far as the mortar is concerned, only one study was found related to the type of mortar used [Oz, 1994]. This study, based on a collection of real site fragments of mortar from a building under reconstruction, indicates that the lime used was probably hydraulic lime; the predominant sand size was from 0.5 to 2 mm and that no particles of cement were found, as it is expected. Furthermore, the relation water/lime was probably superior to 1.0. Based on these observations it was decided that the masonry filling would consist of hydraulic lime with intersections of tiles and broken bricks. A 1.75/2 relation was set for the water/lime relation; a 1/3 relation was set for the lime/sand relation (this is the typical relation used in construction works); as for the sand, a 1/1 relation was set for the sand of river/sand of megrim. Previous studies [Carvalho, 2007] indicate that the mechanical resistance in compression, in accordance with EN1015-11 [EN1015-11, 1999], of such a composition of mortar does not exceed 1.5 MPa being at 28 days or at 195 days indicating it is a low strength mortar. Three months was the drying time for the masonry.

4.4. Description of the experimental set-up

Each wall was put on top of the horizontal reaction beam with heavy ropes. The M24 screws were inserted in the omega plates screw holes. Aiming to avoid the lateral collapse to the sides, the walls were supported with lateral braces, enabling the heavy cords to be removed. Then, lateral roller bearings (red) were placed under the mounted frame (yellow). The lateral braces and heavy cords were then removed. This can be seen in **Figure 4-19 (a) to (c)**.

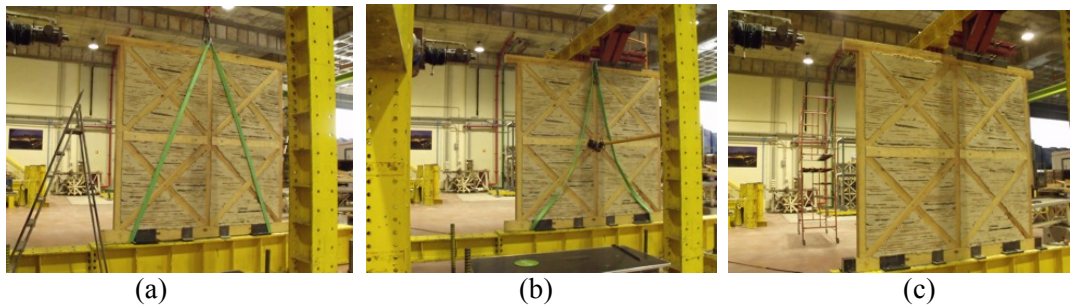


Figure 4-19: Wall on top of the horizontal reaction beam (a) with heavy cords, (b) with lateral braces and (c) with lateral roller bearings

Figure 4-20 (a) and (b) show the details of the horizontal bearings, left bearing and right bearing, respectively. **Figure 4-20** (c) presents the pre-stressing scheme of the horizontal reaction beam to the ground.

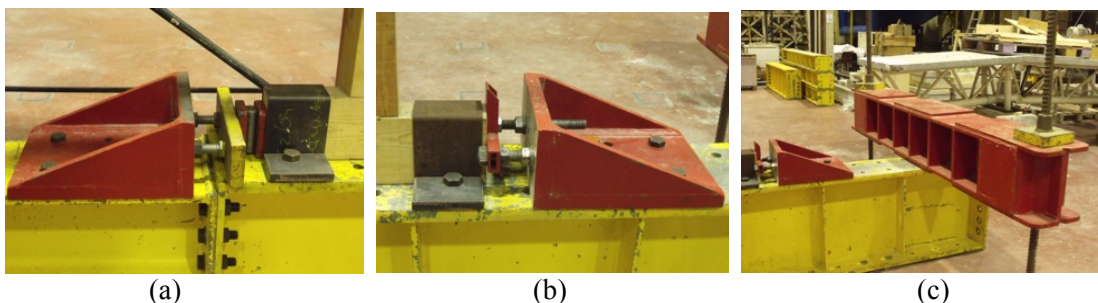


Figure 4-20: (a) Left horizontal bearing; (b) Right horizontal bearing; (c) Pre-stressing scheme

Lastly, the final layout of the experiment included the placing of a load cell in front of the actuator, placing of a linear variable displacement transducer (LVDT) on the back of the structure and mounting of the applied vertical loading through four hydraulic jacks. This all is shown in **Figure 4-21**.

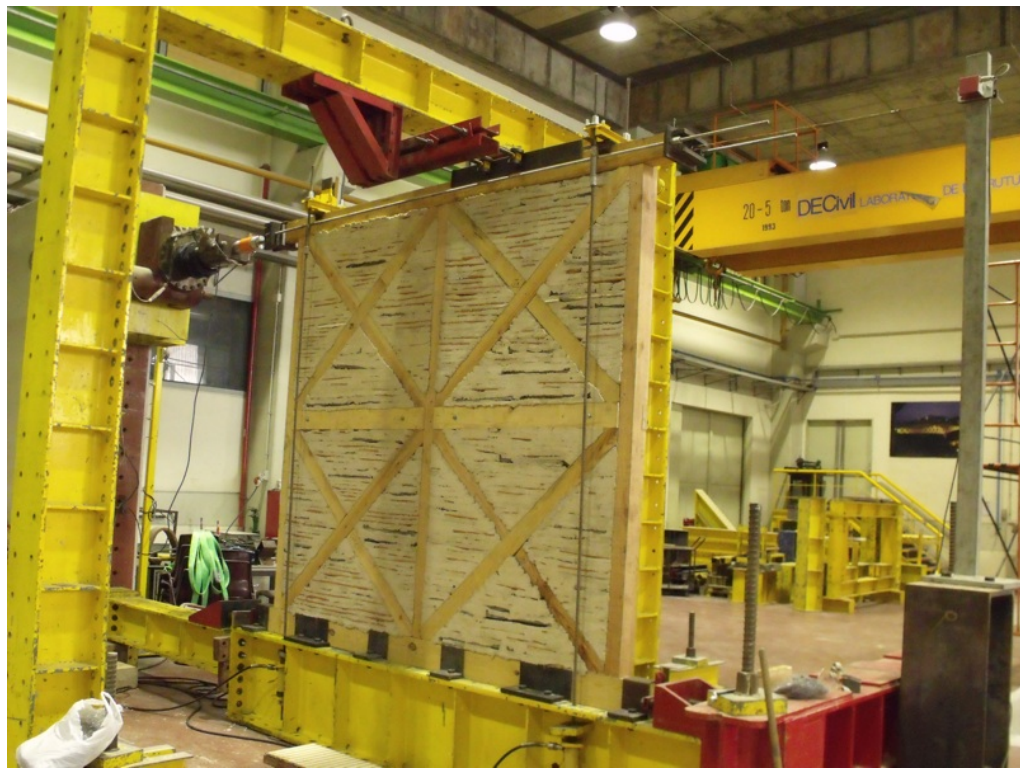


Figure 4-21: Final layout of the experiment with load cell, LVDT and jacks

The test specimen described in this section is illustrated in a schematic way in **Figure 4-22.**

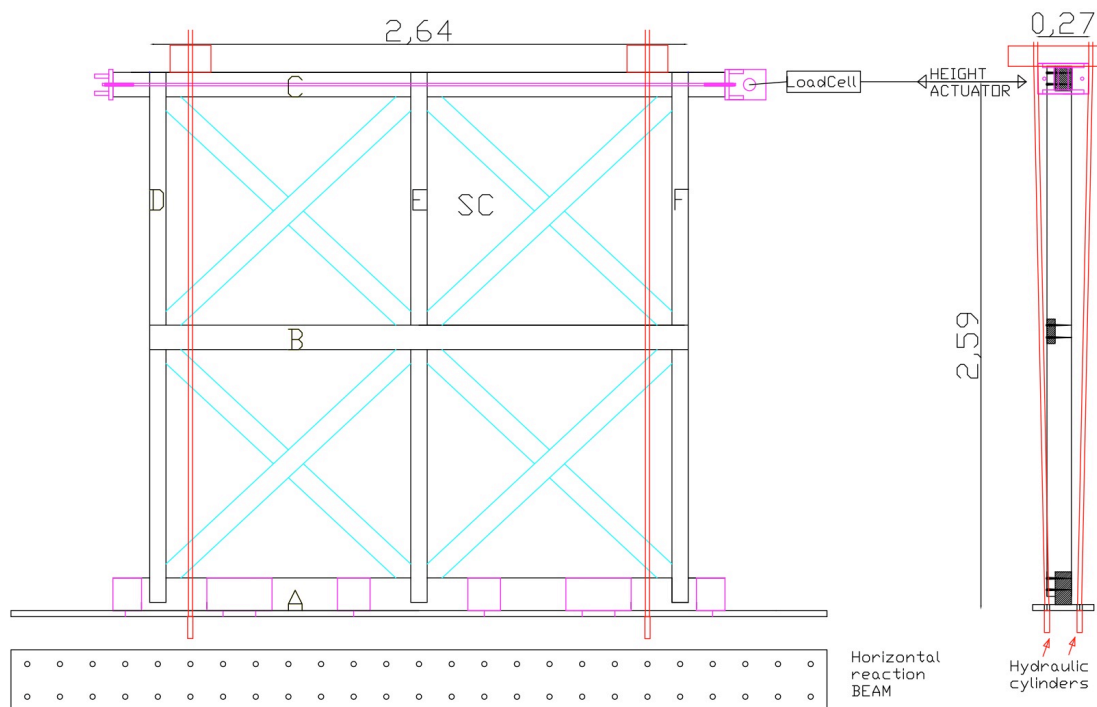


Figure 4-22: Schematic drawing of specimen SC mounted

Figure 4-23 shows a schematic of the anchorage system onto the horizontal reaction beam.

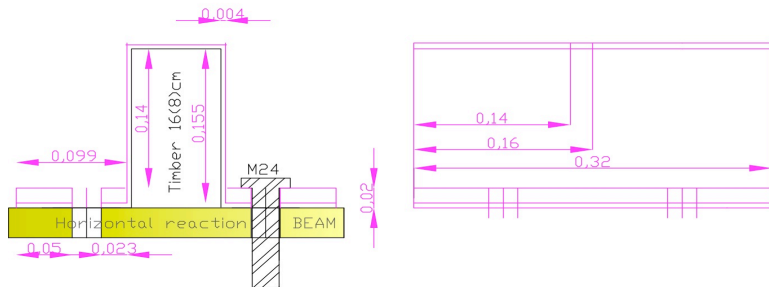


Figure 4-23: System of anchorage onto the horizontal reaction beam

In **Figure 4-23** one can see that the wall is anchored to the horizontal reaction beam at the bottom with steel braces in the shape of omegas that embrace the lower beam (section $16 \times 8 \text{ cm}^2$), which are anchored to the horizontal reaction beam with M24 (353 mm^2 section area) bolts. The anchorage system is very stiff and can firmly take the shear and moment reactions and avoid the rigid body motion of the lower beam while loaded (uplift forces). A total of sixteen M24 bolts were used.

The walls were tested with the loading applied at the top of the wall, using a 1000 kN capacity actuator with a 400 mm stroke. Data from two transducers placed on the specimen was recorded. The load from the actuator with a load cell in front of the actuator and the lateral displacement at the top of the wall via a LVDT, placed at the back of the wall, were recorded. All data was acquired using a personal computer running Visual Basic. Transverse movement of the specimen during testing (out-of-plane) was resisted with a system of lateral roller bearings, as has been previously mentioned. The weights of the walls are: 0.766 ton; 0.756 ton and 0.766 ton, for wall 1, 2 and 3, respectively. The three walls were built at the same time.

4.5. Definition of the loading protocol

The CUREE protocol [Krawinkler *et al.*, 2000] for ordinary ground motions was used to study the cyclic behaviour of the “frontal” walls. The loading protocol is tailored specifically for use with wood structural components. It consists of cyclic displacement sequences increasing in amplitude throughout the test; each segment consists of a primary cycle with amplitude defined as a multiple of the reference displacement. The primary cycle is followed by a series of cycles with amplitude equal to 75% of the primary cycle. The sequences of the cycle vary in length from 3 to 7 cycles. The input displacements for each of the tests performed can be seen in **Figure 4-24**. All tests were conducted such that the initial position of the actuator was at a half stroke allowing the maximum deflection in each direction (+-200 mm). The tests were conducted at a rate of 0.25 mm/s. The data was read at a rate of 1 mm/sample as well as, in terms of force, at a rate not higher than 0.25 kN/sample.

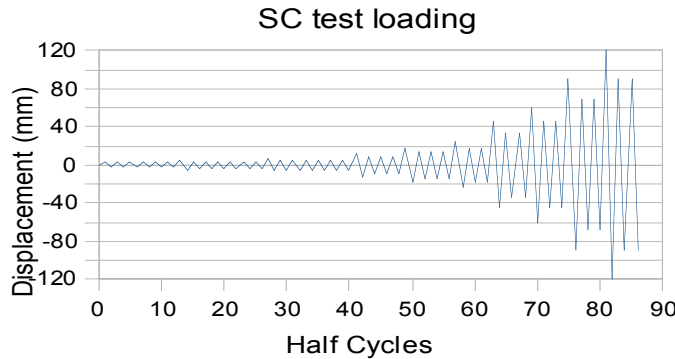


Figure 4-24: The loading protocol for the tests performed

In this study, the calculation of the reference displacement was not done, as it would imply one specimen to be tested under monotonic loading as suggested in the CUREE protocol. Instead, a maximum displacement in the loading protocol equal to the maximum displacement obtained at the LNEC experimental testing [Pompeu Santos, 1997], that is 120 mm, was set. Nevertheless, these specimens are one module higher than the ones tested herein; for this reason it is expected that specimens SC1 to SC3 (wall 1 to wall 3) can attain a lower maximum displacement. Accordingly, in experiments of specimens SC1, SC2 and SC3, the structures were seen to stand heavy damage at a displacement of around 90 mm. For safety reasons in experiments SC1 and SC2 the experiment was stopped at this displacement level; nevertheless, in experiment SC3 the test was carried out up to a displacement of 120 mm since it was the last structures being tested.

4.6. Vertical loading calculation

The vertical loading to be imposed on the test structure was determined based on Eurocode 1 [CEN, 2002] and is given by Equation 4-1:

$$\text{Design load} = \text{dead load} + 0.3 \times \text{live load} \quad (\text{Equation 4-1})$$

It was considered that the wall was placed on the first floor of a *Pombalino* building, which is composed of three storeys plus ground floor and attic (five floors in total). For the calculations of the vertical loads, the dead and live loads were multiplied by three. The side of influence of the walls was considered to be of four metres. For the vertical loads to be imposed on the structure it was considered to be as shown in Table 4-1.

Table 4-1: Vertical loads imposed in specimen SC1 to SC3

Loads	(kN/m ²)	Side of influence (m)	Nº of storeys	Total (kN/m)
Live load	2	4	3	24
Dead load-partition walls	0.1	4	3	1.2
Dead load-wooden floors	0.7	4	3	8.4
Dead load-ceilings	0.6	4	3	7.2
Dead load-“frontal” walls (x2)	-	-	-	6.0

The output is a total vertical load of 30 kN/m along the wall (per metre of wall). The vertical loading was distributed along 4 hydraulic jacks each one with a total force of 19.2 kN and kept constant during the test.

4.7. Results

The results obtained for specimens SC1, SC2 and SC3 can be seen in **Figure 4-25**, **Figure 4-32** and **Figure 4-36**, respectively. The hysteretic behaviour of the “frontal” walls subjected to cyclic loading was similar in terms of the general hysteresis shape observed and nonlinear behaviour characterizing the monotonic envelope. Pinching behaviour was observed in the reloading cycles associated with strength degradation in the response and generally fat loops can be identified dissipating reasonable amounts of energy. High ductility in the response (around 3) was also noticed. The strength of the walls is around 50 kN. The ultimate displacement obtained without collapse of the structure is around 90 mm resulting in an ultimate drift of around 3.5% (the correct value will be calculated in section 5.7.2.).

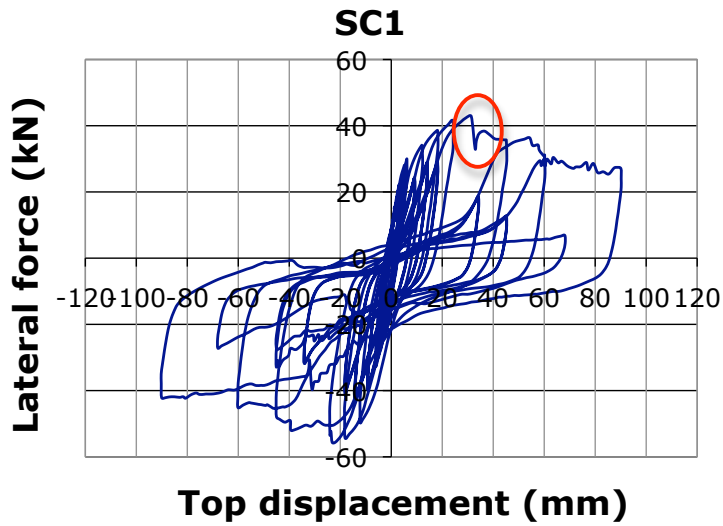


Figure 4-25: Hysteresis curve of wall SC1

During the experimental tests the masonry started immediately (at low displacements) to detach from the wood elements. This can be seen in **Figure 4-26**. Inside the wood elements it stops them from buckling in the plane of the wall. Until a displacement of 90 mm in experiments SC1 to SC3, the out-of-plane collapse of the masonry was not observed. Nevertheless, since it was detached from the wood truss, it was at risk of this type of collapse occurring. It is believed by the author that in the case of a real earthquake, given the dynamic loading instead of static and the loading in the two orthogonal directions, the masonry, at least of the upper modules, would soon collapse to the sides, leaving the wood truss without any infills.

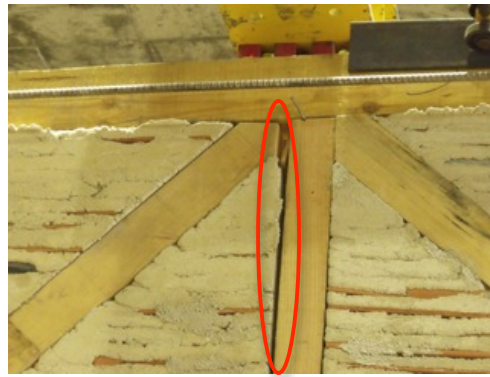


Figure 4-26: Detachment of the masonry from the wood truss

In specimen SC1 the failure mode of the wall is the failure of the connections (upper connections) by the cracking of the wood elements. This is shown in **Figure 4-27 (a) to (c)**. The cracking of the wood elements at the upper connections starts early at a displacement of around 30 mm. This point can be easily identified in the positive direction of forces in the hysteresis curve of wall SC1 (see **Figure 4-25**). Suddenly the lateral resistance of the wall decreased as can be seen in the figure at this point marked with a red circle.

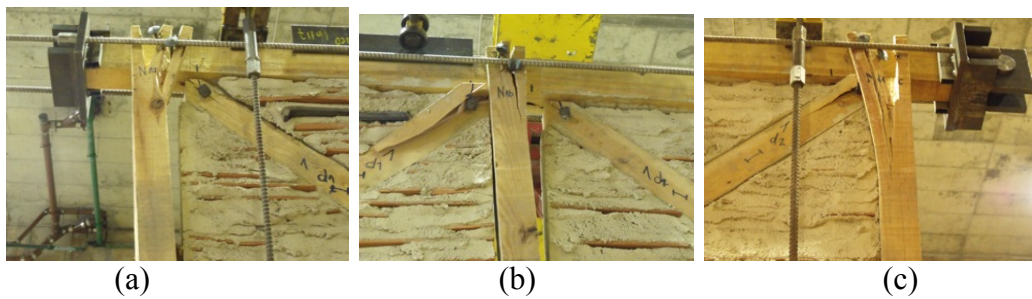


Figure 4-27: Failure by cracking of the wood at the connections: (a) N1a, (b) N1b, (c) N1c.
Photo at a displacement of plus 90 mm

On the same specimen, notwithstanding, the failure of the connection N1d by pulling out of the nails can be seen. This is depicted in **Figure 4-28** and corresponds to a displacement positive of 90 mm. To be noticed that the pulling out of the nail at node N1d is facilitated because the node is a corner node.



Figure 4-28: Failure by pull out of nails at connection N1d at a displacement of plus 90 mm

In **Figure 4-29** and **Figure 4-30** it is possible to compare the behaviour of the diagonals of the wood truss at positive loadings (in the figures when the wall is pushed from right to the left) and at negative loadings (in the figures when the wall is pushed from left to the right). From these figures it is possible to state that the diagonals do not have any tension resistance given that its connection/nailing to the nodes does not seem to work in tension: a space is opened between the node and the diagonal. When the load reverses, the space closes and the load is transmitted to the diagonals enabling them to work in compression.



Figure 4-29: Detailing of the connections at a loading of plus 60 mm (from the right to the left)



Figure 4-30: Detailing of the connections at a loading of minus 60 mm (from the left to the right)

In specimen SC1 the mode of failure was essentially the failure of the connections by cracking of the wood elements at the connections/nodes. This happened for the upper row of connections, where the horizontal load was imposed. The failure of these connections in such terms is mainly due to the fact that these were designed as corner connections with no continuity towards the next storey of the vertical wood elements. Nevertheless, in reality it could happen that this continuity of the vertical elements towards the next storey exists, also because it is assumed that the tested walls are placed on the first floor. Additionally, the nails used seem to have slight bigger section dimensions than the ones found in reality in these walls, leading to the failure of the surrounding wood instead of the pulling out of the nails. For these reasons, it was decided to avoid this type of failure in the next tested walls. Therefore, it was decided to reinforce the upper and lower connections in the SC2 and SC3 specimens with some steel plates, as it is represented in **Figure 4-31** (a) and (b). The connections that were reinforced were N2a, N2b, N2c, N2g, N2h and N2i at specimen SC2 and

N3a, N3b, N3c, N3g, N3h and N3i at specimen SC3; which are the upper and lower rows of connections.

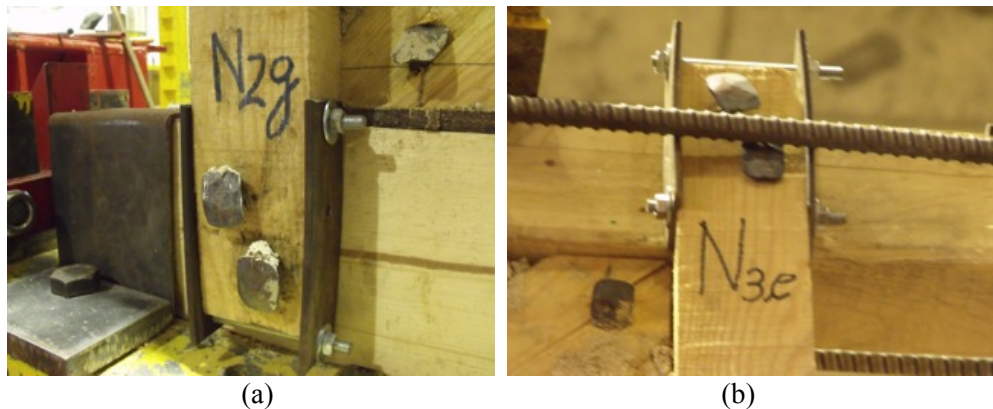


Figure 4-31: Reinforcement layout at the upper and lower rows of connections in specimen:
(a) SC2 and (b) SC3

The results obtained from experiment SC2 can be seen in **Figure 4-32**.

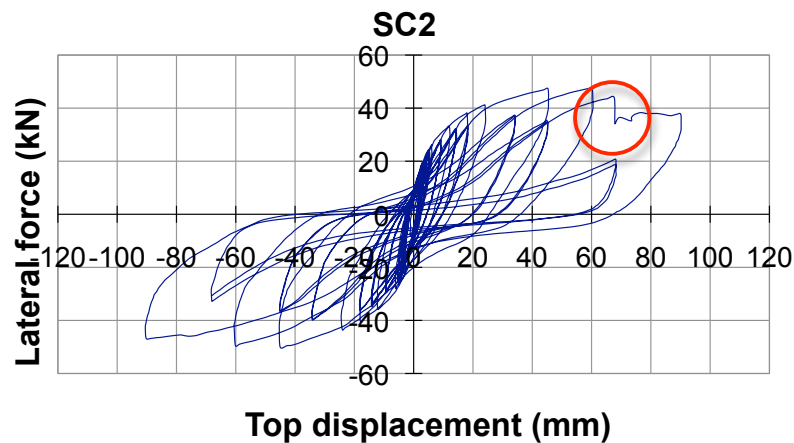


Figure 4-32: Hysteresis curve of wall SC2

It was observed that the reinforcement of the upper and lower connections worked very well in preventing the failure of these connections with the cracking of the wood elements. In fact, these connections also did not fail by other means such as the pulling out of the nails, during the whole test. This is shown in **Figure 4-33 (a)** and (b), where the connections N2a and N2c can be observed to have no relevant damage at the maximum displacement of 90 mm.

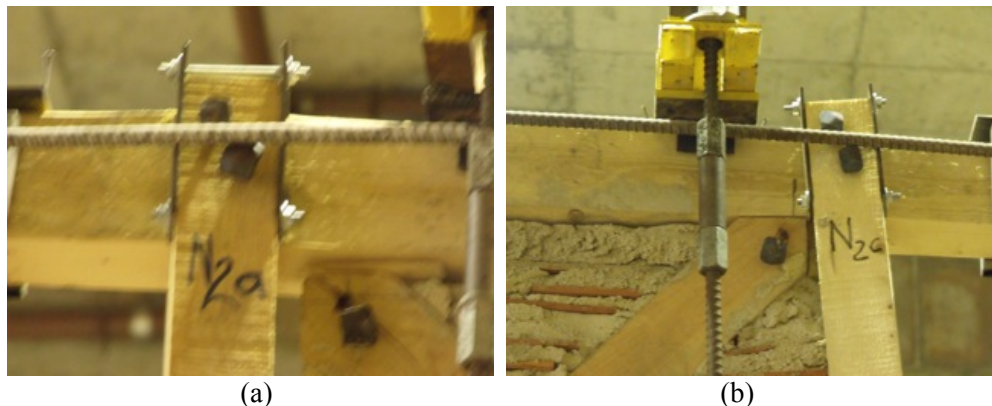


Figure 4-33: Behaviour of the upper connections at displacement of 90 mm. (a) Node N2a, (b) Node N2c

Nevertheless, at connection N2d almost pulling out of the nails was seen as observed in experiment SC1. This is represented in **Figure 4-34**. No pull out of the nails was observed in the upper and lower rows of connections, namely Na to Nc and Ng to Ni. This is due to the fact that the nailing system is very strong (the nails are very thick) when compared to the ones seen in the real site walls tested. As previously mentioned the dimensions of the nails used here are the only ones found on the market that were made using forged steel and with a reasonable length to be used in these walls.



Figure 4-34: Behaviour of the connection N2d with almost pull out of nails

It was observed in the tested specimen SC2 that the failure mode was the buckling and consequently out-of-plane failure of one of the diagonals for the upper modules. This happened at a displacement easy to identify in the graphic of the hysteretic behaviour of wall SC2, which is marked with a red circle. It can be seen that the failure of the diagonal occurred at a displacement of around 65-70 mm in the positive direction of forces. In the negative direction of forces it is observed that no failure has occurred for such displacement and until 90 mm. It was decided to stop the test at a displacement of 90 mm since the diagonal that failed left the respective module heavily damaged. The collapse of the diagonal can be seen in **Figure 4-35 (a)** and (b).



Figure 4-35: Buckling of diagonal in the upper module: (a) front; (b) back

The results obtained for specimen SC3 are shown in **Figure 4-36**.

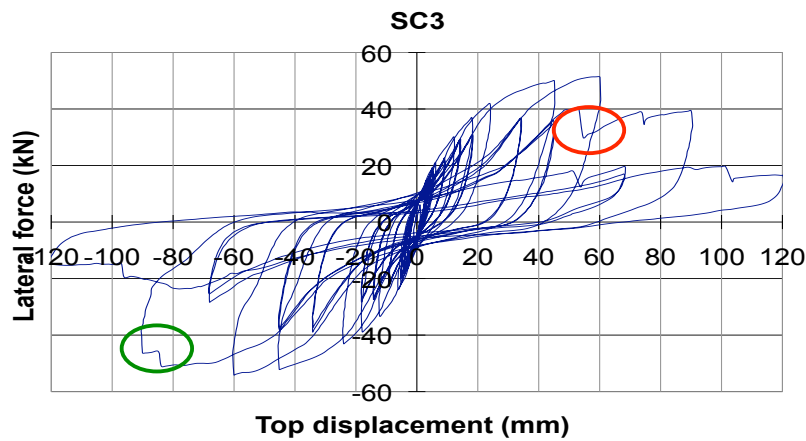


Figure 4-36: Hysteresis curve of wall SC3

Again the detachment of the masonry panel from the wood truss can be observed, see **Figure 4-37**. This happens at low displacements as in the previous tests.



Figure 4-37: Detachment of the masonry panel from the wood truss

From **Figure 4-38**, the collapse mechanism of the third “frontal” wall can be predicted; at a displacement of 60 mm in the positive direction the compressed diagonal starts to

bend outside the plane of the wall, leading further ahead to the out-of-plane failure of the upper module.



Figure 4-38: Initial out of plane instability of the upper left module, displacement of 60 mm in the positive direction of loading

Further ahead the same diagonal, as in experiment SC2, collapses, as it is illustrated in **Figure 4-39 (a) and (b)**. This picture corresponds to a displacement of 90 mm in the positive direction of loading. After this failure there was a decrease in the strength of the wall that can be observed in **Figure 4-36**, marked with a red circle.



Figure 4-39: Failure by buckling of the upper left module diagonal, displacement of 90 mm in the positive direction of loading: (a) side, (b) back

When the wall was loaded in the negative direction another diagonal failed, the one from the lower left module. This is shown in **Figure 4-40 (a) and (b)** and the associated drop in strength is marked with a green circle in **Figure 4-36**.



Figure 4-40: Failure of diagonal of lower left module: (a) front, (b) back; at displacement of 90 mm in the negative direction of loading

Finally, the general state of the wall corresponding to a displacement of 120 mm in the positive direction of loading is represented in Figure 4-41 (a) and (b). Figure 4-41 (b) has a part of the masonry collapsed, this happened immediately after taking the photograph of Figure 4-41 (a).

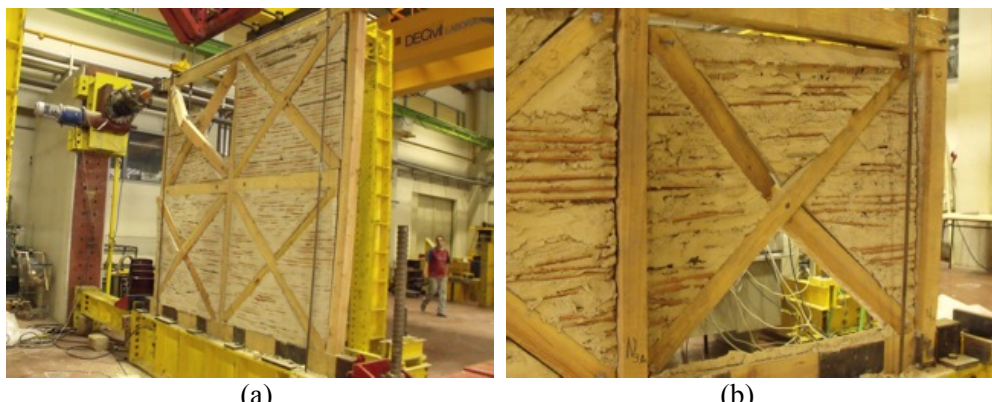


Figure 4-41: General state of the wall corresponding to a displacement of 120 mm in the positive direction of loading: (a) complete wall, (b) lower left module

It is important to mention the similarity between the results obtained here for the hysteretic behaviour of the three walls built in the laboratory and the results obtained for the hysteretic behaviour of the three site specimen walls tested in LNEC [Pompeu Santos, 1997]. For both experimental campaigns, the general shape of the curves are the same and in both cases strength degradation and pinching behaviour occurred. In terms of maximum strength, the results are also similar with slightly higher values for the higher real site walls. Finally, in terms of ultimate displacement it is observed that the tested walls at LNEC present slightly higher values of displacement before being heavily damaged; this is reasonable to observe, as the tested walls in LNEC are one module higher when compared to the walls built in the LERM laboratory. In terms of ultimate drift, the results are similar for the two walls being around 3.5% (see section 5.7.2. for exact value). Finally, the only discrepancy between the two tests is the strength degradation that is higher in the LNEC walls than in the walls tested in the present study.

Plotting the maximum force obtained for the outer cycles of loading for both the positive and negative directions it is possible to obtain the experimental envelope curves for the three walls. These can be seen in **Figure 4-42**.

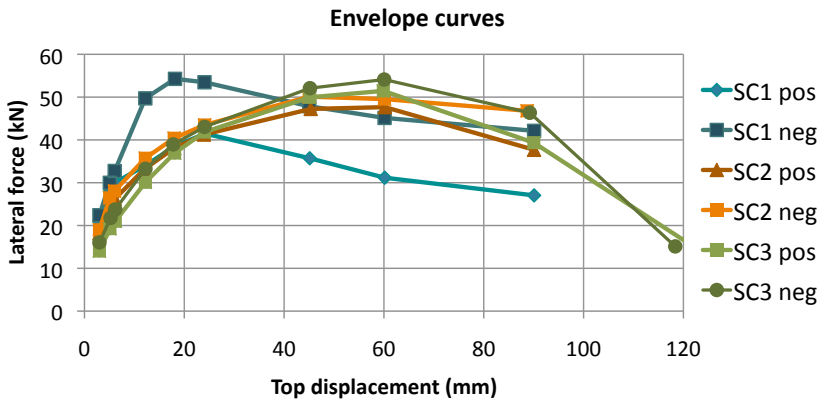


Figure 4-42: Experimental envelope curves

It is observed that, as expected, the envelope curves, for both positive and negative directions of loading, are very similar for SC2 and SC3 walls. Additionally, for SC1 the results are a bit different because of the reasons presented previously that is a different failure mode. On the contrary, there is not an apparent justification of why the envelope for “SC1 neg” is slightly different from the others for low displacements. In **Table 4-2** one can see the summary of the values of maximum displacement, maximum force and cumulative energy obtained for the three tests.

Table 4-2: Summary of values obtained for tests

Specimen	Maximum	Maximum	Cumulative
	Displacement (mm)	Force (KN)	Energy (J)
SC1	90	51.27	25957
SC2	90	50.10	27502
SC3	120	51.11	26270

In **Figure 4-43** the cumulative energy dissipated by the three walls is presented. The cumulative energy, CE, dissipated by the walls is calculated by Equation 4-2:

$$CE = \sum_i \int_{\delta_{i-1}}^{\delta_i} F(\delta) d\delta \approx \sum_i \frac{F_i + F_{i-1}}{2} (\delta_i - \delta_{i-1}) \quad (\text{Equation 4-2})$$

Where the subscript i is the i^{th} force-displacement ($F-\delta$) data point.

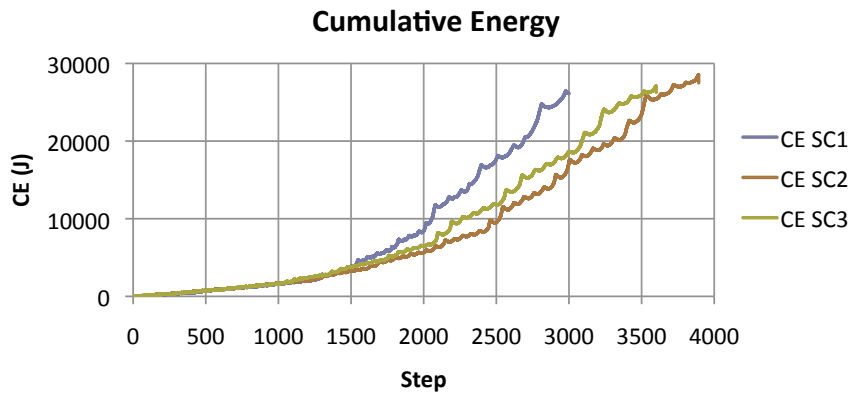


Figure 4-43: Cumulative energy for the three tests, walls SC1, SC2 and SC3

From **Figure 4-43** it is evident that the cumulative energy varies exponentially with the time step.

If for each value of drift the secant stiffness, K , related to the maximum force is plotted, it is possible to obtain the stiffness degradation for each value of drift, in relation to the initial stiffness K_0 . This is seen in **Figure 4-44**.

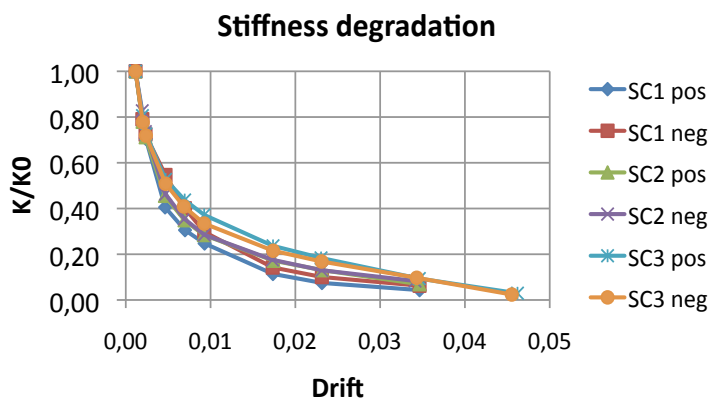


Figure 4-44: Stiffness degradation for the three tests, walls SC1, SC2 and SC3

It is observed that the secant stiffness decreases exponentially with the value of drift.

Being aware that the number of previous experimental results is very limited, one can say that the results obtained herein are important for further work in modelling the behaviour of such walls. The hysteresis curves defined can be incorporated into softwares to analyse the behaviour of “frontal” walls under reversed cyclic loading or in simpler models, taking advantage of the envelope curves, to analyse the behaviour of “frontal” walls under monotonic loading. However, further validation with more extensive test data is clearly needed before any model can be used with confidence for this purpose.

4.8. Conclusions

The research work presented focused on obtaining the experimental cyclic behaviour of the so-called “frontal” walls. This was accomplished through static cyclic shear testing with imposed displacements on such walls. This is original research since very little is known in the literature about the cyclic behaviour of such walls. Nonetheless, the authors believe that further experimental work should be carried out, for instance on walls of different sizes or for other combinations of vertical loading or even on specimens without the masonry fillings. The results obtained lead to the definition of the base force – top displacement experimental relationship. This should be useful for the further development of analytical models of these walls.

The hysteretic behaviour of the “frontal” walls subjected to cyclic loading is characterized by nonlinear behaviour described by a monotonic envelope. Pinching behaviour associated with strength degradation is also observed. Generally fat loops can be identified, showing reasonable amounts of energy dissipation. The response is also highly ductile. The ductility of the walls, calculated based on the experimental results as shown in **Figure 4-42**, is around 3 (90 mm/30 mm). It is important to point out the resemblance between the results obtained here and the results obtained in the other similar experimental tests developed by Pompeu Santos [1997], validating the experimental results obtained here.

It might be important to mention again that the lime used in the present work was hydraulic lime since it was based on the study by the Oz company [1994]. Nevertheless, the author knows that air lime was also used in old *Pombalino* buildings. In this way, air lime could also have been used for the present study.

4.9. Bibliography

Cruz H., Moura J.P. and Sporiti Machado J., 2001, The use of FRP in the strengthening of timber reinforced masonry load-bearing walls, Historical Constructions, Guimarães, page 847.

Carvalho J., 2007, Caracterização Mecânica de Paredes Resistentes em Alvenaria de Pedra Através de ensaios não destrutivos; Master thesis, Instituto Superior Técnico (IST) (in Portuguese).

Eurocode 1: Actions on structures - Part 1-1: General actions -Densities, self-weight, imposed loads for buildings, EN 1991-1-1, 2002, Comission of the European Communities (CEN), Brussels.

EN1015-11- Methods of test for mortar for masonry. Part 1.1 Determination of flexural and compressive strength of hardened mortar , august 1999.

Krawinkler, H, Parisi F, Ibarra L, Ayoub A. and Medina R, 2000, Development of a testing protocol for wood frame structures. CUREE-Caltech Woodframe Project Rep., Stanford University, Stanford, California.

Mascarenhas J, 2005, Sistemas de Construção; V-O Edifício de rendimento da Baixa Pombalina de Lisboa, Materiais Básicos 3º Parte: O Vidro. Livros Horizonte (in Portuguese).

Meireles H, Bento R, 2010, Cyclic Behaviour of Pombalino “frontal” walls, Proc. of the 14th European Conference on Earthquake Engineering, Ohrid, Macedonia.

OZ Empresa Lda, work developed for Intergaup, 1994, Levantamento e Apoio à Modelação estrutural dos Edifícios do BCP da Rua Augusta e Rua dos Correeiros em Lisboa (Caracterização dos materiais) (in Portuguese).

Pompeu Santos, 1997, Ensaios de Paredes Pombalinas. Nota Técnica Nº15/97, NCE/DE, LNEC Lisboa (in Portuguese) .

Pompeu Santos, 1999, Laboratory Tests on Masonry walls taken from an Ancient Building in Lisbon. Procc. of the 34th Meeting of CIB W023 Comission in October 1997 in Lisbon, CIB Publication 231, pg. 89-94.

5. Development and validation of a macro-element for “frontal” walls

5.1. Summary

This chapter describes the proposal of a macro-element for “frontal” walls. This is obtained by means of the development of a hysteretic model to describe the cyclic behaviour of the *Pombalino* “frontal” walls. The hysteretic model, based on phenomenological approach, aims to reproduce the response of a wall under general monotonic, cyclic or earthquake loading and is based on a minimum number of path-following rules. The model is constructed using a series of exponential and linear functions. There is a total of nine identifiable parameters in this model to capture the nonlinear hysteretic response of the wall. These are all calibrated with experimental data. In particular, the analytical model proposed herein is calibrated based on the experimental testing performed and presented previously in Chapter 4. The model developed [Meireles *et al.*, 2011] also accounts for characteristics such as pinching effect, strength and stiffness degradation that have been observed in the experimental data. Then, the envelope curve for different wall sizes (height and length) was obtained, since in reality one can find other wall sizes in a single building.

5.2. Introduction

Preliminary research is found in the development of simplified or elaborated models for the analysis of the seismic behaviour of *Pombalino* “frontal” walls. An interesting linear elastic model in SAP 2000 [1998] was done in the work of Cardoso [2003]. A simple truss model was used to characterize the behaviour of the “frontal” walls. The results were also compared to the experimental results performed in LNEC [Pompeu Santos, 1997]. The main conclusion of the work was that one must consider a relatively low Young’s modulus of the wood in order to match the experimental results initial stiffness of the wall; or, alternatively, one must consider that the diagonals of the truss model do not work under tension. The later assumption is more plausible.

An example of an elaborate model of *Pombalino* “frontal” walls was done by Kouris and Kappos [2011]. This paper focuses on the description of the seismic response of timber-frame structures by means of a detailed analytical model. Although elastic analysis can adequately identify regions with high stresses, it fails to capture the redistribution of stresses and the ensuing failure mechanisms. The simulation of timber-frame masonry is made here using a plasticity model. Non-linear laws for the materials, such as a trilinear stress-strain curve for monotonic loading of timber and a Mohr-Coulomb contact law for wooden members, are used to express their behaviour under moderate and high stress levels. An associated flow rule is assumed and Hill’s yield criterion is adopted with isotropic work-hardening. An important aspect, which the present thesis author also takes into consideration, is that masonry infills are not included in the model due to their insignificant contribution after the initial elastic stage of the response. The proposed finite element model is intended for a detailed

non-linear static analysis of parts of a building. A simplified model with beam and link elements with non-linear axial springs is also developed. Both models are validated using experimental results from LNEC [Pompeu Santos, 1997]. A good match was found between the results of the numerical analyses and those of the tests for most stages of the response.

Although one cannot find identical *Pombalino* “frontal” walls worldwide in other building typologies, there are some buildings built nowadays made of timber that use wood shear walls. These buildings are very common in the United States and Canada and it is thought to be an interesting contribution to the present work the brief description of such wood shear walls. According to Lindt and Walz [2003] the majority of residential and many low-rise commercial structures in the United States are constructed using light-frame wood construction. The main lateral force resisting mechanism for light-frame wood structures are wood shear walls. A wood shear wall consists of dimensional lumber sheathed with plywood, oriented strand board, or other sheathing material. Lateral forces acting on the wall are resisted primarily by the sheathing and are transferred to framing members via nailed connections. Through this composite action, a shear wall system is able to effectively dissipate energy and transfer lateral loads into the foundation of a building. Since the 1940’s a great deal of experimental research has been conducted to quantify both static and dynamic characteristics and subsequently the behaviour of wood shear walls. In addition many static and dynamic numerical models have been developed to describe shear wall behaviour during simulated earthquake loading. For a full review of shear wall testing and modelling studies one can refer to Walz [2001].

5.3. Lateral displacement mechanisms

From the observation of the experimental testing carried out in this work it was possible to define two lateral displacement mechanisms of the loaded wall. The first, which can be called equivalent rocking (as an analogy to the behaviour of masonry walls under lateral loads – see Chapter 6), sketched in **Figure 5-1**, is referred to the rigid body movement of the wall, rotating at the base of the structure (point r - connection Nh - **Figure 4-13**). The connections Ng and Ni (see **Figure 4-13**) are loaded and displace up and down, respectively. This can be seen in **Figure 5-2**. The lower beam is fixed to the reaction beam by the omega-shaped steel braces. In this particular lateral displacement mechanism the diagonal braces are not compressed or tensioned so they are not under stress. The same happens to the masonry filling area, which is merely rotated but not compressed. The angle between the horizontal and vertical elements is kept the same (90°). As the structure is displaced by α , the connections/nodes Ng and Ni are displaced by ℓ , upwards and downwards, respectively (**Figure 5-2**).

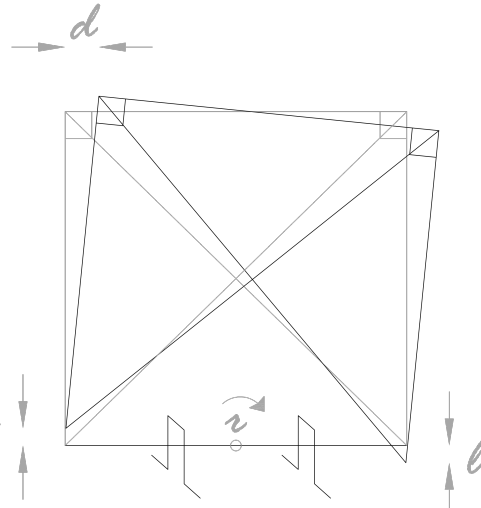


Figure 5-1: Equivalent rocking lateral displacement mechanism

From **Figure 5-2** one can see that the movement of the node downwards is resisted by the compression of the horizontal timber element, which suffers compression perpendicular to the grains. The movement of the node upwards is resisted with the connection by the stressing (shear) of the nails. It should be noted that the horizontal timber element is fixed to the horizontal reaction beam.

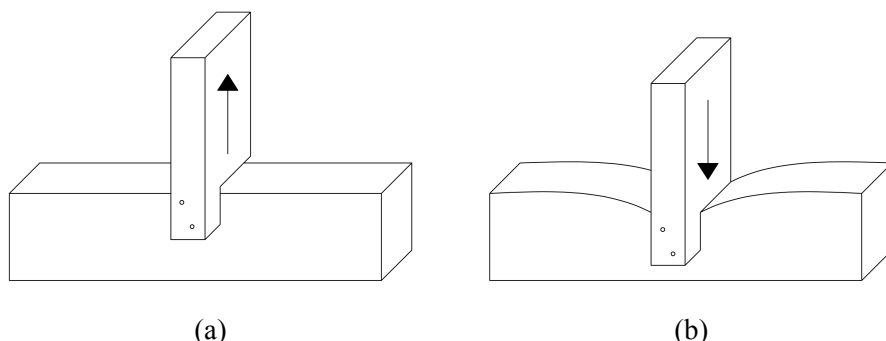


Figure 5-2: (a) Behaviour of the connection Ng , upwards movement (b) Behaviour of the connection Ni , downwards movement

The second lateral displacement mechanism of the loaded wall can be called equivalent shear and is associated with the distortion of the panel. The vertical and horizontal members are now drawing angles between each other that are no longer 90° . Some diagonal braces are then shortened since these are under compressing loads. Since the connection between the diagonals and vertical/horizontal members hardly resist in tension, the diagonal braces are never stretched, as can be seen in the sketch of **Figure 5-3**. In this case the masonry filling areas are rotated but also compressed at some locations. However, as will be seen later, the compressed area is a very small percentage of the total area. When the wall panel laterally displaces α , it distorts γ and the compressed diagonal braces shorten l (**Figure 5-3**).

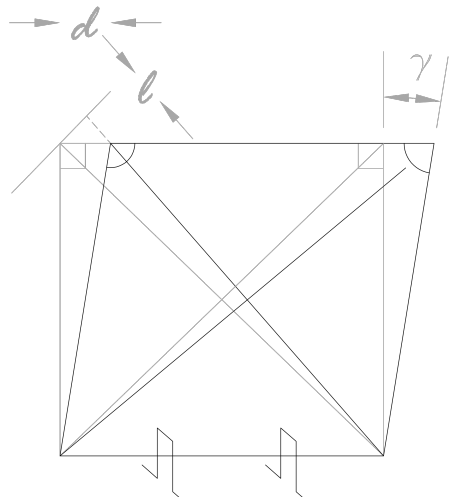


Figure 5-3: Equivalent shear lateral displacement mechanism

If one takes a look at what happens for the real size wall one can sketch **Figure 5-4** and **Figure 5-5**, referring to the displacement of the wall close to collapse. Even though the displacement of the nodes Ng and Ni was not instrumented, by observation it is possible to say that these nodes did not display upwards or downwards more than 10 mm around collapse point. This leads to a top displacement of around 17 mm (**Figure 5-4**). If it is assumed a displacement associated with distortion (equivalent shear) of 90 mm around the collapse point, this means that the wall displayed by rocking $17/(90+17) = 16\%$ of the total displacement at collapse. The variation in length of the compressed diagonals is 32 mm (**Figure 5-5**).

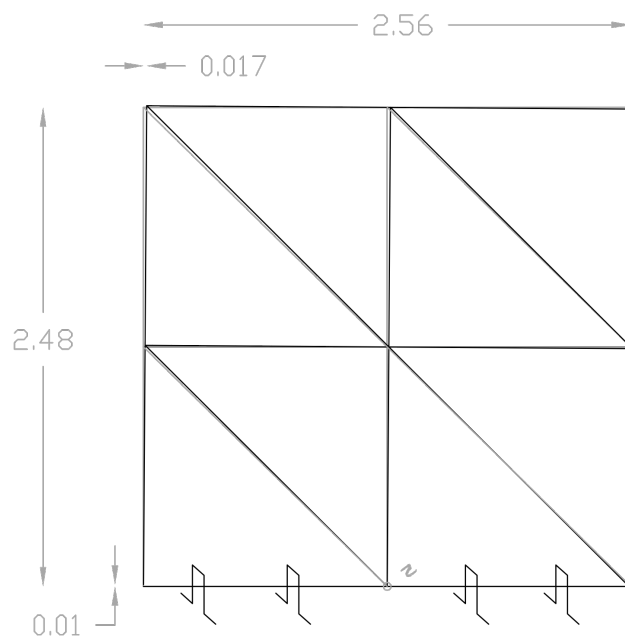


Figure 5-4: Lateral displacements due to equivalent rocking at collapse (units in m)

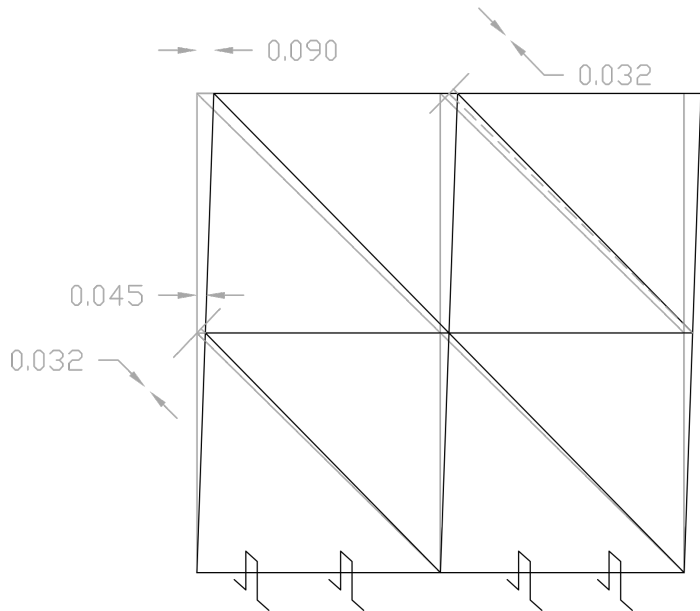


Figure 5-5: Lateral displacements due to equivalent shear at collapse [units in m]

5.4. Masonry filling

The behaviour of the masonry filling when the structure is displaced horizontally was analysed. **Figure 5-6** represents a cross diagonal module (the real size specimen tested is composed of 4 modules) at the displacement around collapse. The module is only distorted, since when the module is rotated the masonry rotates too, but it is not compressed. The original masonry area inside one module was calculated to be 1,036 m². When the panel is distorted the masonry triangles rotate and some of them are compressed. The area of the masonry triangles, which has been compressed, is calculated (in AutoCAD) to be 0.025 m², when the wall was close to collapse. This value is limited to 2.4% of the total masonry area, which is considered to be low, indicating low influence of the masonry filling on the strength of the panel. The undistorted panel is plotted in **Figure 5-6 (a)** and the distorted one in **Figure 5-6 (b)**. The area of the compressed masonry filling is represented by hatching. The red dashed lines are the midsections of the wood elements; the diagonals are light blue and the pink dashed line is the original size of the masonry triangles.

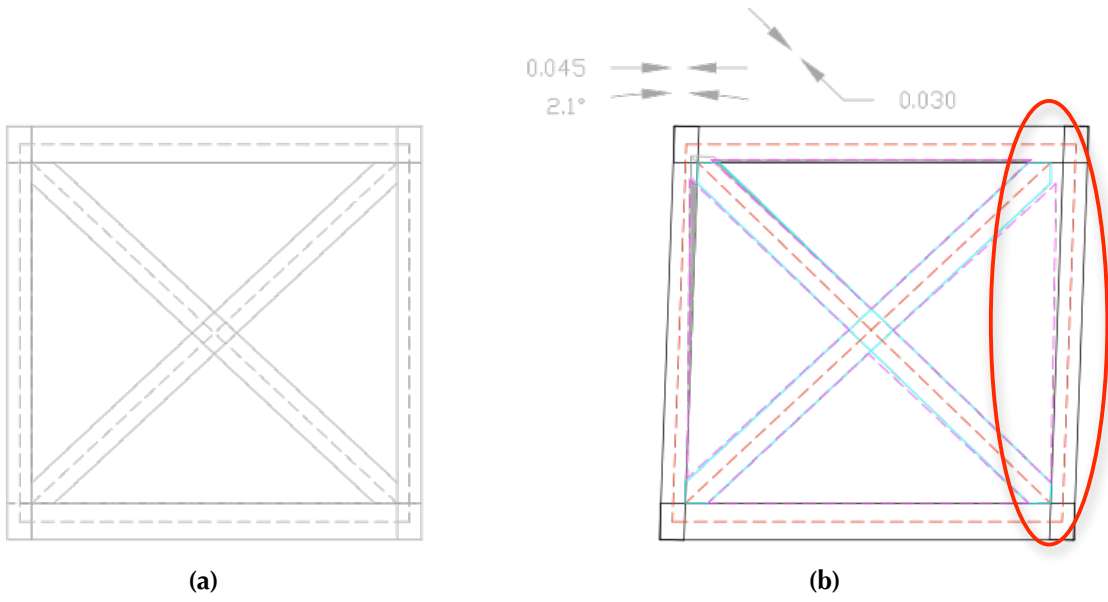


Figure 5-6: (a) Original module (b) distorted module at collapse

Figure 5-6 (b) also shows the detachment of the masonry filling from the vertical timber element on the right and the gap that is formed at the diagonal that is loose. Two aspects can now be pointed out. First, it can be seen that the diagonal, which is not compressed, is not working under tension but is loose, instead. Second, a gap is formed at the top of this diagonal and this will lead to the pinching effect on the structure. These observations are backed up by the experimental tests and can be seen in **Figure 5-7**. The detachment of the masonry filling from the timber frame is shown on the right-hand side. Additionally, it can be seen that a gap opened at the end of the loose diagonal.

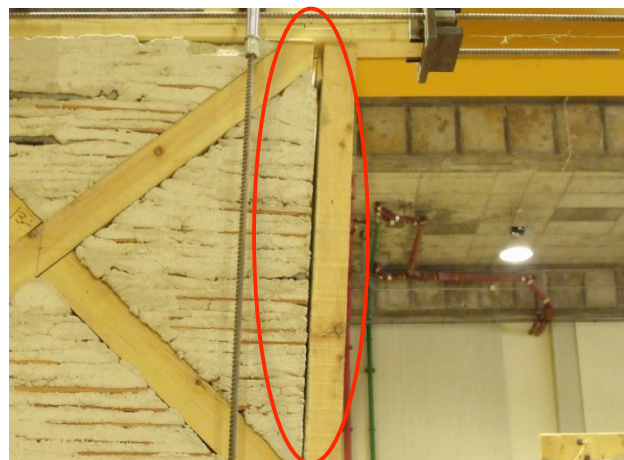


Figure 5-7: Gap between loose diagonal and timber frame and detachment of masonry filling from timber frame

These considerations are valid for the case close to collapse where one has seen that the contribution of the masonry filling is negligible for the strength of the panel. If the case of the very first initial conditions is considered one must assume that the masonry filling plays a not negligible role on the stiffness of the panel. This is because the masonry filling is displayed side by side with the timber. Nevertheless,

the gaps are formed very early in the experimental tests and the masonry filling also detached early from the timber frame.

5.5. Pinching effect

The hysteresis curve for the tested walls showed significant pinching effect. Pinching in a structure is usually related to gaps and residual displacements. One can analyse, as an example, what happens when two members linked by a connector (of any type - nail, screw, rivet, etc.) are cyclically loaded. Let us assume that the connector is rigid and that the material of the members surrounding the connector is being deformed. **Figure 5-8** shows how residual displacements and gaps are formed when the member is pulled and pushed.

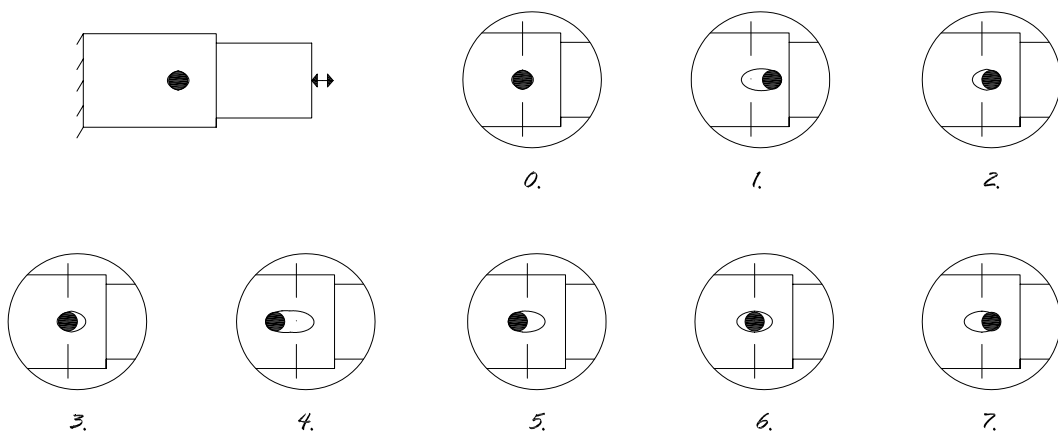


Figure 5-8: Sketch of pinching effect

If the hysteresis curve for this loading was plotted the hysteretic behaviour shown in **Figure 5-9** would be obtained, where the pinching effect is clearly identified. The numbering used in **Figure 5-9**, for the different paths of the curve, represents the numbers in **Figure 5-8**.

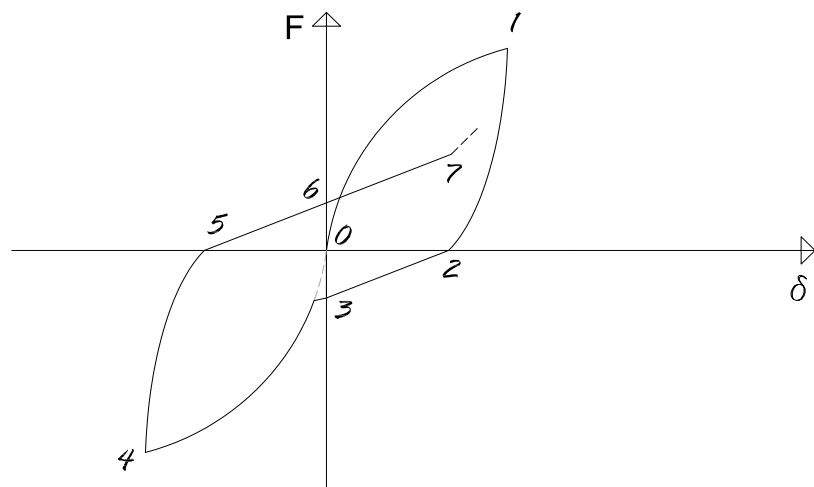


Figure 5-9: Hysteresis behaviour with pinching effect

The pinching effect is explained as follows:

0. Initial positioning of the connector with no gaps.
1. Pulling of the member. The connector compresses the material to the right.
2. The load starts decreasing until zero. The gap narrows but there are residual displacements.
3. Pushing of the member. The connector moves back to the initial position. The load required for this is very low. There is a residual gap at the right.
4. The connector starts compressing the material to the left.
5. The load starts decreasing until zero. The gap narrows but there are residual displacements.
6. Pulling of the member. The connector moves back to the initial position. The load required for this is very low. Two residual gaps can be seen on the right and left.
7. The connector moves until the residual displacement on the right. The stiffness required for this is not the same as the initial stiffness.

A similar effect takes place for the wall panel tested. Gaps are opened between the diagonals and the vertical/horizontal members (see **Figure 5-7**); gaps also appear at the connections of the vertical/horizontal members, which lead to residual displacements, as can be seen in **Figure 5-10**. Another important source of pinching might also be associated with the masonry's attachment to and detachment from the timber frame, as can also be seen in **Figure 5-6 (b)** and **Figure 5-7**.



Figure 5-10: Pull-out of nails leading to gaps and residual displacements; masonry crack

5.6. Proposed macro-element model

The macro-element developed was a non-linear beam with a hysteretic behaviour for the shear response on phenomenological basis. This hysteresis rule developed is defined by 9 independent physical or mathematical parameters and incorporates stiffness and strength degradations and pinching effect. The associated hysteresis rule is developed based on the experimental tests carried out and the parameters are calibrated by such results.

The author has developed in Matlab (see Annex B) a program with the proposed hysteresis model. After this, the proposed model was implemented in a structural software program called TREMURI with programming language Visual Basic. An introduction to the program TREMURI will be given in section 6.2. The whole features of the proposed hysteretic model were incorporated into this software package enabling the performance of static and dynamic nonlinear analyses with this macro-element.

5.6.1. Hysteresis model - Presentation of the model

A hysteresis model was developed based on a minimum number of path-following rules that can reproduce the response of the wall tested under general monotonic, cyclic or earthquake loading. The model was calibrated according to the experimental results obtained. It was constructed using a series of exponential functions and linear functions. This model uses 9 parameters to capture the nonlinear hysteretic response of the wall. **Figure 5-11** shows the assumed load-deformation behaviour of the wall.

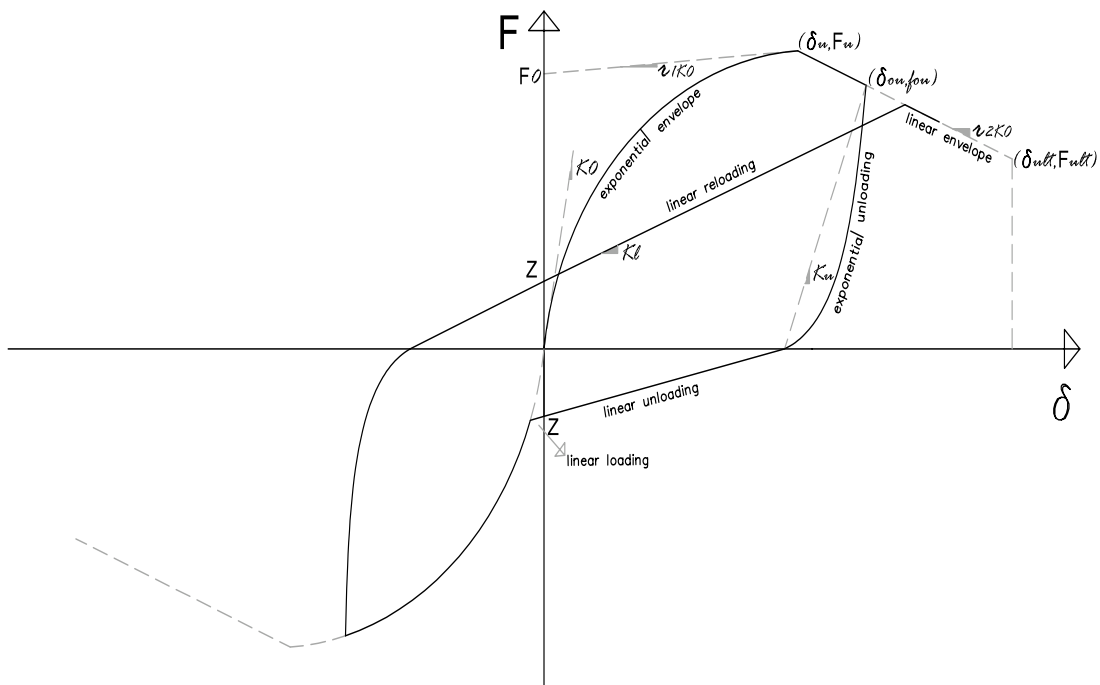


Figure 5-11: Hysteresis model

5.6.2. Path-following rules

The first step for obtaining a hysteresis model is to define the envelope curve. It is assumed that the envelope curve is independent of the loading history and coincides approximately with the load-deformation curve obtained under monotonic loading. Once the envelope is determined the loading and unloading paths must be described. Loading (or reloading) paths are identified as cases where the displacement, δ , and the gradient of the displacement, $\Delta \delta$, both have the same signs ($\delta * \Delta \delta > 0$). In contrast, unloading paths correspond to cases where the displacement and the gradient of the displacement have opposite signs ($\delta * \Delta \delta < 0$).

The path-following rules are such that the structure loaded in the first cycle will draw the envelope curve. It follows an unloading path at a certain point and the loading in the opposite direction. A *linear loading* branch is defined in the model so as to have a transition between the point Z (**Figure 5-11**) and the envelope curve when the structure is loaded in the opposite direction for the first time. The meaning of point Z is explained later. Afterwards, when the structure is loaded again in the initial direction, it will reload with a reloading path, which is not the same as the envelope path. When the structure reloading path reaches the envelope curve it means the structure is being loaded for the first time for those displacements; then, the envelope curve is followed again. Once more, unloading can happen at any point.

The procedures for constructing the envelope, the loading/reloading and unloading curves within the model are discussed in the next sections. For clarity the equations presented in those sections are only for positive displacement of the hysteretic loops. Implementation of these equations for the negative displacement region implies the reversal of the sign for certain variables and the use of an absolute value in others.

5.6.3. Definition of the envelope curves

The monotonic pushover response of the wall is modelled using one exponential and one linear function. The exponential function defines the ascending branch (*exponential envelope*) and the linear function the descending branch (*linear envelope*). The envelope curve is defined by 6 identifiable parameters that must be fitted to experimental data. The parameters, illustrated in **Figure 5-11**, are F_0 , K_0 , r_1 , r_2 , δ_u and δ_{ult} . The respective mathematical functions are in **Equation 5-1**:

$$F = \begin{cases} \left(F_0 + r_1 K_0 \delta \right) \cdot \left(1 - e^{(-K_0/F_0)\delta} \right) & \text{for } \delta \leq \delta_u \quad (a) \\ F_u + r_2 K_0 (\delta - \delta_u) & \text{for } \delta_u \leq \delta \leq \delta_{ult} \quad (b) \\ 0 & \text{for } \delta > \delta_{ult} \quad (c) \end{cases} \quad (\text{Equation 5-1})$$

The exponential function used to describe the ascending branch (Equation 5-1 (a)) was first proposed by Foschi [1974] and later used by Folz and Filiatrault [2001] to model the response of wood shear walls for the CUREE model. Beyond the displacement δ_u , which corresponds to the ultimate load F_u the load-carrying capacity is reduced.

Failure of the wall under monotonic loading occurs at displacement δ_{ult} . It has been assumed the wall's monotonic deformation capacity δ_{ult} is defined as the deformation at which the applied load drops to **80%** of the maximum (ultimate) load F_u that was applied to the specimen. In this case, δ_{ult} is already defined based on r_2 , δ_u and F_u . So, the number of identifiable parameters is reduced to 5.

5.6.4. Definition of the unloading curves

Observation of the hysteretic loops of the walls tested in the present work, and of the walls tested at LNEC [Pompeu Santos, 1997], showed a curved shape unloading branch until the zero force intercept and a relatively linear branch from that point until the zero displacement intercept, Z , was verified. It also reveals a degrading unloading stiffness if one considers this stiffness to be K_u in **Figure 5-12** (K_{u1} to K_{u3}). This degradation is related to the point of the start of the unloading δ_{ou} ; the unloading stiffness is decreasing with increasing values of δ_{ou} . An exponential function that is capable of capturing this fact has been defined. The mathematical formulation is presented in the following **Equation 5-2**:

$$\begin{cases} F = K_u(\delta - \alpha\delta_{ou})e^{\lambda u(\delta - \delta_{ou})} & (a) \\ K_u = \frac{f_{ou}}{\delta_{ou}(1-\alpha)} & (b) \end{cases} \quad (\text{Equation 5-2})$$

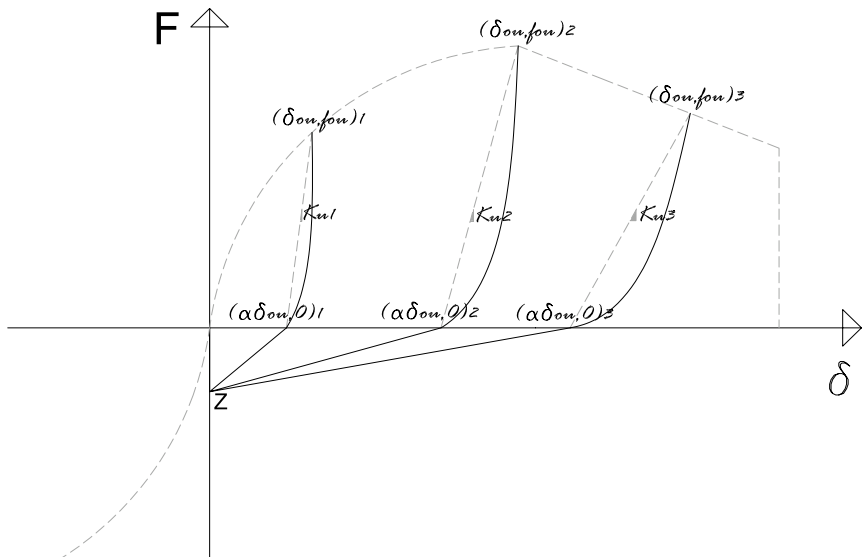


Figure 5-12: Hysteresis model: unloading

The variables δ_{ou} and f_{ou} are the initial unloading displacement and force, respectively. (Equation 5-2 satisfies the boundary conditions $F(\delta = \delta_{ou}) = f_{ou}$ and $F(\delta = \alpha \delta_{ou}) = 0$. The unloading exponential curve requires the knowledge of 2 identifiable parameters α and λ_u , which respectively define the displacement intercept point and the shape of the exponential curve. These two parameters must be calibrated with experimental data. The parameter α is fixed for all the loops or for all values of δ_{ou} ; on the contrary, the parameter λ_u is not constant and will be a function of δ_{ou} , as is explained later. During the unloading process, the variables δ_{ou} and f_{ou} are known and thus are not parameters that need to be defined.

When the unloading starts at point (δ_{ou}, f_{ou}) it will reach the point $(\alpha \delta_{ou}, 0)$. Then, a linear function (*linear unloading*) is defined from this point until the point $(0, Z)$ where the force intercept parameter is called Z . The experimental data shows that the pinched hysteresis loops do not pass exactly through the same force intercept but are very close to it. For simplicity of the model the same force intercept was assumed for all the loops. This parameter, Z , has to be calibrated with experimental data.

5.6.5. Definition of the reloading curves

One important characteristic that could be observed in the response of these walls is the degradation of the restoring force, commonly known as strength degradation. In this situation, it is observed that the reloading curve does not reach the point of maximum displacement (δ_{max}, F) at the envelope curve but instead points to a point that is lower by a certain amount of force (for instance a), see Figure 5-13. As a consequence the stiffness also decreases by a certain amount, or it degrades (stiffness degradation). The strength degradation in the model was estimated by calculating the force reduction parameter a for each level of damage. The damage is assumed to be related to the maximum displacement (or the maximum drift) attained so far and is a variable that is calculated at each loop based on the whole history of the force-displacement response. In this way, a linear reloading curve is drawn from the point Z to the damaged point that remains below the point (δ_{max}, F) . At the beginning of a reloading path the initial point at y -intercept, Z , is known. The force reduction parameter a is calibrated based on the experimental results and is not a fixed parameter since it varies according to the damage built up in the structure.

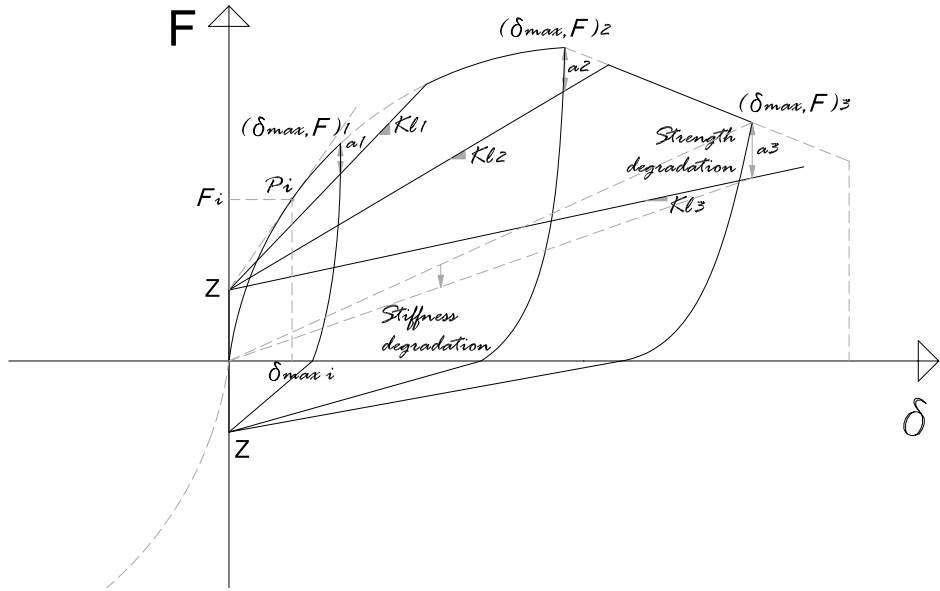


Figure 5-13: Hysteresis model: reloading

Strength degradation is thus estimated directly but stiffness degradation is accounted for indirectly in this modelling technique. In other models, however, strength degradation is accounted for indirectly.

One aspect of this modelling is the fact that for all the lower or equal values of damage associated with displacement at point P_i (δ_{max}^i, F^i) the linear reloading curve will always point to the point P_i and never to a lower value. It can be said that no damage is seen for this point or before it. Point P_i is calculated as the point belonging to the envelope curve and the linear function that starts at Z and is tangential to the envelope curve. This is to prevent the linear reloading curve from having a low derivative for small initial values of displacement when there is no assumed damage, or even to prevent it from having negative derivatives for very small values of displacement (given that the linear reloading curve starts at Z and not at origin). As a consequence, the reloading gradient K_l is constant until the point P_i and then decreases with increasing damage. The formula for determining δ_{max}^i (and thus the point P_i) and rl ($rl*K_0=K_l$) at point P_i is defined in **Equation 5-3**:

$$\begin{cases} F'(\delta_{max}^i) = E'(\delta_{max}^i) \\ F(\delta_{max}^i) = E(\delta_{max}^i) \end{cases} \Leftrightarrow \begin{cases} rlK_0 = r_l K_0 \cdot (1 - e^{-K_0 \delta_{max}^i / F_0}) + (F_0 + r_l K_0 \delta_{max}^i) \cdot K_0 / F_0 \cdot e^{-K_0 \delta_{max}^i / F_0} \\ rlK_0 \delta_{max}^i + Z = (F_0 + r_l K_0 \delta_{max}^i) \cdot (1 - e^{-K_0 \delta_{max}^i / F_0}) \end{cases}$$

$$\Leftrightarrow \begin{cases} rl = \dots \\ \delta_{max}^i = \dots \end{cases}$$

(Equation 5-3)

Where $F(\delta)$ and $E(\delta)$ are, respectively, the linear curve that goes from Z to P_i and the exponential envelope curve.

5.6.6. Small cycle hysteresis

The rules previously described define complete loops, which are loops that undergo complete unloading. In order to have a more general model, one that could be subjected to any type of loading, and not restricted to cyclic loading, one also needs to account for situations where reloading can happen at any place during the loading/unloading history. This leads to small cycle or incomplete cycle hysteresis. Crisafulli [1997] focused on the issue of incomplete cycle hysteresis when related to concrete elements and conducted tests on standard concrete cylinders with different combinations of complete and incomplete loops. The most important conclusions drawn herein were that the successive inner loops do not affect the plastic deformation and remain inside the cycle defined for the complete unloading and reloading curves. This is shown in **Figure 5-14**:

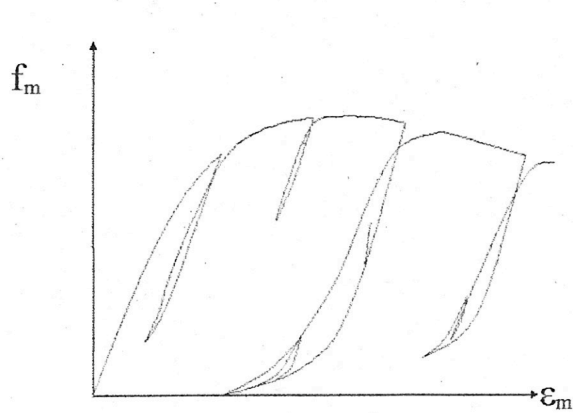


Figure 5-14: Typical cyclic response with small cycle hysteresis for concrete [Crisafulli, 1997]

In the proposed model herein defined, because of the lack of any other information or data, it was simply assumed that the structure would reload with a linear branch (*linear reloading small cycle*) until it would reach the previously defined *linear reloading* branch. This would happen both if the reloading would take place at the *exponential unloading* branch or at the *linear unloading* branch. The new linear branch defined has the derivative K_0 , equal to the initial stiffness. **Figure 5-15** shows these assumptions.

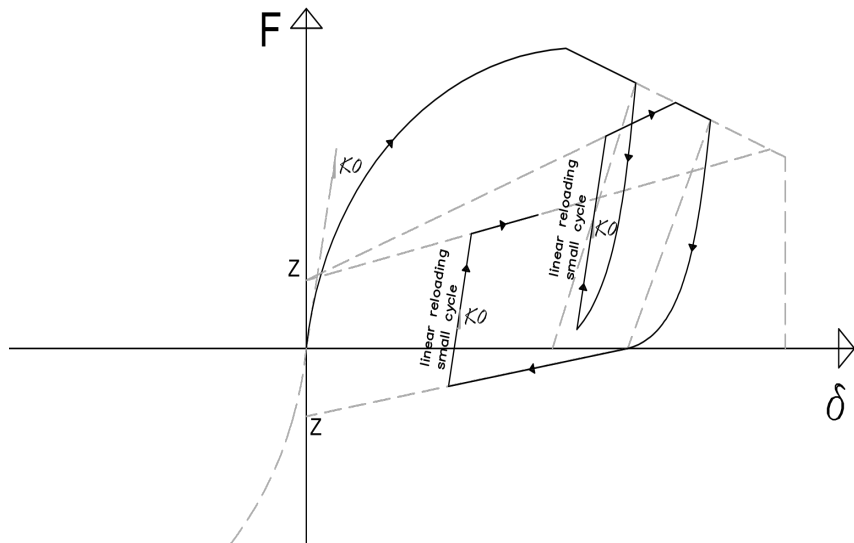


Figure 5-15: Model assumptions for the small cycle hysteresis

5.7. Calibration of the parameters

The parameters associated with the hysteresis model must be fitted to experimental data. This can be accomplished by least-square regression of the functions or by the averaging of point parameters. Given the fact that experimental test SC1 failed by cracking of the wood elements at the connections different from the failure mode of experiments SC2 and SC3 and that the failure mode of SC1 is not expected to happen in reality, it was decided that the parameters of the hysteresis model should only be calibrated for experiments SC2 and SC3. Moreover, by looking at [Figure 4-42](#) it is clear that the envelope curve of experiment SC1 is quite different from the other two (SC2 and SC3). Nevertheless, by doing so we are reducing the number of tests to be used to calibrate the model. The author is aware of the limitation involved in the reduced number of tests to be used to calibrate the model. On the other hand, it would not be possible to use the 1997 LNEC tests to calibrate the model since the specimens tested are different in height (they have 3x2 modules while the tested ones herein have 2x2 modules).

5.7.1. Force intercept parameter - Z

The force intercept parameter is called Z. For simplicity of the model the same force intercept for all the loops was assumed, which is not far away from reality. Based on the experimental data one can plot all the force intercepts, be they positive or negative, and obtain the average point Z. [Figure 5-16](#) shows all the force intercepts and the average value obtained for Z ($Z=10.16$ KN with a standard deviation of 3.65).

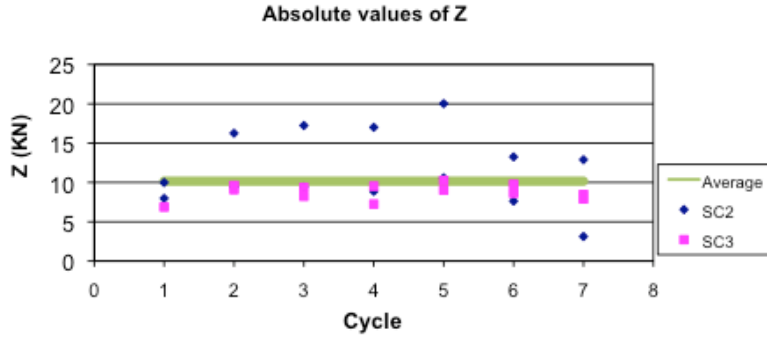


Figure 5-16: Average force intercept point Z

5.7.2. Envelope curve parameters - F_0 , K_0 , r_1 , r_2 , F_u , δ_{ult}

The values obtained for the envelope curve parameters can be seen in **Table 5-1**.

Table 5-1: Envelope curve parameters

F_0 (kN)	37.0
r_1	0.04
K_0 (kN/mm)	6.1
r_2	-0.045
F_u (kN)	50.8
δ_{ult} (mm)	93.71 (3.8% drift)

As explained before, failure of the wall under monotonic loading occurs at displacement δ_{ult} . It has been assumed the monotonic deformation capacity of the wall, δ_{ult} , is defined as the deformation at which the applied load drops to **80%** of the maximum (ultimate) load F_u that was applied to the specimen. Therefore, δ_{ult} is already defined based on r_2 , δ_u and F_u . This corresponds to a ultimate drift of 3.8%. Accordingly, the couple values of (F_u , δ_u) and (F_{ult} , δ_{ult}) are the following depicted in Table 5-2.

Table 5-2: Couple values of (F_u , δ_u) and (F_{ult} , δ_{ult})

δ_u (mm)	F_u (kN)	δ_{ult} (mm)	F_{ult} (kN)
56.68	50.8	93.71	40.7

The value of K_0 has been taken from the experimental initial stiffness at a displacement of 3 mm. The average value as been assumed based on the SC2 and SC3 test results. The values of F_0 and r_1 have been determined by least-square regression of the function *envelope exponential*. **Figure 5-17** shows the *exponential envelope* curve for the calibrated parameters and the corresponding experimental points for both negative and positive loading. Here it can be seen how well the obtained analytical *exponential envelope* curve fits the experimental envelope points.

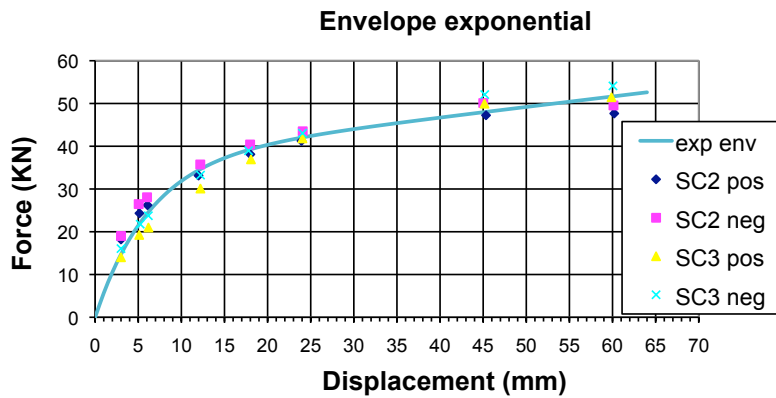


Figure 5-17: Analytical *exponential envelope* curve and experimental points

The value of r_2 has been calculated by least-square regression of the function *envelope linear*. **Figure 5-18** shows the *linear envelope* curve for the calibrated parameter, r_2 , and the corresponding experimental points for both negative and positive loading. Here, it can be seen how well the analytical linear envelope curve fits the experimental envelope points.

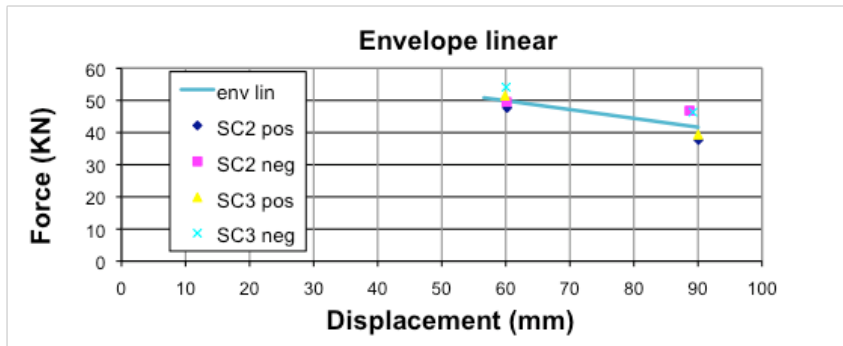


Figure 5-18: Analytical *linear envelope* curve and experimental points

5.7.3. Unloading curve parameters - α , λ_u

The value of α is taken as the average of all the obtained experimental values of α for positive or negative displacements. The value of α is estimated at 0.55 with a standard deviation of 0.11. The plot of **Figure 5-19** shows the values of α as a function of the experimental unloading points δ_{ou} . Here, it can be seen how well the value of α fits the experimentally obtained points.

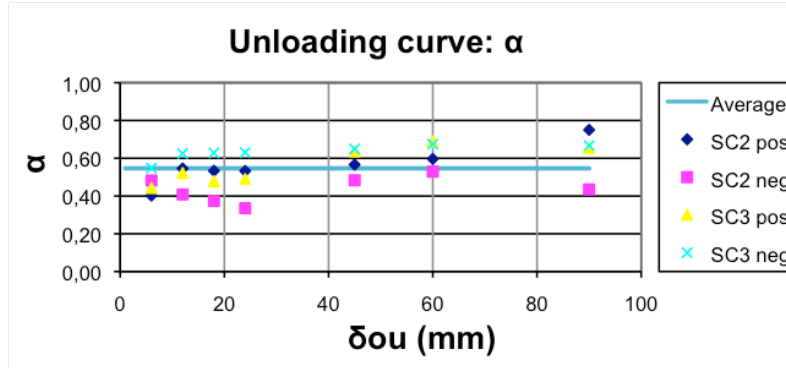


Figure 5-19: Unloading curve parameter α

The value of λ_u is the one defining the shape of the unloading exponential curve, as has been mentioned previously. The plot of the values of λ_u as a function of the unloading point δ_{ou} is shown in the **Figure 5-20**. Based on these results, it has been decided that the parameter λ_u cannot be a constant value but is better approximated by a logarithmic function dependent of δ_{ou} . The equation for λ_u as a function of δ_{ou} is given by **Equation 5-4**:

$$\lambda_u = -0.087 \ln(\delta_{ou}) + 0.4593 \quad (\text{Equation 5-4})$$

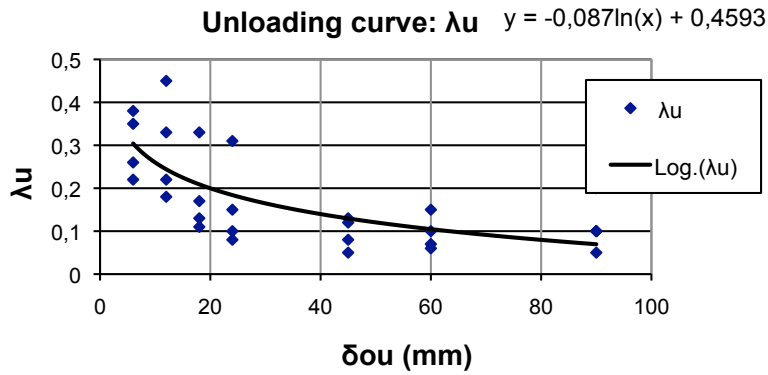


Figure 5-20: Unloading curve parameter λ_u

5.7.4. Reloading curve parameter - a

In the defined model, the strength degradation was estimated by calculating the force reduction parameter a for each level of damage. **Figure 5-21** depicts the experimentally obtained values of a as a function of the maximum drift obtained so far. Here the damage of the wall is associated with the inter-storey drift of the wall. Inter-story drift is a key parameter for the control of damage in wood framed buildings [Filiatruau, 2002]. In **Figure 5-21**, the linear approximation by least-square regression is also presented for the parameter a . The equation of a as a function of

the damage (maximum drift, Δx) of the wall is obtained approximately by means of **Equation 5-5**:

$$a = 5.06 * \Delta x \quad (\text{Equation 5-5})$$

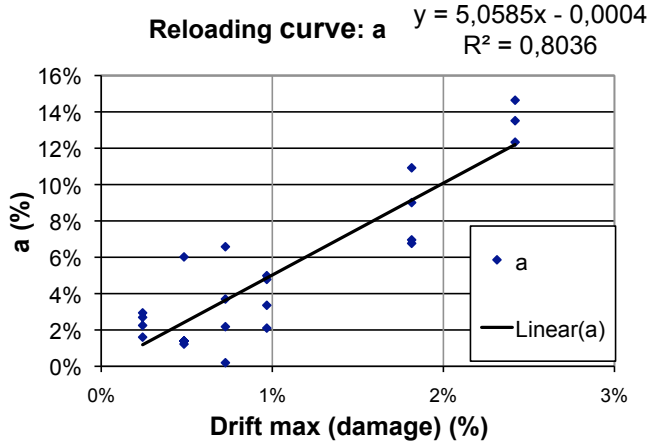


Figure 5-21: Parameter a as a function of the damage

As a consequence, it is possible to calculate the reloading stiffness K_l (or the corresponding coefficient $r_l = K_l/K_0$). As has been explained previously, the reloading stiffness K_l (or the corresponding coefficient r_l) is constant until the point P_i . In the following plot of **Figure 5-22** the reloading curve coefficient, r_l , is presented as a function of the damage (or the maximum drift). Here r_l at point P_i equals 0.375 (and the displacement, δ^i , at point P_i equals 6.5 mm). The values of r_l end for the maximum drift established of 3.8% associated with the collapse of the wall.

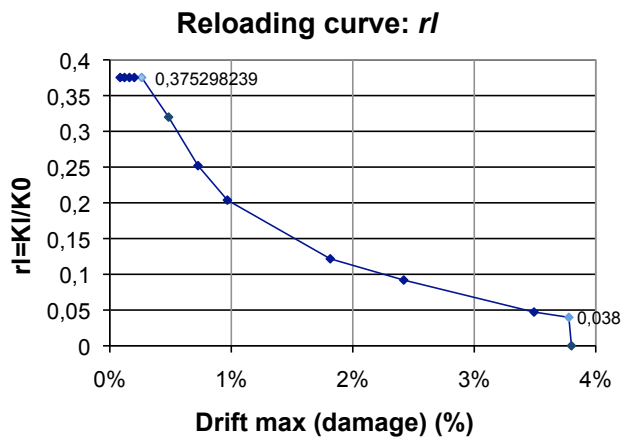


Figure 5-22: Reloading curve coefficient r_l as a function of damage

5.8. Experimental versus analytical hysteresis

A plot has been drawn for comparison of the hysteresis curves obtained experimentally and the hysteresis curve developed analytically. A good matching is obtained as can be seen in **Figure 5-23**.

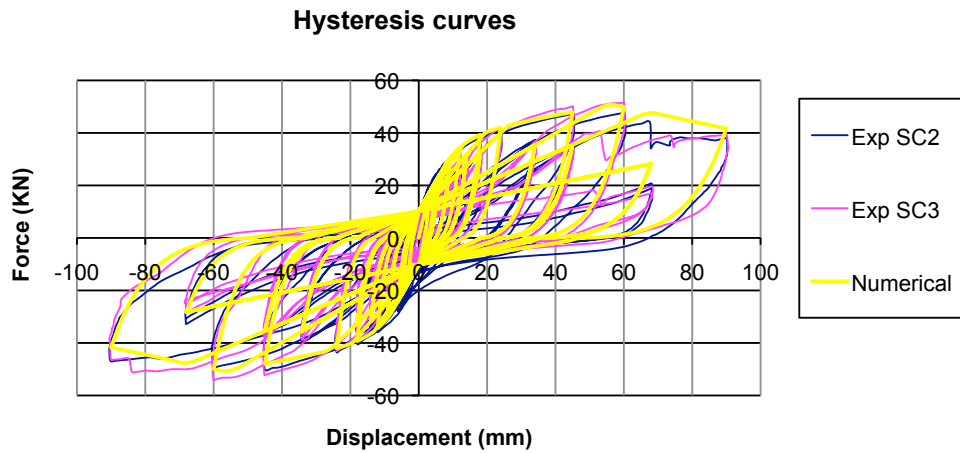


Figure 5-23: Experimental versus analytical hysteresis

The accuracy of the model response is determined using one error indicator, which is the cumulative energy error (CEE). The CEE is defined in **Equation 5-6**:

$$CEE = \frac{|CE_{test} - CE_{anal}|}{|CE_{test}|} \quad (\text{Equation 5-6})$$

Where CE_{test} and CE_{anal} are the cumulative energy dissipation of the hysteresis of the experimental testing and of the analytical model, respectively.

The total percentage error in cumulative energy dissipated between the fitted model and the actual cyclic test data is 9% for the test SC2 and 14% for the test SC3, indicating a good match between the analytical model and the experimental results.

5.9. Examples of hysteretic model responses for different input loading

In the following figures one can see examples of the responses of the developed hysteretic model for a given input loading. Some comments are presented for each test.

Test 1

Figure 5-24 shows the input loading for test 1. **Figure 5-25** shows the respective model response.

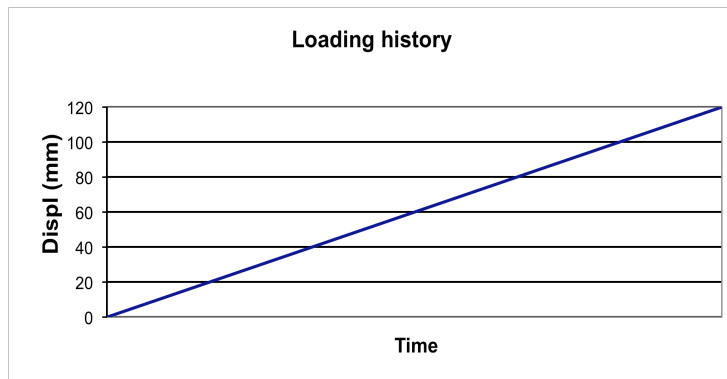


Figure 5-24: Input loading for test 1

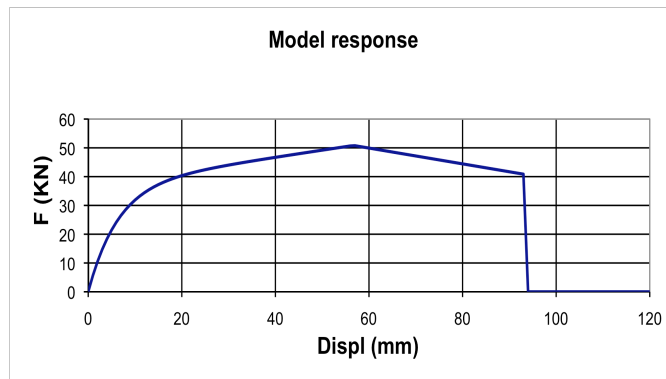


Figure 5-25: Model response for test 1

The model outputs the envelope curve for positive displacement history.

Test 2

Figure 5-26 shows the input loading for test 2. **Figure 5-27** shows the respective model response.

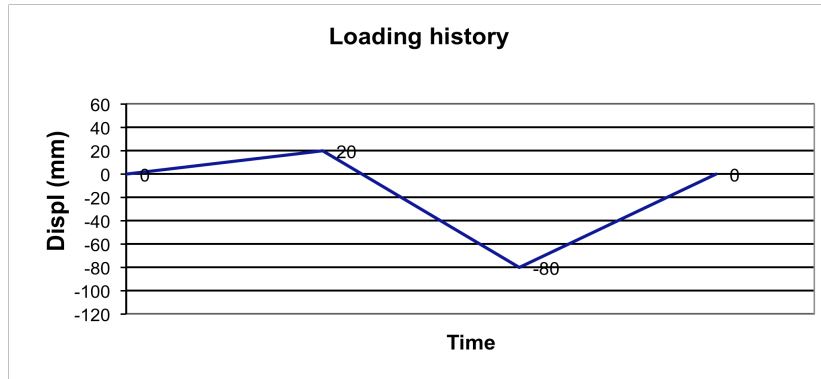


Figure 5-26: Input loading for test 2

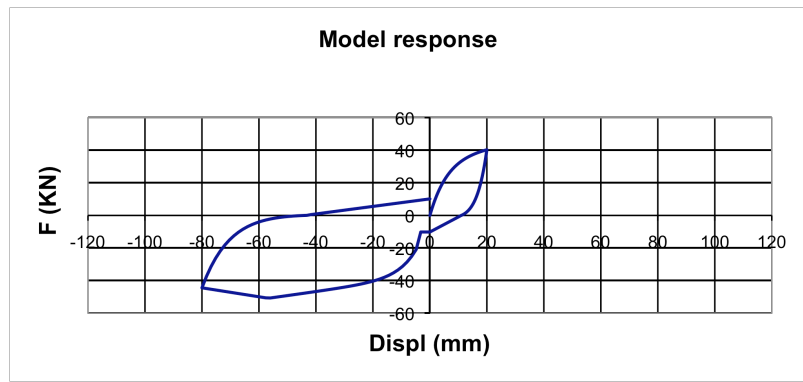


Figure 5-27: Model response for test 2

The first cycle for positive and negative displacements follows the envelope; unloading at different displacements presents different unloading stiffness, K_u .

Test 3

Figure 5-28 shows the input loading for test 3. **Figure 5-29** shows the respective model response.

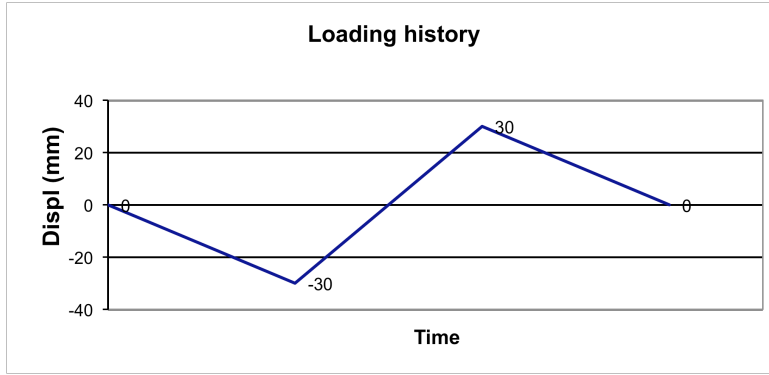


Figure 5-28: Input loading for test 3

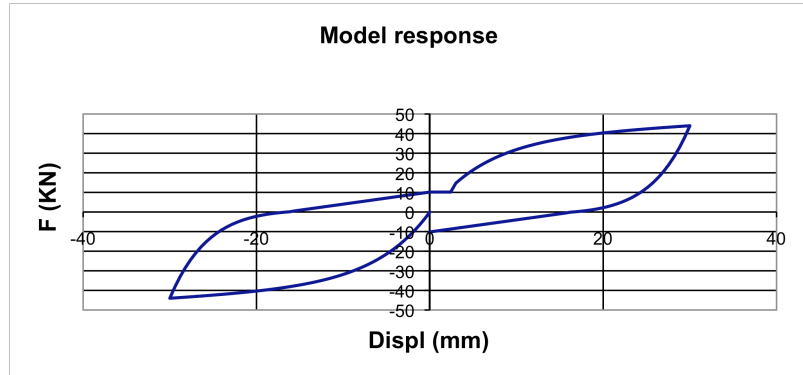


Figure 5-29: Model response for test 3

The loading starts for negative displacements, so the *linear loading* is seen in the positive axis.

Test 4

Figure 5-30 shows the input loading for test 4. **Figure 5-31** shows the respective model response.

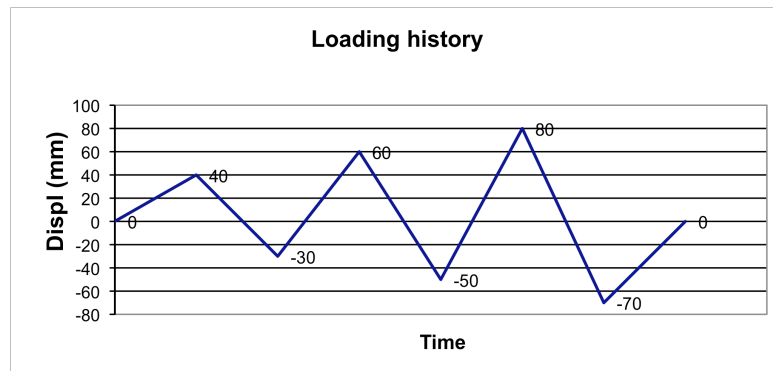


Figure 5-30: Input loading for test 4

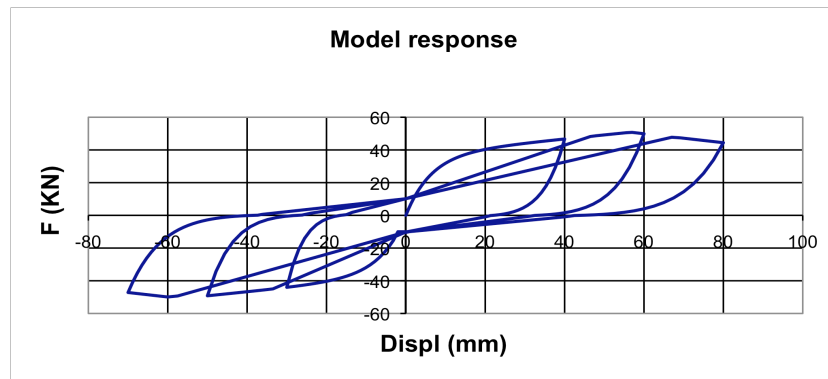


Figure 5-31: Model response for test 4

The reloading curves are seen for different levels of damage. The damage for positive displacements is independent from the damage for negative displacements (negative displacements happen when the structure is loaded in the opposite direction).

Test 5

Figure 5-32 shows the input loading for test 5. **Figure 5-33** shows the respective model response.

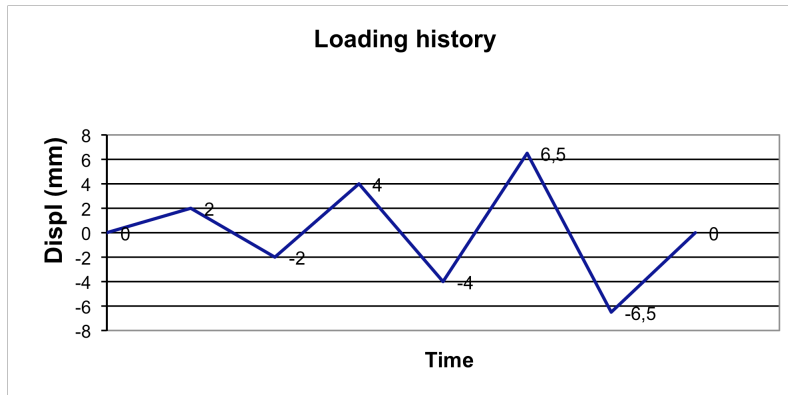


Figure 5-32: Input loading for test 5

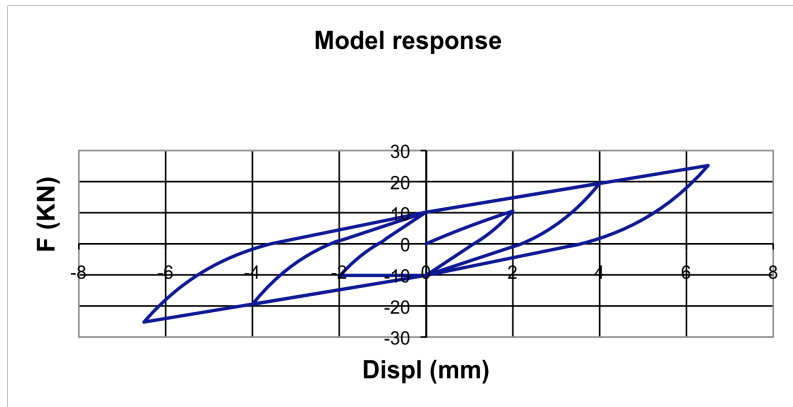


Figure 5-33: Model response for test 5

Behaviour of the hysteresis model for small displacement cycles when the first loading loop has a displacement smaller than δ_i (6.5 mm), which is the displacement corresponding to point P_i already mentioned.

5.10. Other configurations of walls

5.10.1. Experimental initial stiffness estimation

The initial stiffness was estimated experimentally at 3 mm displacement of the loaded wall. **Table 5-3** shows the values of the positive and negative loading force at the cycle displacement of 3 mm.

Table 5-3: Positive and negative loading force at 3mm displacement for all the tests

Tests	Positive loading force at 3 mm (kN)	Negative loading force at 3 mm (kN)
SC1	20.83	-22.40
SC2	18.20	-19.01
SC3	14.03	-16.06

The value obtained experimentally for the initial stiffness is the average of all the tests (SC1, SC2 and SC3) and is $K_0 = 6.1 \text{ KN/mm}$.

5.10.2. Analytical modelling of the wall

An analytical model of the wall was performed in SAP 2000 [1998] in order to obtain a valid structural model that could predict the behaviour of the wall in its linear stage (i.e. in order to predict the initial stiffness). The model was calibrated according to the initial stiffness obtained. The analytical model has the following properties:

- a) The diagonals of the wall are not able to work under tension (only compression)
- b) Shell elements were used to model the masonry
- c) Pinned connections were used at the nodes
- d) Rigid links were used to connect the shell elements of the masonry to the diagonals in order to simulate the thickness of the diagonals
- e) At the supports, springs were used to simulate the effect of rigid body movement (the mentioned equivalent rocking)
- f) Vertical loads applied were matching the ones from the experimental testing

Figure 5-34 shows the mentioned analytical model:

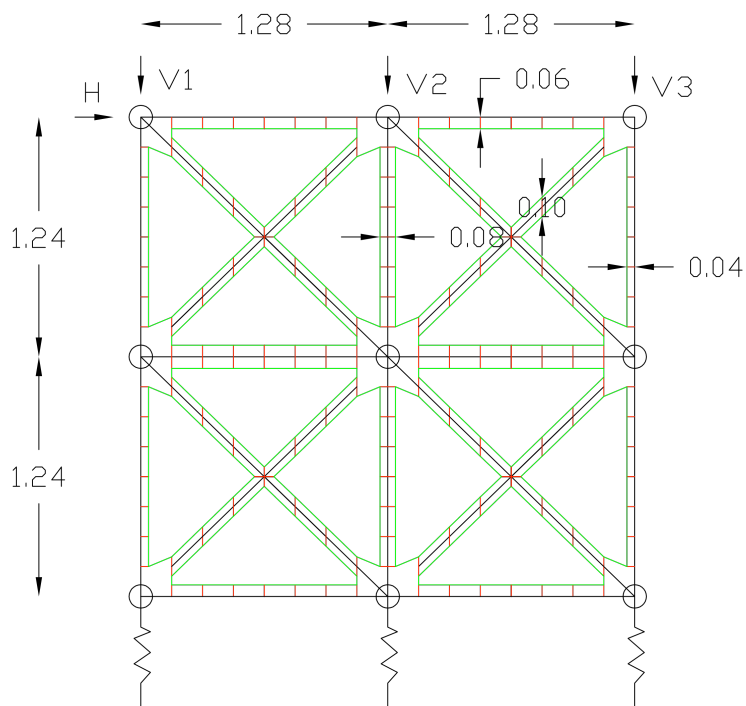


Figure 5-34: Analytical model adopted for estimating initial stiffness (units in meters)

In the sketch of **Figure 5-34**, the green lines define the areas of the masonry shell elements; the red lines define the rigid links adopted and the black lines define the timber elements. It can be seen how the timber elements are not connected to the pinned nodes in one direction; this is to simulate the fact that these elements do not work under tension. In the figure, H is the horizontal force applied and $V1$, $V2$ and $V3$ are the vertical forces applied. The springs at the supports are depicted. The

springs are modelling the effect of rigid body movement while the wall was being tested. Has seen in section 5.3. the nailed connections at the bottom are moving upwards and downwards and this constitutes the rigid body movement. Note that the bottom horizontal wood beam is very well fixed to the horizontal steel reaction beam of the experimental apparatus so the rigid body movement only comes from the displacement of the nailed connections. The springs are calibrated in order that the model matches the initial experimental stiffness of the walls tested. To be noticed that one could assume that the calibrated spring stiffness is the same regardless the panel configuration, i.e., the same one of panel 2x2 for panels 3x2 or 2x4, since the spring is representing a nailed connection and these are the same for all the panels. Additionally, it has been assumed in this work that the tension stiffness of the connection is the same as the compression stiffness of the connection and represented by the same spring. In lack of any other data this assumption was simpler; nevertheless, one could have assumed different stiffnesses in the connection under tension and compression.

The mechanical properties of the wood and masonry assumed for the analytical model of the wall are based on the following discussion.

In relation to the wood, the wood species *Pinus Pinaster* (*Pinho Bravo Ait.*) was used. The national laboratory for civil engineering (LNEC) published a norm [Pinho bravo para estruturas, 1997] where information about physical properties, mechanical and durability issues are gathered for the purpose of using this specie for structural use. Here only Portuguese *Pinus Pinaster* was adopted for the tests carried out over a decade! **Table 5-4** presents the mechanical properties of the wood according to the results obtained in LNEC for quality classes E and EE. The quality class is assigned based on the Portuguese norm NP4305 [1995]. The pine used belongs to quality class E.

Table 5-4:Mechanical properties of wood according to LNEC

Mechanical properties		Quality class	
Characteristic (k) or mean (mean) values		EE	E
Bending strength (MPa)	$f_{m,k}$	35	18
Tensile strength parallel to grain (MPa)	$f_{t,0,k}$	21	10.8
Tensile strength perpendicular to grain (MPa)	$f_{t,90,k}$	0.49	0.46
Compression strength parallel to grain (MPa)	$f_{c,0,k}$	24.7	18
Compression strength perpendicular to grain (MPa)	$f_{c,90,k}$	7.3	6.9
Shear strength (MPa)	$f_{v,k}$	3.4	2.0
Modulus of elasticity parallel to grain (GPa) (Characteristic value)	E_{mean}	14	12
	$E_{0,05}$	9.38	8.0
Modulus of elasticity perpendicular to grain (GPa)	$E_{90,\text{mean}}$	0.46	0.4
Shear modulus, mean (GPa)	G_{mean}	0.87	0.75
Density, mean (kg/m ³)	ρ_{mean}	610	580
Density, characteristic value (kg/m ³)	ρ_k	490	460

Nevertheless, for the quality class E (NP 4305), the *Pinus Pinaster Ait.* is classified into the strength class C18 of the European norm EN338 [2003]. **Table 5-5** shows the mechanical properties associated with such a class.

Table 5-5: Mechanical properties of wood according to European norm

Poplar and softwood species		C18
Strength properties (MPa)		
Bending	$f_{m,k}$	18
Tension parallel	$f_{t,0,k}$	11
Tension perpendicular	$f_{t,90,k}$	0.5
Compression parallel	$f_{c,0,k}$	18
Compression perpendicular	$f_{c,90,k}$	2.2
Shear	$f_{v,k}$	2
Stiffness properties (GPa)		
Mean modulus of elasticity parallel	E_{mean}	9
5% modulus of elasticity parallel	$E_{0,05}$	6
Mean modulus of elasticity perpendicular	$E_{90,mean}$	0.3
Mean shear modulus	G_{mean}	0.56
Mean density (kg/m ³)	ρ_{mean}	380
Density, characteristic value (kg/m ³)	ρ_k	320

One can see how the values obtained in the two tables are almost identical for the strength properties. With respect to the stiffness properties there are some discrepancies in that these values are higher for the first table, where only Portuguese *Pinus Pinaster* was tested. The same happens with respect to the density. These values are marked in bold in both tables.

It was decided that the properties of the timber given by LNEC's norm, Pinho bravo para estruturas [1997] be used, since these were tested only on Portuguese timber. In this way **Table 5-6** shows the values adopted for the mechanical properties of wood.

Table 5-6: Mechanical properties adopted for wood

Mechanical property	Value	Reference
E_{wood} (MPa)	12000	LNEC [1997]
ρ_{wood} (kg/m ³)	580	LNEC [1997]
v	0.2	Technical Tables [1998]

With respect to the masonry, in Carvalho [2007] was carried out some testing on cylinder specimen of hydraulic mortar. The relation lime/sand is 1/3, the same as the one used in the experimental testing of the *Pombalino* "frontal" walls. Within the tests it was calculated the properties of 770 MPa at 195 days for the Young's modulus (E) at 1/3 of failure. This value can be used for the modelling of the masonry used in the *Pombalino* "frontal" walls although the masonry here is not only hydraulic mortar but is composed of a mixture of hydraulic mortar with broken bricks and tiles.

The value for the Poisson ratio, v, is assumed to be 0.2 for the masonry; being 0.3 for natural stone [Technical Tables, 1998]. Then, the values adopted here for the mechanical properties of masonry are presented in **Table 5-7**:

Table 5-7: Mechanical properties adopted for masonry

Mechanical property	Value	Reference
$E_{masonry}$ (MPa)	770	Carvalho [2007]
$\rho_{masonry}$ (KN/m ³)	22	Technical Tables [1998]
v	0.2	Technical Tables [1998]

The results obtained in SAP 2000 for the calculation of the initial stiffness are showed as followed. For finding the appropriate spring stiffness, 3 spring stiffnesses were tried – 6000, 10 000 and 15 000 KN/m. The horizontal displacement of nodes (Na), (Nb) and (Nc), (see Figure 4-13 for the positioning of the nodes), and the vertical displacements of nodes (Ng), (Nh) and (Ni) are presented in Table 5-8, Table 5-9 and Table 5-10. The loads applied are H=30 kN; V1&V3=19.2 kN and V2=38.4 kN.

Table 5-8: Results for spring stiffness of 6 000 KN/m. (results in mm)

Kspring (KN/m) 6000						
	(Na)	(Nb)	(Nc)	(Ng)	(Nh)	(Ni)
Load case	Horizontal Displacement			Vertical Displacement		
Dead	-0.23	-0.23	-0.21	-4.25	-4.30	-4.25
Horiz	10.48	10.48	10.55	4.84	0.00	-4.85

Table 5-9: Results for spring stiffness of 10 000 KN/m. (results in mm)

Kspring (KN/m) 10000						
	(Na)	(Nb)	(Nc)	(Ng)	(Nh)	(Ni)
Load case	Horizontal Displacement			Vertical Displacement		
Dead	-0.23	-0.23	-0.21	-2.54	-2.60	-2.50
Horiz	6.70	6.70	6.80	2.90	0.00	-2.90

Table 5-10: Results for spring stiffness of 15 000 KN/m (results in mm)

Kspring (KN/m) 15000						
	(Na)	(Nb)	(Nc)	(Ng)	(Nh)	(Ni)
Load case	Horizontal Displacement			Vertical Displacement		
Dead	-0.23	-0.23	-0.21	-1.69	-1.74	-1.69
Horiz	4.85	4.85	4.92	1.93	0.00	-1.94

A comparison was made between the analytical model with springs at supports - C2x2 and without springs at supports - C2x2_nospr. The condensed results for finding the best spring stiffness are shown in Table 5-11.

Table 5-11: Ratio of analytical over experimental stiffness for different spring stiffness

Model	V1,V3 (KN)	V2 (KN)	H (KN)	K _{spring} (KN/m)	Top horiz displ(mm)	K _{anal} (KN/mm)	K _{anal} /K _{exp}
C2x2_nospr	19.2	38.4	30	-	1.2	25	4.1
C2x2	19.2	38.4	30	6000	10.3	2.9	0.5
C2x2	19.2	38.4	30	10000	6.5	4.6	0.8
C2x2	19.2	38.4	30	15000	4.6	6.4	1.0

In the table, K_{anal} is the analytical estimation of initial stiffness and K_{exp} is the experimental value of initial stiffness. It can be seen in the table that the spring stiffness that makes the model have an initial stiffness equal to the experimentally obtained stiffness is the last row of numbers with $K_{\text{spring}} = 15000 \text{ KN/m}$. This is the spring stiffness used for the subsequent models.

5.10.3. Initial stiffness for other configurations of walls and for other Young's modulus

The main purpose of this section is to estimate the initial stiffness for other configurations of walls and also for another Young's modulus (this could represent the case where a different wood species would be used). **Figure 5-35** shows the configurations of walls studied. These configurations are present throughout the buildings as has been mentioned previously.

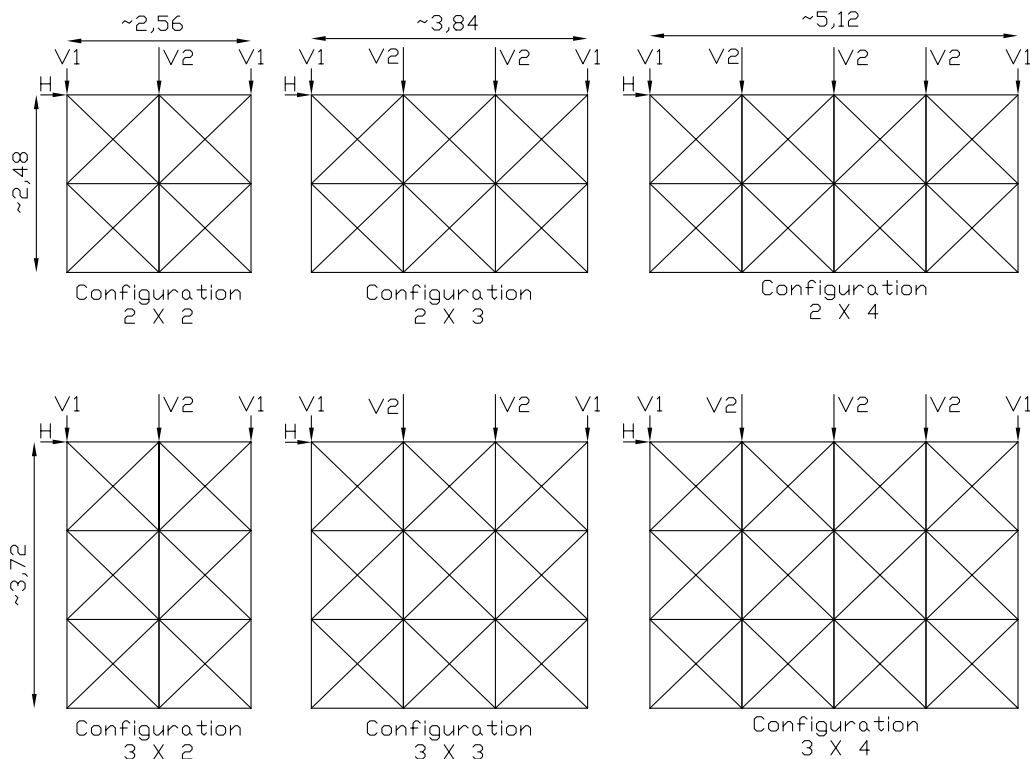


Figure 5-35: Configurations of walls studied

The configuration 2x2 is the configuration that has been tested in the laboratory in the present work; the configuration 3x2 is the configuration tested in the laboratory of LNEC in 1997 [Pompeu Santos, 1997]. The others are possible existing configurations. **Table 5-12** shows the values obtained analytically (K_{anal}) for the initial stiffness of the different configurations of walls and for different values of the Young's modulus of wood (E_{wood}). For each model configuration, three different values of E_{wood} were analysed: 6000 MPa; 12000 MPa and 20000 MPa. The structural models used are the same as the previously presented model for configuration 2x2.

Table 5-12: Initial stiffness for different configurations of walls and different modulus of elasticity of wood

Model Configuration	V1 (KN)	V2 (KN)	Horizontal Force (KN)	$E_{masonry}$ (MPa)	E_{wood} (MPa)	Top horiz displ (mm)	K_{anal} (KN/mm)
2x2	19.2	38.4	30	770	6000	5.2	5.7
2x2					12000	4.6	6.4
2x2					20000	4.3	7.0
2x3	19.2	38.4	30	770	6000	2.2	13.6
2x3					12000	1.9	15.8
2x3					20000	1.8	16.7
2x4	19.2	38.4	30	770	6000	1.1	27.2
2x4					12000	0.9	33.3
2x4					20000	0.8	37.5
3x2	19.2	38.4	30	770	6000	11.7	2.6
3x2					12000	10.3	2.9
3x2					20000	9.6	3.1
3x3	19.2	38.4	30	770	6000	6.9	4.3
3x3					12000	4.4	6.8
3x3					20000	4.0	7.5
3x4	19.2	38.4	30	770	6000	2.6	11.5
3x4					12000	2.2	13.6
3x4					20000	2.0	15.0

As can be seen from **Table 5-12**, the stiffness of the modelled configurations increases for increasing values of E_{wood} , which is expected. One can also see that configuration 3x2 is the one with the lowest stiffness while configuration 2x4 is the one with the highest stiffness. Moreover, increasing the height of the wall makes the structure more flexible (lowers the stiffness) and increasing its length makes the structure more rigid (increases its stiffness), as expected.

5.10.4. Strength associated with collapse of most loaded diagonal

At this stage, it was estimated the compression force (strength) on the most loaded diagonal of the tested configuration 2x2. The idea is afterwards to estimate the strength associated with the collapse of the most loaded diagonal on other configurations of walls. The structural models developed in SAP 2000 [1998] for determining the most loaded diagonal are simple trusses with springs at the bottom and pinned connections at member ends (**Figure 5-36**). In this way, the contribution of the masonry at maximum strength is neglected. At this stage it is extensively detached from the truss elements and considerably cracked at some locations, as has been discussed before. The stiffness of the spring is the same as previously estimated.

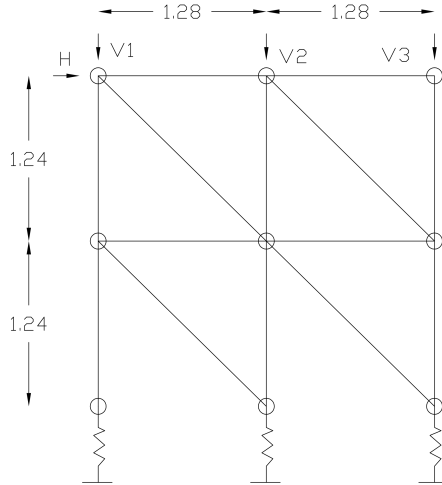


Figure 5-36: Analytical/structural model adopted for estimating collapse load

The distribution of the forces on the structure (axial forces on the truss) per unit loads (vertical and horizontal) is presented in **Figure 5-37**.

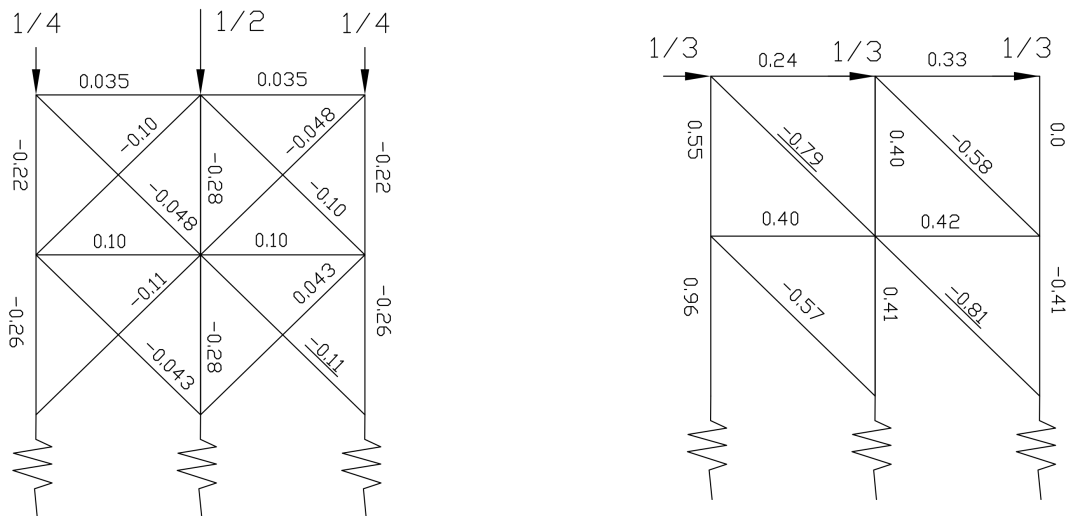


Figure 5-37: Axial forces in members for wall being loaded with unit loads ($E_{wood}=12\ 000$ MPa, configuration 2x2)

For the loads applied at the experimental tests carried out at the current work, it was obtained the following results (see **Table 5-13** and **Equation 5-7**) for the axial force acting in the most loaded diagonal, $F_{diagonal}$, (in this case the average of the two most loaded diagonals with values 0.79 and 0.81- average 0.80 was taken). The value of F_u (kN) is obtained from experiments SC2 and SC3 and is the maximum horizontal force associated with these experiments (strength).

Table 5-13: Axial force acting on the most loaded diagonal

Configuration	$F_{vertical}$ (kN)	Factor F_v	F_u (kN)	Factor F_u	$F_{diagonal}$ (kN)
C2x2	76.8	-0.11	50.8	-0.80	-49.09

$$F_{\text{diagonal}} = -0.11 \times 76.8 - 0.80 \times 50.8 = -49.09 \text{ KN}$$

(Equation 5-7)

This value obtained of **-49.09** kN is the force at the most loaded diagonal when the structure attains its maximum strength of F_u .

As a comment one can say that the distribution of loads on the structure depends very little on the values of E_{wood} – wood Young's modulus, therefore one would neglect this factor. For instance if one changes the value of E_{wood} to 6000 MPa one has the distribution of loads presented in **Figure 5-38**.

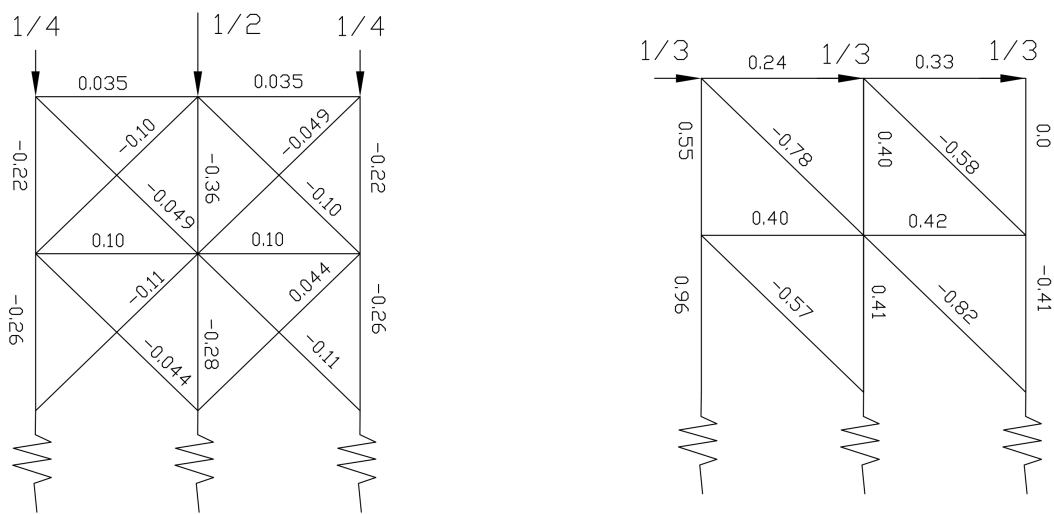


Figure 5-38: Axial forces in members for wall being loaded with unit loads with $E_{\text{wood}} = 6000$ MPa

Thus, from the two figures it is noticed that the values are practically identical for a E_{wood} of 12000 MPa and a E_{wood} of 6000 MPa, so we have neglected this dependency.

5.10.5. Estimation of strength for other configurations of walls

It is then required to estimate the value of F_u for other configurations of walls. It is assumed that, when the most loaded diagonal in a structure with another configuration reaches the value -49.09 kN it then fails by buckling. In this way, one can calculate the horizontal force, F_u , associated with each configuration. In **Figure 5-39** to **Figure 5-43** one can see the axial forces in the members for walls being loaded with unit loads for all the configurations studied.

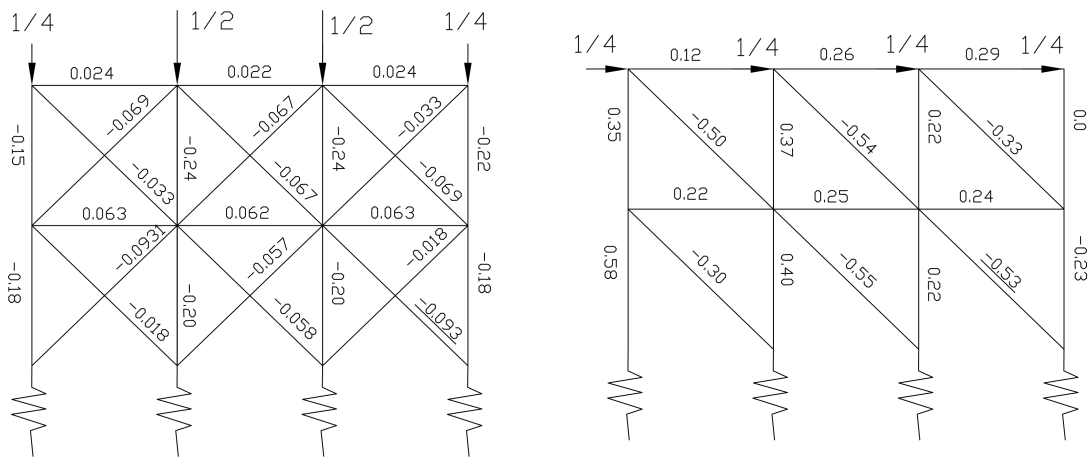


Figure 5-39: Axial forces in members for wall being loaded with unit loads, Conf 2x3

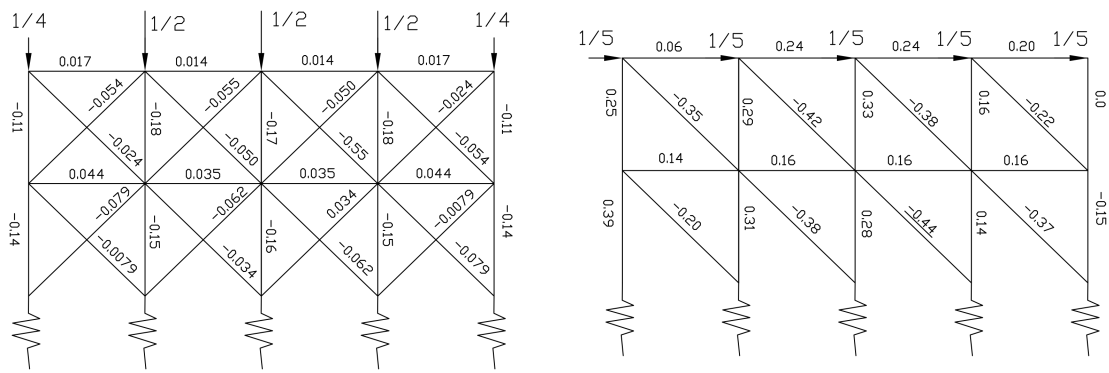


Figure 5-40: Axial forces in members for wall being loaded with unit loads, Conf 2x4

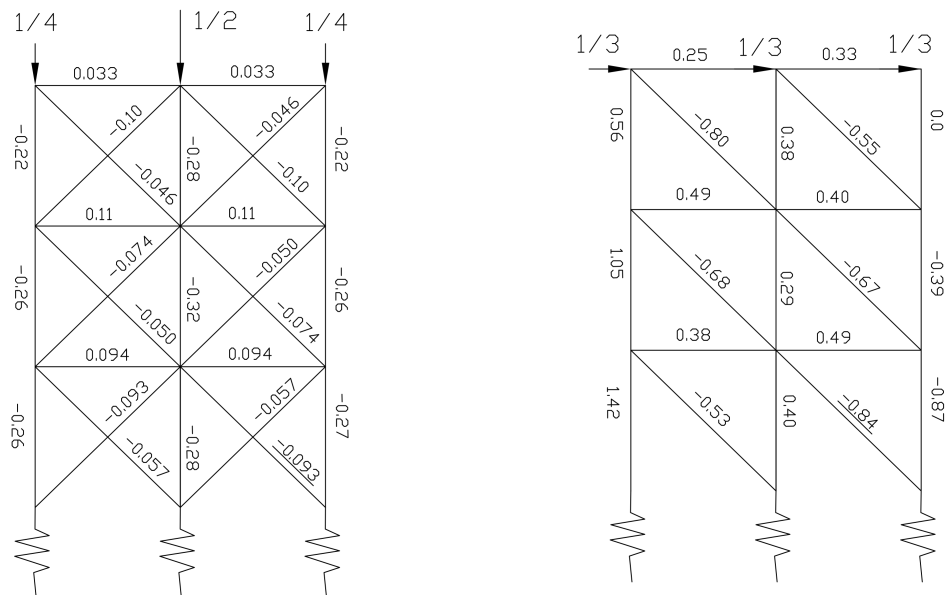


Figure 5-41: Axial forces in members for wall being loaded with unit loads, Conf 3x2

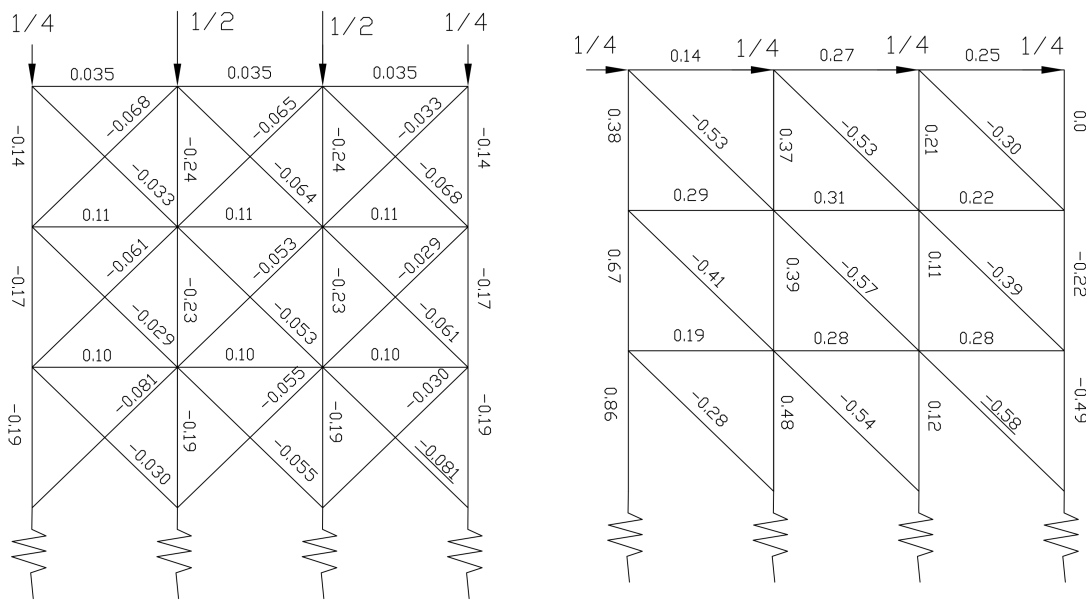


Figure 5-42: Axial forces in members for wall being loaded with unit loads, Conf 3x3

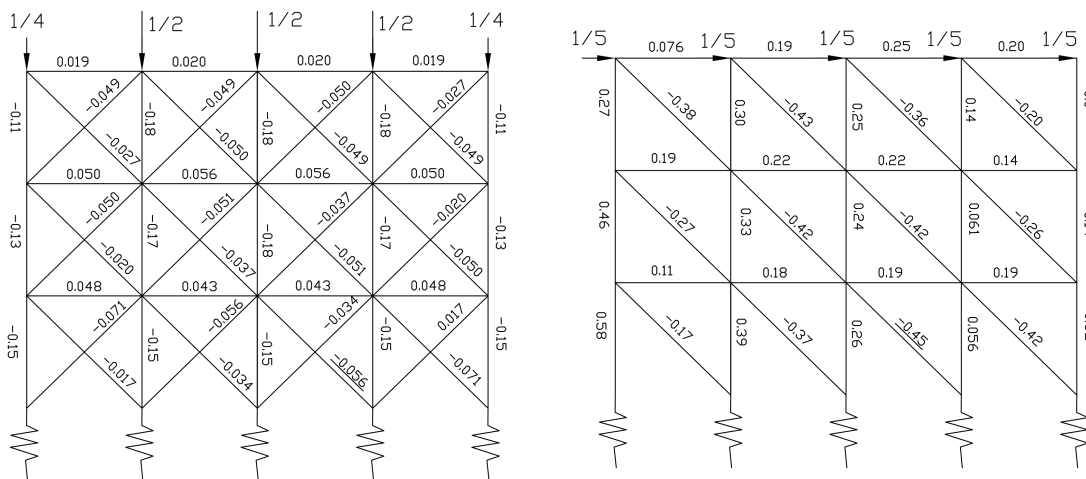


Figure 5-43: Axial forces in members for wall being loaded with unit loads, Conf 3x4

Table 5-14 shows the calculation of F_u for the other configurations of walls.

Table 5-14: Calculation of F_u for the other configurations of walls

Configuration	$F_{\text{vertical}} (\text{kN})$	Factor F_v	$F_{\text{diagonal}} (\text{kN})$	Factor F_u	$F_u (\text{kN})$
2x3	115.2	-0.093	-49.09	-0.53	72.41
2x4	153.6	-0.062	-49.09	-0.44	111.6
3x2	76.8	-0.093	-49.09	-0.84	49.94
3x3	115.2	-0.081	-49.09	-0.58	68.55
3x4	153.6	-0.056	-49.09	-0.45	89.97

According to the values obtained the configuration with the highest strength (F_u) is the configuration 2x4, which is followed by configuration 3x4. The configuration with the lowest strength is configuration 3x2.

5.10.6. Envelope curves for other configurations of walls

The envelope curve determined for other configurations of walls is based on the following assumptions:

- a- The initial stiffness, K_0 , is taken from the analytical analysis done for a certain wall configuration and a certain value of E_{wood} .
- b- The value of F_u , which is the maximum strength attained by the wall, is determined previously for each wall based on the assumptions presented previously and the wall configuration.
- c- The value of r_1xK_0 , r_2xK_0 and ζ ($\zeta = F_0/F_u$) are constant for all wall configurations and taken as the experimental values obtained for the configuration 2x2.
- d- The value of F_{ult} (denotes failure) is also known as 80% of the value of F_u .

Table 5-15 presents the constant values of ζ , r_1xK_0 and r_2xK_0 .

Table 5-15: Constant values of ζ , r_1xK_0 and r_2xK_0

ζ	0.728
r_1xK_0	0.244
r_2xK_0	-0.2745

Table 5-16 shows the values of K_0 , F_u and F_{ult} for different configurations of walls and with regards to K_0 , $E_{wood} = 12\ 000$ MPa.

Table 5-16: Values of K_0 , F_u and F_{ult} for different configurations of walls ($E_{wood}=12\ 000$ MPa)

Configuration	K_0 (kN/mm)	F_u (kN)	F_{ult} (kN)
2x2	6.4	50.8	40.64
2x3	15.8	72.41	57.93
2x4	33.3	111.6	89.28
3x2	2.9	49.94	39.95
3x3	6.8	68.55	54.84
3x4	13.6	89.97	71.98

One can see that the configuration with both the highest stiffness and the highest strength is configuration 2x4. The configuration with the lowest stiffness and the lowest strength is configuration 3x2. **Figure 5-44** depicts the envelope curves for different configurations of walls and how they behave with regards to the analytically obtained envelope curve for the configuration 2x2. The curves obtained are for values of $E_{wood} = 12\ 000$ MPa; for other values the initial stiffness K_0 would change accordingly. By keeping r_2xK_0 constant the value of the ultimate displacement of C2x4 is the highest; nevertheless, this might not be the case in reality. Experimental testing on different configurations is important to assess their behavior.

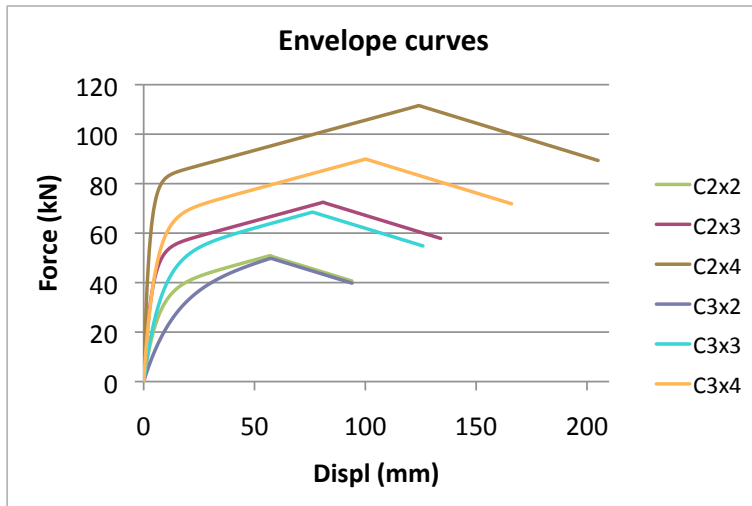


Figure 5-44: Various envelope curves for different wall configurations

5.10.7. Estimation of hysteresis curve for experimental test G2 of LNEC

A plot has been drawn for comparison of the hysteresis curve of specimen G2 obtained experimentally in LNEC [Pompeu Santos, 1997] and the hysteresis curve to be predicted analytically for this test. The analytical curve was estimated based on the previous discussions (see section 5.10.6) and for a configuration of 3x2 as were the walls tested in LNEC. A reasonable matching is obtained as can be seen in **Figure 5-45**. Some comments can be drawn. The envelope curve is reasonably well predicted. The unloading curves are very well predicted. The only discrepancy seen is with the reloading paths as these have a much lower slope in the experimental hysteresis than in the analytical plot. This is because the strength degradation is much higher for the experimental tests carried out in LNEC when compared to the experimental tests developed in this work (and subjected to the calibration of the hysteresis model). Note that, in the present work, only specimen G2 of LNEC is analysed since this is the only one with the same truss layout as the specimen tested here (G1 and G3 have different truss layouts since they were taken from the walls surrounding the stairs).

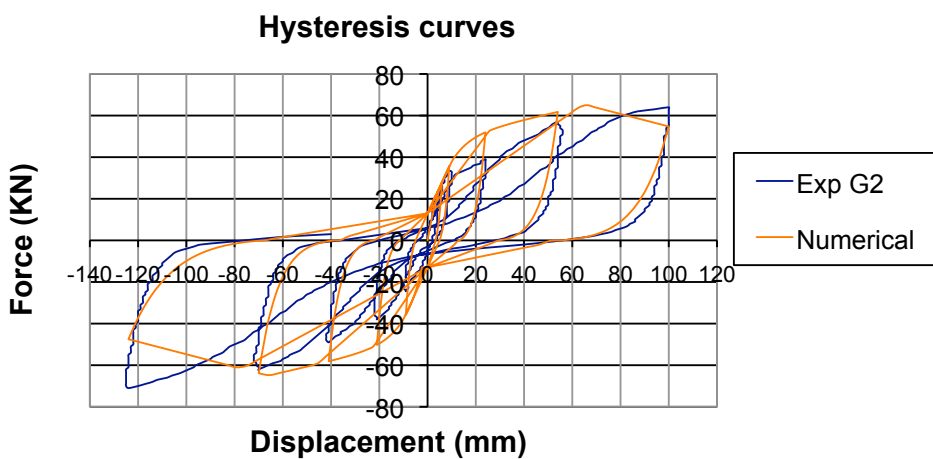


Figure 5-45:LNEC experimental versus analytical hysteresis

5.11. Conclusions

In this chapter it has been demonstrated that the diagonals of the “frontal” walls do not work under tension (the same was considered in the work of Cardoso [2003]). Moreover, the fact that the masonry filling of the “frontal” walls plays an insignificant role on the strength of the panel (the same was considered in the work of Kouris and Kappos [2011]) is demonstrated. Notwithstanding, the masonry filling should play a significant effect on the stiffness of the panel. Furthermore, it has been observed that the sources of pinching are the gaps opened between the diagonals and the vertical/horizontal members, the gaps associated with pulling out of nails and the masonry’s attachment and detachment from the timber frame.

A new hysteretic model for wood “frontal” walls has been developed. This is the first hysteretic model developed for such walls in the literature, justifying its relevancy. The hysteretic model is governed by path-following rules and is composed of linear and exponential functions. It is governed by 9 identifiable parameters. These parameters have been calibrated with experimental test results. The total percentage error in cumulative energy dissipated between the fitted model and the actual cyclic test data is 9% for the test SC2 and 14% for the test SC3, accounting for the good performance of the model. The model developed also accounts for characteristics such as pinching effect, strength and stiffness degradation that have been observed in the experimental data. The results obtained here are essential for further work in modelling the behaviour of such walls under monotonic, cyclic or earthquake loading.

Furthermore, the envelope curves for other wall sizes (height and length) have been predicted, since in reality one can find different wall sizes in a single building. It was shown that the configuration with both the highest initial stiffness and highest strength is the configuration 2x4 (two modules in height and four modules in length). On the other hand, the configuration with the lowest initial stiffness and lowest strength is the configuration 3x2 (three modules in height and two modules in length).

The effect of the number of cycles was not taken into account when defining the hysteresis model or macro-element. This shall be evaluated in further work.

In the next chapter, the authors will model a complete building in TREMURI and make use of the developed macro-element to include the “frontal” walls.

5.12. Bibliography

3Muri Program release 3.2.11 <http://www.stadata.com> (solver algorithm developed by Lagomarsino S., Galasco A., Penna A., Cattari S.)

Carvalho J., 2007, Caracterização Mecânica de Paredes Resistentes em Alvenaria de Pedra Através de ensaios não destrutivos; Master thesis, Instituto Superior Técnico (IST) (in Portuguese).

Cardoso M. R. P., 2003, Vulnerabilidade Sísmica de um Edifício Pombalino, Master Thesis, (IST), The Technical University of Lisbon.

Crisafulli F.J., 1997, Seismic behaviour of reinforced concrete structures with masonry infill, Ph.D. Thesis, Department of Civil Engineering, University Canterbury, New Zealand.

EN 338, 2003, Structural timber – Strength classes, European standard, CEN

Filiatral A, Isoda H, Folz B, 2002, Hysteretic damping of wood framed buildings, Engineering Structures 25, 416-471.

Foschi R.O., 1974, Load-slip characteristics of nails, Wood Sci., 7(1), 69-76.

Folz B and Filiatral A, 2001, Cyclic analysis of wood shear walls, Journal of Structural Engineering ASCE, 433-441

Kouris and Kappos, 2011, Detailed and simplified non-linear models for timber framed masonry structures, Journal of Cultural Heritage.

Lindt J and Walz M, 2003, Development and Application of Wood Shear Wall Reliability Model, Journal of Structural Engineering, ASCE, pp 405-413.

Meireles H, Bento R, Cattari S, Lagomarsino S, 2011, The proposal of a hysteretic model for internal wooden walls in *Pombalino* buildings, Proc. of the 2011 World Congress on Advances in Structural Engineering and Mechanics (ASEM11plus), Seoul, South Korea.

NP 4305, 1995, Madeira Serrada de Pinho Bravo para estruturas, classificação visual

Pinho Bravo para estruturas, 1997, Madeira para construção, M2, LNEC

Pompeu Santos, 1997, Ensaios de Paredes Pombalinhas. Nota Técnica Nº15/97, NCE/DE, LNEC Lisboa (in Portuguese) .

SAP 2000, 1998, Three Dimensional static and dynamic finite element analysis and design of structures, version 7.4.2, CSI, computers and structures, inc, Structural and Earthquake engineering software, Berkeley, California, USA.

Technical Tables, 1998, Brazão Farinha JS, Correia dos Reis A, Edições Técnicas E.T.L. Lda

Walz M., 2001, Development and application of a nonlinear hysteretic wood shear wall model, MS Thesis, Dept. of Civil and Environmental Engineering, Michigan Technological University, Houghton, USA.

6. Macro-element approach for the seismic analysis of a *Pombalino* building

6.1. Summary

The current chapter focuses on the modelling and on the seismic assessment of a typical *Pombalino* building with a structural software where the previously described macro-element has been incorporated. The software used was the structural program 3Muri (www.stadata.com), which enables nonlinear static and dynamic analyses to be performed. Here, only nonlinear static analyses were carried out. The structure is modelled by using macro-elements for the masonry panels and also for the “frontal” walls. By using 3Muri pushover analyses were performed and the capacity curves in both directions evaluated. In each direction, by intersecting the capacity curve with the demand spectrum one is able to obtain the performance point and, assuming a lognormal distribution probability function, fragility curves are obtained. The most important application of such curves is in loss estimation studies. Beyond this, the performance of the *Pombalino* buildings was evaluated, not only in their original state but also with some retrofitting schemes. Fragility curves and damage probability plots were also obtained for such retrofitted schemes.

6.2. Overview of methods used

It is widely understood that unreinforced masonry (URM) buildings are among the most vulnerable structures when facing earthquakes [Karimi and Bakhshi, 2006]. Evaluating the seismic performance of these buildings and proposing some effective methods to retrofit them against earthquakes will be an essential step in the current state of the art knowledge of these structures.

From the observation of the damage caused by past earthquakes (in URM buildings) it is possible to classify the damage mechanisms into two main categories: first-mode and second-mode of failure [Giuffré, 1993]. The first mode of failure is related to out-of-plane failure mechanisms such as overturning of the walls. This is observed to happen when inadequate connections between walls or between walls and diaphragms exist in the building. When a good connection exists between the structural elements (walls and diaphragms) then the building tends to behave as a whole and the dangerous out-of-plane failure mechanisms tend to be avoided. In this case, the second mode of failure tends to be predominant and this is characterized by the in plane resistance of the walls, meaning shear, sliding-shear or rocking failure mechanisms.

In the global seismic response of the URM buildings the role of the horizontal diaphragms (floors) is also very important. In fact, evidence shows that adequately rigid diaphragms in plan and good wall-to-diaphragm connections allow the avoidance of out-of-plane overturning or flexural mechanisms relating to walls or building portions. The adequately rigid horizontal diaphragms in plan permit also the accurate distribution of forces towards the walls and allows the building to behave as

a three dimensional structure. On the other hand, overly flexible horizontal diaphragms lead to the elements of the building to behave independently and the out-of-plane behaviour of each wall to be heightened. A summary of the aspects of the influence of the rigid/flexible horizontal diaphragms in buildings can be written as follows:

Flexible floor:

- Does not transmit forces from one wall to another.
- The walls behave independently.
- The overall resistance of the building is given by the strength of the weakest wall.
- The convergence of the software is more difficult.

Rigid floor:

- The building behaves like a box.
- The forces in the walls are redistributed from the failing walls to the remaining walls.
- The overall resistance of the building is given by strength of all the walls belonging to it, exhibiting a higher resistant shear.
- No problems converging the results in the software.

When the in-plane stiffness of the walls is prevalent for the URM building failure mechanism, the failure mechanisms of a rectangular panel may be the following three types: shear failure (diagonal cracking); rocking/flexure failure; sliding-shear failure (see **Figure 6-1**). For a rectangular panel, the geometry, the mechanical parameters of the masonry and the axial load level lead to one of these different failure mechanisms. In **Figure 6-1** one can see that shear failure shows diagonal cracks that can follow the mortar joints pattern or pass through the masonry units; rocking failure occurs when the unit shows overturning and flexion in its plane and one can see the compressed edges; finally, sliding-shear failure occurs when low levels of vertical loads are applied and horizontal cracks usually form.

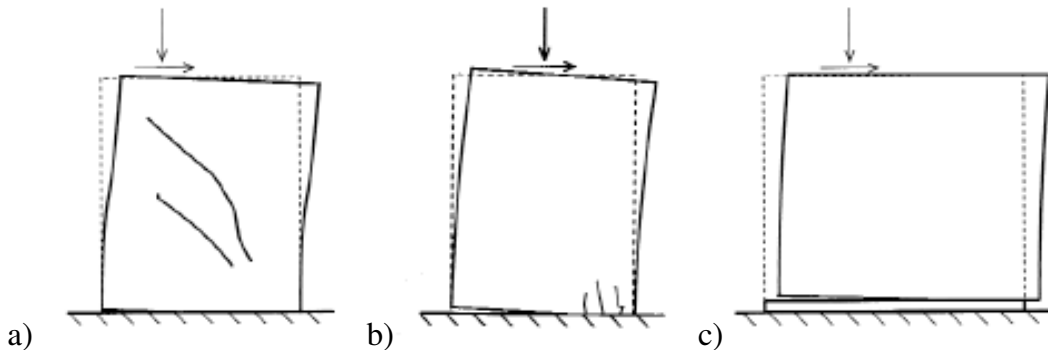


Figure 6-1: In-plane failure mechanisms (second-mode): a) shear failure (diagonal cracking); b) rocking/flexure failure; c) sliding-shear failure [Macchi and Magenes 2002]

In **Figure 6-2** one can see the crack patterns obtained in real panels after being damaged by earthquakes.

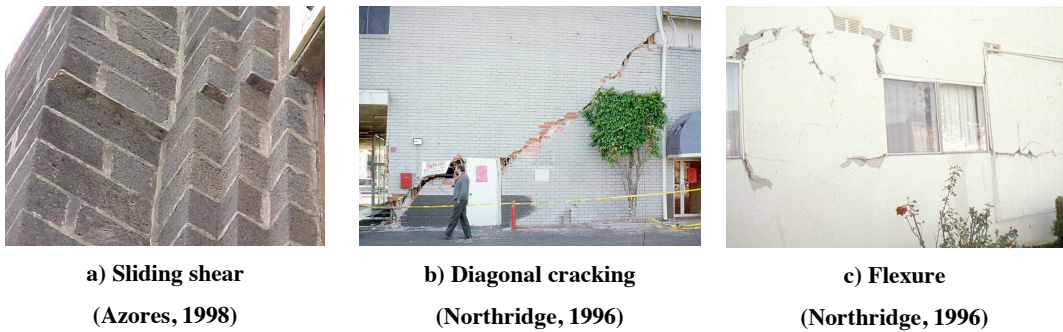


Figure 6-2: Masonry panels failure mechanism observation [Costa, 2007]

Each failure mode of the panels portrayed may have a given equation to describe it. The strength of a masonry panel will be given by the minimum of the three strengths associated with each of the three failure modes. The computation of the strength of a masonry panel is very dependent on the level of axial load (although dependent on other parameters such as panel geometry as has been said previously). For a certain masonry panel (given dimensions and material properties) it is possible to obtain a graph representative of the variation of possible failure modes with the level of axial load, as represented in **Figure 6-3**. For low levels of axial load it is seen that the rocking-flexure and the shear-sliding failure modes are prevailing in the response of the panel while for medium levels of axial load the scenario changes and the shear-diagonal cracking failure mode is dominating the response; finally, for high levels of axial load the rocking-flexure failure mode is dominating the response.

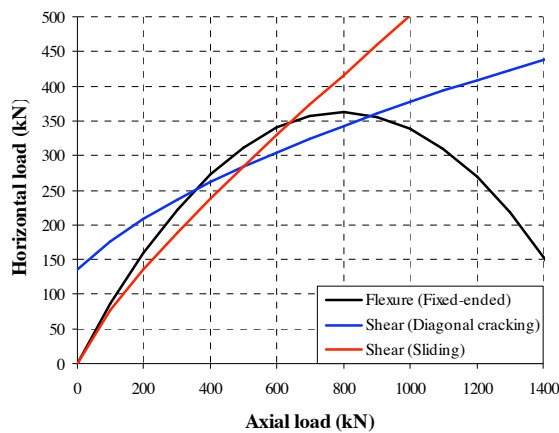


Figure 6-3: Influence of axial load on panels failure modes [Costa, 2007]

For a masonry wall the total behaviour is due to the combination of masonry panels (macro-elements, see **Figure 6-4**). Again, from the observation of past earthquakes, it has been seen that cracks are mainly concentrated in the piers (vertical panels) and in the spandrels (horizontal panels coupled with the vertical panels), while in the joints between these elements there is no observed damage. For this reason the equivalent frame model was developed to model URM buildings and this can be seen in **Figure 6-5**. The typical failure modes that can occur in the piers and spandrels are the three types described previously.

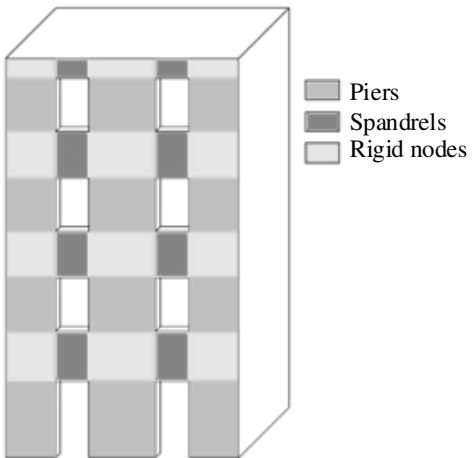


Figure 6-4: Masonry panels for a wall. [Cattari *et al.*, 2005]

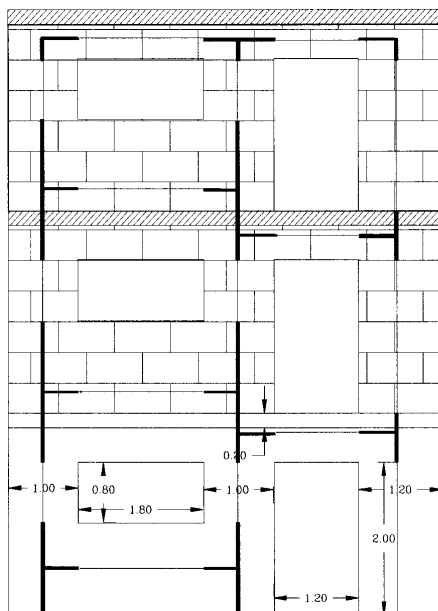


Figure 6-5: Equivalent frame model for a masonry wall [Kappos *et al.*, 2002]

6.2.1. Software TREMURI

In the recent past, in order to model masonry structures, very sophisticated and complex analysis tools (finite element models) or very simplified methods were used. This is because there was no analytical tool in between the two approaches that could be a viable way to analyse such structures. For this reason, by means of the effective macro-element approach, an accurate, yet without heavy computational load, modelling strategy was developed for the analysis of masonry structures; this program, developed at the university of Genoa, is called TREMURI. Case studies and examples, both from experimental testing and the observation of earthquake damaged structures, show the effectiveness of the modelling technique and its seismic analyses capabilities. TREMURI is able to perform nonlinear static analyses as well as nonlinear three-dimensional time-history analyses. This innovative modelling tool was used in the current work.

In order to model complete 3D structures, the program assembles 2D nodes macro-elements that represent the nonlinear behaviour of the masonry panels. By means of internal variables, the macro-element considers the shear-sliding damage failure mode and its evolution, the rocking mechanisms with toe-crushing effects and the diagonal shear failure mode. URM buildings can be obtained by assembling, again, plane structures (walls and floors). Mixed structures can be also modelled by introducing additional elements representing the nonlinear response of structural members other than masonry (reinforced concrete beams, shear walls, reinforced masonry, steel and wooden members).

The TREMURI program development has been carried out for the last 15 years. As a first development, Brencich and Lagomarsino [1998] implemented the frame-type modelling of in-plane wall static response, by connecting rigid nodes, piers and spandrel beam macro-elements. The implemented FORTRAN code (without any graphical interface) allowed performance of cyclic nonlinear static analyses of single walls. Later on, Lagomarsino started the implementation of the nonlinear dynamic analysis procedure. In the following years (1999-2001) the code was completely rewritten in Visual Basic by Galasco. A new graphical user interface was then implemented. Then, the new development team (Lagomarsino, Penna and Galasco) included several new features: nonlinear truss/beam elements for tie-rods and struts (no-tension/no-compression gap elements), time-history analysis procedure and a newly developed pushover analysis algorithm. Since 2001 a new computer program, was again rewritten starting from the previous 2D program. The new tool, oriented towards 3D modelling and analysis included several new specific features such as: 3D frame-type modelling of wall structures, 3D time-history analysis procedure with 3 components of ground acceleration, orthotropic membrane elements for modelling flexible diaphragms (floors, roofs), modal analyses, etc. Other features have been implemented up until now, for instance, several nonlinear reinforced concrete elements (beams, columns and shear walls) were introduced [Cattari and Lagomarsino 2006]; this allowed extending the program capabilities to mixed reinforced concrete-masonry structures.

6.2.2. Nonlinear static procedures

The nonlinear static procedures (pushover analysis) have become a standard method for estimating seismic deformation demands in building structures as well as their local and global capacities [Villaverde, 2007]. In nonlinear static procedures, a model of the structure is defined considering the nonlinear force-deformation behaviour of its elements, thus developing a nonlinear model of the structure. Then, by subjecting the multi-degree-of-freedom (MDOF) structure to a monotonically increasing lateral load pattern, colloquially known as “pushover”, we obtain the base shear-lateral displacement relationship, commonly known as capacity curve. The load pattern may have different shapes in height. In the Eurocode 8 [2004] two lateral load patterns are prescribed, the uniform and the modal lateral load pattern. In the first a load pattern proportional to the masses in each node is established; in the second one the load pattern is proportional also to the first mode shape of the structure. For the drawing of the capacity curve, the lateral displacement is often taken to be a roof displacement, either the centre of mass of the building’s roof or, in case of flexible floors, the

average of the roof nodes displacements; or any other representative node usually taken from the top of the building.

Afterwards, the goal is to define the target displacement so as to evaluate the resulting internal deformation and forces at a certain earthquake performance level. The target displacement is estimated based on the specific hazard of the site (represented by means of a smooth design elastic response spectrum curve) and should approximate the maximum level of deformation expected in the structure for that seismic demand. Typically this is achieved by means of an equivalent single-degree-of-freedom (SDOF) system representing the overall behaviour of the MDOF system under analysis. The SDOF system is characterized by an idealized bilinear hysteretic model determined based on the capacity curve obtained for the MDOF system. For these analyses, inelastic spectrum (N2 method [Fajfar, 2000]) or elastic spectrum with equivalent damping (Capacity Spectrum Method [Freeman, 1998]) can be applied.

Some limitations can be pointed out immediately in these conventional procedures. One is the assumption that, while obtaining the capacity curve, the structure has a time-independent lateral displacement shape (invariant load patterns are used). The other is the fact that reducing a MDOF system in to an equivalent SDOF system based on a fixed transformation shape (usually the first elastic mode shape) is a limiting approach, especially for irregular structures. In both cases the higher mode effects are not taken into account properly. Nevertheless, for regular and low to medium-rise frame buildings invariant patterns seem to give an adequate estimation of the element deformations and base shear demands of the structure.

The N2 method was chosen to be applied in this work. The N2 method (N stands for nonlinear analysis and 2 stands for two mathematical models) is the current nonlinear static procedure adopted in the Eurocode 8 [2004]. The basic steps of the method are the following [Fajfar, 2000]:

1. DATA: Constructing a nonlinear model of the structure. In addition to the data needed for the usual elastic analysis, the nonlinear force-deformation relationships for structural elements under monotonic loading are required. The seismic demand is here defined in the form of an elastic (pseudo) acceleration response spectrum, S_{ae} , in which spectral accelerations are given as a function of the natural period of the structure, T .
2. SEISMIC DEMAND IN AD FORMAT: Starting from the acceleration spectrum the inelastic spectrum is defined in acceleration-displacement (AD) format.
 - a) Determine elastic spectrum in AD format. For an elastic SDOF system the following relation applies (**Equation 6-1**):

$$S_{de} = S_{ae} \left(\frac{T}{2\pi} \right)^2 \quad (\text{Equation 6-1})$$

Where S_{ae} and S_{de} are the values of the elastic acceleration and displacement spectrum, respectively, for a period T and a fixed damping ratio.

- b) Determine inelastic spectra for constant ductilities. For an inelastic SDOF system with a bilinear force-deformation relationship, the acceleration spectrum (S_a) and the displacement spectrum (S_d) can be determined according to **Equation 6-2** and **Equation 6-3**:

$$S_a = \frac{S_{ae}}{R_\mu} \quad (\text{Equation 6-2})$$

$$S_d = \frac{\mu}{R_\mu} S_{de} = \frac{\mu}{R_\mu} \cdot \left(\frac{T}{2\pi} \right)^2 S_{ae} = \mu \left(\frac{T}{2\pi} \right)^2 S_a \quad (\text{Equation 6-3})$$

Where μ is the ductility factor defined as the ratio between the maximum displacement and the yield displacement, and R_μ is the reduction factor due to ductility, i.e., due to the hysteretic energy dissipation of ductile structures. In the simpler version of the N2 method, it is made use of a bilinear graph of the reduction factor R_μ as a function of the period T (**Equation 6-4** and **Equation 6-5**).

$$R_\mu = (\mu - 1) \frac{T}{T_c} + 1 \quad T < T_c \quad (\text{Equation 6-4})$$

$$R_\mu = \mu \quad T \geq T_c \quad (\text{Equation 6-5})$$

Where T_c is the characteristic period of the ground motion. It is typically defined as the transition period where the constant acceleration segment of the response spectrum (the short period range) passes to the constant velocity segment of the spectrum (the medium period range). Equation 6-3 and Equation 6-5 suggest that, in the medium and long period ranges, the equal displacement rule applies, i.e., the displacement of the inelastic system is equal to the displacement of the elastic system with the same period.

3. **PUSHOVER ANALYSIS:** A pushover is performed by subjecting the structure to a monotonically increasing pattern of lateral forces. Under incrementally increasing lateral loads various structural elements yield sequentially. Using a pushover analysis, a characteristic nonlinear force-displacement relationship of the MDOF system (capacity curve) can be determined.
4. **EQUIVALENT SDOF SYSTEM:** In the N2 method, seismic demand is determined by means of response spectrum. Consequentially, the structure should, in principle, be modelled as a SDOF system. Different procedures have been used to determine the characteristics of an equivalent SDOF system, one of them was selected for the N2 method and is based on the following formulas:
 - a) determine mass m^* (**Equation 6-6**):

$$m^* = \sum_i m_i \Phi_i$$
(Equation 6-6)

Where m^* is the equivalent mass of the SDOF system and Φ is the assumed displacement shape and is normalized (the value at the top is equal to 1). Any reasonable shape can be used for Φ , but the elastic first mode shape is usually adopted. It is assumed that the displacement shape Φ is constant, i.e., that it does not change during the structural response to ground motion. This is one of the most critical assumptions within the procedure.

b) transform MDOF quantities to SDOF quantities (**Equation 6-7**, **Equation 6-8** and **Equation 6-9**):

$$D^* = \frac{D_t}{\Gamma}$$
(Equation 6-7)

$$F^* = \frac{V}{\Gamma}$$
(Equation 6-8)

$$\Gamma = \frac{\sum_i m_i \Phi_i}{\sum_i m_i \Phi_i^2}$$
(Equation 6-9)

Where D^* and F^* are, respectively, the displacement and force of the equivalent SDOF system; D_t and V are, respectively, the top displacement and base shear of the MDOF system and Γ is usually called the modal participation factor. The constant Γ controls the transformation from the MDOF system to the SDOF system and vice-versa. Note that the same constant Γ applies for the transformation of both displacement and forces. In this way, the initial stiffness of the equivalent SDOF system remains the same as that defined by the capacity curve of the MDOF system.

c) determine an approximate elasto-plastic force-displacement relationship: in order to determine a simplified (elastic-perfectly plastic) force-displacement relationship for the equivalent SDOF system, engineering judgement has to be used. Some guidelines are given in the national documents of some countries.

d) determine yield strength F_y^* , yield displacement D_y^* and period T^* : the elastic period of the idealized bilinear system T^* can be determined as (**Equation 6-10**):

$$T^* = 2\pi \sqrt{\frac{m^* D_y^*}{F_y^*}}$$
(Equation 6-10)

Where F_y^* and D_y^* are the yield strength and displacement, respectively, of the approximate elasto-plastic diagram.

e) determine the capacity diagram (acceleration versus displacement-AD): finally the capacity diagram in AD format is obtained by dividing the forces in the force-deformation (F^*-D^*) diagram by the equivalent mass m^* (**Equation 6-11**):

$$S_a = \frac{F^*}{m^*} \quad (\text{Equation 6-11})$$

5. SEISMIC DEMAND FOR SDOF SYSTEM: a) determine the reduction factor R_μ : both the demand spectrum and the capacity diagram are plotted in the same graph. The intersection of the radial line corresponding to the elastic period of the idealized bilinear system (T^*) with the elastic demand spectrum S_{ae} defines the acceleration demand (strength) required for elastic behaviour and the corresponding elastic displacement demand. The yield acceleration S_{ay} represents both the acceleration demand and the capacity of the inelastic system. The reduction factor R_μ can be determined as the ratio between the accelerations corresponding to the elastic and inelastic systems (**Equation 6-12**):

$$R_\mu = \frac{S_{ae}(T^*)}{S_{ay}} \quad (\text{Equation 6-12})$$

b) determine displacement demand S_d : if the elastic period T^* is larger than or equal to T_c , the inelastic displacement demand S_d is equal to the elastic displacement demand S_{de} (**Equation 6-13**), i.e. it is assumed that the ductility demand, defined as $\mu = S_d/D_y^*$, is equal to R_μ (**Equation 6-14**).

$$S_d = S_{de}(T^*) \quad T^* \geq T_c \quad (\text{Equation 6-13})$$

$$\mu = R_\mu \quad (\text{Equation 6-14})$$

If the elastic period of the system is smaller than T_c , the ductility demand can be calculated from the rearranged **Equation 6-4** as (**Equation 6-15**):

$$\mu = (R_\mu - 1) \frac{T_c}{T^*} + 1 \quad T^* < T_c \quad (\text{Equation 6-15})$$

The displacement demand can be determined either from the definition of ductility or from **Equation 6-3** and **Equation 6-15** as (**Equation 6-16**):

$$S_d = \mu D_y^* = \frac{S_{de}(T^*)}{R_\mu} \left(1 + (R_\mu - 1) \frac{T_c}{T^*} \right) \quad (\text{Equation 6-16})$$

In both cases ($T^* < T_c$ and $T^* \geq T_c$) the inelastic demand in terms of accelerations and displacements corresponds to the intersection point of the capacity diagram with the demand spectrum corresponding to the ductility demand μ . At this point, the ductility factor determined from the capacity diagram and the ductility factor associated with the intersecting demand spectrum are equal. Note that all steps in the procedure can be performed numerically without using graphs.

6. GLOBAL SEISMIC DEMAND FOR MDOF SYSTEM: The displacement demand for the SDOF system, S_d , is transformed into the maximum top displacement D_t of the MDOF system (target displacement) by using **Equation 6-7**.
7. LOCAL SEISMIC DEMANDS: Perform pushover analysis of MDOF system up to the top displacement D_t and determine local quantities corresponding to D_t .
8. PERFORMANCE EVALUATION: Compare local and global seismic demands with the capacities for the relevant performance level.

6.2.3. Fragility analysis

One method of evaluating the performance of buildings in earthquakes is through the use of fragility curves. Fragility curves describe the conditional probability of a class of buildings reaching or exceeding a specified level of damage (probability of failure), for a given level of ground motion. Fragility curves are characterized into two types: empirical and analytical. Empirical fragility curves (or post-earthquake investigation methods) are developed using real damage data obtained from observations on previously occurred earthquakes. Analytical fragility curves are constructed based on mechanical methods applied to a given construction, usually developed with specific structural software.

The main ingredients of fragility curves are:

- 1- Ground motion characterization

The seismic demand is one of the main ingredients of the fragility curves and is represented on the horizontal axis of the plot. Many different parameters can be used to characterize the severity of the ground motion (for instance macro-seismic intensity, peak ground acceleration – PGA, design ground acceleration on type A ground – a_g , cumulative absolute velocity – CAV, Arias intensity – AI, and so on). In the present work, a_g has been chosen for representing ground motion. In any case, the values of a_g can be easily transformed into the values of PGA simply by multiplying the parameter S (soil factor). On the other hand, it is well known that the ground motion on rock may be amplified due to stratigraphical and/or topographical effects. Since risk is obtained from the convolution of hazard, vulnerability and exposure, in some studies, the site effects are incorporated in the vulnerability definition and in others in the hazard part. In this work, local site amplification effects were included in the hazard part as can be understood later.

2- Damage levels or damage limit states

In order to construct fragility curves it is necessary to establish a damage scale with well defined damage limit states. The damage scale used in this work includes 4 levels of damage: slight damage (1); moderate damage (2); heavy damage (3) and collapse (4).

3- Building classes

Classes of buildings should be defined by grouping together structures that are expected to have similar seismic behaviour. The most important factors affecting the earthquake response of the building are: the type of materials used in the construction, the type of vertical and horizontal bearing structure, the period of construction and the number of storeys. It is well known that the number of storeys plays a crucial role in defining the seismic behaviour of the structure, being directly related to the height of the building and hence to the period of vibration. So, the number of storeys has a strong effect on both structural capacity and demand. For what concerns masonry, the quality of masonry also plays an important role and should be considered. On the other hand, with regards to the horizontal bearing structure, rigid floors should be distinguished from flexible floors.

According to Mander [1999], if structural capacity and seismic demand are random variables that roughly conform to either a normal or a log-normal distribution then, following the *central limit theorem*, it can be shown that the composite performance outcome will be lognormally distributed. Therefore, the probabilistic distribution is expressed in the form of a fragility curve given by a log-normal cumulative probability density function. The cumulative probability density function may be written as (**Equation 6-17**):

$$P[D_k | a_g] = \phi\left[\frac{1}{\beta_k} \ln\left(\frac{a_g}{a_{g,k}}\right)\right] \quad (\text{Equation 6-17})$$

According to **Equation 6-17**, the fragility curves give the probability that the damage is equal to or higher than a certain damage state D_k , as a function of the design ground acceleration a_g . In this equation ϕ is the normal cumulative distribution function. Fortunately, only two parameters are needed to define such a curve: β_k is the normalized standard deviation of the natural logarithm of the acceleration threshold $a_{g,k}$. The variable $a_{g,k}$ is the reference design ground acceleration that produces damage state D_k ($k=1,2,3,4$).

Uncertainty can be formally classified as *aleatory* uncertainty and *epistemic* uncertainty. Aleatory uncertainty characterizes the inherent randomness in the behaviour of the system under study; they are characterized by frequency distributions. Examples of aleatory uncertainties are material properties. Epistemic uncertainty characterizes the lack of knowledge about the appropriate value to use for a quantity that is assumed to have a fixed value. Epistemic uncertainties are reduced through increased understanding, research or increased data. Epistemic uncertainties are characterized degrees of belief and should not be given a frequensic interpretation.

Examples of epistemic uncertainty are the uncertainty in the definition of the limit states of damage or the unknown level of accuracy in the structural software used for the analysis.

Various uncertainties exist and their quantification is complex. The uncertainties can be implemented in **Equation 6-17** for the fragility analysis by means of the factor β . β incorporates aspects of uncertainty and randomness in both capacity and demand. β is sometimes referred to as the coefficient of dispersion and is the element responsible for “shaping” the fragility curve to be more or less steep (more steep if β is small). The value of β is given by **Equation 6-18** in terms of the various uncertainties to be quantified. To be noticed that this equation is only valid if the uncertain variables are mutually independent in a statistical sense, which is not entirely true in practice but is a commonly adopted approximation.

$$\beta = \sqrt{\beta_1^2 + \beta_2^2 + \dots + \beta_n^2} \quad (\text{Equation 6-18})$$

Where β_i ($i=1, 2, \dots, n$) represent the various uncertainties. These can be uncertainty in the demand (variability of seismic action), in the capacity (variability of the input parameters), in the definition of the limit states of damage, in the software model used, etc.

According to [Mander, 1999], in the case of bridges, based on both theoretical calibrations and empirical fragility curves from data gathered on the 1994 Northridge and 1989 Loma Pietra earthquakes, it is recommended that $\beta = 0.6$. This is not far from the value used in the presented analysis (see section 6.7.2).

6.2.4. Soil-structure interaction

As has been presented in Chapter 2, *Pombalino* buildings have foundations with practically direct contact with ground. The wooden piles present are only 1,5 m long and cannot be considered as indirect foundations like the reinforced concrete piles present in some of the recent structures. When an earthquake strikes neither the structural displacements nor the ground displacements, are independent of each other. The process in which the response of the soil influences the motion of the structure and the motion of the structure influences the response of the soil is termed as soil-structure interaction (SSI).

Conventional structural design methods neglect the SSI effects. Neglecting SSI is reasonable for light structures in relatively stiff soil such as low-rise buildings and simple rigid retaining walls. The effect of SSI, however, becomes prominent for heavy structures resting on relatively soft soils and in this way, it could be present on the analysed *Pombalino* buildings since these are relatively heavy and stiff buildings resting on soft soil, as seen in Chapter 3.

Considering soil-structure interaction makes a structure more flexible and thus, increasing the natural period of the structure compared to the corresponding rigidly supported structure. Moreover, considering the SSI effect increases the effective damping ratio of the system. The smooth idealization of design spectrum suggests smaller seismic response with the increased natural periods and effective damping

ratio due to SSI. With this assumption (the fact that the increase in natural period of the building will not lead to increased spectral accelerations), it can be considered that herein one can neglect the SSI analysis according to ASCE 41-07 [2007]. Previously, neglecting SSI would reduce very much the complication in the analysis of the structures but nowadays simpler methods of analysis can be found like in ASCE 41-07 [2007]. In the analysed case study, SSI has not been taken into account. If later one desires this could be done for future work.

6.3. Case study

The building that was chosen to be analysed in this study tries to replicate a typical *Pombalino* building as described in Chapter 2 of the current work. On the other hand, a building in downtown Lisbon that had been the subject of previous analysis and evaluation was sought as well so that information would be available with respect to the plan architecture of the building. In this way, a building was found that had been the subject of research in the study by Cardoso [2003]. This existing building is located at 210 to 220 on the street *Rua da Prata* and the historical background and architectural drawings are also present in the book *Baixa Pombalina: Passado e Futuro* (Pombaline downtown: Past and Future) [Santos, 2000]. This building is recognized by the existence of a pharmacy in the ground floor, which is covered by a well-decorated panel of blue tiles, dating from 1860. Nevertheless, as is usual in the *Pombalino* buildings of downtown, this building has been subject to some alterations with respect to the original layout. In this particular case one floor has been added to the original layout of 4 floors plus roof, making a total number of 5 floors plus attic. In the current study, given that study of a typical *Pombalino* building was intended, only 4 floors plus roof were considered in the layout, so the last floor below the roof was eliminated in the drawings and modelling. The drawings that are subsequently showed are based on the drawings present in the study mentioned by Cardoso [2003]. The front façade of the building is depicted in **Figure 6-6**:



Figure 6-6: Sketch of façade of building (front) – units in metres

The building has six entries on the main façade and a height of approximately 15 m until the last floor (without the height of the roof). The openings have a width of 1.66 m, the door on the ground floor a height of 3.5 m, the balcony on the first floor a height of 3 m and the windows on the second and third floors a height of 2 m. The backyard façade of the building can be seen in **Figure 6-7**:

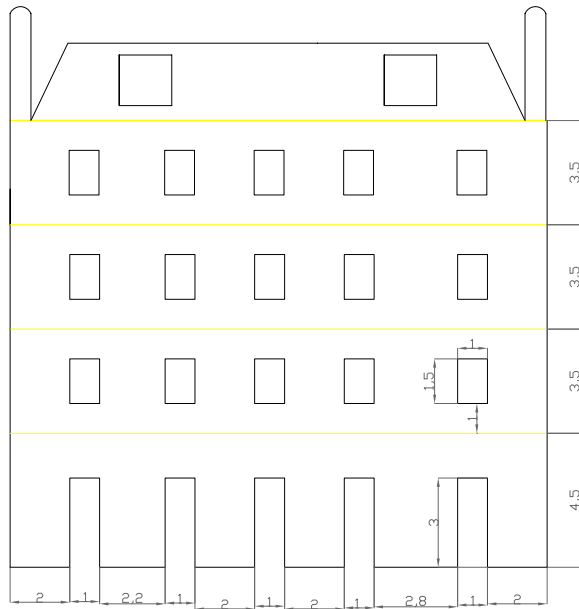


Figure 6-7: Sketch of façade of building (backwards) – units in metres

At the back the openings are smaller and have a width of 1 m. At ground floor level the height of the door is 3 m and on the first, second, and third floors there are windows of 1.5 m high. There are only 5 entries. The plan drawings of the building are shown in **Figure 6-8** and **Figure 6-9** for the ground floor and upper floors, respectively.

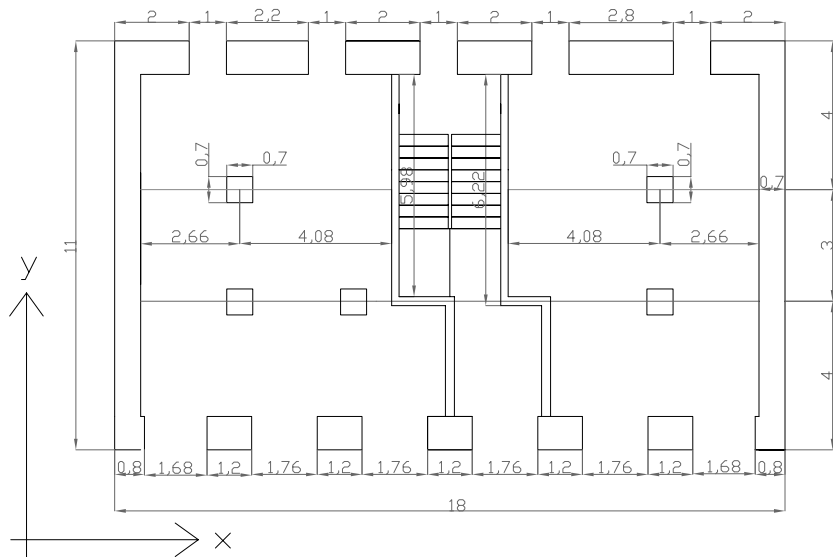


Figure 6-8: Sketch of the plan view of building: ground floor – units in metres

The plan of the building has dimensions of $18 \times 11 \text{ m}^2$ referring to the façade and gable walls, respectively. The ground floor has 5 internal piers with dimensions of $0.7 \times 0.7 \text{ m}^2$. There are stairs in the middle of the building facing towards the back façade. These have brick masonry staircases only on the ground floor (on the upper floors the staircases are “frontal” walls) with a thickness of 0.24 m. On the ground floor, the staircase brick masonry walls up to the front of the building with a small misalignment towards the right. On the ground floor, the front and back façade piers as well as the internal piers are made of stone masonry. The gable walls as well as the front and back façades of the upper floors are constituted of rubble masonry.

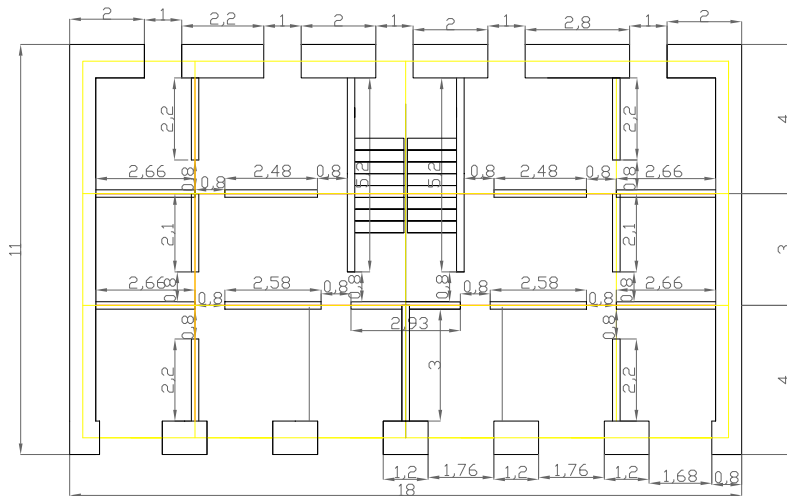


Figure 6-9: Sketch of the plan view of building: upper floors – units in metres

On the upper floors (from the first to the third floor) one can find the “frontal” walls. There are two alignments of “frontal” walls parallel to the façades and five alignments (including the staircase) of “frontal” walls parallel to the gable walls. Connecting the “frontal” walls there are openings (doors) of 0.8 m. The structural elements with their respective type of material and thickness/area can be found on Table 6-1:

Table 6-1: Thickness/area and material of building components

Element	Material	Thickness/area
Piers (ground floor)	Stone masonry	$0.7 \times 0.7 \text{ m}^2$
External walls (façade and backwards):		
Ground floor	Stone masonry	0.90 m
1 st floor	Rubble masonry	0.85 m
2 nd floor	Rubble masonry	0.80 m
3 rd floor	Rubble masonry	0.75 m
Spandrels	Rubble masonry	0.20 m
Gable walls	Rubble Masonry	0.70 m
Staircase (ground floor)	Brick Masonry	0.24 m
Internal walls (ground floor)	Brick Masonry	0.24 m
“frontal” walls	Masonry/wood	0.15 m

From the previous table, the external walls (façade and backwards) reduce in thickness the higher they are, being of 0.90 m on the ground floor and 0.75 m on the

third floor. The floors have sections and dimensions that are shown in **Figure 6-10**. The joists of the floors have a section of $10 \times 20 \text{ cm}^2$ and the wood pavement a thickness of 2 cm.

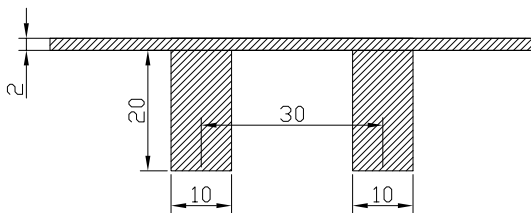


Figure 6-10: Sections of floor joists and pavement (material wood) – units in cm

The floors are supported by the front and back façades and by the “frontal” walls; the stairs are supported by the staircase. The distribution of the actions of the floors and stairs are presented in **Figure 6-11**.

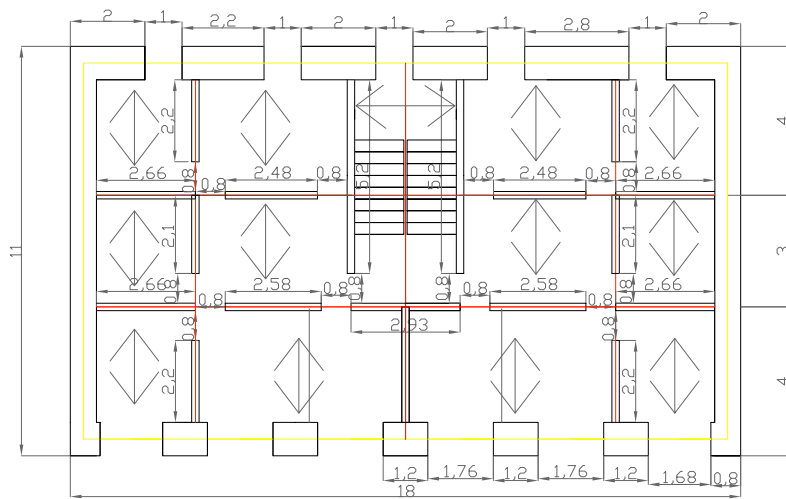


Figure 6-11: Sketch of plan view of building: floor actions – units in metres

The building was modelled in the software called TREMURI. The mechanical characteristics of the masonry types used are presented in **Table 6-2**. These values were obtained from the Italian normative [Italian Technical Code, 2008; Circolare 2 febbraio, 2009, n. 617, table C8A.2.1] where, for each description (class) of a type of masonry, a maximum and minimum value of the mechanical characteristics is present. It was decided, after selecting the masonry types to be adopted, to use the mean value of each class. Here, for masonry types stone masonry and brick masonry, it has been assumed that the masonry is already cracked and so a 50% reduction factor was used for the Young's Modulus and the Shear modulus. For the case of the rubble masonry this does not happen, since another source of information to obtain the Young's Modulus (**E**) was consulted. This has been some experimental testing carried out on one gable wall on the ground floor on a buildings in downtown that was being demolished [Pompeu Santos, 1997]. The value obtained here for **E** was about 1000 MPa being in accordance with the value of the chosen class of masonry – rubble masonry – with uncracked stiffness as can be seen in **Table 6-2**, second row. In any case, since the building is essentially rubble mansory, a sensitivity study on the

mechanical characteristics of this masonry could be done in future work. In another study carried out at the LERM laboratory recently and after decisions were taken with respect to the work presented here (see www.severes.org, report 2, from 2011), a specimen of rubble masonry with air lime and hydraulic lime, built in the laboratory, was tested. The results for the hydraulic lime were slightly different from the ones used here. In compression tests with specimen of $0.4 \times 0.4 \times 0.4 \text{ m}^3$ it was obtained 0.546 GPa for E and 8.0 MPa for f_m . In diagonal compression tests with the specimen of $1.2 \times 1.2 \times 0.7 \text{ m}^3$ it was obtained 0.252 GPa for G and 0.258 MPa for τ_0 .

Table 6-2: Mechanical characteristics of masonry types

Masonry type	Average Young's Modulus E [GPa]	Average Shear Modulus G [GPa]	Weight W [KN/m ³]	Average Compressive Strength f _m [MPa]	Average Shear Strength τ ₀ [MPa]
Stone Masonry	2.8*	0.86*	22	7	0.105
Rubble Masonry	1.23	0.41	20	2.5	0.043
Brick Masonry	1.5*	0.5*	18	3.2	0.076

* cracked stiffness assumed, 50% of the value in the table was used

The mechanical characteristics of the wood considered in this work are 12 GPa for the Young's Modulus and 0.2 for the Poisson ratio. The stairs have been modelled as floors with the following cross sections: $10 \times 10 \text{ cm}^2$ for the joists and 2 cm for the pavement. The joists run every 30 cm. In order to model the connections between "frontal" walls (referring to the top of the internal doors), in every floor, a timber beam has been included with section $10 \times 10 \text{ cm}^2$. In reality, and depending on the quality of the construction, at ground floor level quadripartite vaults, normal vaults or no vaults at all or only timber beams making the ground floor structure may exist. The chosen modelling approach has been to model only timber beams on the ground floor. However, the weights of the vaults have been considered in the analysis as presented in **Table 6-3**. The cross section of the timber beams considered has a width of 20 cm and a height of 30 cm. They are shown in **Figure 6-12**. In the same figure, the five ground floor pillars and the two sets of ground floor brick masonry walls are also depicted.

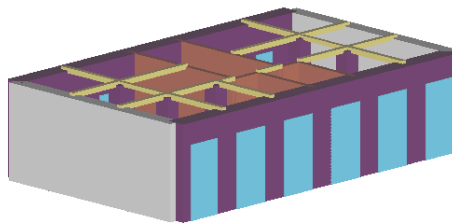


Figure 6-12: Ground floor modelling elements

The actions considered on the structure are the self-weight loads given by the weights of the roof, the floors, the ceilings, the partition walls and the "frontal" walls themselves combined with the live loads respectively given by Eurocode 1 [CEN,

2002]. The vertical loading to be imposed on the structure was determined based on Eurocode 1 [CEN, 2002], according to **Equation 4-1**.

Table 6-3: Vertical loads considered

Load type	Element	Value	Location
Live load	-	2 kN/m ²	Floors
Live load	-	4 kN/m ²	Stair floor
Dead load	Stairs	0.7 kN/m ²	Stair floor
Dead load	Compartment walls	0.1 kN/m ²	Floors
Dead load	Wooden floors	0.7 kN/m ²	Floors
Dead load	Ceilings	0.6 kN/m ²	Floors
Dead load	“Frontal” wall	3.0 kN/m	“Frontal” walls
Dead load	Vaults	3.5 kN/m	Masonry walls ground floor
Dead load	Gable walls roof	17.3 kN/m	Masonry walls 4 th floor
Dead load	Roof	4.4 kN/m	Masonry walls 4 th floor

The final model of the building is presented in **Figure 6-13**. Here, represented in grey are the parts of the structure that are composed of rubble masonry; in purple are the parts of the structure that are composed of stone masonry; in green (dark and light depending on the size) are the “frontal” walls and in light brown are the timber beams connecting the “frontal” walls.

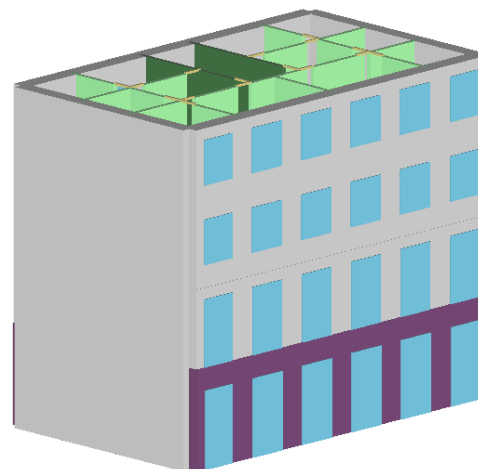


Figure 6-13: Final model of the building

Figure 6-14 identifies the alignments of the different structural elements in the plan view of the building.

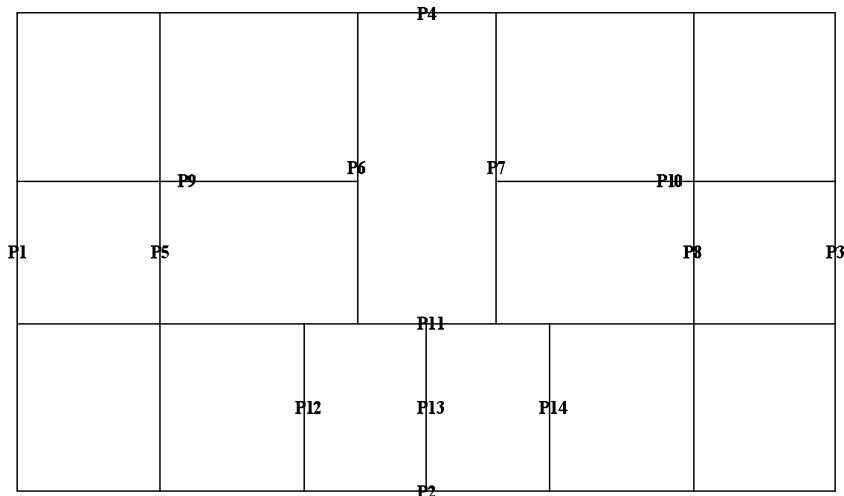


Figure 6-14: Numbering the alignments of the elements of the model

The software creates a mesh of macro-elements for each alignment and this can be viewed for front and back façades in **Figure 6-15** and **Figure 6-16**, respectively. The software attributes a colour to each element of the façades. In red are the macro-element piers; in green are the macro-element spandrels and in blue are the parts of the façade where no damage is foreseen (rigid nodes).

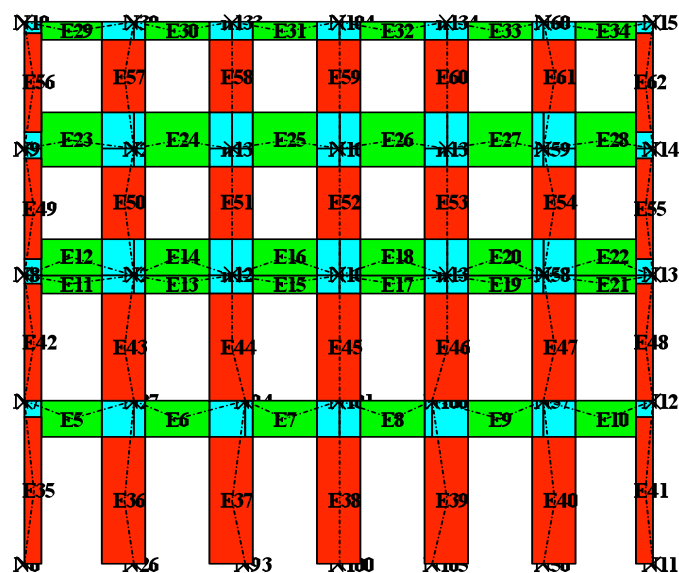


Figure 6-15: Macro-element mesh of front façade

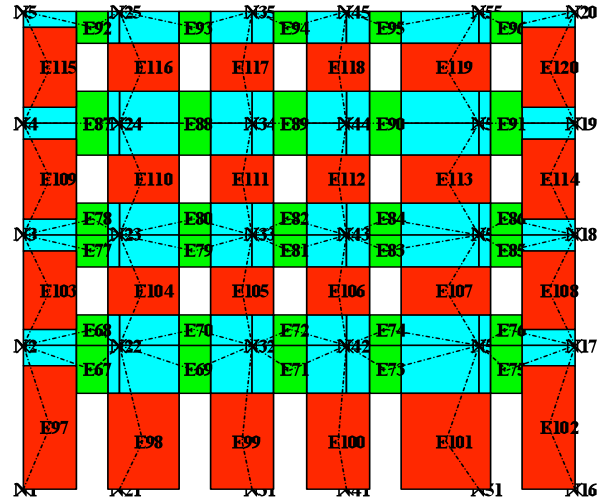


Figure 6-16: Macro-element mesh of back façade

6.4. Original building – analysis and results

By original building one refers to the building selected for analysis in the present work, without any retrofitting scheme. However, it should be noted, that, in reality, a considerable part of the building stock probably exists that is not in its original state but has been subjected to changes in its structural system. Many buildings have incorporated reinforced concrete elements or steel elements and/or the “frontal“ walls have been removed. It is foreseen that these changed buildings will have a behaviour that is worse than the original building analysed in this chapter.

Pushover analyses were carried out for both xx and yy directions (see **Figure 6-8**) and for two lateral load patterns:

- Load pattern proportional to the mass (uniform) and
- Load pattern proportional to the mass and height (triangular)

The pushover curves obtained are presented in **Figure 6-17**.

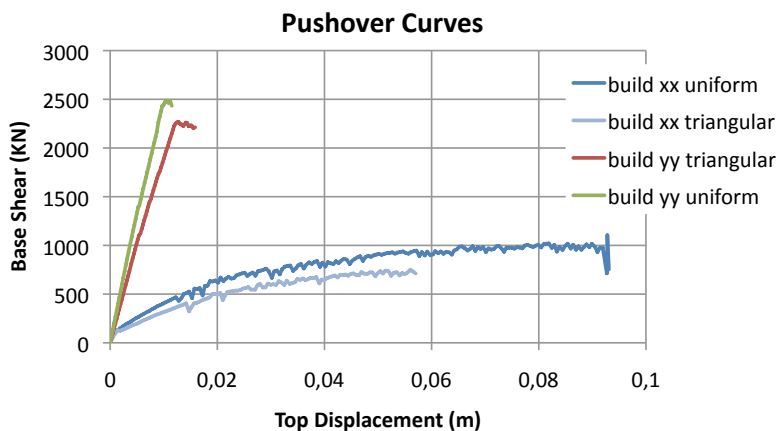


Figure 6-17: Pushover curves for original building in the two directions for both uniform and triangular load patterns

Based on the results obtained it is evident that the stiffness and strength is much higher in the yy direction than in the xx direction, actually, no opening is present in the two exterior walls in the yy direction. On the other hand, the ductility of the system is much higher on the xx direction and is practically non-existent in the yy direction. In fact, in xx direction piers are very slender (due to the opening's configuration) and with a very moderate coupling provided by spandrels (which show a “weak” behaviour due to the lack of other tensile resistant element coupled to them): thus, a prevailing flexural response occurs associated to higher drift than in case of the shear failure. In general the structure exhibits a soft storey failure mode; moreover, since floors are quite flexible, a very moderate redistribution of seismic loads may occur among masonry walls.

Comparing the results obtained with the two lateral load patterns, it can be seen how the *mass x height* load pattern (triangular) is more demanding than the load pattern proportional to the mass only (uniform load pattern), since the curves run below the later ones. Nevertheless, the difference is not so substantial. It has been decided, for the subsequent analyses, to consider only the load pattern proportional to the mass only. This is because the triangular load pattern is more advisable in structures which have a first mode with triangular shape and have a high participation factor on the first mode of vibration in a certain direction. However, this does not happen in masonry structures because these may have a first mode shape not so much triangular and, moreover, normally have a low participation factor for the first mode (in the order of 30% only). On the other hand, with triangular load pattern one has damage concentrated on the last floors (for the in-plane situation) and this is not what happens with masonry structures.

The criteria showed in **Figure 6-18** and based on the Italian normative [Italian Technical Code, 2008; Circolare 2 febbraio, 2009, n. 617, chapter C.7.3.4.1 and C.7.8.1.5.4] has been selected for the bi-linearization of the force – displacement relationships of the system. The maximum force (F_{max}) is calculated; then, the 70% of F_{max} permits the calculation of the stiffness of the bi-linearized system. The maximum force of the bi-linearized system (F_y) is defined based on the equal areas rule between the two plots.

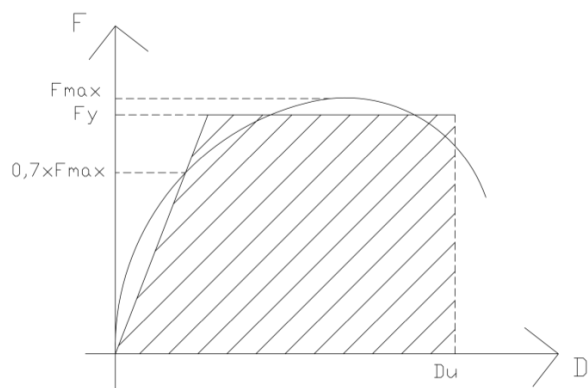


Figure 6-18: Bi-linearization of the force-displacement relationships

The bi-linearized curve in the xx direction can be seen in **Figure 6-19**. First an ultimate displacement, D_u , was selected based on the last value of the pushover curve, and then the system was bi-linearized according to the rules previously described.

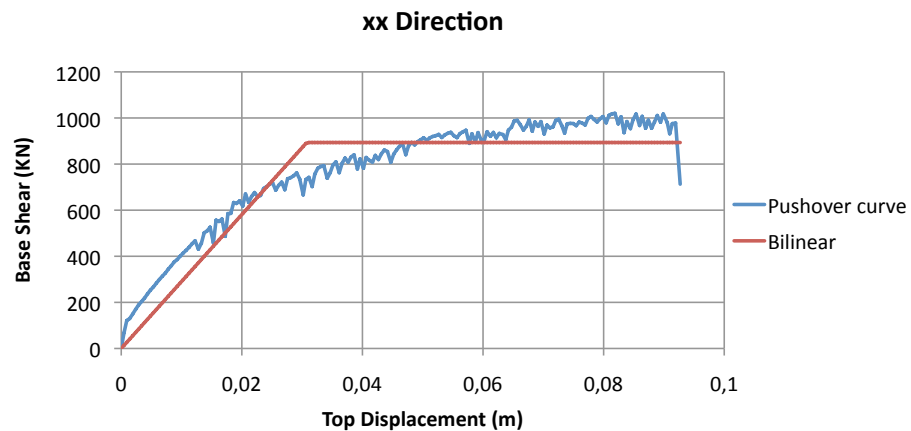


Figure 6-19: Bi-linearized curve in the xx direction for original building

The bi-linearized curve in the yy direction is presented in **Figure 6-20**.

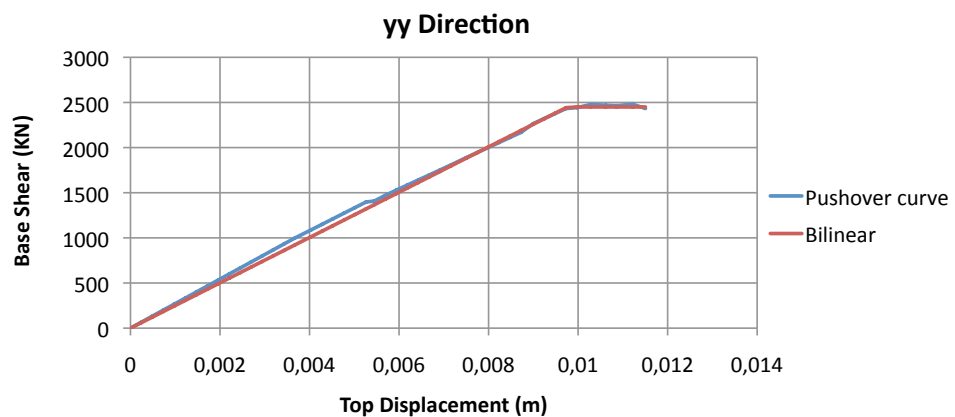


Figure 6-20: Bi-linearized curve in the yy direction for original building

The corresponding values of the ultimate displacement selected (D_u), the maximum force accomplished (F_{max}), the force at 70% of the maximum force ($0.7F_{max}$), the displacement at 70% of the maximum force ($Displ\ 0.7$), the stiffness (K), the area under the pushover curve (Area), the maximum force of the bi-linear system (F_y) and the area under the bi-linear system (Area bilinear) are presented in **Table 6-4** for the two directions.

Table 6-4: Bi-linear values for the two directions

Du xx (m)	Du yy (m)
0.0927	0.0115
Fmax xx (KN)	Fmax yy (KN)
1020.2	2480.0
0.7Fmax xx (KN)	0.7Fmax yy (KN)
714.2	1736.0
Displ 0.7 xx (m)	Displ 0.7 yy (m)
0.024586	0.006918
K xx (KN/m)	K yy (KN/m)
29047.3	250936.7
Area xx (KN.m)	Area yy (KN.m)
71.84	19.71
Fy xx (KN)	Fy yy (KN)
893.5	2450.0
Area bilinear xx (KN.m)	Area bilinear yy (KN.m)
71.84	19.71

It can be noticed that the area under the pushover curve is the same as the area under the bi-linear curve, as required. The modal participation factor in the two directions (Γ_{xx} and Γ_{yy}), the equivalent mass in the two directions (m^*_{xx} and m^*_{yy}) and the elastic period of the idealized bilinear systems in the two directions (T^*_{xx} and T^*_{yy}) are defined in **Table 6-5**.

Table 6-5: Modal participation factors, equivalent mass and period of vibration in the two directions

Γ_{xx}	Γ_{yy}
1.33	1.43
$m^*_{xx} (\text{Kg})$	$m^*_{yy} (\text{Kg})$
683212.77	593475.25
$T^*_{xx} (\text{s})$	$T^*_{yy} (\text{s})$
0.964	0.306

Then, capacity diagrams in AD format are obtained for the two directions (**Figure 6-21** and **Figure 6-22**).

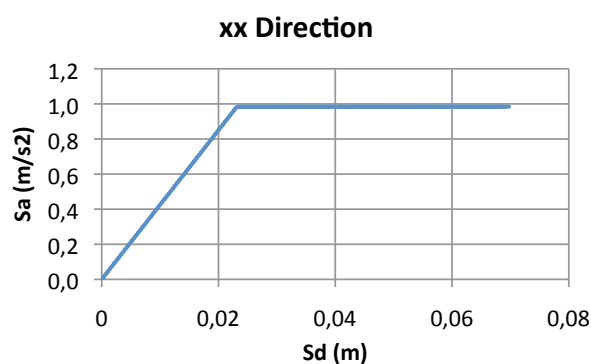


Figure 6-21: Capacity diagram in AD format in the xx direction

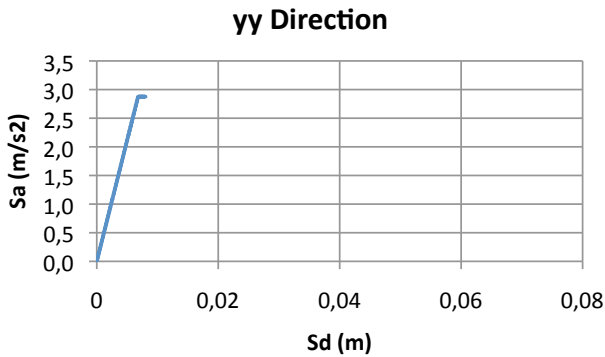


Figure 6-22: Capacity diagram in AD format in the yy direction

Finally, and according to the N2 method, the different quantities defined in section 6.2 are calculated for each earthquake type (1 and 2) and for each direction (**Table 6-6**).

Table 6-6: N2 method parameters for each earthquake type and each direction

	xx direction	yy direction
EQ type 1	EQ type 1	
$T^* \geq T_c$	$T^* < T_c$	
R_μ	3.558	1.955
$S_{de}(T^*)$ (m)	0.082	0.013
S_d (m)	0.082	0.020
S_d^{MDOF} (m)	0.109	0.028
a_g^{\max} (m/s ²)	1.271	0.837
D_u / S_d^{MDOF}	0.847	0.410
EQ type 2	EQ type 2	
$T^* \geq T_c$	$T^* \geq T_c$	
R_μ	1.680	1.813
$S_{de}(T^*)$ (m)	0.039	0.012
S_d (m)	0.039	0.012
S_d^{MDOF} (m)	0.052	0.018
a_g^{\max} (m/s ²)	3.049	1.105
D_u / S_d^{MDOF}	1.794	0.650

The values of D_u (ultimate displacement of the structure) must be compared with the values from S_d^{MDOF} (demand displacement of the structure, $S_d^{MDOF} = \Gamma \cdot S_d$). If the ratio D_u / S_d^{MDOF} is larger than 1 then the structure is verified according to the Eurocode 8 criterion, if not then the structure does not comply and should be strengthened. The values of a_g^{\max} are the values corresponding to the maximum admissible ground acceleration for the ultimate displacement of the structure, D_u . These values should be compared with the values of the demand: $a_g=1.5$ m/s² for earthquake type 1 and $a_g=1.7$ m/s² for earthquake type 2. The following formulas are used for the calculation of a_g^{\max} (**Equation 6-19** and **Equation 6-20**):

$$a_g^{\max} = \frac{F_y^*/m^*}{2.5S\eta} \left[1 + \frac{T^*}{Tc} \left(\frac{Du/\Gamma}{F_y^*/m^*(T^*/2\pi)^2} - 1 \right) \right] \quad \text{for } T^* < Tc \quad (\text{Equation 6-19})$$

$$a_g^{\max} = \frac{Du/\Gamma}{2.5S\eta} \frac{(2\pi)^2}{T^* Tc} \quad \text{for } T^* \geq Tc \quad (\text{Equation 6-20})$$

According to the results obtained, the structure does NOT fulfil the requirements of the Eurocode 8 criterion based on the N2 method for the following situations: earthquake type 1 and xx direction, earthquake type 1 and yy direction and earthquake type 2 and yy direction. It only fulfils the requirement for earthquake type 2 in the xx direction. Since the requirements must be fulfilled for all the situations, one can conclude that the original structure (structure without any kind of retrofitting) does NOT fulfil the requirements of the Eurocode 8 criteria based on the N2 method. For that reason, several retrofitting techniques are proposed in the following sections.

6.5. Strengthening solutions

The heritage value of the *Pombalino* buildings is recognized now in Portugal. People are becoming more and more conscious and regard these buildings as a common heritage. The common responsibility to safeguard them for future generations is recognized. Nevertheless, it has not been always like this and the buildings have suffered severe changes throughout the centuries. Back in 1964, the Second International Congress of Architects and Technicians of Historical Monuments, in Venice, adopted 13 resolutions, the first one being the International Restoration Charter, better known as the Venice Charter (see <http://www.international.icomos.org/venicecharter2004/>), and the second one, put forward by UNESCO, provided for the creation of the International Council on Monuments and Sites (ICOMOS). The Venice Charter stated that it is essential that the principles guiding the preservation and restoration of ancient buildings should be agreed and laid down on an international basis, with each country being responsible for applying the plan within the framework of its own culture and traditions. Later on in 2004, the term *reversibility* of intervention, not mentioned in the Venice Charter, has in the meantime become common in connection with conservation/ restoration/ renovation issues and the conservation/ preservation measures of monuments. Of course, our monuments with all their later changes and additions which indeed are to be accepted on principle as part of the historic fabric are the result of irreversible historic processes, but one should try that new interventions should be reversible.

The following strengthening solutions proposed have been mainly based on engineering judgement after careful study of the basic configuration of the *Pombalino* structure. The basic configuration of the typical *Pombalino* building that has been analyzed is characterized by quite flexible wooden floors (not able to provide a satisfying seismic load redistribution among masonry walls in non-linear phase) and weak spandrels (without any tensile resistant element coupled to them). Pushover analyses performed on this basic configuration showed a significant difference between the seismic capacity of the building in xx and yy directions, in particular: the stiffness and strength is much higher in the yy direction than in the xx direction; but

on the other hand, the ductility of the system is much higher on the xx direction and is practically non-existing in the yy direction. Due to the configuration of ground floor, a soft storey failure mechanism has been stressed. As known, all the above mentioned aspects - strength, stiffness and ductility - play a fundamental role in the seismic assessment and neither of two directions seems provide an effective system against the earthquake.

Due to this, the following retrofitting schemes have been proposed and analysed:

- 1- Increase the in-plane stiffness of floors (transforming flexible floors into rigid floors);
- 2- Increase the in-plane stiffness of floors plus reinforcement of the five ground floor pillars;
- 3- Increase the in-plane stiffness of floors plus inclusion of four shear walls on the ground floor;
- 4- Increase the in-plane stiffness of floors plus inclusion of eight steel frames on the ground floor;
- 5- Increase the in-plane stiffness of floors plus inclusion of tie-rods at front and back façades.

The first one is the most evident and the one that will be seen to be the most effective and crucial improvement to the structure. The second one will not be seen to bring too much additional improvements to the seismic behaviour of the structure and the last three are seen to be added improvements to the structure if one wishes to increase the earthquake resistance of the building even more.

The first intervention may be reversible or not, depending however on the type of intervention as will be seen in section 6.5.1. All the other interventions are reversible except for the second one regarding the reinforcement of the five ground floor pillars.

6.5.1. Increase the in-plane stiffness of floors

Traditional timber floors are typically flexible. As has been mentioned in the introduction the increase of the in-plane stiffness of floors is an evident and most effective method of improving the seismic behaviour of old masonry structures. This is mainly because the increase of in-plane stiffness of floors enables the horizontal forces to be redistributed between the failing walls to the adjacent remaining walls and the structure behaves like a box. A significant role in the stability of the entire building is assigned to the floors. These structures are required, in addition to an adequate performance level, a remarkable rigidity and an efficient connection to the supporting walls, especially in what concerns seismic actions. For this reason, the restoration of a floor is an opportunity to improve the behaviour and efficiency of the entire structure.

A technique well spread for the in-plane reinforcement of wooden floors, consists on placing over the existing deck a concrete slab, usually reinforced with a metallic net, and anchored to the existent floor by pins or connectors fixed on the top edge of the beams, which cross the planking and are embedded in the concrete slab and connected to the metallic net, **Figure 6-23**.

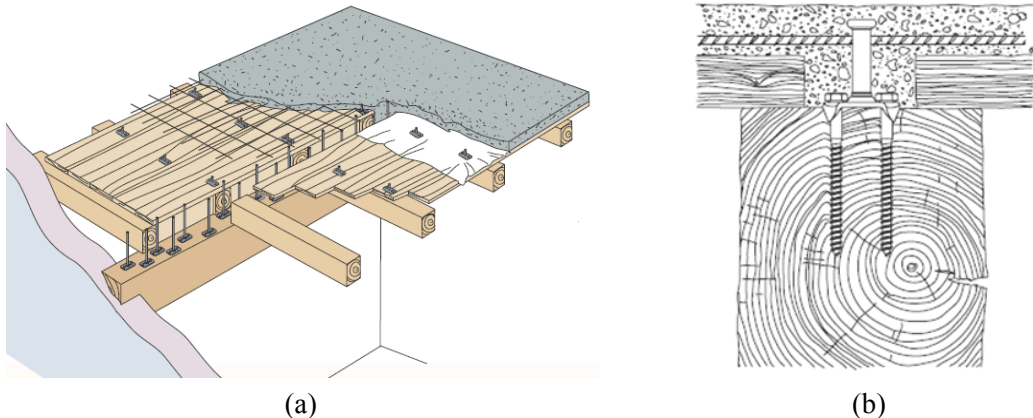


Figure 6-23: (a) Example of the reinforcement of a wooden floor with a cooperating reinforced-concrete slab, (www.tecnaria.com) (b) Basic connectors Tecnaria (www.tecnaria.com)

The structural particularity of this type of intervention is the connection between wood and concrete, designed to transmit shear forces parallel to the structure, between the beams and slab. There's no advantage in overlaying the slab without linking it to the pre-existent structure, because the two structures would work independently. Finally, it should be noted that this reinforcement technique, developed in the last 20 years, allows to significantly increase the floor's in-plane bending stiffness, however, it leads to a weight gain for the deck, resulting in increase of the seismic actions. Thus, it is important to limit the concrete thickness to 5 to 10 cm. The technique is also not reversible.

Another possible technique is the idea of including on the floor a horizontal bracing composed of steel ties and arranged in crosses (Figure 6-24) and this technique has been developed for many decades. Care is taken to improve the connection between the floor and the masonry wall with L-shaped steel plates (see Figure 6-24). On the contrary to the previous technique this one does not increases the weights of the floors and is reversible.



Figure 6-24: In-plane stiffening with metallic diagonals and reinforcement of connection floor-wall [picture from Edifer]

In order to model the increase of in-plane stiffness of floors, the shear stiffness of the floors was increased by an order of 100.

Pushover analyses were carried out for both xx and yy directions. The contribution that each alignment (walls) has to the base shear of the building was also evaluated in both directions. For this purpose, and taking the xx direction as an example, (**Figure 6-25**) a graph was plotted with, firstly, the total base shear as a function of the top displacement (“Building” legend), secondly, the base shear corresponding to the façade masonry walls (P2 and P4 alignments) as a function of the respective top displacement of that alignment (“P2” and “P4” legend) and, thirdly, the base shear corresponding to the alignments of the “frontal” walls as a function of the respective top displacement of that alignment (“P11”, “P9” and “P10” legend).

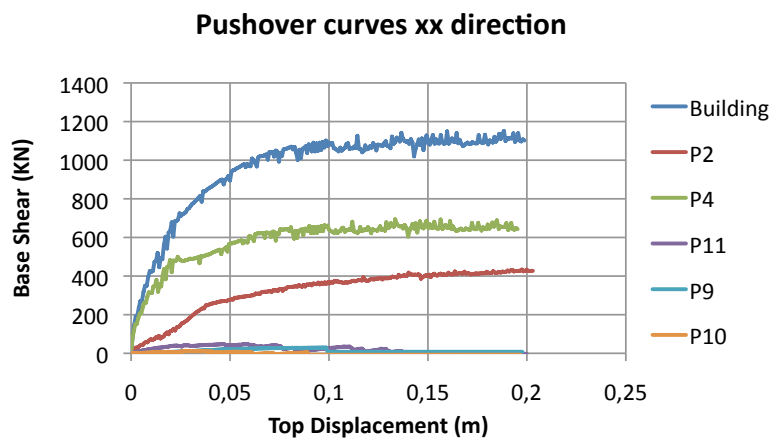


Figure 6-25: Pushover curves, contribution of each wall to the base shear, xx direction

The same was done in the yy direction as presented in **Figure 6-26**. The number of the alignments can be seen again in **Figure 6-14**.

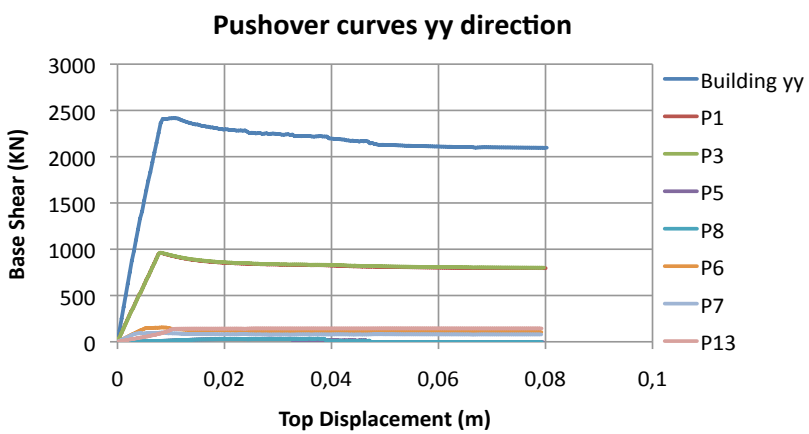


Figure 6-26: Pushover curves, contribution of each wall to the base shear, yy direction

Based on the previous graphs, the highest contribution to the base shear comes from the outside masonry walls. The contribution to the base shear given by the internal walls is not negligible but is very small. In other words, the “frontal” walls/internal

walls alignments contribute very little to the total base shear of the building, the majority of this force being a contribution of the surrounding masonry walls. This is because the “frontal” walls do not have continuity in height, they are interrupted at ground, floor and not because of their lower stiffness when compared to the masonry walls.

With respect to the fact that the “frontal” walls have lower stiffness when compared to the surrounding masonry walls, one can confirm this by taking a look at **Figure 6-27**. Here a comparison is made between a “frontal” wall of dimensions C2x2 and a masonry wall of equivalent dimensions (height 2.48 m; width 2.56 m; thickness 0.15 m). The masonry wall is composed of rubble masonry. The masonry panel has strength (73 kN) associated to shear failure for a vertical stress over the compressive strength of the panel of 0.2. It is represented an ultimate drift of 0.4% for the masonry panel.

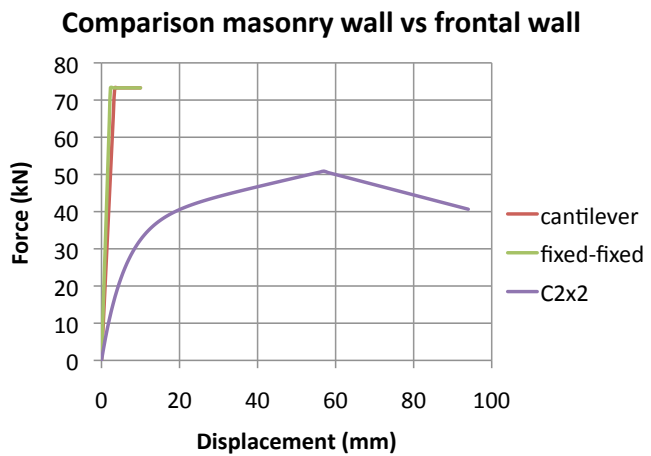


Figure 6-27: Comparison between a masonry wall and a “frontal” wall of the same dimensions

The stiffness is calculated for a masonry panel for a fixed-fixed and a cantilever support conditions according to **Equation 6-21** and **Equation 6-22**, respectively.

$$K = \left(\frac{H^3}{12EI} + \frac{H}{A_v G} \right) \quad \text{Equation 6-21}$$

$$K = \left(\frac{H^3}{3EI} + \frac{H}{A_v G} \right)^{-1} \quad \text{Equation 6-22}$$

By observing **Figure 6-27** one can see how the “frontal” walls have lower stiffness when compared to a masonry wall of approximately the same size. From this observation one can conclude that the stiffness of the “frontal” wall is much lower when compared to the thick surrounding masonry walls of the *Pombalino* buildings.

In **Figure 6-28** the pushover curves in the xx and yy directions are compared for retrofitted building 1 (rigid floor).

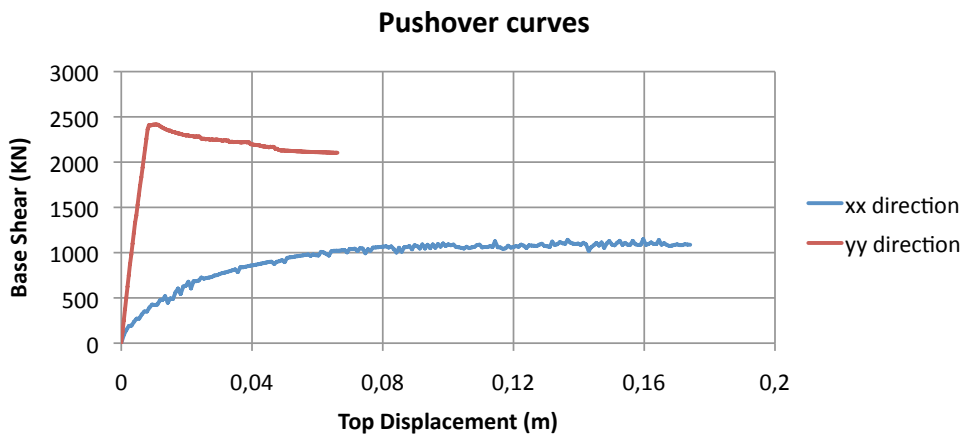


Figure 6-28: Pushover curves for retrofitted building 1 in the two directions

From the results obtained it can be seen again how the stiffness and strength is more pronounced in the yy direction than in the xx direction. This is because on the yy direction there are no openings in the masonry walls. When compared to the case of flexible floors, the increase of ductility in the pushover curves is evident in both directions but mainly in the yy direction.

For this strengthened solution, the ultimate displacement (D_u) was defined based on the value of the pushover curve corresponding to a drift value of 1.2 % of the pillars on the ground floor; it is assumed that, when the pillars reach this value of drift, they collapse and this is assumed to be the collapse of the building. The pillar drifts as a function of the top displacement are represented in Figure 6-29 for the xx direction. The pillar drift of 1.2% corresponds, in the xx direction, to a top displacement of 0.174 m. The pillar numbers can be identified in Figure 6-8.

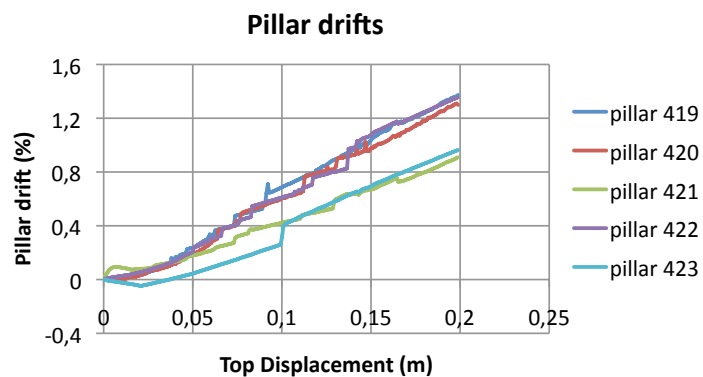


Figure 6-29: Pillar drifts as a function of the top displacement in the xx direction

The bi-linearized curve for the xx direction can be seen in Figure 6-30.

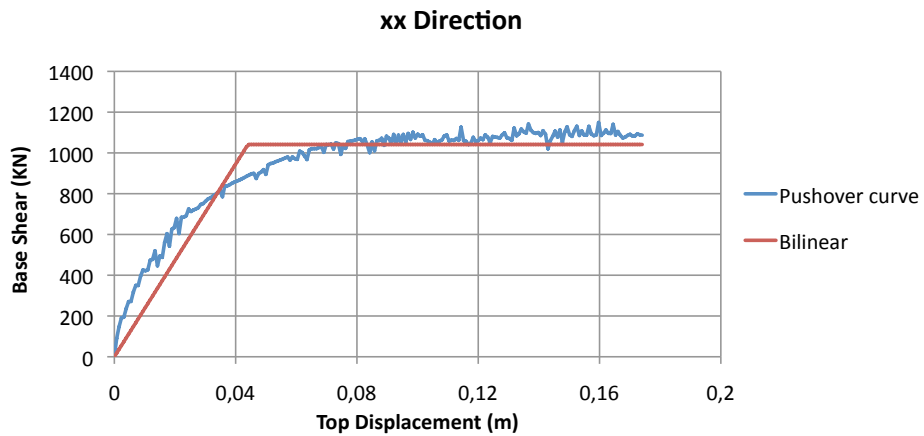


Figure 6-30: Bi-linearized curve in the xx direction for retrofitted building 1

For the yy direction, the variation of the drift of the pillars with top displacement is represented in **Figure 6-31**. The pillar drift of 1.2% corresponds, in the yy direction, to a top displacement of 0.066 m.

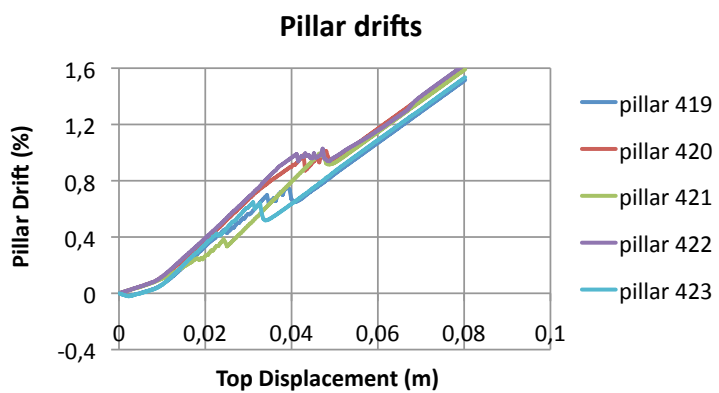


Figure 6-31: Pillar drifts as a function of the top displacement in the yy direction

The bi-linearized system in the yy direction can be seen in **Figure 6-32**.

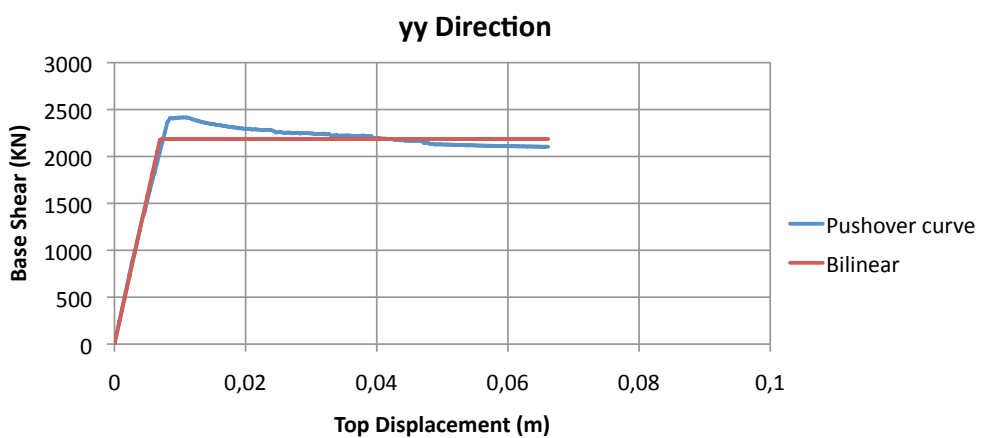


Figure 6-32: Bi-linearized curve in the yy direction for retrofitted building 1

The corresponding values of the ultimate displacement selected (D_u), the maximum force accomplished (F_{max}), the force at 70% of the maximum force (0.7 F_{max}), the displacement at 70% of the maximum force (Displ 0.7), the stiffness (K), the area under the pushover curve (Area), the maximum force of the bi-linear system (F_y) and the area under the bi-linear system (Area bilinear) are given in **Table 6-7** for the two directions for the retrofitted building 1.

Table 6-7: Bi-linear values for the two directions

D_u xx (m)	D_u yy (m)
0.1741	0.0661
F_{max} xx (KN)	F_{max} yy (KN)
1149.4	2416.0
0.7F_{max} xx (KN)	0.7F_{max} yy (KN)
804.6	1691.2
Displ 0.7 (m)	Displ 0.7 (m)
0.034047	0.00537
K xx (KN/m)	K yy (KN/m)
23630.9	314930.9
Area xx (KN.m)	Area yy (KN.m)
163.5	138.8
F_y xx (KN)	F_y yy (KN)
1041.3	2186.9
Area bilinear xx (KN.m)	Area bilinear yy (KN.m)
163.5	138.8

Table 6-8 presents the values of the modal participation factor in the two directions (Γ_{xx} and Γ_{yy}), the equivalent mass in the two directions (m^*_{xx} and m^*_{yy}) and the elastic period of the idealized bilinear system in the two directions (T^*_{xx} and T^*_{yy}).

Table 6-8: Modal participation factors, equivalent mass and period of vibration in the two directions

Γ xx	Γ yy
1.41	1.42
m^* xx (Kg)	m^* yy (Kg)
660130.77	638234.64
T^* xx (s)	T^* yy (s)
1.050	0.283

The capacity diagram in AD format is obtained for the two directions (**Figure 6-33** and **Figure 6-34**).

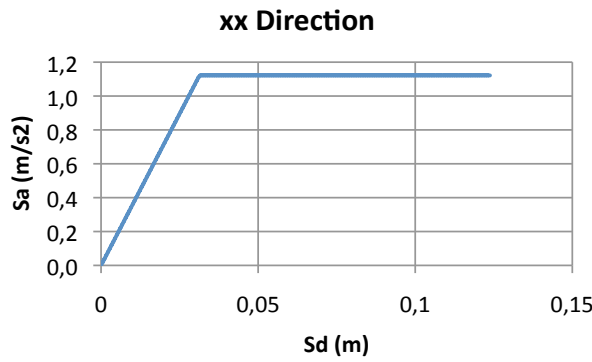


Figure 6-33: Capacity diagram in AD format in the xx direction for retrofitted building 1

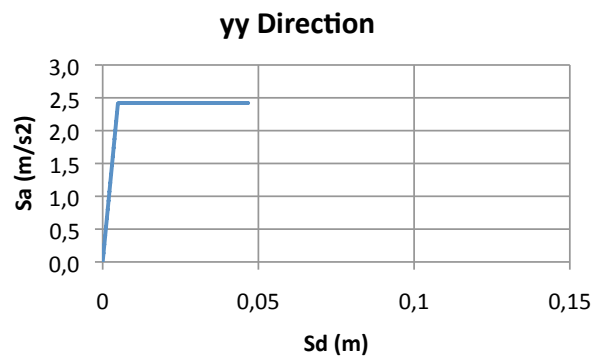


Figure 6-34: Capacity diagram in AD format in the yy direction for retrofitted building 1

Finally, and according to the N2 method, the different quantities are calculated for each earthquake type and each direction (**Table 6-9**).

Table 6-9: N2 method parameters for each earthquake type and each direction

	xx direction	yy direction
Rμ	EQ type 1	EQ type 1
Sde(T*) (m)	T*>=Tc	T*<Tc
Sd (m)	2.865	2.324
Sd^{MDOF} (m)	0.090	0.011
a_g^{max} (m/s²)	0.126	0.026
D_u/ Sd^{MDOF}	2.068	3.239
	1.379	2.501
Rμ	EQ type 2	EQ type 2
Sde(T*) (m)	T*>=Tc	T*>=Tc
Sd (m)	1.353	2.328
Sd^{MDOF} (m)	0.042	0.011
a_g^{max} (m/s²)	0.060	0.016
D_u/ Sd^{MDOF}	4.964	6.955
	2.920	4.091

The structure fulfils the requirements of the Eurocode 8 criteria based on the N2 method for all the situations (earthquake type 1 for xx and yy directions and earthquake type 2 for xx and yy directions) since D_u / S_d^{MDOF} is always greater than one. Retrofitting the structure by in-plane stiffening of diaphragms increases its resistance towards earthquakes and enables the structure to comply with the Eurocode 8 code criterion.

6.5.2. Increase the in-plane stiffness of floors plus reinforcement of five ground floor pillars

The pillars of the ground floor are a sensitive part of the masonry structure. It was realized that piers on the ground floor were very susceptible to failure. In fact, once they failed the whole building would fail also since it would lose its support. One measure that was thought of was to implement the reinforcement of the pillars on the ground floor as an additional measure, keeping the in-plane stiffening of the floors. To model this strengthened solution the stiffness and strength of the masonry associated with the pillars was multiplied by a factor of 1.4. This factor comes from the Italian normative [Italian Technical Code, 2008; Circolare 2 febbraio, 2009, n. 617, table C8A2.2].

Pushover analyses were carried out for both xx and yy directions. The pushover curves in the xx and yy directions are compared in **Figure 6-35** for retrofitted building 2 (rigid floor plus reinforced pillar).

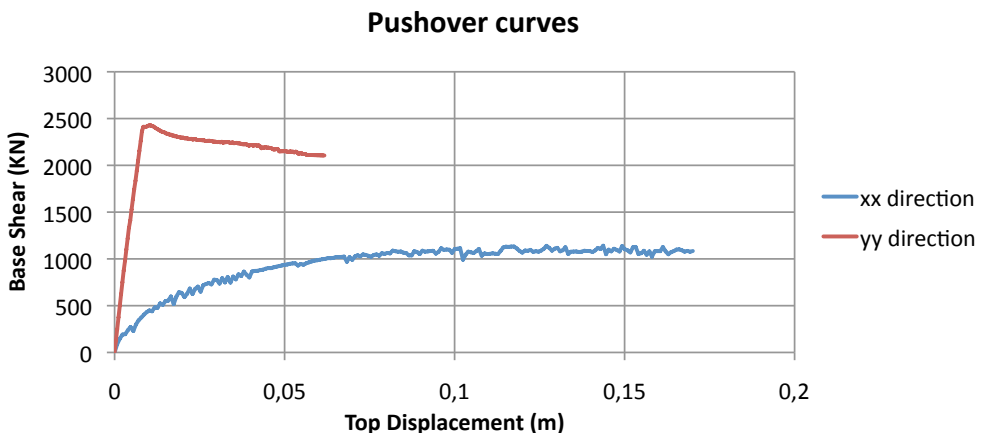


Figure 6-35: Pushover curves for retrofitted building 2 in the two directions

As it can be seen from the graph above, the stiffness and strength is again more pronounced in the yy direction than in the xx direction. Moreover, the pushover curves are almost identical to the previous case of only stiffening the floors (retrofitting building 1). The increase of pillar stiffness and strength does not significantly affect the pushover curves, maybe because the increase in stiffness and strength is not too pronounced.

Again, the ultimate displacement (D_u) was selected based on the value on the pushover curve corresponding to the drift of the ground floor pillars equal to 1.2%. The drifts of the different pillars as a function of the top displacement are represented

in **Figure 6-36** for the xx direction. The pillar drift of 1.2% corresponds, in the xx direction, to a top displacement of 0.170 m, almost identical to the previous case of only stiffening the floors.

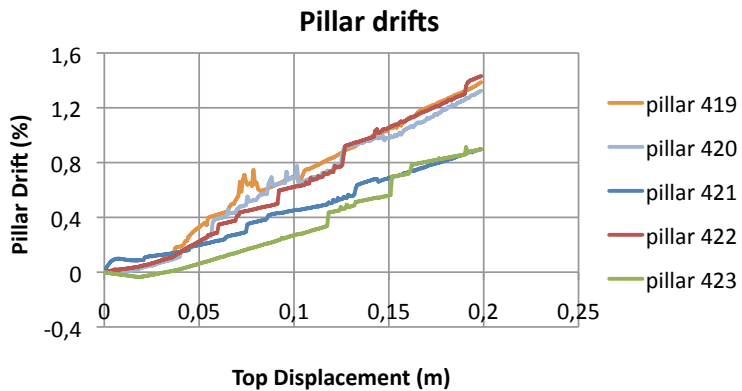


Figure 6-36: Pillar drifts as a function of the top displacement in the xx direction

The bi-linearized system in the xx direction can be seen in **Figure 6-37**.

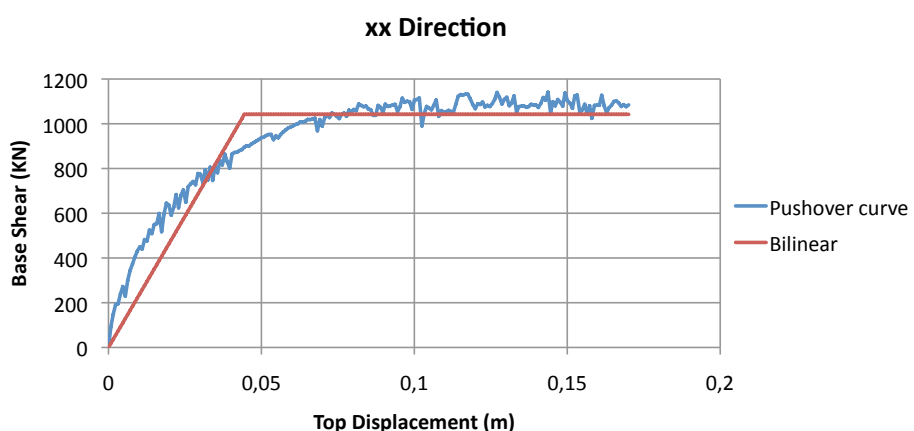


Figure 6-37: Bi-linearized curve in the xx direction for retrofitted building 2

Figure 6-38 represents, for the yy direction, the drift of the pillars versus the top displacement. The pillar drift of 1.2% corresponds, in the yy direction, to a top displacement of 0.062 m, similar to the previous case, retrofitted building 1.

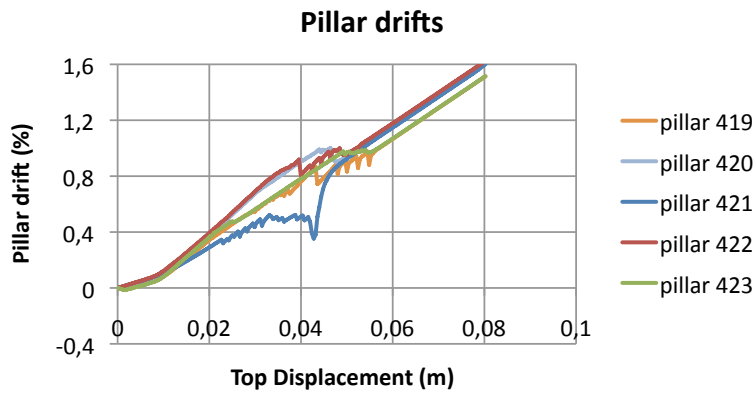


Figure 6-38: Pillar drifts as a function of the top displacement in the yy direction

The bi-linearized curve in the yy direction can be seen in **Figure 6-39**.

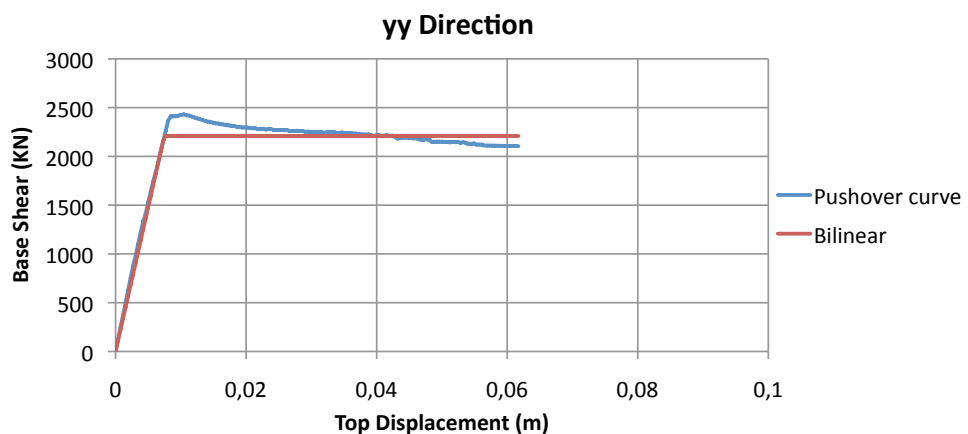


Figure 6-39: Bi-linearized curve in the yy direction for retrofitted building 2

The bilinear values for the two directions are presented in **Table 6-10** and the modal participation factor in the two directions (Γ_{xx} and Γ_{yy}), the equivalent mass in the two directions (m^{*xx} and m^{*yy}) and the elastic period of the idealized bilinear system in the two directions (T^{*xx} and T^{*yy}) are defined in **Table 6-11**. Both tables present the values for the retrofitted building 2.

Table 6-10: Bi-linear values for the two directions

Du xx (m)	Du yy (m)
0.1701	0.0617
Fmax xx (KN)	Fmax yy (KN)
1141.1	2431.1
0.7Fmax xx (KN)	0.7Fmax yy (KN)
798.7	1701.8
Displ 0.7 xx (m)	Displ 0.7 yy (m)
0.0341	0.0058
K xx (KN/m)	K yy (KN/m)
23438.7	295862.1
Area xx (KN.m)	Area yy (KN.m)
159.5	130.0
Fy xx (KN)	Fy yy (KN)
1042.0	2208.9
Area bilinear xx (KN.m)	A bilinear yy (KN.m)
159.5	130.0

Table 6-11: Modal participation factors, equivalent mass and period of vibration in the two directions

Γ_{xx}	Γ_{yy}
1.41	1.42
$m^*_{xx} (Kg)$	$m^*_{yy} (Kg)$
659574.34	638002.26
$T^*_{xx}(s)$	$T^*_{yy}(s)$
1.054	0.292

The capacity diagram in AD format is obtained for the two directions (**Figure 6-40** and **Figure 6-41**). Finally, and according to the N2 method, the different quantities are calculated for each earthquake type (1 and 2) and for each direction (**Table 6-12**).

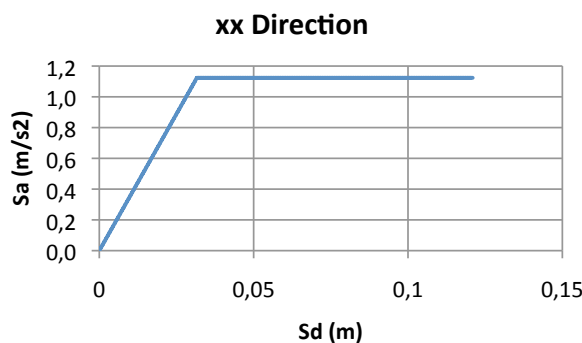


Figure 6-40: Capacity diagram in AD format in the xx direction for retrofitted building 2

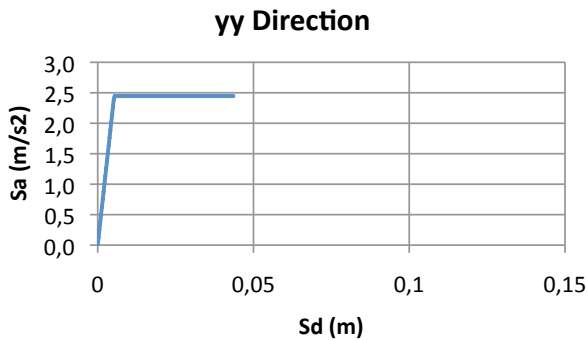


Figure 6-41: Capacity diagram in AD format in the yy direction for retrofitted building 2

Table 6-12: N2 method parameters for each earthquake type and each direction

	xx direction	yy direction
R μ	EQ type 1	EQ type 1
Sde(T*) (m)	T*>=Tc	T*<Tc
	2.850	2.300
Sd (m)	0.090	0.012
Sd ^{MDOF} (m)	0.090	0.019
a _g ^{max} (m/s ²)	0.127	0.027
Du/ Sd ^{MDOF}	2.014	2.957
R μ	1.342	2.250
Sde(T*) (m)	EQ type 2	EQ type 2
	T*>=Tc	T*>=Tc
Sd (m)	1.346	2.234
Sd ^{MDOF} (m)	0.043	0.012
a _g ^{max} (m/s ²)	0.043	0.012
Du/ Sd ^{MDOF}	0.060	0.017
	4.832	6.292
	2.843	3.701

The structure fulfils the requirements of the Eurocode 8 criteria for all the situations (earthquake type 1 and 2 and xx and yy directions) since Du/ Sd^{MDOF} is superior to one. Retrofitting the structure by in-plane stiffening of diaphragms together with reinforcement of the pillars increases its resistance towards earthquakes and enables the structure to comply with the Eurocode 8 criterion. Nevertheless, it is seen that the reinforcement of the pillars as additional measure of retrofitting does not bring any significant additional benefit to the seismic behaviour of the structure and thus is not recommended.

6.5.3. Increase the in-plane stiffness of floors plus inclusion of four shear walls on the ground floor

The inclusion of shear walls is a typical procedure for improving the seismic resistance of a building. It was decided that the inclusion of four shear walls on the ground floor be modelled according to the scheme presented in **Figure 6-42**. The shear walls are 48 cm thick and are composed of brick masonry. It was decided that the

shear walls should only be placed in the xx direction since this direction is the most vulnerable one and is the weakest direction (after the strengthening of the diaphragms). In this way the following results are only presented for the xx direction given that no additional retrofitting was included in the yy direction.

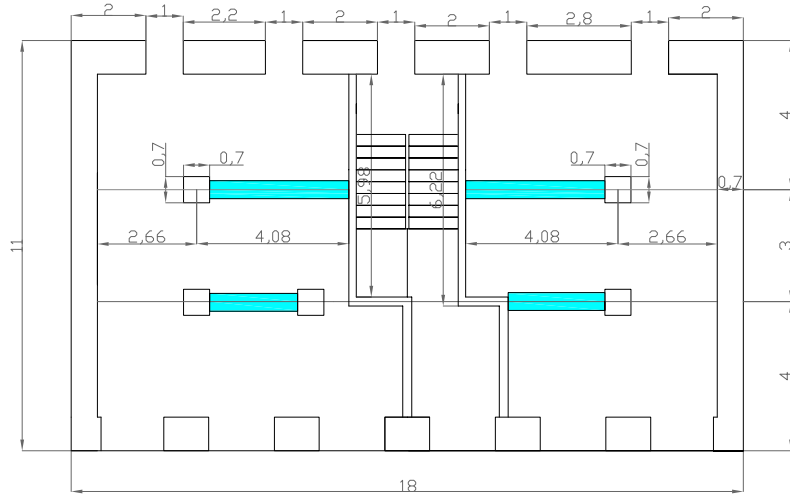


Figure 6-42: Positioning of the four shear walls at ground floor – units in meters

Pushover analysis was carried out for the xx direction. The pushover curves in the xx are compared in **Figure 6-43** for this strengthened building (rigid floor plus shear wall) to the pushover curve previously obtained in the yy direction.

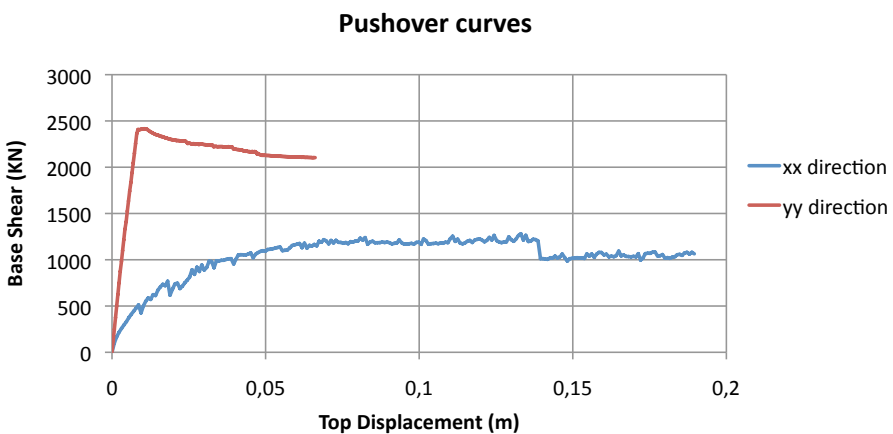


Figure 6-43: Pushover curves for retrofitted building 3 in the two directions

As in the previous cases, the stiffness and strength is more pronounced in the yy direction than in the xx direction. On the other hand, and comparing these results with the case of the rigid floor only it is seen that the stiffness and strength of the pushover curve has increased in the xx direction. This is obviously because the inclusion of the shear walls on the xx direction on the ground floor has a significant effect on the increase of stiffness and strength of the building. From the graph, one can see also a drop in this pushover curve. This is the point where the shear walls fail and the pushover curve comes down and back to the line defined by the pushover curve of the building with rigid floor but without shear walls.

Once again, the ultimate displacement was selected based on the value on the pushover curve corresponding to the drift of the pillars on the ground floor of 1.2%. The pillar drifts as a function of the top displacement is represented in **Figure 6-44** for the xx direction. The pillar drift of 1.2% (for the most critical pillar) corresponds, in the xx direction, to a top displacement of 0.190 m.

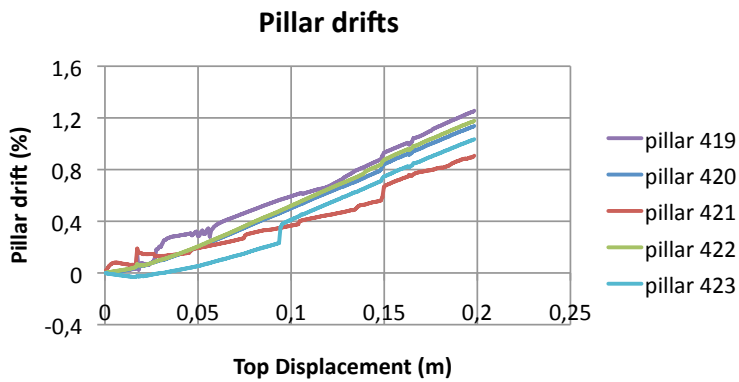


Figure 6-44: Pillar drifts as a function of the top displacement in the xx direction

The bi-linearized curve in the xx direction can be seen in **Figure 6-45**.

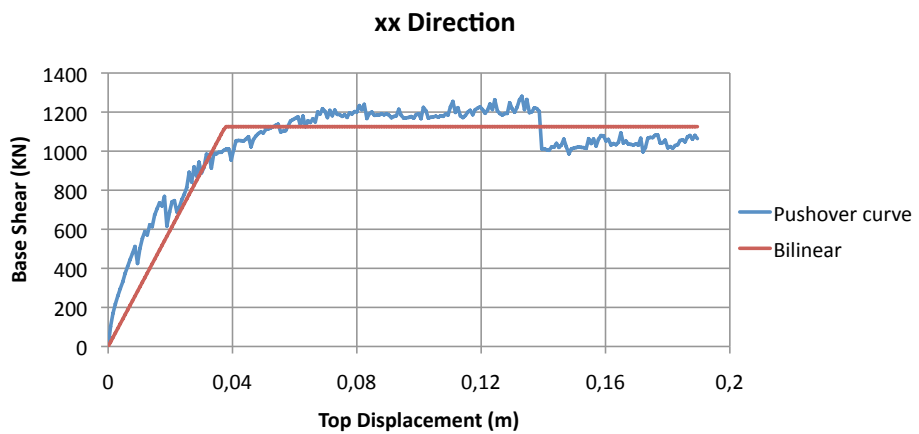


Figure 6-45: Bi-linearized curve in the xx direction for retrofitted building 3

Table 6-13 presents the bi-linear values defined for the xx direction for retrofitted building 3.

Table 6-13: Bi-linear values for the xx direction

Du xx (m)
0.1897
Fmax xx (KN)
1281.0
0.7Fmax xx (KN)
896.7
Displ 0.7 xx (m)
0.0300
K xx (KN/m)
29862.1
Area xx (KN.m)
196.5
Fy xx (KN)
1125.5
Area bilinear xx (KN.m)
196.5

The modal participation factor (Γ_{xx}), the equivalent mass (m^*_{xx}) and the elastic period of the idealized bilinear system (T^*_{xx}), all in the xx direction and for retrofitted building 3 are presented in **Table 6-14**.

Table 6-14: Modal participation factors, equivalent mass and period of vibration in the xx direction

Γ_{xx}
1.42
m^*_{xx} (Kg)
633180.83
T^*_{xx} (s)
0.915

The capacity diagram in AD format is obtained for the xx direction (**Figure 6-46**).

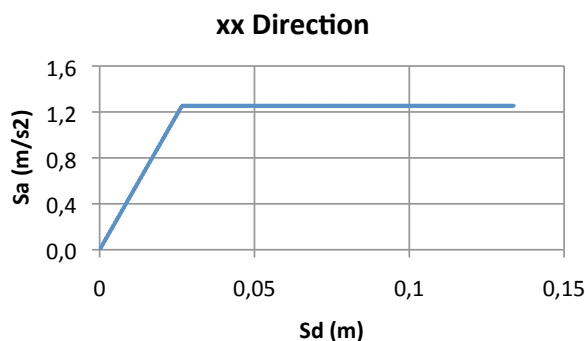


Figure 6-46: Capacity diagram in AD format in the xx direction for retrofitted building 3

Finally, according to the N2 method, the different quantities are calculated for each earthquake type (1 and 2) and for the xx direction (**Table 6-15**).

Table 6-15: N2 method parameters for each earthquake type in the xx direction

xx direction	
	EQ type 1
R_u	T*>=T _c
S_{de}(T*) (m)	2.942
S_d (m)	0.078
S_d^{MDOF} (m)	0.078
D_u/ S_d^{MDOF}	0.111
a_g^{max} (m/s²)	2.565
D_u/ S_d^{MDOF}	1.710
EQ type 2	
R_u	T*>=T _c
S_{de}(T*) (m)	1.389
S_d (m)	0.037
S_d^{MDOF} (m)	0.037
D_u/ S_d^{MDOF}	0.052
a_g^{max} (m/s²)	6.155
D_u/ S_d^{MDOF}	3.621

The structure fulfils the requirements of the Eurocode 8 criterion for all the situations since the ratio D_u/ S_d^{MDOF} is always greater than one. Retrofitting the structure with shear walls together with stiffening of the diaphragms enables the structure to comply with the Eurocode 8 criterion. The additional inclusion of shear walls with respect to the case of a rigid floor only gives additional stiffness and strength to the structure and enables it to withstand higher earthquake accelerations as is shown in **Table 6-15**. So, this strengthened solution is recommended as an additional retrofitting strategy, apart from the architectural limitations of this solution as is mentioned in section 6.5.4.

6.5.4. Increase the in-plane stiffness of floors plus inclusion of eight steel frames on the ground floor

The inclusion of eight steel frames on the ground floor comes from the idea that including shear walls with no openings on the ground floor is not a very much welcoming idea from the architectural and functional perspective. The ground floors of these buildings are often used as restaurants, cafés or stores facilities and the inclusion of shear walls here is not very convenient from the point of view of the owners. The eight steel frames (pillars and beams) are each one composed of four HEA140 cross sections. Again, it was decided that the steel frames should be placed only in the xx direction since this direction is the most vulnerable one and is the weakest direction. It was decided that the inclusion of eight steel frames on the ground floor be modelled according to the scheme presented in **Figure 6-47**.

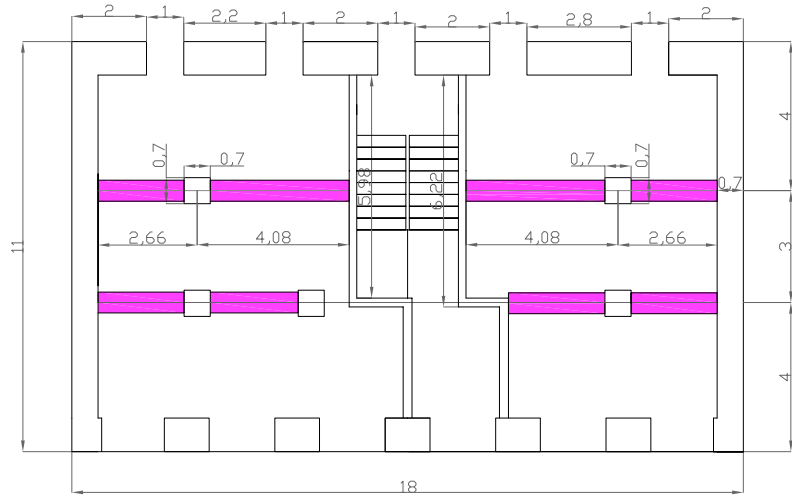


Figure 6-47: Positioning of the eight steel frames at ground floor – units in meters

Pushover analyses were carried out and the capacity curves were obtained for this retrofitted building (rigid floor plus steel frames). The capacity curves in the xx and yy directions are compared in **Figure 6-48**.

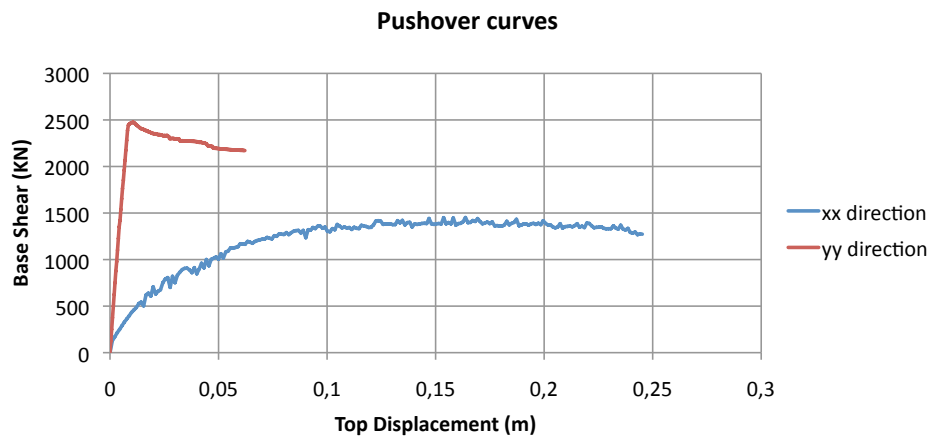


Figure 6-48: Pushover curves for retrofitted building 4 in the two directions

Comparing these results with the case of a rigid floor only (retrofitted building 1) it is seen that the strength of the pushover curve has increased in the xx direction (the retrofitted direction). This is obviously because the inclusion of the steel frames in the xx direction on the ground floor has a significant effect on the increase of strength of the building in this direction. Comparing these results with the previous case of the inclusion of rigid floors with shear walls on the ground floor one verifies that the strength of the building increases for the case of the inclusion of steel frames.

Again, the ultimate displacement was selected based on the value on the pushover curve corresponding to the drift of the pillars on the ground floor of 1.2%. The pillar drifts as a function of the top displacement can be seen in **Figure 6-49** for the xx direction. The pillar drift of 1.2% corresponds, in the xx direction, to a top displacement of 0.245 m.

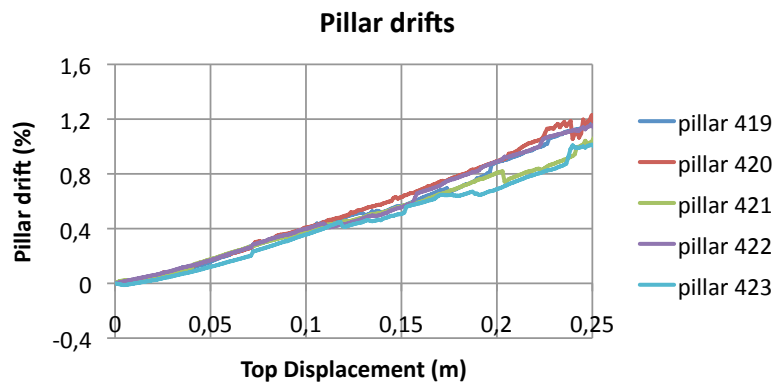


Figure 6-49: Pillar drifts as a function of the top displacement in the xx direction

The bi-linearized curve in the xx direction is represented in **Figure 6-50**.

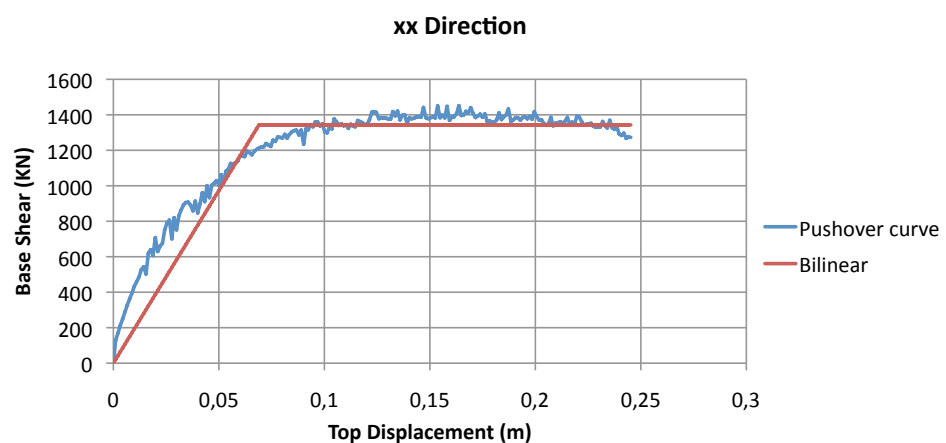


Figure 6-50: Bi-linearized curve in the xx direction for retrofitted building 4

The bi-linear values for the xx direction for retrofitted building 4 are seen in **Table 6-16**.

Table 6-16: Bi-linear values for the xx direction

Du xx (m)
0.2452
Fmax xx (KN)
1451.6
0.7Fmax xx (KN)
1016.1
Displ 0.7 xx (m)
0.0522
K xx (KN/m)
19459.1
Area xx (KN.m)
294.3
Fy xx (KN)
1343.1
Area bilinear xx (KN.m)
294.3

The modal participation factor (Γ_{xx}), the equivalent mass (m^*_{xx}) and the elastic period of the idealized bilinear system (T^*_{xx}) are represented in **Table 6-17** all for the xx direction.

Table 6-17: Modal participation factors, equivalent mass and period of vibration in the xx direction

Γ_{xx}
1.41
m^*_{xx} (Kg)
655743.64
T^*_{xx} (s)
1.534

The capacity diagram in AD format is obtained for the xx direction (**Figure 6-51**).

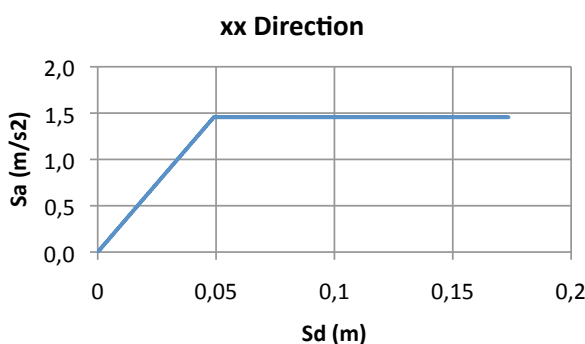


Figure 6-51: Capacity diagram in AD format in the xx direction for retrofitted building 4

At last, the different quantities of the N2 method are calculated for each earthquake type and the xx direction (**Table 6-18**).

Table 6-18: N2 method parameters for each earthquake type in the xx direction

xx direction	
	EQ type 1
R_μ	T*>=T _c
S_{de}(T*) (m)	2.010
S_d (m)	0.099
S_d^{MDOF} (m)	0.099
a_g^{max} (m/s²)	0.139
D_u/ S_d^{MDOF}	2.651
	1.768
EQ type 2	
R_μ	T*>=T _c
S_{de}(T*) (m)	0.949
S_d (m)	0.047
S_d^{MDOF} (m)	0.047
a_g^{max} (m/s²)	0.066
D_u/ S_d^{MDOF}	6.363
	3.743

Retrofitting the structure with steel frames together with the stiffening of the diaphragms enables the structure to comply with the Eurocode 8 criterion. The additional inclusion of steel frames with respect to the case of a rigid floor only gives additional strength to the structure and enables it to withstand higher earthquake accelerations as can be seen from **Table 6-18**. Thus, it is recommended as an additional retrofitting strategy.

6.5.5. Increase the in-plane stiffness of floors plus inclusion of tie-rods at front and back façades

The input file of the software was prepared for the case of tie-rods at the front and back façades. In the model bar elements with prestressing were introduced. The tie-rods are placed at the top of the piers (placed along the spandrels), connecting the piers between each other. They are pre-stressed, pre-stressing the spandrels. The tie-rods are of 2.4 cm in diameter and made of steel. An initial strain of 20% the yielding strain of the steel was used. The tie-rods were only placed in the xx direction, the most vulnerable one (if one strengthens the diaphragms). Pushover analyses were carried out. The pushover curves in the xx and yy directions are compared in **Figure 6-52** for this strengthened solution (rigid floors plus tie-rods).

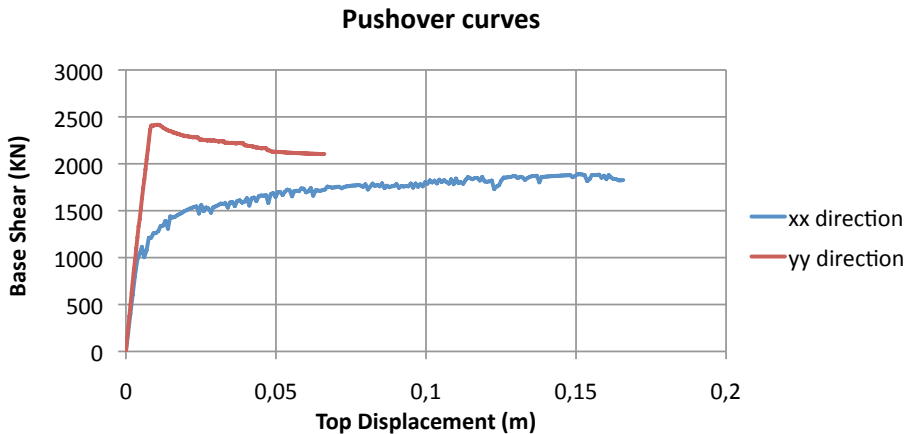


Figure 6-52: Pushover curves for retrofitted building 5 in the two directions

In this case it is seen how the stiffness and strength increases significantly in the xx direction. The stiffness in the xx direction is now similar to the stiffness in the yy direction. The strengths are almost similar too. It is also seen that the inclusion of tie-rods in the front and back façades in the xx direction has a more significant effect on the pushover curve than the inclusion of shear walls or steel frames on the ground floor.

The ultimate displacement was selected based on the value on the pushover curve corresponding to the drift of the pillars on the ground floor of 1.2%. The pillar drifts as a function of the top displacement can be seen in **Figure 6-53** for the xx direction. The pillar drift of 1.2% corresponds, in the xx direction, to a top displacement of 0.166 m.

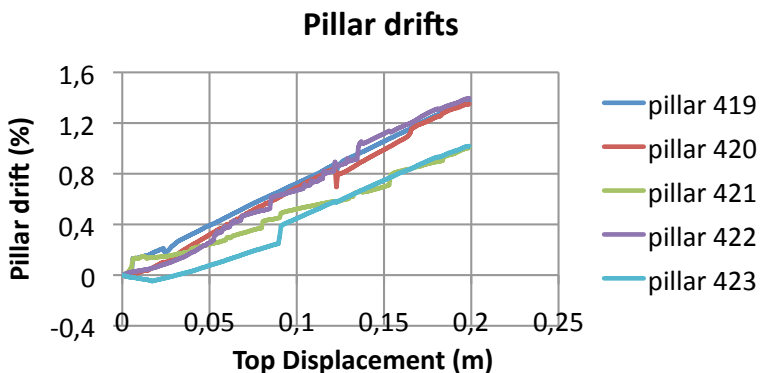


Figure 6-53: Pillar drifts as a function of the top displacement in the xx direction

The bi-linearized curve in the xx direction is represented in **Figure 6-54**:

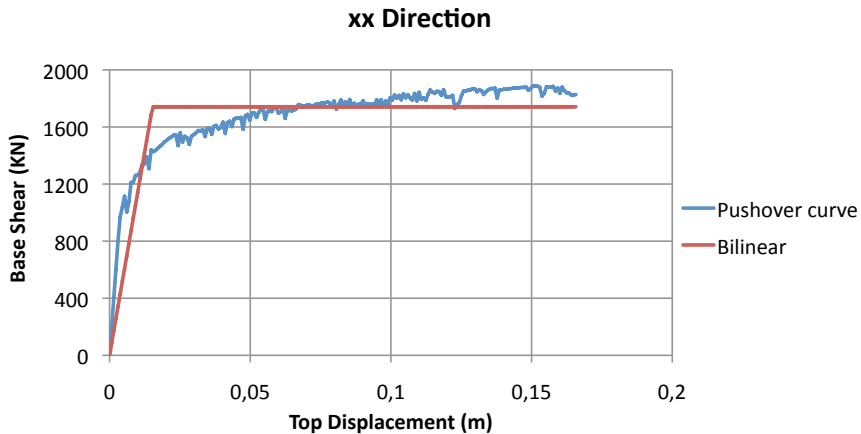


Figure 6-54: Bi-linearized curve in the xx direction for retrofitted building 5

Table 6-19 shows the bi-linear values for the xx direction for retrofitted building 5.

Table 6-19: Bi-linear values for the xx direction

Du (m)
0.1657
Fmax (kN)
1888.3
0.7Fmax (kN)
1321.8
Displ 0.7 (m)
0.0116
K (kN/m)
114126.0
Area (kN.m)
278.6
Fy (kN)
1741.6
Area bilinear (kN.m)
278.6

The modal participation factor (Γ_{xx}), the equivalent mass (m^{*}_{xx}) and the elastic period of the idealized bilinear system (T^{*}_{xx}) are represented in **Table 6-20** for the xx direction.

Table 6-20: Modal participation factors, equivalent mass and period of vibration in the xx direction

Γ_{xx}
1.41
m^{*}_{xx} (Kg)
660351.07
T^{*}_{xx} (s)
0.478

From **Table 6-20** one can see how the elastic period of the idealized bilinear system decreases significantly, as expected. The capacity diagram in AD format is obtained for the xx direction (**Figure 6-55**).

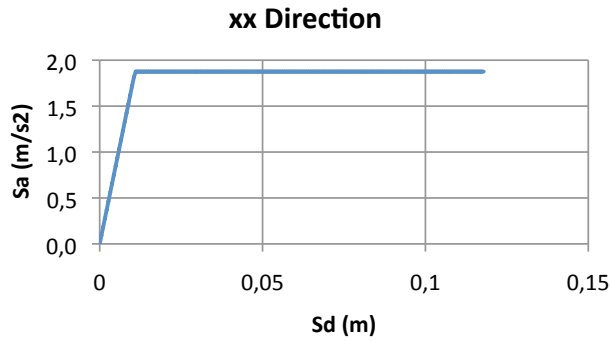


Figure 6-55: Capacity diagram in AD format in the xx direction for retrofitted building 5

In the end, the different quantities based on the N2 method are calculated for each earthquake type and the xx direction (**Table 6-21**).

Table 6-21: N2 method parameters for each earthquake type in the xx direction

EQ type 1	
R μ	T*<T _c
S _{de} (T*) (m)	2.998
S _d (m)	0.033
S _d ^{MDOF} (m)	0.038
a _g ^{max} (m/s ²)	0.054
D _u / S _d ^{MDOF}	4.430
	3.096
EQ type 2	
R μ	T*>=T _c
S _{de} (T*) (m)	1.777
S _d (m)	0.019
S _d ^{MDOF} (m)	0.019
a _g ^{max} (m/s ²)	0.027
D _u / S _d ^{MDOF}	10.388
	6.111

Retrofitting the structure with tie-rods at the front and back façades together with stiffening of the diaphragms enables the structure to comply with the Eurocode 8 criterion. The additional inclusion of tie-rods with respect to the case of the rigid floor only, gives significant additional stiffness and strength to the structure, in the xx direction, and enables it to withstand higher earthquake accelerations as can be seen from **Table 6-21**. Thus, it is recommended as an additional retrofitting strategy.

6.6. Comparison of the several retrofitting strategies

In order to have a better perspective of the benefits that each of the retrofitting strategies has, a graph was defined, comparing the capacity curves for all the cases studied. **Figure 6-56** and **Figure 6-57** show the comparison of the capacity curves for the xx and yy directions, respectively.

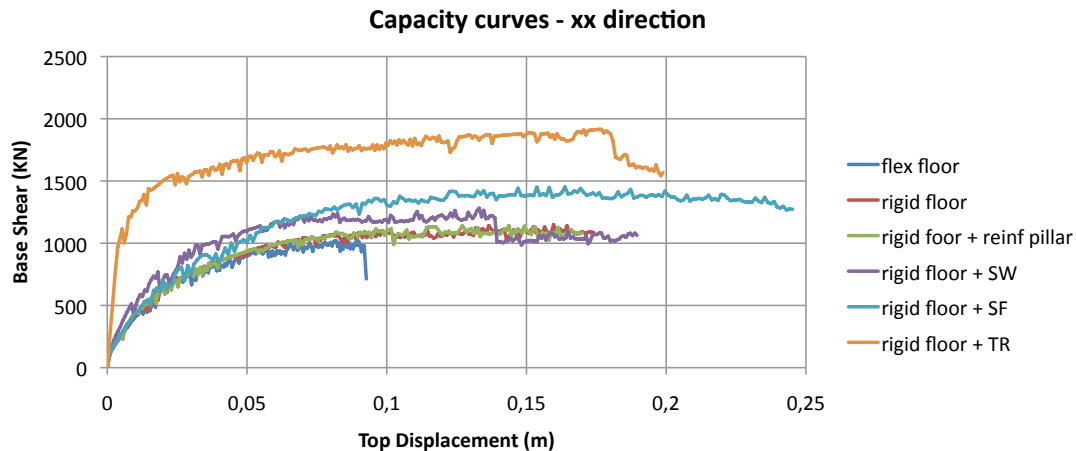


Figure 6-56: Capacity curves comparison in the xx direction

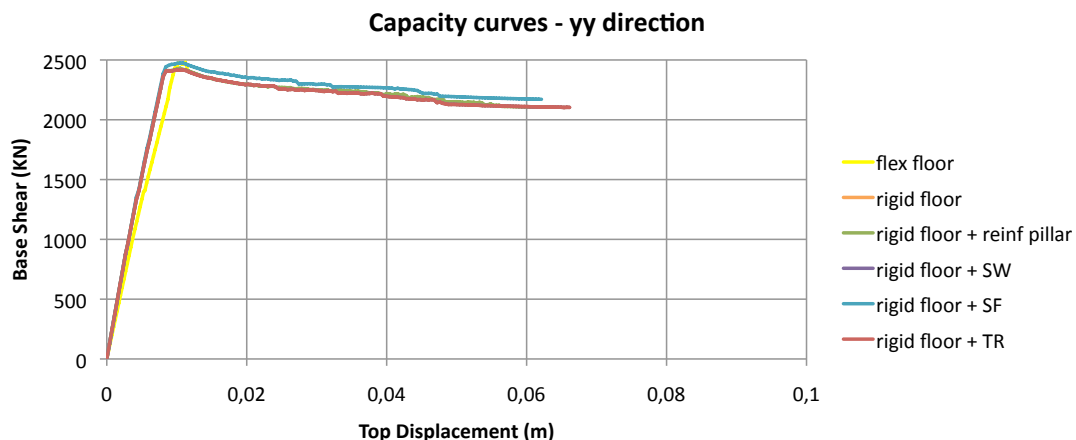


Figure 6-57: Capacity curves comparison in the yy direction (note: "rigid floor+reinf pillar", "rigid floor+SW" and "rigid floor+TR" coincides with "rigid floor")

Based on the results obtained, in the xx direction, going from the flexible floor situation to the rigid floor situation, one has an increase in the ultimate displacement D_u , while the initial stiffness and strength are the same. Moving from the case of rigid floor to the case of rigid floor with reinforced pillars brings no additional increase in ultimate displacement, stiffness or strength. Going from the case of rigid floor to the case of rigid floor with shear walls one can observe that an increase in stiffness and strength is obtained. Moving from the situation of rigid floor to the case of rigid floor plus steel frame one observes that the initial stiffness is maintained but the strength is increased and also the ultimate displacement. Finally, going from the situation of rigid floor only to the situation of rigid floor with tie-rods a significant increase in the initial stiffness is reached as well as in the strength value.

In the yy direction one can observe that all the curves are the same except the curve for the flexible floor since the only intervention influencing the yy direction has been the stiffening of the floors. All the other strengthening solutions have focused only in the xx direction.

The improvement of the several retrofitting strategies can also be evaluated by means of the maximum admissible ground acceleration, a_g^{max} . The values obtained for the xx and yy directions and for the original plus retrofitted situations are represented in **Figure 6-58**.

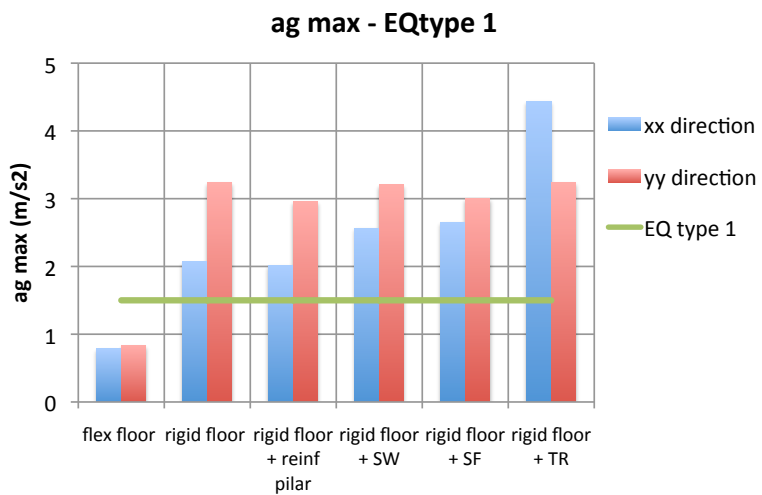


Figure 6-58: Maximum admissible ground acceleration, a_g^{max} , for the original and retrofitted buildings

The values of a_g^{max} are plotted in **Figure 6-58** for the most demanding situation, which is earthquake type 1. The values of a_g^{max} should, in this way, be compared to the value of 1.5 m/s^2 in order to assess if the structure fulfills the criteria in Eurocode 8 or not. As can be observed from the plot, retrofitting the structure with any of the retrofitting strategies makes the structure comply with the Eurocode 8 criterion based on the N2 method. Comparing the several retrofitting strategies one can observe that stiffening the floors is sufficient for the structure to comply with this criterion. Nevertheless, if it is intended to have a better performance one should either include shear walls or steel frames in the ground floor or tie-rods on the façades. Including tie-rods on the front and back façades increases the seismic performance in the xx direction quite significantly and enables it to perform better. In the yy direction the values of a_g^{max} are similar for all the retrofitting strategies since it was decided only to strengthen the most vulnerable direction after strengthening the diaphragms, i.e., the xx direction, (before strengthening the diaphragms the most vulnerable direction is the yy direction with negligible ductility).

6.7. Fragility analysis

6.7.1. Definition of damage limit states

Damage limit states have been established. The damage scale used in this work includes four levels of damage (plus the case of no damage): slight damage (1), moderate damage (2), heavy damage (3) and collapse (4). Damage limit states $S_{d,k}$ ($k=1$ to 4) are directly identified on the capacity diagrams in AD format as a function of the yielding displacement S_{dy} and the ultimate displacement S_{du} (**Figure 6-59** and **Equation 6-23**). These are based on the proposal present in Lagomarsino and Giovinazzi [2006].

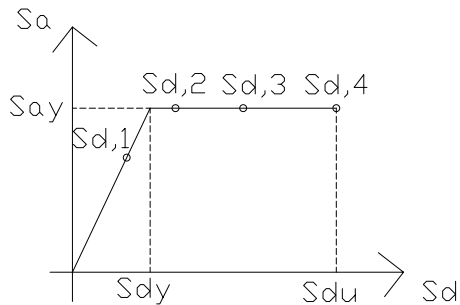


Figure 6-59: Damage limit states on the capacity diagram

$$\begin{aligned}
 S_{d,1} &= 0.7S_{dy} \\
 S_{d,2} &= 1.5S_{dy} \\
 S_{d,3} &= 0.5(S_{dy} + S_{du}) \\
 S_{d,4} &= S_{du}
 \end{aligned} \tag{Equation 6-23}$$

Slight damage (1) indicates a condition still far from the reaching of the maximum strength and corresponds to local damage in few structural elements. Moderate damage (2) corresponds to the maximum value of the restoring force in the pushover curve, and is located, in terms of spectral displacement, after the yielding condition of the equivalent bilinear (taking into consideration that the actual behaviour is curvilinear). Collapse (4) is defined on the basis of the ultimate displacement conditions for structural walls. Finally, heavy damage (3) lies in an intermediate position between moderate damage and collapse.

6.7.2. Fragility curves and damage probabilities

The values for the various uncertainties are defined in **Table 6-22** for each damage limit state. The uncertainties are various such as the uncertainty in the software model used (β_{model_error}), the uncertainty associated with the variability of the input parameters ($\beta_{capacity}$), the uncertainty associated with the variability of the seismic action (β_{demand}) and the uncertainty in the definition of the limit states (β_{limit_state}).

Table 6-22: Values of the various uncertainties for each damage limit state

β_k	damage limit state			
	1	2	3	4
β_{model_error}	0.25	0.25	0.25	0.25
$\beta_{capacity}$	0.35	0.35	0.37	0.38
β_{demand}	0.20	0.20	0.20	0.20
β_{limit_state}	0.24	0.26	0.18	0.14
β_{total}	0.53	0.54	0.51	0.49

The values of the β_{model_error} , the $\beta_{capacity}$ and the β_{limit_state} were all taken from Pagnini *et al* [2011]. The β_{demand} was intuitively assumed given not enough information was available for a more precise estimation of this value. In the paper of Pagnini *et al* [2011] a procedure for the probabilistic damage scenario assessment of masonry buildings on a large scale was presented. Starting from a non-linear mechanical model, an analytical description of the capacity curve and damage thresholds for in-line positioned aggregates are derived, which leave free a certain number of geometrical, mechanical and constructive parameters. Structural performance is assessed according to a probabilistic approach, which takes into account the actual variability of the structural response and seismic demand. For each limit state, fragility curves are determined, firstly, by expressing structural capacity and damage limit states as an analytical function, secondly, by obtaining the inelastic displacement demand according to the N2 method analytically and thirdly, by defining safety margins for each limit state. Values in **Table 6-22** show that the variability of the input parameters ($\beta_{capacity}$) is the main contributor to β_{total} .

6.7.2.1. Original building

In **Table 6-23** and **Table 6-24** one can see the parameters of the lognormal distribution function for the case of the original building, for earthquake type 1 and 2 and for the xx and yy directions.

Table 6-23: Parameters of the lognormal distribution function for the earthquake type 1 for both xx and yy directions

damage limit state	EQtype 1 xx direction				EQtype 1 yy direction			
	1	2	3	4	1	2	3	4
$a_{g,k}$ (m/s ²)	0.299	0.640	0.848	1.271	0.545	0.776	0.806	0.837

Table 6-24: Parameters of the lognormal distribution function for the earthquake type 2 for both xx and yy directions

damage limit state	EQtype 2 xx direction				EQtype 2 yy direction			
	1	2	3	4	1	2	3	4
$a_{g,k}$ (m/s ²)	0.717	1.535	2.036	3.049	0.671	0.958	1.032	1.105

Figure 6-60 and **Figure 6-61** show the fragility curves for the case of the original building.

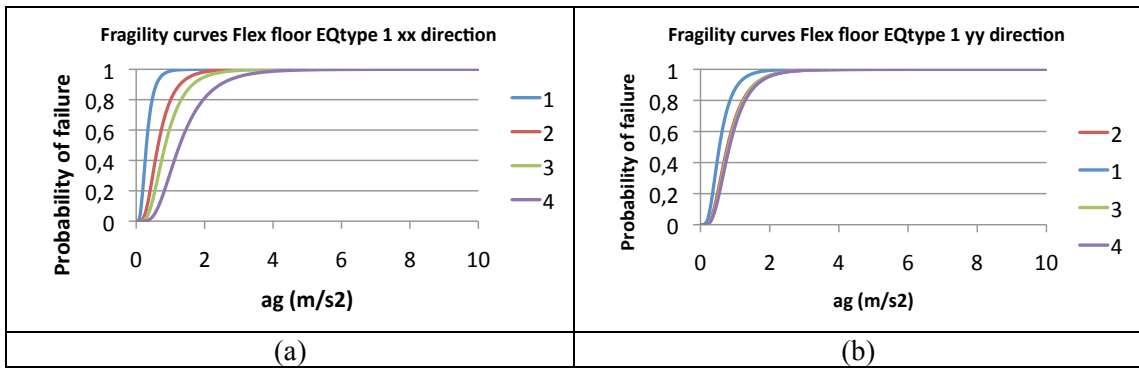


Figure 6-60: Fragility curves for earthquake type 1 (a) xx direction (b) yy direction

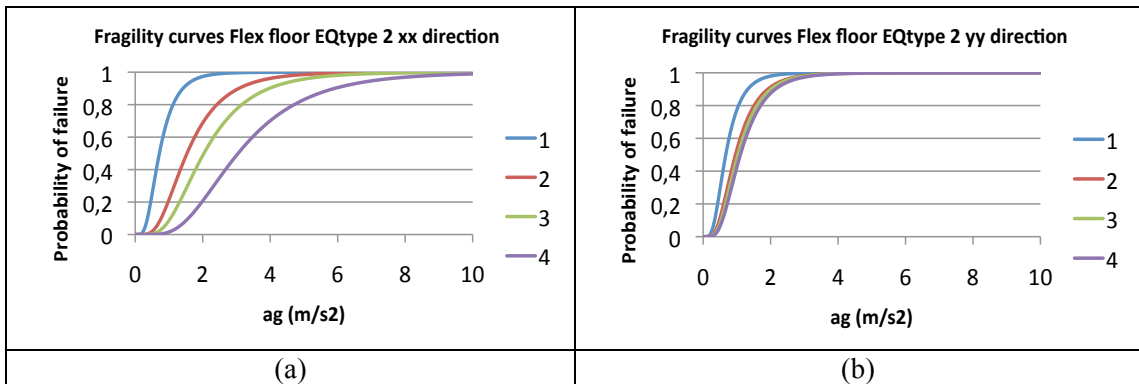


Figure 6-61: Fragility curves for earthquake type 2 (a) xx direction (b) yy direction

From the results obtained, it is possible to observe that the more demanding situations are for earthquake type 1 for both directions and for earthquake type 2 for the yy direction. In fact, as has been said in section 6.4, the case “earthquake type 2 and xx direction” is able to comply with the criterion present in Eurocode 8 and based on the N2 method, for the seismic input of downtown Lisbon.

In **Figure 6-62** and **Figure 6-63** one can see the damage probabilities for the case of the original building and for earthquakes type 1 and 2 for the xx and yy directions. In this figure P0 represents the case of having “no damage”, P1 the probability of having “slight damage”, P2 the probability of having “moderate damage”, P3 the probability of having “heavy damage” while P4 the case of reaching “collapse”.

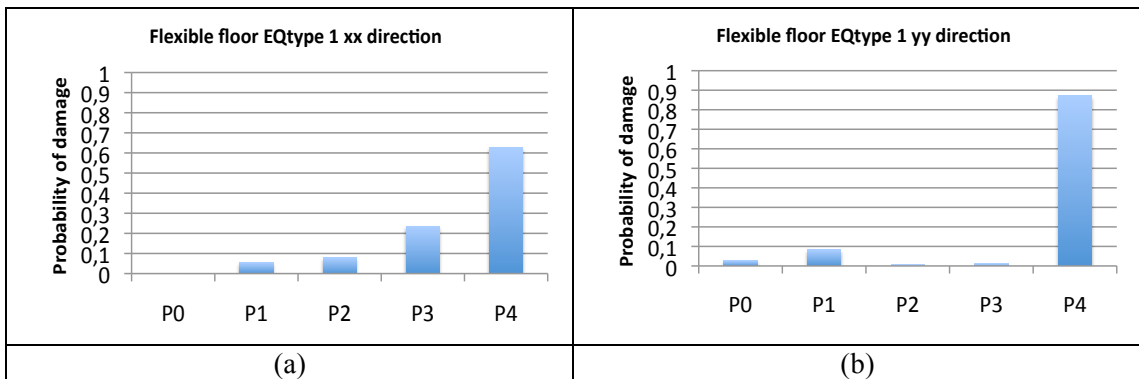


Figure 6-62: Damage probabilities for earthquake type 1 in the (a) xx direction (b) yy direction

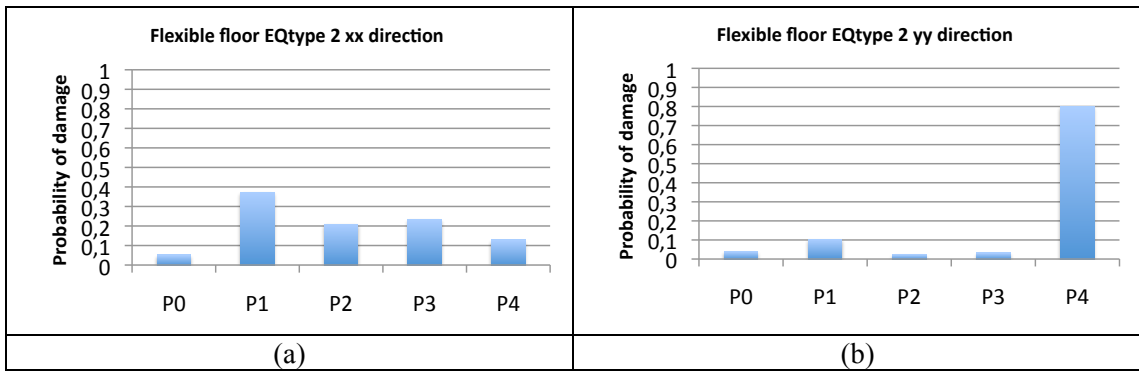


Figure 6-63: Damage probabilities for earthquake type 2 in the (a) xx direction (b) yy direction

As expected, one can see that the cases earthquake type 1 xx and yy directions and earthquake type 2 yy direction have, for downtown Lisbon seismic input, a high probability of reaching collapse. In the case of earthquake type 2 in the xx direction, the probability of reaching collapse decreases substantially and the highest probability is P1 (having slight damage).

6.7.2.2. Increase the in-plane stiffness of floors

In **Table 6-25** and **Table 6-26** one can see the parameters of the lognormal distribution function for the case of the rigid floor building for both earthquake types and for both directions.

Table 6-25: Parameters of the lognormal distribution function for the earthquake type 1 for both xx and yy directions

damage limit state $a_{g,k}$ (m/s^2)	EQtype 1 xx direction				EQtype 1 yy direction			
	1	2	3	4	1	2	3	4
	0.369	0.791	1.298	2.068	0.475	0.821	1.950	3.239

Table 6-26: Parameters of the lognormal distribution function for the earthquake type 2 for both xx and yy directions

damage limit state $a_{g,k}$ (m/s^2)	EQtype2 xx direction				EQtype2 yy direction			
	1	2	3	4	1	2	3	4
	0.886	1.899	3.115	4.964	0.537	1.151	3.861	6.955

In **Figure 6-64** and **Figure 6-65** one can see the fragility curves for the case of the rigid floor building.

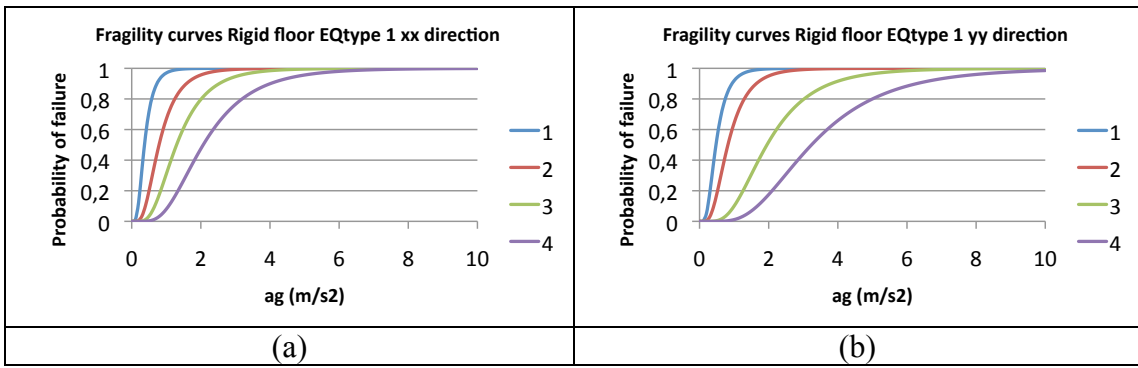


Figure 6-64: Fragility curves for earthquake type 1 (a) xx direction (b) yy direction

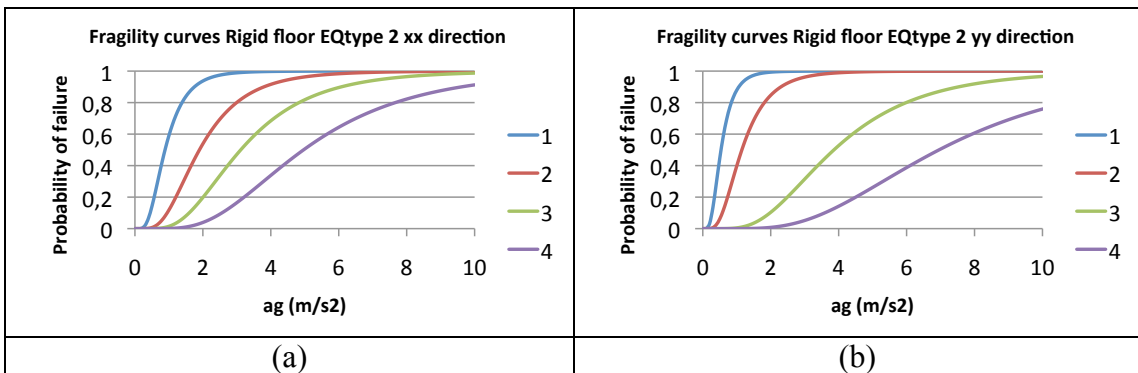


Figure 6-65: Fragility curves for earthquake type 2 (a) xx direction (b) yy direction

The results obtained show that the fragility curves change substantially from the case of the original building to the case of an original building with stiffened floors. This happens for both directions but mainly in the yy direction. It is also observed that the most demanding case is earthquake type 1 and xx direction.

Figure 6-66 and **Figure 6-67** represent the damage probabilities for the case of the rigid floor building for both earthquake types and both directions.

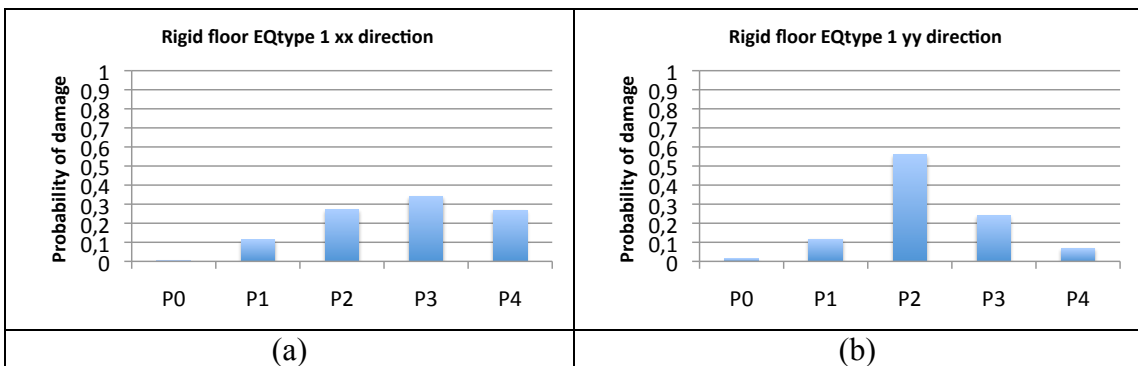


Figure 6-66: Damage probabilities for earthquake type 1 in the (a) xx direction (b) yy direction

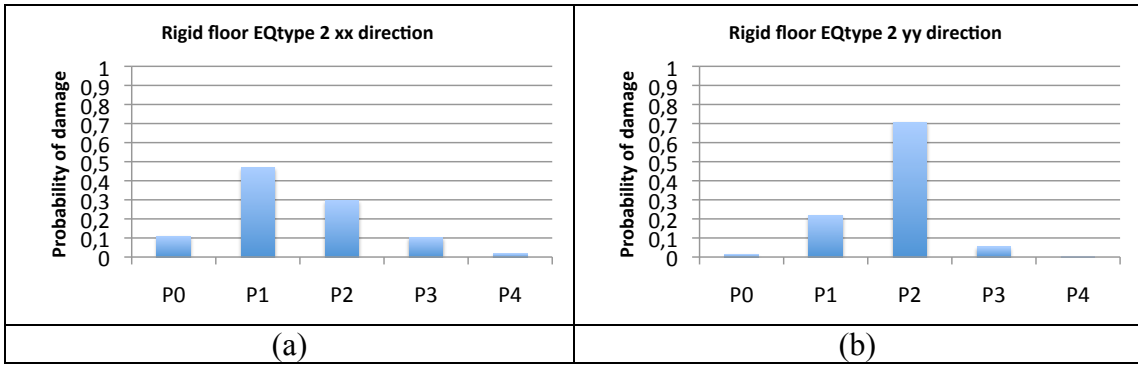


Figure 6-67: Damage probabilities for earthquake type 2 in the (a) xx direction (b) yy direction

One can see that the probability of reaching collapse has decreased significantly from the previous case of flexible floor to this retrofitting solution. The most demanding situation can also be observed in the damage probability plots and is the case of earthquake type 1 in the xx direction. In the yy direction, the damage is concentrated on P2 (moderate damage).

6.7.2.3. Increase the in-plane stiffness of floors plus reinforcement of five ground floor pillars

In **Table 6-27** and **Table 6-28** one can see the parameters of the lognormal distribution function for the case of the rigid floor building with reinforced pillars for both earthquake types and both directions.

Table 6-27: Parameters of the lognormal distribution function for the earthquake type 1 for both xx and yy directions

damage limit state $a_{g,k}$ (m/s^2)	EQtype 1 xx direction				EQtype 1 yy direction			
	1	2	3	4	1	2	3	4
	0.368	0.788	1.270	2.014	0.563	0.824	1.809	2.957

Table 6-28: Parameters of the lognormal distribution function for the earthquake type 2 for both xx and yy directions

damage limit state $a_{g,k}$ (m/s^2)	EQtype2 xx direction				EQtype2 yy direction			
	1	2	3	4	1	2	3	4
	0.883	1.892	3.047	4.832	0.548	1.174	3.537	6.292

Figure 6-68 and **Figure 6-69** show the fragility curves for the case of the rigid floor building with reinforced pillars.

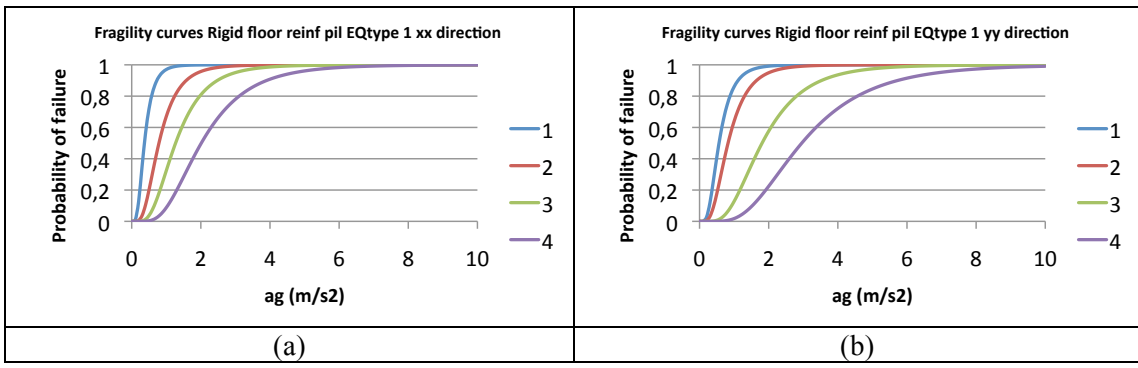


Figure 6-68: Fragility curves for earthquake type 1 (a) xx direction (b) yy direction

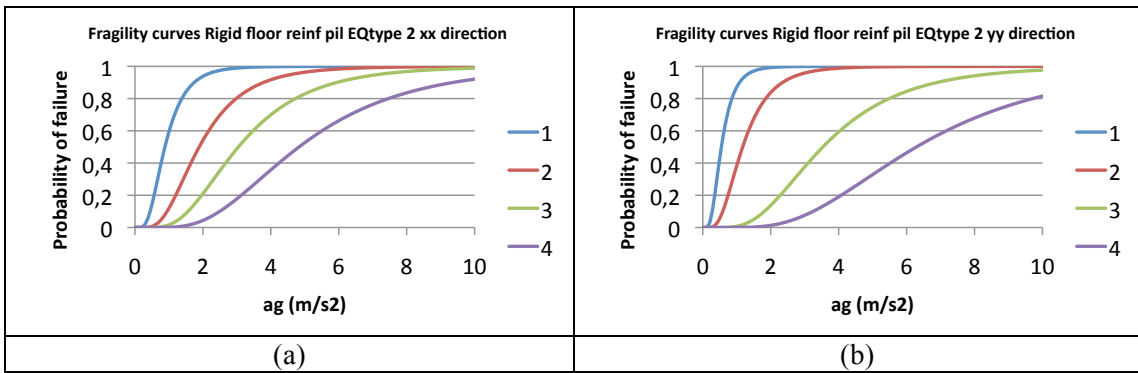


Figure 6-69: Fragility curves for earthquake type 2 (a) xx direction (b) yy direction

The comments that can be written at this stage are the fact that the fragility curves are almost the same as the previous case of stiffening only the floors. As has been said in section 6.5.2, stiffening the floors together with reinforcing the 5 ground floor pillars does not bring any additional benefit to the seismic performance of the whole structure.

In **Figure 6-70** and **Figure 6-71** one can see the damage probabilities for the case of the rigid floor building with reinforced pillars for both earthquake types and both directions.

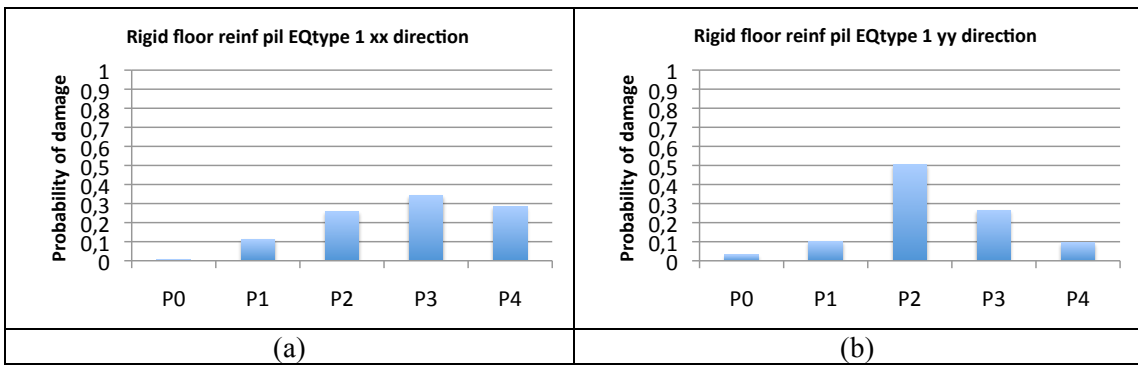


Figure 6-70: Damage probabilities for earthquake type 1 in the (a) xx direction (b) yy direction

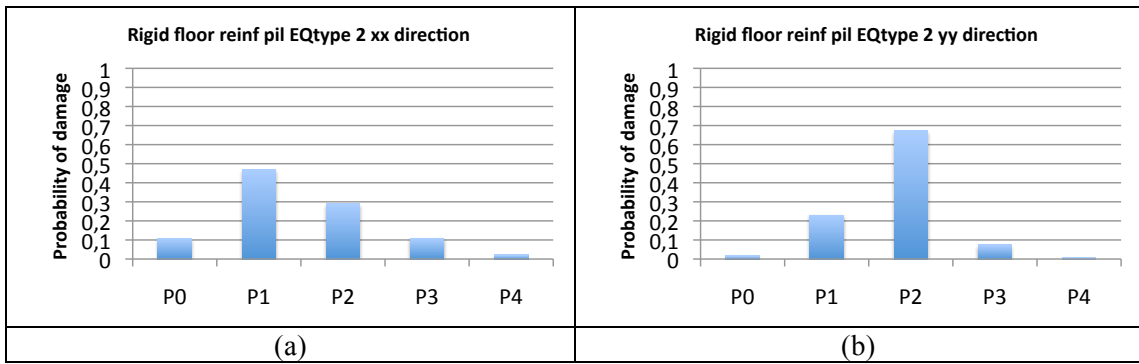


Figure 6-71: Damage probabilities for earthquake type 2 in the (a) xx direction (b) yy direction

The damage probability plots are practically identical to the previous case of stiffening the floors only. This is maybe because the increase in stiffness and strength in the pillars is not too pronounced.

6.7.2.4. Increase the in-plane stiffness of floors plus inclusion of four shear walls on the ground floor

In **Table 6-29** and **Table 6-30** one can see the parameters of the lognormal distribution function for the case of the rigid floor building with shear walls, for earthquake type 1 and 2 and for both directions.

Table 6-29: Parameters of the lognormal distribution function for the earthquake type 1 for both xx and yy directions

damage limit state	EQtype 1 xx direction				EQtype 1 yy direction			
	1	2	3	4	1	2	3	4
$a_{g,k}$ (m/s^2)	0.360	0.771	1.539	2.565	0.467	0.809	1.927	3.202

Table 6-30: Parameters of the lognormal distribution function for the earthquake type 2 for both xx and yy directions

damage limit state	EQtype2 xx direction				EQtype2 yy direction			
	1	2	3	4	1	2	3	4
$a_{g,k}$ (m/s^2)	0.863	1.850	3.694	6.155	0.531	1.139	3.821	6.882

Figure 6-72 and **Figure 6-73** represents the fragility curves for the case of the rigid floor building with shear walls.

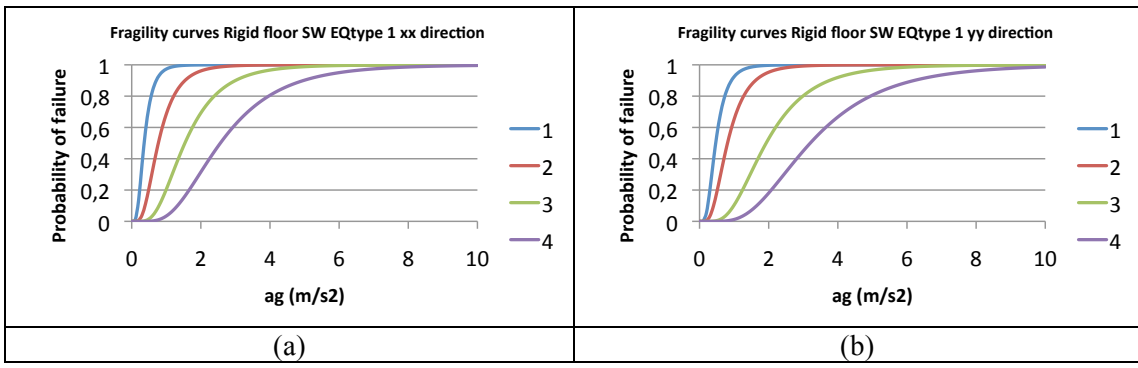


Figure 6-72: Fragility curves for earthquake type 1 (a) xx direction (b) yy direction

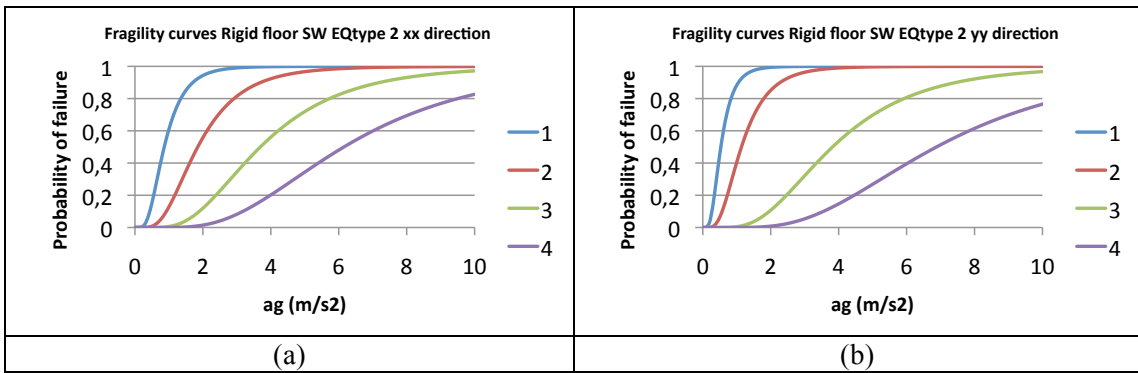


Figure 6-73: Fragility curves for earthquake type 2 (a) xx direction (b) yy direction

In the yy direction, because no additional retrofit has been placed in this direction, the plots are the same as in the case of rigid floor only. In the xx direction, if one looks carefully, one can observe that the fragility curves move towards the right a small amount, indicating that the inclusion of shear walls has had some effect on these curves.

Figure 6-74 and **Figure 6-75** show the damage probabilities for the case of the rigid floor building with shear walls.

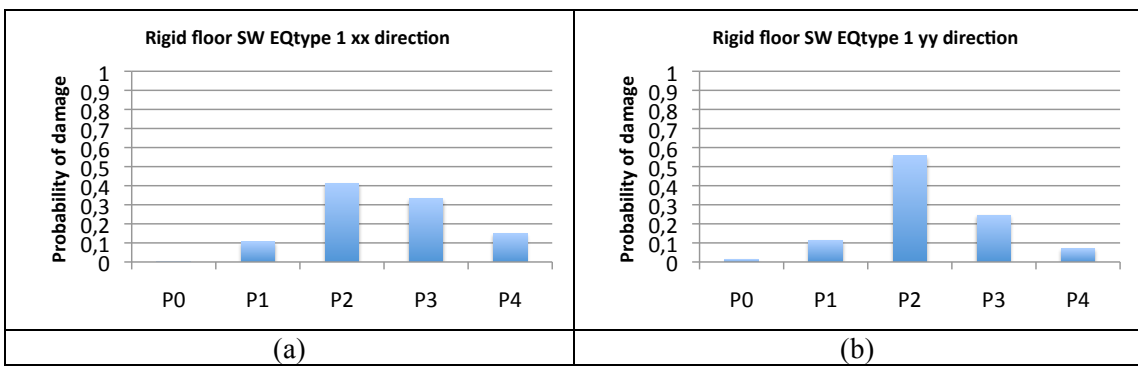


Figure 6-74: Damage probabilities for earthquake type 1 in the (a) xx direction (b) yy direction

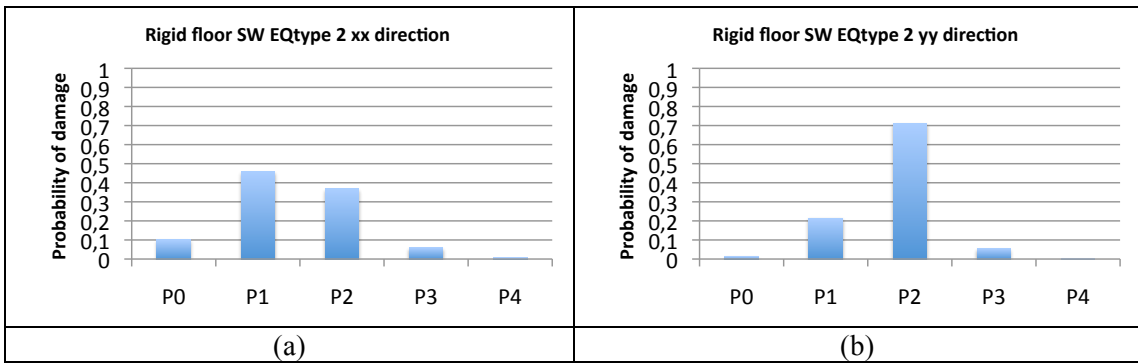


Figure 6-75: Damage probabilities for earthquake type 2 in the (a) xx direction (b) yy direction

From the results obtained, one can observe that, in the xx direction, the probability of damage moves towards the left. In this case and for earthquake type 1, the highest probability of damage is P2 instead of P3, as in the case of the rigid floor only. In earthquake type 2 one can see that P3 and P4 decrease, increasing P2.

6.7.2.5. Increase the in-plane stiffness of floors plus inclusion of steel frames on the ground floor

In **Table 6-31** and **Table 6-32** one can see the parameters of the lognormal distribution function for the case of the rigid floor building with steel frame for both earthquakes and both directions.

Table 6-31: Parameters of the lognormal distribution function for the earthquake type 1 for both xx and yy directions

damage limit state $a_{g,k}$ (m/s^2)	EQtype 1 xx direction				EQtype 1 yy direction			
	1	2	3	4	1	2	3	4
	0.522	1.119	1.699	2.651	0.480	0.839	1.840	3.006

Table 6-32: Parameters of the lognormal distribution function for the earthquake type 2 for both xx and yy directions

damage limit state $a_{g,k}$ (m/s^2)	EQtype2 xx direction				EQtype2 yy direction			
	1	2	3	4	1	2	3	4
	1.253	2.685	4.077	6.363	0.553	1.185	3.589	6.388

In **Figure 6-76** and **Figure 6-77** the fragility curves for the case of the rigid floor building with steel frame are represented.

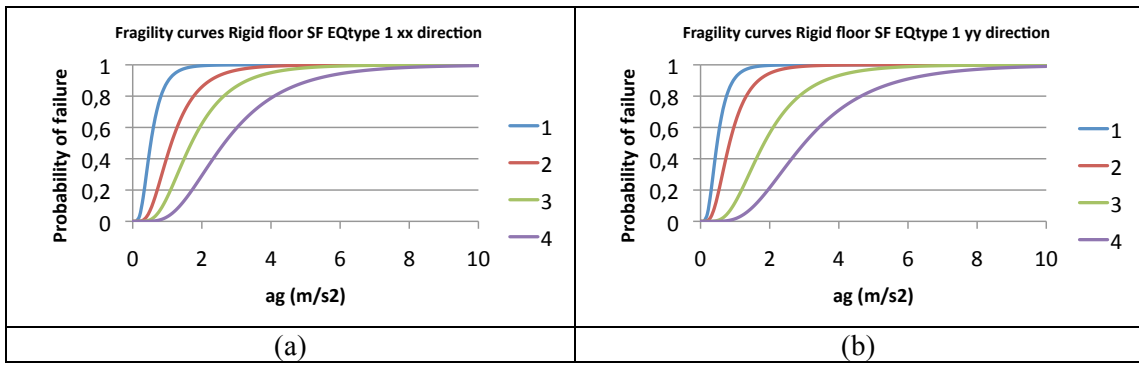


Figure 6-76: Fragility curves for earthquake type 1 (a) xx direction (b) yy direction

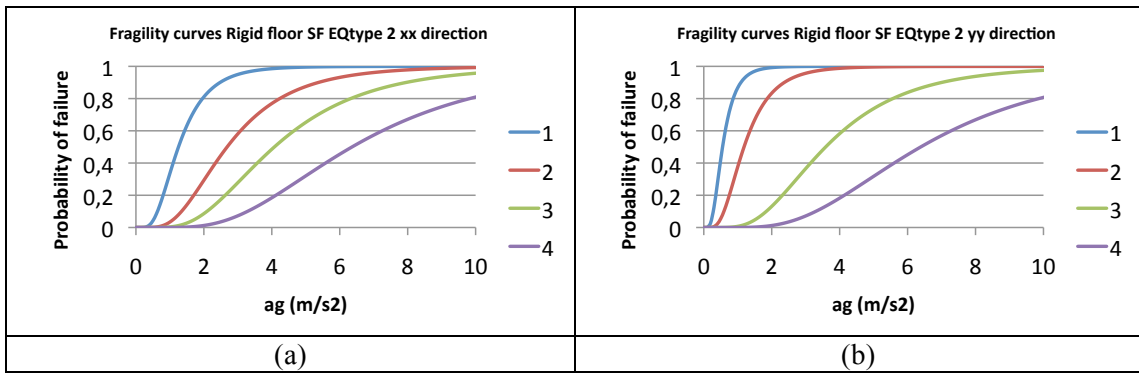


Figure 6-77: Fragility curves for earthquake type 2 (a) xx direction (b) yy direction

From the results obtained, one can observe that the fragility curves move towards right when compared to the case of rigid floor only. This happens only in the xx direction obviously.

Figure 6-78 and **Figure 6-79** show the damage probabilities for the case of the rigid floor building with steel frame.

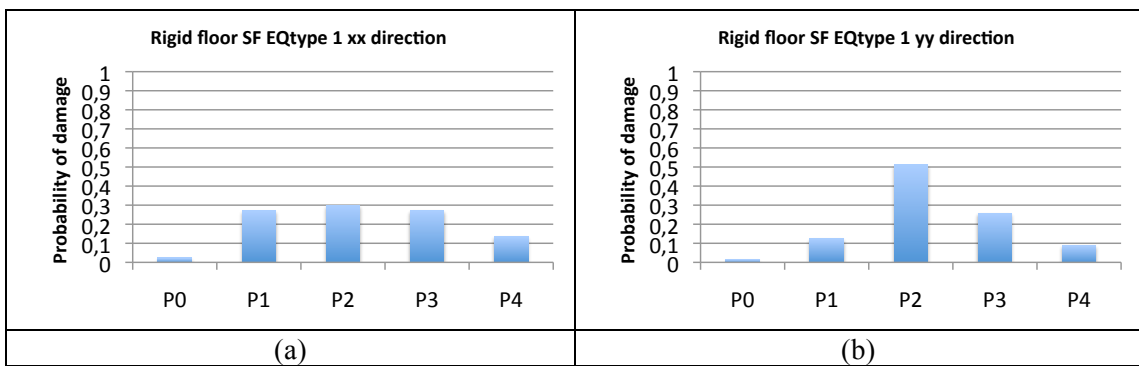


Figure 6-78: Damage probabilities for earthquake type 1 in the (a) xx direction (b) yy direction

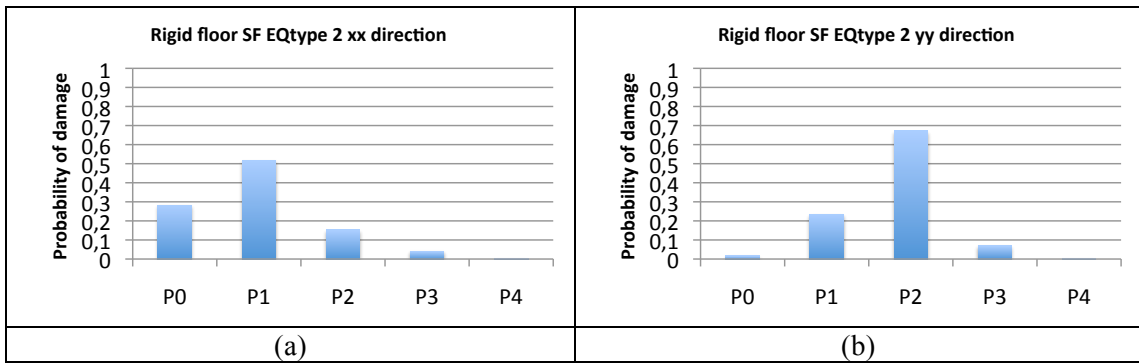


Figure 6-79: Damage probabilities for earthquake type 2 in the (a) xx direction (b) yy direction

Comparing this solution with the strengthened solution of rigid floor with shear walls one can observe that this solution seems to be a slightly better solution than the previous case. For earthquake type 1, P3 decreases and P1 increases. For earthquake type 2, P2 decreases and P0 increases.

6.7.2.6. Increase the in-plane stiffness of floors plus inclusion of tie-rods at front and back façades

In **Table 6-33** and **Table 6-34** one can see the parameters of the lognormal distribution function for the case of the rigid floor building with tie-rods, for earthquake type 1 and 2 and for xx and yy directions.

Table 6-33: Parameters of the lognormal distribution function for the earthquake type 1 for both xx and yy directions

damage limit state $a_{g,k}$ (m/s ²)	EQtype 1 xx direction				EQtype 1 yy direction			
	1	2	3	4	1	2	3	4
	0.357	0.712	2.469	4.430	0.475	0.820	1.950	3.239

Table 6-34: Parameters of the lognormal distribution function for the earthquake type 2 for both xx and yy directions

damage limit state $a_{g,k}$ (m/s ²)	EQtype2 xx direction				EQtype2 yy direction			
	1	2	3	4	1	2	3	4
	0.683	1.464	5.682	10.388	0.537	1.151	3.862	6.956

In **Figure 6-80** and **Figure 6-81** one can see the fragility curves for the case of the rigid floor building with tie-rods.

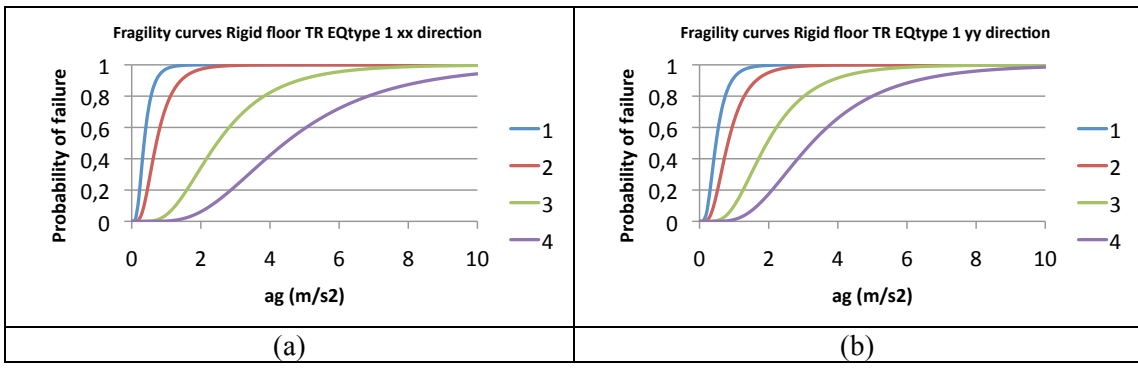


Figure 6-80: Fragility curves for earthquake type 1 (a) xx direction (b) yy direction

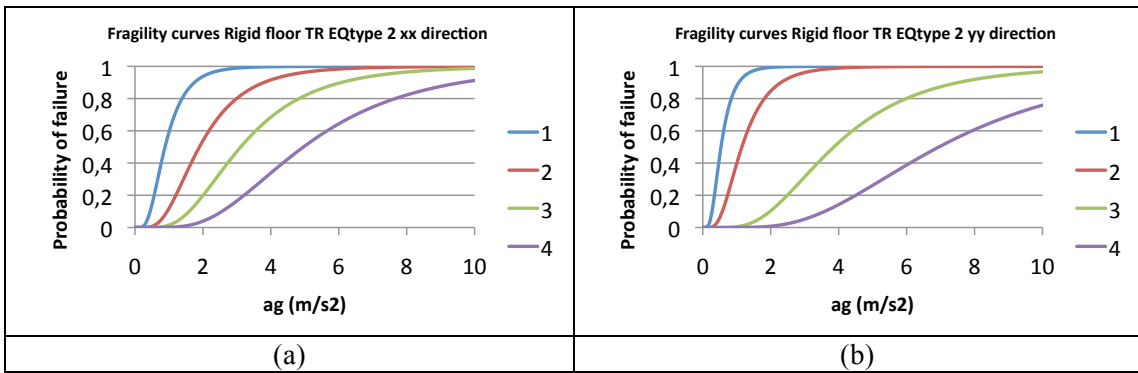


Figure 6-81: Fragility curves for earthquake type 2 (a) xx direction (b) yy direction

One can observe again that the fragility curves move towards the right, in the xx direction, when compared to the case of the rigid floor only. The yy direction is kept the same.

Figure 6-82 and **Figure 6-83** show the damage probabilities for the case of the rigid floor building with tie-rods.

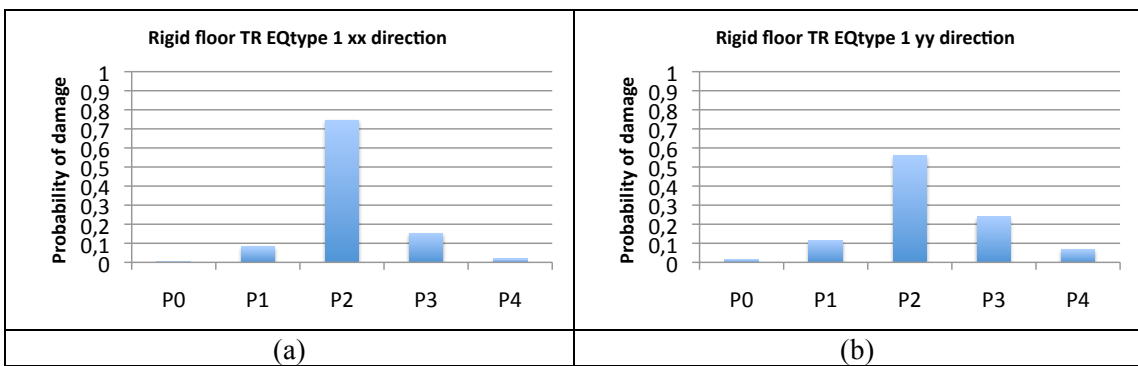


Figure 6-82: Damage probabilities for earthquake type 1 in the (a) xx direction (b) yy direction

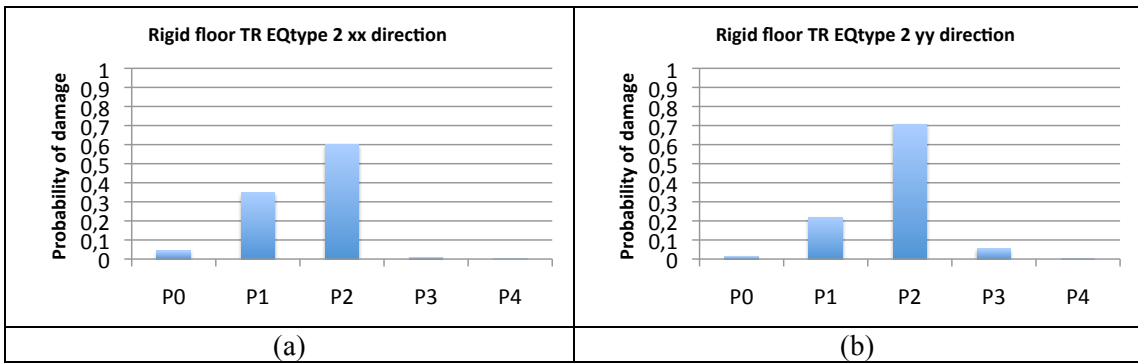


Figure 6-83: Damage probabilities for earthquake type 2 in the (a) xx direction (b) yy direction

In this case the results are quite interesting. If for earthquake type 1, in the xx direction, one has that the strengthened solution of including tie-rods in the façades is more beneficial than the previous retrofitting strategies; for earthquake type 2, it seems to be less interesting than including shear walls and steel frames. In the latter case, P2 increases and P1 and P0 decrease (even though P3 also decreases).

6.7.2.7. Comparison between original building and retrofitted cases

The damage probability plots have all been set together for comparison purposes. **Figure 6-84** represents the probability of damage for earthquake type 1 in the xx direction for all the cases studied.

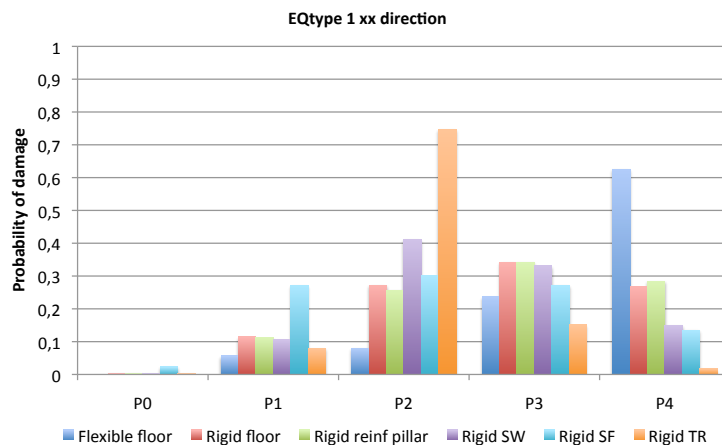


Figure 6-84: Probability of damage for earthquake type 1 in the xx direction

Based on the results obtained, it is clear that building without retrofitting presents the highest value for probability of damage P4 (collapse). Retrofitting the building by stiffening the floors enables this value to be reduced significantly. Retrofitting the building by stiffening the floors and reinforcing the five ground floor pillars does not improve the situation any further. Retrofitting the building by stiffening the floors and including shear walls or steel frames does improve the the situation slightly, reducing the value of P4 and spreading it more through P3 to P1. The retrofitting scheme that improves the seismic performance of the building the most, with respect to the previous cases, is the case of the inclusion of tie-rods in the front and back façades.

This significantly reduces the damage probability of P4. Nevertheless, this retrofitting possibility seems to very much increase the damage probability of P2 when compared to the other retrofitting strategies.

In **Figure 6-85** one can see the damage probabilities for earthquake type 1 in the yy direction for all the cases studied.

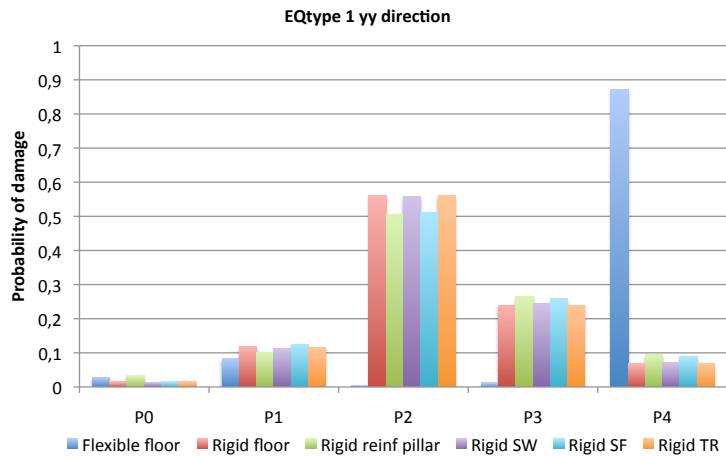


Figure 6-85: Probability of damage for earthquake type 1 in the yy direction

In the yy direction, there is a high probability of reaching collapse (P4) for the building without retrofitting. Simply by stiffening the floors one is able to reduce this probability drastically, shifting the value to P2 (moderate damage).

Figure 6-86 represents the probability of damage for earthquake type 2 in the xx direction for all the cases studied.

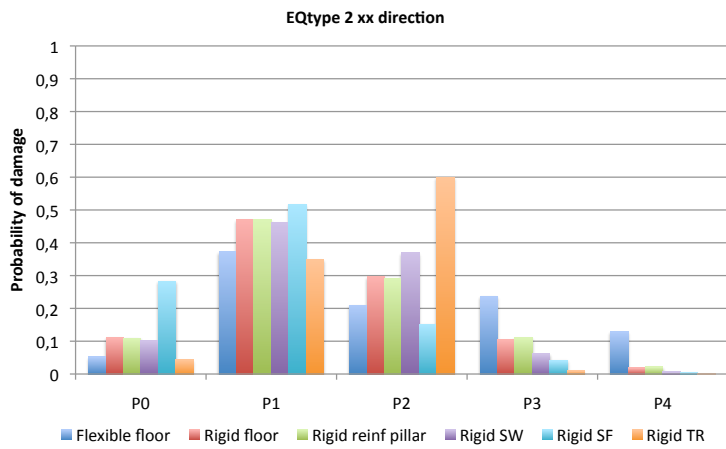


Figure 6-86: Probability of damage for earthquake type 2 in the xx direction

It is evident that earthquake type 2 is less demanding than earthquake type 1. The probability of reaching collapse is much lower although it is still higher for the case of the building without retrofitting. For the other cases, it is more marked in damage probability P1 except for the last retrofitting scheme (rigid TR), which is more marked in damage probability P2. This might be because retrofitting the building with

tie-rods makes the structure considerably more rigid. For earthquake type 2, the seismic action increases when the period of vibration is lower.

Figure 6-87 shows the probability of damage for earthquake type 2 in the yy direction for all the cases studied.

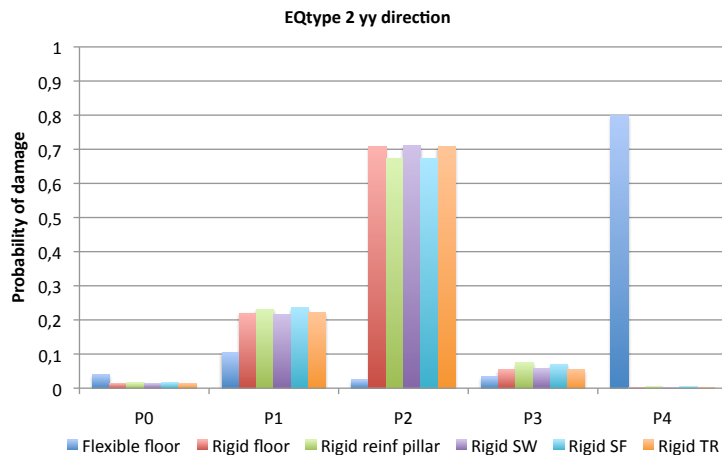


Figure 6-87: Probability of damage for earthquake type 2 in the yy direction

In the yy direction the high probability of damage P4 (collapse) of the building without any type of retrofitting is clear again. Simply by stiffening the floors one is able to lower this probability and increase P2 (moderate damage).

6.8. Conclusions

In the present chapter *Pombalino* buildings were modelled with both external masonry walls and internal “frontal” walls in the same structural model. This is an accomplishment of the present work. The structural model used was based on macro-elements and is an innovative program, which enables the nonlinear modelling of masonry buildings. Thus nonlinear static analyses were carried out in the *Pombalino* buildings. The internal “frontal” walls were also modelled as macro-elements and the behaviour of the structure was evaluated with all its components.

It has been found that the internal “frontal” walls alignments contribute little to the total base shear of the building, the majority of this force is a contribution of the surrounding masonry walls. This is mainly because the “frontal” walls are interrupted on the ground floor and also due to their lower stiffness when compared to the masonry walls. In this way, the “frontal” walls do not make a noticeable contribution to the seismic resistance of the *Pombalino* buildings under inplane actions. On the other hand, the “frontal” walls may play the role of preventing the out-of-plane failure of the masonry façades if they are properly attached to these walls. It has been assumed in the modelling that this is the case and that the out-of-plane failure is prevented both by the proper connections of the “frontal” walls to the masonry façades and later on by the stiffening of the floors and improvement of the connections between the floors and the masonry façades. The out-of-plane failure mode is thus not evaluated in this study but is instead assumed to be prevented by the

proper connections between structural elements. Furthermore, the local out-of-plane mechanisms may be verified separately through suitable existing methods (see Magenes [2006]). In this way, it has been assumed that the building in its *original state* has good connections between structural elements (“frontal” walls, floors and masonry walls). However, in reality this may not be the case. It is important then to improve these connections in any intervention that would be performed on these buildings. It should also be noticed that, as a consequence, the buildings in reality might be even more vulnerable to seismic actions than the *original* building considered in this study. On the other hand, in the existing building stock in downtown Lisbon, there are many buildings, which have been subjected to structural changes. These changes are, for example, removing ground floor masonry walls to have open spaces, removing façade pillars to have a larger entrance or removing “frontal” walls on the upper floors. In this way, it is possible to understand that these altered buildings are even more vulnerable than the *original* building evaluated in this study.

The building in its *original state* does not comply with Eurocode 8 criteria. It is thought to be because the floors are flexible. Simply by stiffening the floors one is able to have a structure that complies with the ultimate limit state. Additional retrofitting of the structure is possible and advisable if one wants to increase its resistance towards earthquakes. The most profitable solution (which is also the most complicated in terms of implementation) is the inclusion of tie-rods in the lintels at the front and back façades. The solution of including shear walls is also advisable but has architectural drawbacks; the solution of including steel frames on the ground floor is advisable and has few architectural drawbacks. The solution of reinforcing the five ground floor pillars is seen to bring no additional benefit to the structure and is therefore not recommended.

For future research it is possible to carry out a sensitivity study on the mechanical characteristics of the masonry types present in this type of buildings. Moreover, it is possible in future research to conduct loss estimation studies with the results obtained. The current trend in seismic risk analysis and loss estimation involves the use of fragility curves derived from nonlinear static and dynamic analyses of representative structures. It is also possible, as a further research step, to improve the estimation of the beta coefficients with the response surface method.

6.9. Bibliography

3Muri Program release 3.2.11 <http://www.stadata.com> (solver algorithm developed by Lagomarsino S., Galasco A., Penna A., Cattari S.).

ASCE/SEI, 2007, “Seismic Rehabilitation of Existing Buildings – ASCE Standard 41-07”, American Society of Civil Engineers, Reston, Virginia.

Brencich A. and Lagomarsino S., 1998, A Macro-elements dynamic model for Masonry Shear walls, Proc. STRUMAS IV – 4th International Symposium on Computer methods in Structural Masonry, E&FN Spon, London, pp 67-75.

Cardoso M. R. P., 2003, Vulnerabilidade Sísmica de um Edifício Pombalino, Master Thesis, (IST), The Technical University of Lisbon.

Cattari S. and Lagomarsino S., 2006, Nonlinear Analysis of mixed masonry and reinforced concrete buildings, 1st ECEES, Geneva, Switzerland.

Cattari S., Curti E., Galasco A., Resemini S., 2005, Linear and non linear seismic analysis of masonry buildings: theory and application examples according to OPCM 3274/03 e 3431/05, E100 – Series *Edilizia–Progettare e Costruire*, Esselibri-Simone Edition, Naples. (in Italian).

Circolare 2 febbraio, 2009, n. 617, Ministero delle Infrastrutture e dei Trasporti. /Istruzioni/ /per l'applicazione delle "Norme Tecniche per le Costruzioni" di cui al D.M. 14/01/2008/. G.U. n. 47 del 26/2/09 suppl. ord. n. 27 (In Italian).

Costa A.A., 2007, Experimental testing of lateral capacity of masonry piers. An application to seismic assessment of AAC masonry buildings, Master thesis dissertation, European School for Advanced studies in Reduction of Seismic Risk- ROSE School.

EN 1998-1, Eurocode 8: Design of structures for earthquake resistance - Part 1: General rules, seismic actions and rules for buildings, 2004, CEN, Brussels.

Eurocode 1: Actions on structures - Part 1-1: General actions -Densities, self-weight, imposed loads for buildings, EN 1991-1-1, 2002, Comission of the European Communities (CEN), Brussels.

Fajfar P, 2000, A Nonlinear Analysis Method for Performance-Based Seismic Design, Earthquake Spectra, vol. 16, n° 3.

Freeman S.A., 1998, Developement and use of Capacity Spectrum Method, *Procc. of the 6th U.S. National Conference of Earthquake Engineering*, Seatle.

Galasco M., Lagomarsino S., Penna A., Cattari S. 2002, TREMURI program, Seismic Analysis of 3D masonry buildings, University of Genoa.

Giuffrè A., 1993, Safety and preservation of historical centres: the Ortigia example, Laterza Edition, Bari (in Italian).

Italian Technical Code, 2008, D.M. 14/1/2008, Official Bullettin no. 29 of February 4 2008 (In Italian).

Kappos A. J., Penelis G. G., Drakopoulos C. G., 2002, Evaluation of Simplified Models for Lateral Load Analysis of Unreinforced Masonry Buildings, Journal of Structural Engineering, pp. 890-897.

Karimi K. and Bakhshi A., 2006, Development of Fragility Curves for Unreinforced Masonry Buildings before and after Upgrading using Analytical Method, 1st European Conference on Earthquake Engineering and Seismology, Geneva.

Lagomarsino S. and Giovinazzi S., 2006, Macroseismic and mechanical models for the vulnerability and damage assessment of current buildings, Bulletin of Earthquake Engineering.

Magenes G, 2006, Masonry building design in seismic areas: recent experiences and prospects from a European standpoint, First European Conference on Earthquake Engineering and Seismology, Geneve Switzerland.

Macchi G. & Magenes G., 2002. In Giangreco E. (collated by), Structures engineering, Ed. Vol III, pp. 69-143. UTET, Turin. (in Italian).

Mander J.B., 1999, Fragility curve Development for Assessing the Seismic Vulnerability of Highway Bridges, University at Buffalo, State University at New York.

Pagnini LC, Vicente R, Lagomarsino S, Varum H, 2011, A mechanical model for the seismic vulnerability of old masonry buildings, Earthquakes and structures, vol 2, no 1, pp.25-42.

Pompeu Santos, 1997, Ensaios de Paredes Pombalinas. Nota Técnica Nº15/97, NCE/DE, LNEC Lisboa (in Portuguese) .

Santos M. H. R., 2000, A Baixa Pombalina: Passado e Futuro, Livros Horizonte, Lisboa.

Villaverde R., 2007, Methods to Assess the Seismic Collapse Capacity of Building Structures: State of the art, Journal of Structural Engineering, ASCE, 57-66.

7. Final conclusions and further work

The thesis presented relates to the seismic vulnerability of *Pombalino* buildings. Herein, first, an introduction to *Pombalino* buildings was made presenting their main characteristics. Secondly, focus was put on the soil where the *Pombalino* buildings are situated, known for its susceptibility to significantly amplify the incident ground motion and cause catastrophic damage as has been seen in the past. At this point, the ultimate objective is to define the seismic action for further assessment of the buildings.

Next, there was the possibility to carry out experimental testing in the IST laboratory (LERM) on the *Pombalino* internal mixed timber-masonry walls (“frontal” walls). Since previous experimental testing on such walls is very limited, these results are very useful for further research. The testing performed was static cyclic shear testing with imposed displacements and the hysteretic behaviour of such walls was determined.

Then, and based on this experimental testing, a macro-element for “frontal” walls was defined. This macro-element is based on a hysteretic model, defined by means of a phenomenological approach, calibrated by the experimental hysteresis obtained.

Finally, the last part of the work was to evaluate the seismic vulnerability of the *Pombalino* buildings. For this purpose a structural model was made with a macro-element approach. In this model, “frontal” walls and masonry walls are modelled as macro-elements and thus both are incorporated in the structural model. The seismic performance of an *original* building and of five retrofitting solutions was evaluated. Non-linear static analyses were performed and also fragility curves and damage probability plots were obtained.

The conclusions of Chapter 3 are related to the soil characterization for seismic assessment. Here, based on the combination of geological and geotechnical data with the H/V spectral ratio technique it was possible to characterize the soil in terms of average shear wave velocity and depth to bedrock estimates as well as mapping the site quarters where significant seismic ground amplification is foreseen. The site average shear wave velocity of the soil, unknown in the literature, is estimated at ~194 m/s. It is reasonably assumed that the same sedimentary process formation has taken place in the basin so that similar soil properties are found throughout the site (as indicated by the geotechnical data) and the average shear wave velocity of the soil obtained is the representative value for the whole site. Moreover, it was possible to classify the soil in the classes of the Eurocode 8 and define the elastic response spectrum for downtown Lisbon in order to then carry out seismic assessment and retrofit.

Solely based on the information gathered from the geotechnical surveys on the resistance of the soil layer, namely the standard penetration resistance, N_{spt} , it would not be possible to classify the site in terms of Eurocode 8 soil classes. The heterogeneity of the soil profile layers is too pronounced in terms of this parameter, with values ranging from 2 up to 60. By conjugating the geotechnical and geological

data for the site with the H/V spectral ratio technique on ambient vibrations, it is possible to obtain a fine site characterization.

One of the most important conclusions to point out is the ease of obtaining important site characteristics with very few resources and contrary to more common geophysical prospecting techniques, which would not be suitable for the academic work being conducted. The H/V spectral ratio technique was found to be a practical means of site characterization in the analysed case study, its major advantages being its attractiveness in terms of the ease of data collection, its consistency and the minor equipment required, with, as a consequence, the associated low cost of the technique.

The conclusions of Chapter 4 are related to the experimental activity conducted in the laboratory. Since very little exists in the literature on the cyclic behaviour of the interior “frontal” walls, the experimental work carried out with static cyclic shear testing with imposed displacements is very important and is original research. Nonetheless, the author believes that further experimental work should be carried out, for instance on walls of different sizes or for other combinations of vertical loading or even on specimens without the masonry fillings or other type of masonry. The results obtained enabled the experimental hysteresis curve to be plotted via the relation force-displacement. This shall be useful for the further development of analytical models for these walls.

The hysteretic behaviour of the “frontal” walls subjected to cyclic loading is characterized by nonlinear behaviour describing the monotonic envelope. Pinching behaviour associated with strength degradation is also observed. Generally fat loops can be identified dissipating reasonable amounts of energy. The response is also highly ductile. It is important to point out the resemblance between the results obtained here and the results obtained in the other similar experimental tests carried out at LNEC thus somewhat validating the experimental results obtained here.

In Chapter 5, the conclusions are related to the macro-element proposed. The macro-element is based on the development of a hysteretic model to describe the cyclic behaviour of the Pombalino “frontal” walls. The hysteretic model developed is the first model developed in the literature and is thus relevant. The hysteretic model is governed by path-following rules and is composed of linear and exponential functions. It is governed by nine identifiable parameters. These parameters have been calibrated with experimental test results. The total percentage error in cumulative energy dissipated between the fitted model and the actual cyclic test data is 9% for the SC2 test and 14% for the SC3 test, accounting for the good performance of the model. The model developed also accounts for characteristics such as pinching effect, strength and stiffness degradation as observed in the experimental data. The results obtained here are essential for further work in modelling the behaviour of such walls in particular, and the *Pombalino* buildings in general, under monotonic, cyclic or earthquake loading.

Furthermore, the envelope curves for other wall sizes (height and length) were predicted, since in reality one can find different wall sizes in a single building. It was verified that the configuration with both highest initial stiffness and highest strength is configuration 2x4 (two modules in height and four modules in length). The configuration with lowest initial stiffness and lowest strength is configuration 3x2

(three modules in height and two modules in length). The effect of the number of cycles was not taken into account when defining the hysteresis model or macro-element. This shall be studied in further work.

The conclusions of Chapter 6 are related to the modelling of the typical *Pombalino* building and to the fragility analyses carried out. In this chapter one was able to model both masonry walls and “frontal” walls with macro-elements, all in the same structural model. This is state of the art research and the software used is also state of the art software since it enables the nonlinear modelling of the masonry buildings. Thus static nonlinear analyses were carried out in the *Pombalino* buildings.

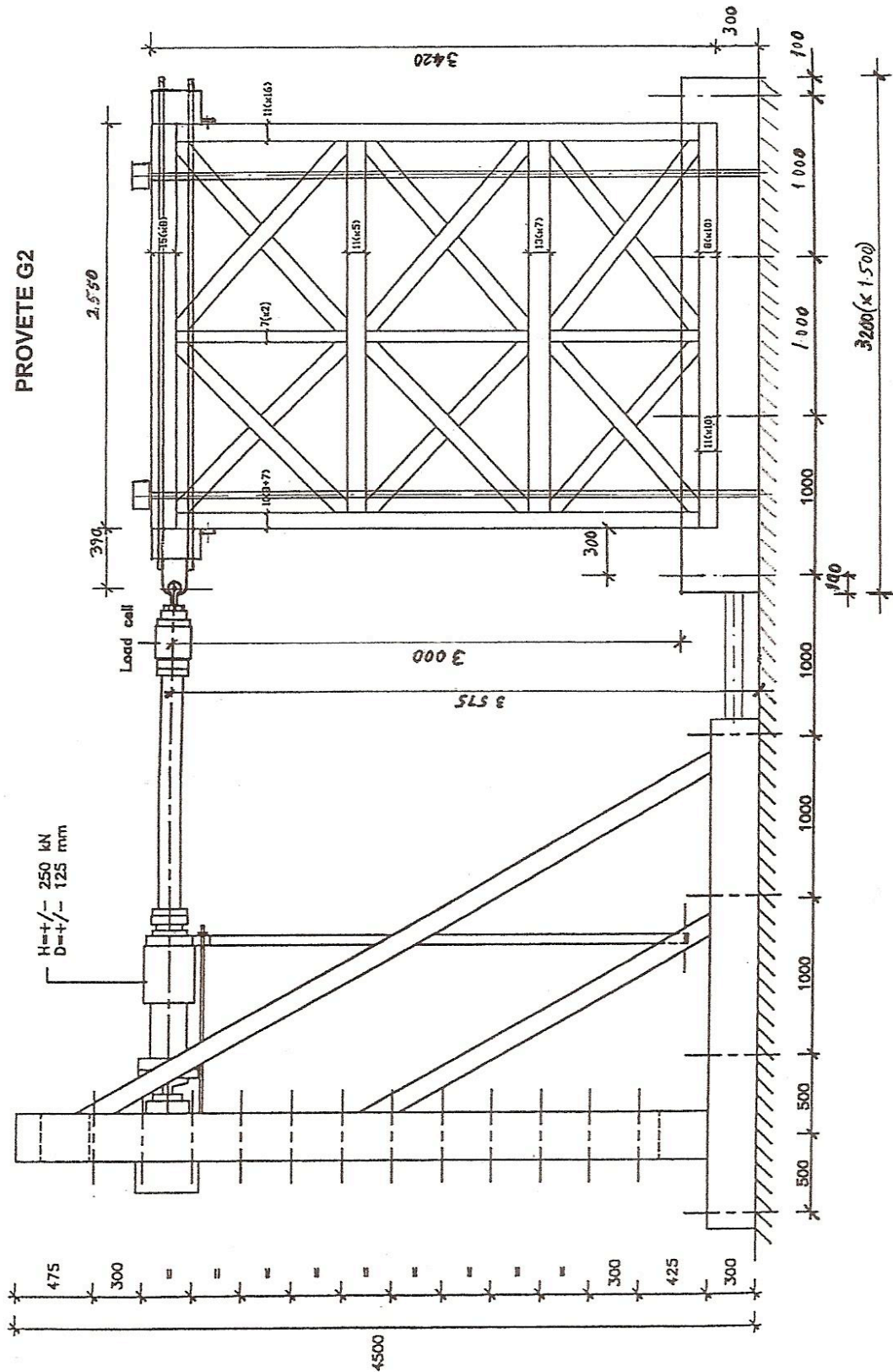
It was found that the internal “frontal” walls alignments contribute little to the total base shear of the building, as the majority of this force is a contribution of the surrounding masonry walls. This is because the masonry walls are very thick and rigid. The “frontal” walls may play the role of preventing the out-of-plane failure of the masonry façades if they are properly attached to these walls. It is important then to improve these connections in any intervention that would be performed on these buildings. In the existing building stock in downtown Lisbon, there are many buildings which have been subjected to structural changes. In this way, it is possible to understand that these altered buildings are even more vulnerable than the *original* building evaluated in this study.

The building in its original state does not comply with the Eurocode 8 criterion based on the N2 method for the ultimate limit state. One reason for this is because of the flexible timber floors. Simply by stiffening the floors one is able to have a structure that complies with the Eurocode 8 criterion. Additional reinforcement of the structure is possible and advisable if one wants to increase its resistance towards earthquakes. The most profitable solution, also the most complicated in terms of implementation, is the inclusion of tie-rods in the lintels for the front and back façades. The solution of including shear walls is also advisable but has architectural drawbacks; the solution of including steel frames on the ground floor is advisable and has few architectural drawbacks. The solution of the reinforcement of the five ground floor pillars is seen to bring no additional benefit to the structure and is therefore not recommended.

It is possible in future research to conduct loss estimation studies based on the results obtained. The current trend in seismic risk analysis and loss estimation involves the use of fragility curves derived from nonlinear static and dynamic analysis of representative structures. It is also possible as a further research step to improve the estimation of the beta coefficients with the response surface method.

Annex A

Schematic drawing of the layout of experiment at LNEC (bigger view)



Annex B

The Matlab code for the hysteresis model

```

dmaxdata(16))/step:dmaxdata(17),dmaxdata(17):(dmaxdata(18)-
dmaxdata(17))/step:dmaxdata(18),dmaxdata(18):(dmaxdata(19)-
dmaxdata(18))/step:dmaxdata(19)];
```

E=zeros(1,length(Dtest));
F=zeros(1,length(Dtest));
D=zeros(1,length(Dtest));
npos=0;
nneg=0;
Dmaxpos(1)=0;
Dmaxneg(1)=0;
Dmaxpos_cycle=zeros(1,length(Dtest));
Dmaxneg_cycle=zeros(1,length(Dtest));

Pmaxpos(1)=0;
Pmaxneg(1)=0;
Driftmaxpos(1)=0;
Driftmaxneg(1)=0;

for i=2:length(Dtest)
%input displacement
D(i)=Dtest(i);
%envelope
if abs(D(i))<=Du
E(i)=sign(D(i))*(beta*Fu+r1*K0*abs(D(i)))*(1-exp(-
K0/(beta*Fu)*abs(D(i)))); %loading exponential
elseif (Du < abs(D(i))) & (abs(D(i))<= Driftult*h)
E(i)=sign(D(i))*Fu+r2*K0*(D(i)-sign(D(i))*Du);
else
E(i)=0;
end

%counting the number of positive and negative cycles (half cycles)
if (D(i)*D(i-1)<=0 & D(i-1)>0)
npos=npos+1
elseif (D(i)*D(i-1)<=0 & D(i-1)<0)
nneg=nneg+1
end

%Force F(i)
%loading
if D(i)*(D(i)-D(i-1))>0 %loading
%damage
if D(i)>0
Dmaxpos_cycle(npos+2)=max(Dmaxpos_cycle(npos+2),D(i));
Dmaxpos(npos+2)=max(Dmaxpos_cycle(:));
Driftmaxpos(npos+2)=Dmaxpos(npos+2)/h;
[j] = find(D == Dmaxpos(npos+2));
Pmaxpos(npos+2)=E(j(1));
elseif D(i)<0
Dmaxneg_cycle(nneg+2)=max(Dmaxneg_cycle(nneg+2),abs(D(i)));
Dmaxneg(nneg+2)=max(Dmaxneg_cycle(:));
Driftmaxneg(nneg+2)=Dmaxneg(nneg+2)/h;;
[k] = find(D == -Dmaxneg(nneg+2));
Pmaxneg(nneg+2)=abs(E(k(1)));
end

if (npos>=1 & nneg>=1) %reloading

```

if D(i)>0
    a=5.0585*Driftmaxpos(npos+1)-0.0004;

    if Dmaxpos(npos+1)<=Dp_i
        re=(Env_Dp_i*(1-a)-gama*Fu)/(K0*Dp_i);
        display('re const')
    elseif (Dp_i<Dmaxpos(npos+1)) &
(Dmaxpos(npos+1)<=Driftult*h)
        re=(Pmaxpos(npos+1)*(1-a)-
gama*Fu)/(K0*Dmaxpos(npos+1));
        display('re curvo')
    else
        re=0;
        display('re zero')
    end
else
    a=5.0585*Driftmaxneg(nneg+1)-0.0004;

    if Dmaxneg(nneg+1)<=Dp_i
        re=(Env_Dp_i*(1-a)-gama*Fu)/(K0*Dp_i);
        display('re const')
    elseif (Dp_i<Dmaxneg(nneg+1)) &
(Dmaxneg(nneg+1)<=Driftult*h)
        re=(Pmaxneg(nneg+1)*(1-a)-
gama*Fu)/(K0*Dmaxneg(nneg+1));
        display('re curvo')
    else
        re=0;
        display('re zero')
    end
end
F(i)=sign(D(i))*gama*Fu+re*K0*D(i);
display('reloading')

if abs(F(i))>abs(E(i))& abs(D(i))>Dp_i
    F(i)=E(i);
    display('reloading envelope')
end
else %loading envelope

    if abs(F(i-1))>abs(E(i-1))
        F(i)=F(i-1);
        display('loading envelope r1')
    else
        F(i)=E(i);
        display('loading envelope')
    end
end
dou=abs(D(i));
fou=abs(F(i));

elseif D(i)*(D(i)-D(i-1))<0 %unloading
    if D(i-1)*F(i-1)<0
        kull=gama*Fu/(alfa*dou);
        F(i)=kull*D(i)-sign(D(i))*gama*Fu;
        display('unloading linear')
    else
        Ku=fou/(dou*(1-alfa));
    end
end

```

```

lmbd_u=-0.0866*log(dou)+0.4593;
F(i)=sign(D(i))*(Ku*(abs(D(i))-alfa*dou)*exp(lmbd_u*(abs(D(i))-dou)));
display('unloading exponential')
end
elseif D(i)==D(i-1)
F(i)=F(i-1);
display('Di=Di-1')

elseif D(i)==0
if (D(i-1)>0)|(F(i-1)<0)
F(i)=-gama*Fu;
elseif (D(i-1)<0)|(F(i-1)>0)
F(i)=gama*Fu;
end
display('Di=0')
end

figure (1)
subplot (2,1,1)
hold on
plot (D,'r.-')
title ('Displacement history')
xlabel ('Time')
ylabel ('Displacement (mm)')

subplot (2,1,2)
plot (D,E,'m.')
title ('Envelope')
xlabel ('Displacement (mm)')
ylabel ('Envelope (kN)')
hold off

figure (2)
hold on
plot (D,F,'b.-')
title ('Hysteresis')
xlabel ('Displacement (mm)')
ylabel ('Force (kN)')

y = [D;F];
fid = fopen('D_F.txt','w');
fprintf(fid,'%4f %12.8f\n',y);
fclose(fid);

```